UNIVERSITY OF SAO PAULO
ESCOLA POLITÉCNICA
MECHANICAL ENGINEERING PROGRAM

BEETHOVEN NARVÁEZ-ROMO

AN EXPERIMENTAL STUDY OF AN AMMONIA-WATER ABSORPTION REFRIGERATION CYCLE USING A NOVEL MODIFIED HORIZONTAL LIQUID FILM ABSORPTION SYSTEM

Sao Paulo

2020

BEETHOVEN NARVÁEZ-ROMO

AN EXPERIMENTAL STUDY OF AN AMMONIA-WATER ABSORPTION REFRIGERATION CYCLE USING A NOVEL MODIFIED HORIZONTAL LIQUID FILM ABSORPTION SYSTEM

Thesis submitted in partial fulfillment of the requirements for the Degree of Doctor in Science of Mechanical Engineering (Energy and Fluids) at the Escola Politécnica of the University of São Paulo

Supervisor: Dr. José Roberto Simões-Moreira

University of Sao Paulo

Escola Politécnica

Revised version

Sao Paulo

2020

Autorizo a reprodução e divulgação total ou parcial deste trabalho, por qualquer meio convencional ou eletrônico, para fins de estudo e pesquisa, desde que citada a fonte.

Este exemplar foi revisado e corrigido em relação à versão original, sob responsabilidade única do autor e com a anuência de seu orientador.

São Paulo, ______ de ____________________ de __________

Assinatura do autor: ________________________

Assinatura do orientador: ________________________

Catalogação-na-publicação

Narváez-Romo, Beethoven
Estudo experimental do ciclo de refrigeração por absorção de amônia-água usando um novo sistema de absorção de filme horizontal / B. Narváez-Romo - versão corr. -- São Paulo, 2020.
245 p.

Tese (Doutorado) - Escola Politécnica da Universidade de São Paulo. Departamento de Engenharia Mecânica.

1.Amônia 2.Transferência de Calor 3.Filme horizontal 4.Refrigeração 5.Absorção I.Universidade de São Paulo. Escola Politécnica. Departamento de Engenharia Mecânica II.t.

BEETHOVEN NARVÁEZ-ROMO

AN EXPERIMENTAL STUDY OF AN AMMONIA-WATER ABSORPTION REFRIGERATION CYCLE USING A NOVEL MODIFIED HORIZONTAL LIQUID FILM ABSORPTION SYSTEM

Thesis submitted in partial fulfillment of the requirements for the Degree of Doctor in Science of Mechanical Engineering (Energy and Fluids) at the Escola Politécnica of the University of São Paulo

Trabalho aprovado. Sao Paulo, 29 de Julho de 2020:

Prof. Dr. José Roberto Simões Moreira – USP (Advisor)

Prof. Dr. Gherhardt Ribatski – EESC/USP

Prof. Dr. Enio Pedone Bandarra Filho – UFU

Prof. Dr. Nisio de Carvalho Lobo Brum – UFRJ

Prof. Dr. Benoit Stutz – UNIV-SMB

BANCA EXAMINADORA

Prof. Dr. José Roberto Simões-Moreira	Instituição EP-USP
Julgamento Aprovado	Assinatura

Prof. Dr. Gherhardt Ribatski	Instituição EESC/USP
Julgamento Aprovado	Assinatura

Prof. Dr.Prof. Enio Pedone Bandarra Filho	Instituição UFU
Julgamento Aprovado	Assinatura

Prof. Dr. Nisio de Carvalho Lobo Brum	Instituição UFRJ
Julgamento Aprovado	Assinatura

Prof. Dr. Benoit Stutz	Instituição UNIV-SMB
Julgamento Aprovado	Assinatura

Sao Paulo

2020

To Júlia and Jhuly

Acknowledgements

First, I would like to thank Prof. Simões-Moreira for the supervision of this thesis. His support was not only limited to the technical field; but he was also fundamental for my personal growth as a researcher. Moreover, the experimental test rig was built partly through the funding from SISEA research team, under the supervision of Prof. Simões-Moreira. Based on our collaborative work and his ingenious solutions, we were able to build a unique and innovative test rig to study the ammonia-water absorption refrigeration cycle. Last but not least, I am grateful for his sincere and trustworthy friendship.

I must express the deepest gratitude to Jhuly and Júlia for their patience and tenderness, respectively. Jhuly's patience gave me time and self-confidence, and Júlia's tenderness filled me with motivation and optimism to finish my Ph.D. program. Also, in memory of my father and mother, I would like to thank them for giving me life. Also, I want to thank my siblings and my whole family, especially Dario Narváez for being my confident.

I would like to extend my acknowledgements to Prof. Dr. Marcos Pimenta and Dr. Jose L. de Paiva. Their comments in the qualification examination were taken into account for the improvement of this thesis. Also, I would like to mention gratitude to Prof. Dr. Silvio de Oliveira and Prof. Dr. Gherhardt Ribatski for sharing the academic experience through their grad coursed. During my Ph.D., I also participated in the thematic project led by Prof. Dr. Ribatski, who helped us with procedures related to the FAPESP funding. Also, I am glad for Prof. M. Chhay of the University of Savoie for the technical discussions and works we have carried out in collaboration. Finally, I want to thank Prof. E. Zavaleta-Aguilar for sharing his experiences about the first experimental apparatus.

I want to thank Amonex do Brasil company and Mr. Werner Flister for the essential help supplying ammonia and advicing us about the best ways to safely manipulate and load the circuit. Let me thank Werner, for his time, and his technical assistance during off-work hours.

Let me extend the acknowledges to my fellows at the Renewable and Alternative Energy Systems Laboratory - SISEA, especially Thyago Miranda for his remarkable collaboration in the manufacturing and assembling of the experimental design. Also, I would like to thank Andrés for his companionship, even for those days that we were working 24 hours continuously at the laboratory. I want to thank Wellorzzon for the holidays worked. Go ahead with this project. Also, I would like to thank Adrienne, Claudio, Eliane, Gustavo, and the other colleges. Furthermore, I want to thank Daniel, Luis, Julian, Sebastian and Rubén for the social interactions and technical discussions during the Ph.D. program. Finally, I would like to thank

Edivaldo and Jefferson for the technical discussions about the automation of the experimental apparatus.

I would like to thank National Research Council (CNPq) and the Administrative Department of Science, Technology and Innovation (COLCIENCIAS) for the personal support. Also, São Paulo Research Foundation (FAPESP), grant No. 2016/09509-1 for the project funding. Finally, I would like to thank FUSP for the personal support during the last months.

Abstract

Narváez-Romo, Beethoven. **An experimental study of an ammonia-water absorption refrigeration cycle using a novel modified horizontal liquid film absorption system** 2020. 244 f. Thesis (PhD program) - Mechanical Engineering Program: Energy and fluids, University of Sao Paulo, Sao Paulo, 2020.

The falling film technology has been widely used in different engineering applications, including in the absorption refrigeration cycles (ARC) because it has a huge potential to be used for heat recovery from thermal sources and from solar energy. Open-source literature review shows different studies over the heat and mass transfer (HMT) behavior for both absorption and generation processes, demanding more experimental results in this field. Moreover, the wettability problems are still present in liquid falling film applications. Therefore, the current work deals with an experimental test rig of an ARC for a 1500 W cooling capacity, allowing to study the absorption process in real operational conditions. Furthermore, the present research study the heat and mass transfer absorption process in a novel configuration, using a horizontal liquid film in ammonia-water mixtures. Firstly, a complete literature review on falling film technology focused on the HMT study in sorption processes was carried out, in which both ammonia-water and lithium bromide-water working fluid were analyzed. Based on that review, a HMT mapping for the most common working fluid was obtained by using a modeling of the absorption refrigeration system. Secondly, a modeling of the ammonia-water absorption process using a new proposal of heat and mass exchanger in which the total wettability is guaranteed was developed. A mathematical model based on the overall balance of mass, ammonia species, and energy equations was carried out. Finally, an ammonia-water absorption refrigeration test was projected, built and tested, in which it allowed studying the ARC as a function of several operational parameters such as strong mass flow rate, generation temperature, weak solution temperature, concentrations, and absorption pressure. Moreover, the horizontal modified liquid film absorber was tested in real operational conditions. According to the theoretical studies, a HMT mapping were obtained for those experimental and analytical correlations, obtaining the possible operating range of the Nusselt number and Sherwood number in some typical operational conditions from ARC's. The heat and mass transfer coefficients were strongly enhanced as the absorption refrigeration cycle achieved vaporization temperatures below $0°C$ for ammonia-water working fluid. Moreover, a parametric study of the ammonia-water absorption process was carried out. Absorber heat rate was improved by using lowest surface temperature and lowest liquid film thickness. Also, studies showed absorption heat rejection decreases as a function of the position into the absorber, whose first plate absorbed about 30% of the total heat of absorption. Based on experimental studies, results showed the operation of the ammonia-water absorption refrigeration cycle, achieving temperatures below $0°C$.

Keywords: Ammonia-water. Absorption process. Heat and mass transfer. Total wettability. Horizontal film. Falling film. Absorption refrigeration cycle

Resumo

Narváez-Romo, Beethoven. **Estudo experimental do ciclo de refrigeração por absorção de amônia-água usando um novo sistema de absorção de filme horizontal** 2020. 244 f. Tese de Doutorado (PhD program) - Programa de Pós-Graduação em Engenharia Mecânica da Escola Politécnica, Universidade de São Paulo, 2020.

A tecnologia por filme descendente tem sido estudada em diferentes aplicações de engenharia; incluindo seu uso em ciclos de refrigeração por absorção (ARC) devido ao grande potencial para serem instalados com fontes de energia residual e energia solar. A revisão bibliográfica apresenta diferentes estudos do comportamento da transferência de calor e massa (HMT) nos processos de geração e absorção, demandando mais resultados experimentais. Ainda, os problemas de molhabilidade seguem presentes em aplicações de filme descendente. Desse modo, o presente trabalho foca-se em projetar e construir uma bancada experimental de um ARC com capacidade frigorifica de $1500W$, permitindo estudar o processo de absorção em condições reais de operação. Também, estuda-se o processo de HMT no processo de absorção em uma nova configuração usando um filme horizontal líquido de solução de amônia-água. Inicialmente, uma detalhada revisão bibliográfica sobre tecnologia de filme descendente focada ao estudo da HMT nos processos de sorção para os fluidos mais comuns foi levantada. Baseado nessa revisão e no modelamento desses ciclos, o mapeamento da HMT para os fluidos mais comuns foi obtido. A seguir, o modelo do processo de absorção usando a nova configuração do trocador de calor e massa caracterizado por uma molhabilidade total foi desenvolvida. O modelo matemático foi baseado nas equações de balanço total de massa, espécie amônia e energia. Finalmente, uma bancada do ARC foi projetada, construída e testada, permitindo estudar o ciclo em função de vários parâmetros de operação como vazão mássica da solução forte, temperatura de geração, temperatura da solução fraca, concentrações, e pressão de absorção. Além disso, o absorvedor de filme líquido horizontal foi testado em condições reais de operação. De acordo aos estudos teóricos, um mapeamento do HMT para essas correlações experimentais e analíticas foi alcançado, obtendo a faixa operacional possível do número de Nusselt e do número de Sherwood em algumas condições operacionais típicas dos ARCs. Os coeficientes de HMT foram aprimoradas à medida que o ARC opera em temperaturas de vaporização abaixo de $0°C$ para a solução de água-amônia. Um estudo paramétrico do processo de absorção de amônia-água foi realizado, sendo que a taxa de calor do absorvedor foi melhorada usando a menor temperatura da parede e a menor espessura do filme líquido. Estudos mostraram que taxa de rejeição do calor de absorção diminui em função da posição no absorvedor, cujo primeiro prato absorveu aproximadamente 30 % do calor total de absorção. Com base em estudos experimentais, os resultados mostraram a operação do ARC de água-amônia, atingindo temperaturas abaixo de $0°C$.

Palavras-chaves: Amônia-Água. Processo de absorção. Transferência de calor e massa. Molhabilidade total. Filme horizontal. Filme descendente. Ciclos de Refrigeração por absorção

List of figures

List of tables

List of abbreviations and acronyms

ABS	acrylonitrile butadiene styrene
ARC	absorption refrigeration cycle
COP	coefficient of performance
CV	control volume
DMAC	dimethylacetamide
EES	Engineering Equation Solver
EG	ethylene glycol
EH	ethyl hexanol
EPDM	ethylene propylene diene monomer rubber
EV-1	expansion valve for the ammonia solution
EV-2	expansion valve for the ammonia-water solution
GAX	generator-absorber heat-exchange
Hg	mercury
HIM	human-machine interface
HR	heat recovery
H_2	hydrogen
H_2O	water
H_2SO_4	sulfuric acid
HPS	high-pressure switch
HTS	high-temperature switch
ILs	ionic-liquids
Li-Br	lithium bromide

$LiNO_3$	lithium nitrate
NI	National Instruments
N_2	nitrogen
NH_3	ammonia
NPT	National Pipe Thread Taper
OSF	offset strip fins
PID	proportional-integral-derivative
PLC	programmable logical controller
VC, Vg, Vp, Vh, Va	valves
Vref	relief valve
VFD	variable frequency drive
VCRC	vapor compression cycle
TFE	trifluoroethanol
TiO_2	titanium dioxide
TR	ton of refrigeration
TRi; i:1-4	external wall temperature at the generator
SC	subcooler
SISEA	Renewable and Alternative Energy System Laboratory
SR	theoretical strong solution rate, Eq. (3.5)

List of symbols

A	area, [m^2]
Ar	Archimedes number, $Ar = D^3 g/\nu^2$, [-]
C_v	flow coefficient, [-]
c_p	specific heat at constant pressure, [J/kg°C]
c_t	mixture molar density, [mol/m^3]
c_a	total molar concentration of ammonia, [mol/m^3]
D	diameter, [m]
D^*	dimensionless diameter, $D^* = D/L_c$, [-]
D_h	hydraulic diameter, [m]
D_{aw}	mass diffusivity, [m^2/s]
e	Euler's number, [-]
E_T	Ackermmn's correction factor, Eq. (2.6) [-]
E_v	Energy heat rate across the interface [W]
f	fouling factor, [-]
f_f	friction factor, [-]
g	acceleration of gravity, [ms^2]
G	mass velocity, [kg/m^2 s]
Ga	Galileu number, $Ga = 1/Ka$, [-]
Gr	Grashof number, $Gr = g\beta_T(T_w - T)/\nu^2$, [-]
h	heat transfer coefficient, [W/m^2 °C]
h^*	corrected heat transfer coefficient, [W/m^2 °C]
i	specific enthalpy, [J/kg]

i_{lv}	vaporization specific enthalpy, [J/kg]
ID	internal diameter, [m]
Ja	Jakob number, $c_p(T_w - T_{sat})/\ \Delta i_{vap}$, [-]
J_H	heat transfer factor, Eq. (2.12) [-]
J_D	mass transfer factor, Eq. (2.13) [-]
k	thermal conductivity, [W/m°C]
k_m	mass transfer coefficient, Eq. (2.22) [m/s]
k_m^*	mass transfer coefficient, Eq. (2.21) [mol/m^2 s]
Ka	Kapitza number, $Ka = g\mu^4/\rho\sigma^3$, [-]
L	length, [m]
L_c	characteristic length or viscous length scale, $L_c = (\nu^2/g)^{1/3}$, [m]
Le	Lewis number, $Le = \mathrm{Sc}/\mathrm{Pr}$, [-]
ln	natural logarithm, [-]
M_m	molecular weight, [kg/mol]
$\dot{m}$	mass flow rate, [kg/s]
$\dot{m}''$	mass flux, [kg/m^{2}s]
$\dot{m}'$	mass rate per length unit, [kg/s m]
N	number of tubes, or plates, [-]
N_{to}	number of turns open [-]
n_a	molar flux, [mol/m^2 s]
n	number of mols, [mol]
Nu	Nusselt number,$\mathrm{Nu} = h\delta/k$, [-]
OD	outer diameter, [m]
P	pressure, [bar] or [Pa] in Eq. (2.18)
P_{wet}	wet perimeter, [m]
ppm	parts per million
Pr	Prandtl number, $\mathrm{Pr} = c_p\mu/k$, [-]
q''	heat flux, [W/m^2]

$\dot{q}$	heat rate, [W]
$\dot{q}'$	heat rate per length unit, [W/m]
Re	Reynolds number, $Re = 4\Gamma/\mu$, [-]
$\Re$	universal gas constant, $\Re = 8314$ [J/mol K]
Rt	thermal resistance, [;°C/W]
S	tube spacing, [m]
s^*	dimensionless vertical tube spacing, $s^* = S/D$, [-]
Sc	Schmidt number, $\mathrm{Sc} = \nu/D_m$, [-]
Sh	Sherwood number, $\mathrm{Sh} = k_m\, L_c/D_m$, [-]
St	Stanton number, $\mathrm{St} = h/\rho\, c_p\, \mu$, [-]
T	temperature, [°C] or [K] in Eq. (2.18)
U	overall heat transfer coefficient, [W/m^2 °C]
v	velocity, [m/s]
V	volume, [m^3/s]
v	specific volume, [m^3/kg]
$\dot{\mathrm{V}}_s s$	volume flow rate [l/h]
W	width or depth, [m]
w	concentration by weight, [kg/kg]
x	concentration-liquid [mol/mol]
y	concentration-vapor [mol/mol]
z	condensing flux concentration [mol/mol]

Greek symbols

β	flat plate inclination angle, [°]
β_T	coefficient of thermal expansion, [1/K]
δ	film thickness, Eq. (2.26) [m]
ΔT	temperature difference, [°C]
ΔT_{lm}	log mean temperature difference, Eq. (2.10) [°C]

Δx_{lm}	log mean concentration difference, Eq. (2.11) [-]
Γ	mass flow rate per length unit on each plate side, [kg/s m]
μ	dynamic viscosity, [Pa s]
ν	kinematic viscosity, [m^2/s]
ρ	mass density, [$\mathrm{kg/m}^3$]
τ_v^*	non-dimensional shear stress, [-]
θ	tube angle or wettability of the tube, [°]

Subscripts

a	ammonia
abs	absorber/absorption
b	bulk
c	cooling/coolant
con	condenser/condensation
$conv$	convective
eq	equilibrium
eva/vap	evaporator/evaporation
g	generator/generation
gen	generator/generation
i	inlet
in	inlet
int	interface
l	liquid
latent	latent
o	outlet
oil	thermal oil
out	outlet
pl	plate

rect	rectifier/rectification
seg	segmented
sen	sensible
sol	solution
ss	strong solution
sub	subcooling
t	total
v	vapor
w	wall or water
ws	weak solution

Superscripts

-	average
i	i^{th} iteration

Table of contents

Chapter 1

INTRODUCTION

Absorption refrigeration cycles (ARC) are driven by using solar energy (Alobaid et al., 2017), waste heat from thermal processes, being ammonia-water and lithium bromide-water working fluids are the dominant technologies. Several test rig has been built; Jiang et al. (2019) built a single effect absorption refrigeration with 3 kW cooling capacity using ammonia-water as working fluid, in which the influence of nanoparticles on the coefficient of performance (COP) is investigated, showing that titanium dioxide (TiO_2) nanoparticles improved the COP of the cycle by 27% when it used a falling film absorber. Han et al. (2014) studied an ammonia-water absorption refrigeration cycle for 11.67 kW cooling capacity driven by low-grade waste heat. Abed et al. (2017) carried out an experimental evaluation of single effect ejector-absorption cycle driven by solar energy. Most of these studies employ falling film technology.

In the last ten years, it has been published 6244 papers having “falling film” as keyword, with 24.5%, 15.1% and $1,3\%$ of these researches were developed in China, USA, and Brazil, respectively. 46% of them are related to the engineering field, especially focused on the studies of heat and mass transfer, as it is shown in *International Journal of Heat and Mass Transfer*, and others scientific journals such as *Heat Transfer Engineering*, *Applied Thermal Engineering*, *International Journal of Refrigeration*, *International Journal of Multiphase*, *Journal of Heat Transfer*. More than 20% of these researches have been developed in the engineering field (SCOPUS-2018), which says, it has been a relevant topic in the last decade.

The falling film technology has been widely used in different engineering applications; some of them are in connection with evaporation processes in the food industry, desalination, and refrigeration processes, just to mention a few. Concerning refrigeration systems, this technology has been deeply studied and continuously developed, especially in absorption refrigeration, because it has a huge potential to be used with heat recovery sources and solar energy. In that way, most of the falling film technology researches have been focused on the design of absorber and desorber components, which have a great importance in the proper cycle operation.

Concerning the heat and mass transfer behavior in sorption processes, several studies have been developed for obtaining empirical correlations. For example, Jeong et al. (1998), Kang et al. (1999), Lee et al. (2002a), Kwon and Jeong (2004), Lee (2007), Bohra (2007), Zavaleta-Aguilar and Simões-Moreira (2015), just to mention a few. However, there are still many challenges to be solved at the phenomenological level. Also, partial wettability is the main problem to use falling film technology as was mentioned by Ribatski and Jacobi (2005).

According to the phenomenological aspects, the challenge is to obtain correlations for real operational ranges of heat and mass transfer for absorption refrigeration cycle; e.g. Jeong et al. (1998) found a heat transfer correlation through Nusselt number, which it only depends on the variation of the Reynolds number. However, mass transfer effects over heat transfer coefficients were not taken into account. Also, the operational condition effects such as pressure, temperature, and concentration over the hydrodynamic and thermal boundary layer were neglected. Kwon and Jeong (2004) treated the Nusselt number just as a function of Reynolds Number, so, they took into account another non-dimensional number to consider of shear effects at the interface. Also, the mass transfer was neglected.

Kang et al. (1999) studied the falling film technology based on extremely low mass flow rate, which was obtained for low Reynolds numbers (15 to 24), a range in which the wettability effects should have great importance over the heat and mass transfer processes. In constructive and operational terms that Reynolds number range may represent a large generation of dry out zones. Moreover, they carried out experimental studies for operational conditions completely out from real operations of an absorber, for example, the inlet temperature of vapor to the absorber ranged above 54.5°C, and the ammonia vapor with a lower purity (maximum value 66.5 % in the mass ratio).

Lee et al. (2002a) studied falling film technology using the model established by Kang et al. (1999). The correlation presents an upper operational range for the Reynolds numbers. However, the ammonia concentration ranged between 10 to 30 % at constant pressure of 101.3 kPa. For the absorption cycle operation, those correlations could be applied to a fixed temperature value at the evaporator, limiting its use for air-conditioning applications, in which the absorber could work at high pressures values. Those correlations were obtained using commercial heat exchangers. Lee (2007) and Bohra (2007) also studied the falling film technology in wide operational ranges, using the same test model established. They used the falling film technology over a horizontal tube bank, where the heat and mass transfer were analyzed inside the absorption process. The Nusselt number as a function of non-dimensional numbers such as Reynolds, Prandtl, and a non-dimensional operational pressure number. In another way, the mass transfer was correlated and expressed by the Sherwood number. They worked with ammonia mass fraction up to 40 %.

In the last years, a continuous attempt to the miniaturization and compactness of the ARC has been carried out; ionic liquid working fluids (Wang; Ferreira, 2017), (Kühn et al., 2020), new pool boiling generator (Staedter; Garimella, 2018a), even a first miniaturized generator-rectifier (Keinath et al., 2019). Although the technical development of such machines has reached an acceptable maturity for industrial purposes, research is still active as more experimental work and theoretical analysis are necessary. For example, one of the challenges consists in reducing electrical consumption and increasing the compactness of sorptions machines to integrate them into other environments (high-efficiency buildings, transport, solar-driven machines, to mention a few new applications). The conception of new technologies implies appropriate sizing rules, depending on the transfer mechanisms. In the open-source literature, the existing correlations to design absorbers show the evolution of each research developed, exposing that the phenomenological aspects of the absorption process applied to refrigeration cycles has not been completely developed, which means that this subject requires more attention. Thus, the experimental study of the ammonia-water absorption refrigeration cycle is still relevant. So, the project's aims follow;

1.1 Objectives

This thesis aims the design, project and test of an ammonia-water absorption refrigeration test rig, in which it allows studying the absorption process and the distillation process as a function of several operational conditions. Also, the new configuration of the absorber aims to improve the wettability problem by introducing the novel modified horizontal liquid film absorption system. The heat and mass transfer coefficient are studied for both absorption and generation processes.

1.2 Organization of the Thesis

This thesis shows an experimental study of the ammonia-water absorption process applied in a real operational conditions for an absorption refrigeration cycle, aiming to analyze the behavior of the heat and mass transfer processes. The organization of this work is as follows.

- Chapter 2 presents the literature review of the falling film technology focused on absorption refrigeration cycles, in which the heat and mass transfer coefficients and non-dimensional numbers are defined. In this part, experimental correlations for the ammonia-water working fluid in ARC's are documented.

- Chapter 3 focuses on the operating principles of the main ARC components that are affected by the equilibrium conditions of the ammonia-water mixture. Also, it defines the molar concentration, highlighting the mass transfer analysis approached from the molar basis, an explanation of the binary diagram for the ammonia-water mixture by establishing relations from temperature-concentration, and enthalpy-concentration diagrams. Consequently, a schematic representation of the distillation and absorption processes is displayed and finally, the current study determines the heat and mass transfer operating range regarding the experimental correlations.

- Chapter 4 shows the absorption process modeling in the new configuration; horizontal liquid film. A mathematical model based on the overall balance of mass, ammonia species, and energy equations is carried out. These equations are solved for a set of control volumes discretized by the finite-difference method and with the heat and mass transfer correlations. A parametric study of the absorption process was performed: surface temperature, plates number, and liquid film thickness.

- Chapter 5 describes the experimental proposal to study the ammonia-water absorption refrigeration cycle and the heat and mass transfer coefficient over a modified horizontal liquid film absorber, detailing the ARC and its three different liquid circuits. Also, it delineates the heat exchanger absorber manufacturing, the safety conditions, and procedures about the ARC. Finally, the instrumentation, data acquisition, and automation machine are defined for the new test rig supported by Thematic Project - FAPESP N 2016/09509 – 1.

- Chapter 6 presents a detailed description of the results and data reduction of the first set of experimental results. The horizontal liquid film absorption and the falling film generator are analyzed, finding the heat and mass transfer coefficients. Finally, a comparison between the current and the available in the literature is developed.

- Chapter 7 consolidates some conclusions and suggestion for future works.

Chapter 2

LITERATURE REVIEW AND THEORETICAL ASPECTS

2.1 Absorption Refrigeration Cycle

Edmond Carré developed the first absorption refrigeration machine in 1850 using a water and sulphuric acid (H_2SO_4) mixture as the working fluid pair, requiring a large quantity of this acid to absorb a small amount of water vapor, in order to achieve the refrigeration effect. However, in 1859, Ferdinand Carré used the ammonia-water pair as working fluid, because of its properties: stability, low normal boiling point, and good ammonia affinity to water (Elvas et al., 2010). Their machine is schematically shown in Fig. (2.1). Currently, lithium bromide-water (LiBr-H_2O) and ammonia-water (NH_3-H_2O) pairs have been the most common working fluid pairs used in commercial ARC. The former operates in vacuum such as in Edmond Carré's machine, and the latter one in a positive pressure, such as in Ferdinand Carré 's machine.

An ARC is constituted by two pressure levels as depicted in Fig. 2.2; the low-pressure level (evaporator and absorber) and the high-pressure level (generator and condenser). These two levels are connected by two expansion valves and one solution pump, in its simplest configuration. The solution pump drives the strong liquid solution from the absorber to the generator in ammonia-water technology. At the generator, the solution flows overheated surface in the falling film generator, whose function is to separate the refrigerant from the liquid solution by using an external heat thermal source $\dot{Q}_{gen}$. Next, the vapor refrigerant is driven to the condenser, rejecting the heat to the environment $\dot{Q}_{con}$. The condensed refrigerant reaches the evaporator, passing through an expansion valve EV-1 and reducing the pressure and its temperature by the Joule-Thomson effect to receive the heat load $\dot{Q}_{eva}$ by the evaporation process. Next, the vapor refrigerant enters the absorber at the vapor state, in which it is absorbed by the weak solution becoming the generator after passing the expansion valve EV-2, and the heat is rejected $\dot{Q}_{abs}$ to an external coolant as the absorption process takes place. Then, the solution is pumped to the generator closing the cycle. The strong solution passes through a heat exchanger before it enters to the generator, pre-heating the solution by using the weak solution in a counter flow configuration.

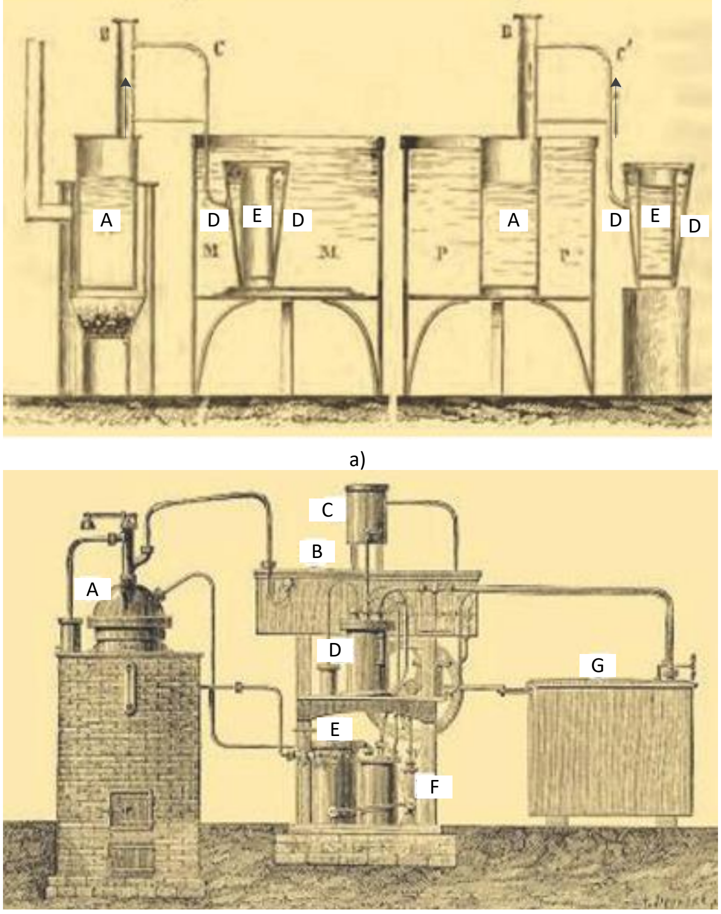

a)

b)

Figure 2.1 – *Apparatus for ice production by Ferdinand Carré; a) production by batches - Letter A: Generator/Absorber, D:Water coolant/Cooled water E:Condenser/Evaporator, and b) industrial production -200kg/h Elvas et al. (2012) Letter A: Generator, B: Condenser, C: Water coolant, D: Absorber, E:Pre-cooler, F: Solution pump, G: Evaporator*

It is worth mentioning that both the absorber and the generator are the main components of the absorption system because there is a simultaneous heat and mass transfer process (Yüksel; Schlünder, 1987a), in which the refrigerant changes phase (Fujita, 1993). In addition, the heat and mass transfer coefficients in those components are characterized by low values (Castro et al., 2009). On the other hand, when an ARC is compared with a vapor compression cycle (VCRC), the former has a lower coefficient of performance (COP)[1], particularly if the absorption machine works beyond its design specifications, e.g. the vaporization temperature, or the cooling thermal load due to the problem of partial evaporation at the evaporator. Additionally, the COP is also sensitive to the heat source temperature in the desorber, the cooling temperature of the evaporator, and the flow rate of the strong solution. Therefore, enhancing the heat and mass transfer process leads to a reduction in costs and in sorption machine size.

Jennings (1935) carried out an experimental study using 1.6 bar steam as the heat thermal source keeping about 115°C for a strong solution and weak solution concentration of w= 39.5 and w= 32.7 % by weight, respectively. All the heat exchangers were built as a flooded configuration in a shell-tube type. It finds that the thermal energy consumption per weak solution mass flow

---

[1] However, an ARC only demands 2% from compressor power consumption (See Appendix. A)

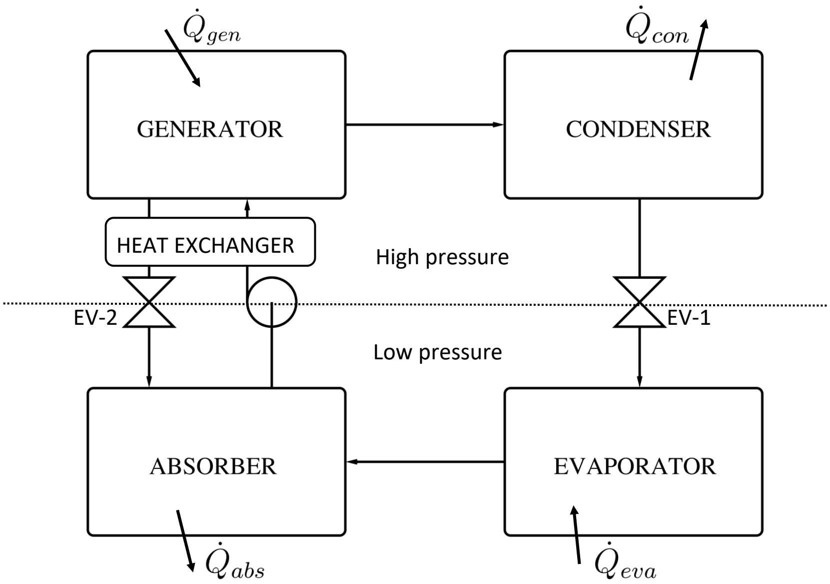

Figure 2.2 – *Schematic diagram of a single-stage absorption refrigeration cycle in which the horizontal dot line separates the high pressure level from the low pressure level*

rate follows as linear fashion, approximately. In 1942, Jones (1942) improved the rectifier of ammonia ARC, increasing the purity degree of ammonia vapor due to the low purity of distilled implies to increase the refrigerant ratio circulating through the evaporator. Moreover, it may create a thermal insulation by ice formation in temperatures below 0°C. Also, Jones (1942) introduced the falling film technology in the new absorber configuration.

The literature review is hitherto focused on some specific category of study: Thome (1999) reviewed of falling film evaporation on both smooth and enhanced tubes focusing on working fluids as alternative refrigerants including ammonia; he found that the falling film technology provides a higher heat transfer coefficient than flooded evaporators. Killion and Garimella (2001) carried out a complete critical review on falling film technology in absorption processes, in which these efforts are focused on analyzing the mathematical model that has been used to the simultaneous heat and mass transfer processes. Ribatski and Jacobi (2005) carried out a critical review of the falling film evaporation process over horizontal tubes (single and tube bundles), covering hydrodynamic studies and the heat transfer coefficient affected by several operation conditions on smooth and enhanced tubes. They pointed out that the falling film technology presents inconveniences due the liquid film maldistribution and dry-out problems, being that these problems may be reduced by the installation of a wire mesh over the distributor (Narváez-Romo; Simões-Moreira, 2014). Other distribution system were optimized by Yi et al. (2020) in a new prototype of the liquid film distributor over a detachable plate falling film. Prost et al. (2006) analyzed the heat transfer behavior of falling film evaporator under several operation conditions for the food industry. They reported some Nusselt number correlations from the literature. Narváez-Romo and Simões-Moreira (2013) carried out a literature review of falling film evaporation, studying the parameters affecting the heat transfer coefficient. Tomforde and Luke (2012) carried out a literature review on falling film absorbers focused on horizontal tubes only, in which lithium bromide-water, and R134a-Dimethylacetamide (DMAC) were the working fluid pairs studied. Also, the falling film technology developed for absorption refrigeration cycles was reviewed by Narváez-Romo et al. (2017), defining a heat and mass transfer mapping as a function of the operational conditions. Also, Altamirano et al. (2019) carried out a review of the absorption machine focused on small-capacity single-effect system.

2.2 Coefficient of performance - COP

The coefficient of performance (COP) is defined as the ratio between the cooling capacity $\dot{Q}_{eva}$ and the thermal energy consumption at the generation process $\dot{Q}_{gen}$ as follows;

$$\mathrm{COP} = \frac{\dot{Q}_{eva}}{\dot{Q}_{gen}} \tag{2.1}$$

The Carnot cycle (Carnot, 1824) limits the maximum theoretical efficiency that a machine may achieve. In the absorption refrigeration cycle, some theoretical conditions must be assumed such as the heat transfer processes (generation, absorption, condensation and evaporation) are developed at a constant temperature under reversible process. The concentration difference between the weak solution and the strong solution is neglected, and other hypotheses are summarized in Sofrata (1993). Having reversible processes as isentropic pumping, the condensation heat rate $\dot{Q}_{con}$ must be equal to $\dot{Q}_{eva}$. Also, $\dot{Q}_{gen}$ should be equal to the absorption heat rate $\dot{Q}_{abs}$. Therefore, the COP for an ideal single-effect absorption cycle is defined by Eq. (2.2) (Sofrata, 1993),

$$\mathrm{COP} = \frac{T_{eva} \cdot T_{con}}{T_{gen} \cdot T_{abs}} \left(\frac{T_{gen} - T_{abs}}{T_{con} - T_{eva}} \right) \tag{2.2}$$

T_{con} and T_{abs} is the condensation temperature and the absorption temperature, respectively, T_{eva} is the evaporation temperature and T_{gen} is the generator temperature, in which all these temperatures must be given in the absolute temperature scale, K. Also, Srikhirin et al. (2001) mentioned that the installation of the heat exchanger between both solution streams may improve the COP up to 60 %. In their review, they also detailed possible technologies used in absorption refrigeration machines

2.3 Component size comparison and performance of ARC for several working fluids

Boman et al. (2017) investigated the behavior of several working fluids based on their thermodynamic properties and heat transfer characteristic applied in a single-effect absorption refrigeration cycle operating in heating or cooling mode. They studied eighty-three (83) potential working fluids, even ionic-liquids absorbents (ILs), being defined as salts in a liquid state containing organic cations and organic anions, being sensible to operate in prolonged high temperatures (Kim et al., 2012). They showed in Fig. (2.3a) the coefficient of performance

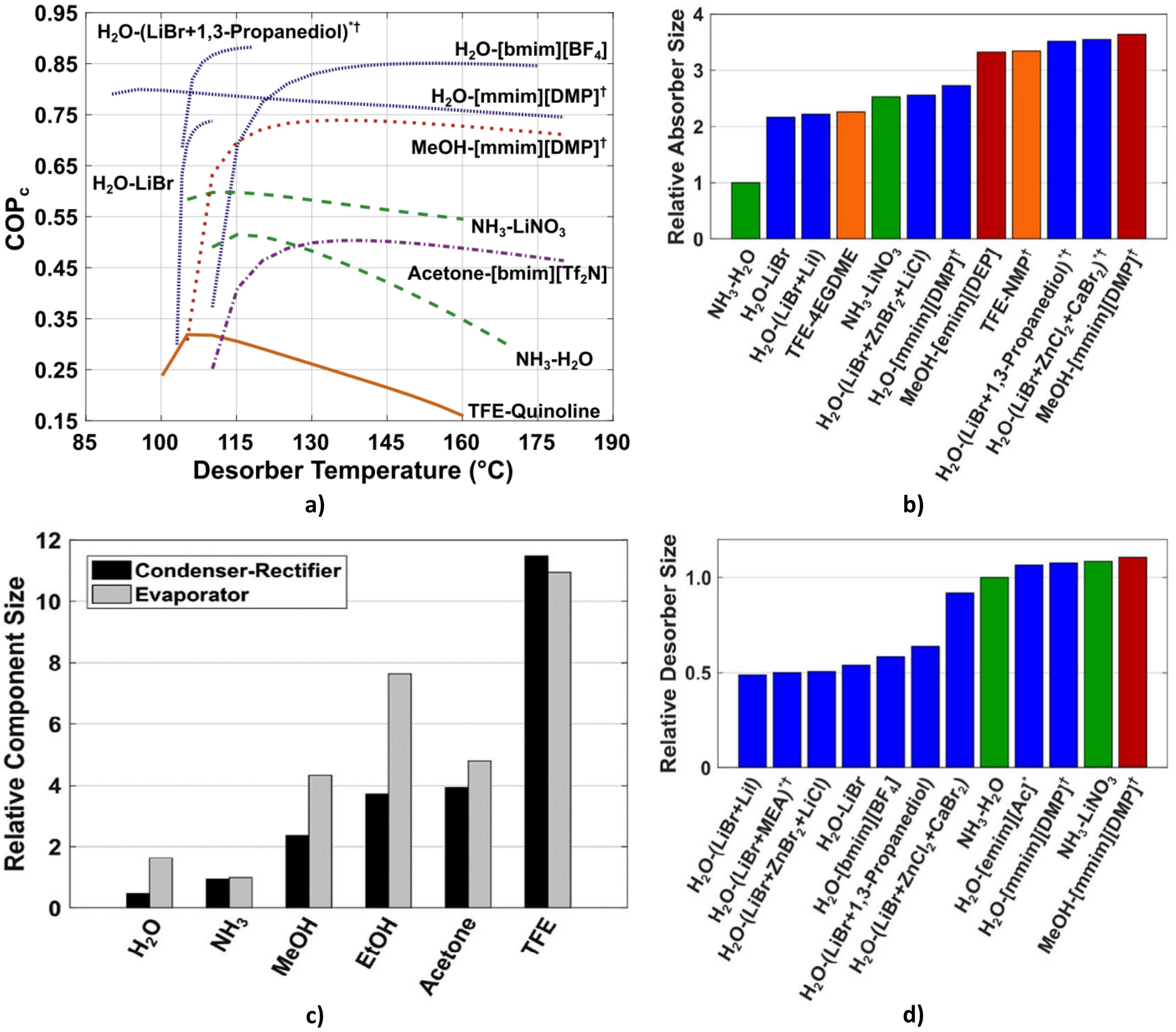

a) b) c) d)

Figure 2.3 – *Analysis of the working fluids (Boman et al., 2017) a) COP for several desorption temperatures, b) comparison of the relative size for the absorber c) condenser and evaporator, and d) generator*

as a function of the generation temperature for several working fluids in which all of them increase to a maximum and then the performance is deteriorated as desorption temperature increases. Based on their studies, it happens as a consequence of high desorption temperature implying low-refrigerant concentrations and demanding a higher energy consumption. However, the explanation may be incomplete because it is false when the absorber is a non-volatile component as the lithium bromide (LiBr) or the lithium nitrate ($LiNO_3$).

Kim et al. (2003) investigated the $2-2-2$ trifluoroethanol (TFE) - quinoline working fluid in a double effect ARC mentioning that in low desorption temperature the effects of the absorbent evaporation may be neglected. Also, they noted the decreasing of the COP as generation temperature increased. It is worthwhile to mention that despite several working fluids present better COP values, the ammonia-water and lithium bromide-water have smaller relative absorber, evaporator and condenser size as shown in Fig. (2.3b and 2.3c). The evaporator size is deeply related to the mass flow rate circulating and having H_2O as refrigerant it must require a minor ratio as the consequence of the latent heat of vaporization of the water, leading a evaporator more compacts. Finally, the ammonia-water desorber is greater than the lithium bromide-water generator as shown in Fig. (2.3d).

Ionic liquid absorbents may be promissory in the future resolving toxicity problems for the ammonia-water mixture and crystallization for the lithium bromide-water. Also, corrosion problems might be mitigated for both cases. However, the studies developed by Kim et al. (2012) in which ionic liquid absorbents are employed with hydrofluorocarbon refrigerants present other disadvantages concerning the substitution of this kind of refrigerant by natural refrigerant fluids. A second alternative is the utilization of the ionic liquid absorbents with water as a refrigerant as shown in Fig. (2.3a). However, the water has a limitation in reference to the evaporation temperature.

2.4 Heat and mass transfer using falling films technology in sorption processes

The current section aims to define theoretical aspects over the heat and mass transfer coefficient calculation, showing a review of the mean definition correlations and the classical hypothesis assumed to compute the heat and mass transfer coefficients. Also, the transfer correlations involving ammonia-water solution systems are discussed, in which each one is classified by application (absorption or desorption) and geometry disposal. Additionally, these correlations are summarized in tables by application range and by test rig specifications as shown in Tabs. (2.2) and (2.3). In the same way, the falling film studies for lithium bromide-water working fluid are well detailed in Appx. (B), where Tabs. (B.2) and (B.3) show the application range of these correlations and a summary of the main numerical/experimental characteristic. Moreover, sorption process modeling usually uses experimental studies carried out with working fluid as water, being the Chun and Seban (1971) and Wilke (1962) studies the most common correlations used in the heat transfer process for ARC. So, a complete revision of these kind of correlations are shown in Appx. (C).

The falling film technology can be used in different applications such as in ARC, having a large heat transfer contact area between the wall surface and the liquid falling film in which it enhances the heat removal for the absorption process case (Yüksel; Schlünder, 1987a). However, the whole heat and mass transfer resistance is concentrated in the thin liquid falling film (Yüksel; Schlünder, 1987a; Taylor; Krishna, 1993). Fig. (2.4a) shows the general falling film technology on horizontal tubes and Fig. (2.4b) the temperature and concentration profiles for the absorptions process in a vertical plate. The generation process is used for evaporation or distillation processes, in which the wall temperature (T_w) is higher than the liquid falling film temperature (T_l), allowing the phase change when the pure substance enters at the saturated condition, or the separation process for no binary azeotrope substance entering at the saturated condition.

On the other hand, in the absorption process, the wall temperature (T_w) is lower than the liquid falling film (T_l), removing the heat of absorption ($\dot{Q}_{abs}$) and absorbing the vapor ($\dot{m}''_{abs}$) into the liquid falling film as shown in Fig. (2.4b), e.g., the heat of absorption is released at the liquid-vapor interface only, yielding an increase of the average film temperature (T_b), which diminishes the vapor solubility and, therefore, the absorption rate is strongly controlled by the intensity of heat removal from the liquid falling film to the coolant ($\dot{q}_c$) (Yüksel; Schlünder, 1987a), while s and S are the inter-tube distances; T_c, T_{int} and T_v are the coolant, interface, and vapor temperature, respectively; x_b, x_{int} and y is the liquid bulk concentration, the concentration of the liquid falling film at the interface, and the vapor concentration, respectively.

2.4.1 Heat and mass transfer coefficient calculation

Thermal resistance analogy is used in falling film technology as shown in Fig. (2.4a), to compute the global or overall heat transfer coefficient (U) between the bulk solution and the cooling or heating fluid, and given by Eq. (2.3),

$$\frac{1}{U} = \frac{1}{\overline{h}_l} + \frac{D_o}{2k_w} \ln\left(\frac{D_i}{D_o}\right) + \frac{D_i}{D_o \overline{h}_c} + f \tag{2.3}$$

where $\overline{h}_l$ is the average heat transfer coefficient on the film, $\overline{h}_c$ is the average convective heat transfer coefficient associated with the secondary fluid, k_w the tube wall thermal conductivity, D_o, and D_i, the external and internal tube diameter, and f represents the fouling factor resistance; $2 \times 10^{-4}\text{m}^2$ °C/W in ammonia-water pair (Kwon; Jeong, 2004; Jeong et al., 1998), or $9 \times 10^{-5}\text{m}^2$ °C/W in lithium bromide-water pair (Florides et al., 2003).

Heat and mass transfer coefficients cannot be directly evaluated from an experimental work. They must be computed from measured quantities (e.g. temperature, concentration, liquid density). This relation involves a difference in temperature, which takes into account, the wall temperature (T_w) and the interface temperature (T_{int}) in most of the cases. However, depending on how viscous sublayers are assumed both near the wall and near the liquid-vapor interface, two partial heat transfer coefficients (h) can be defined (Fig. 2.4b) (Yüksel; Schlünder, 1987a); i) $h_{l,w}$ between the bulk liquid (T_b) and the wall (T_w) as defined in Eq.

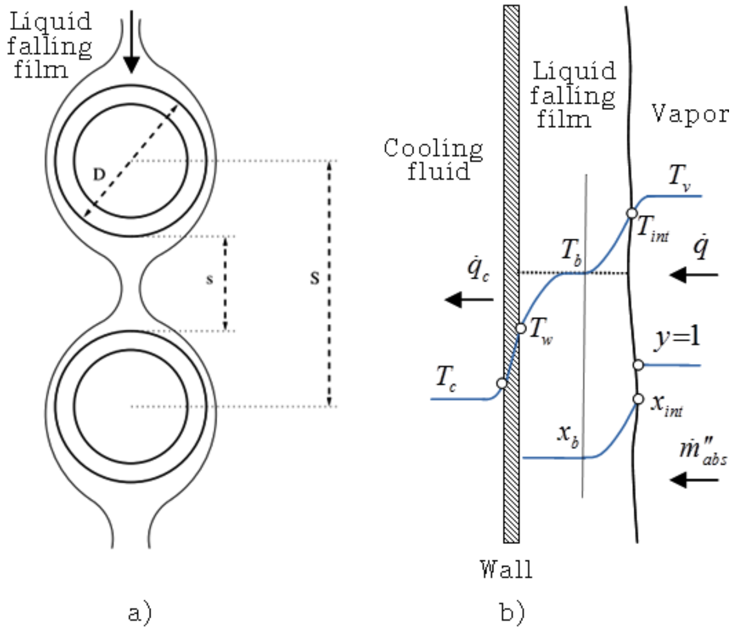

Figure 2.4 – *a) Falling film in horizontal tubes and b) temperature and concentration profiles for the ammonia-water absorptions process in a vertical plate (adapted from (Yüksel; Schlünder, 1987a))*

(2.4), and ii) $h_{l,int}$ between the liquid-vapor interface (T_{int}) and the bulk liquid (T_b) defined in Eq. (2.5),

$$h_{l,w} = \frac{\dot{q}''_c}{T_b - T_w} \tag{2.4}$$

$$h_{l,int} = \frac{\dot{m}''_{abs}\Delta i_{abs}}{T_{int} - T_b}\frac{1}{E_T} \tag{2.5}$$

where, E_T represents the Ackermmn's correction factor given by Eq. (2.6); $\dot{q}_c$, $\dot{m}''_{abs}$ and i_{abs} represent the transferred heat to the cooling fluid, the absorbed mass flow rate per area and the absorption specific enthalpy, respectively; c_p is the specific heat at constant pressure.

$$E_T = \frac{\Delta i_{abs}}{c_p}\frac{\ln(1 + c_p(T_{int} - T_b)/\Delta i_{abs})}{T_{int} - T_b} \tag{2.6}$$

Yüksel and Schlünder (1987a) employed $E_T \cong 1$. This approximation stands for low values of heat flow through the liquid film, assuming a linear profile for temperature (Taylor; Krishna, 1993). Thus, the heat transfer coefficient reads:

$$h_l = \frac{\dot{m}''_{abs}\Delta i_{abs}}{T_{int} - T_w} \tag{2.7}$$

The most commonly used method to compute the overall heat and mass transfer coefficients is the use of the logarithmic mean temperature difference (ΔT_{lm}) due to its simplicity (Fujita; Hihara, 2005). Islam et al. (2003) and Fujita and Hihara (2005) show that the logarithmic mean potential occurring in the overall heat and mass transfer coefficient definition (Eqs. (2.8) and (2.9)) presents wide deviations from experimental results. For this reason, the conventional method takes into account two separate processes of heat and mass transfer; the first one is the heat transfer from the liquid falling film to the cooling fluid, and the second is the absorption of refrigerant from the vapor phase to the coolant, causing errors when there is not a non-linear temperature distribution of the liquid falling film in the absorber cannot be founded. So, the logarithmic mean difference should only be used for low overall heat transfer, (Fujita; Hihara, 2005)

$$U = \frac{\dot{q}'_c}{L\Delta T_{lm}} \tag{2.8}$$

and in the mass transfer coefficient k_m (kg/m^{2}s) definition:

$$k_m = \frac{\dot{m}'_{abs}}{L\Delta x_{lm}} \tag{2.9}$$

where, ΔT_{lm} and Δx_{lm} are the logarithmic mean temperature and concentration differences (Eqs. (2.10) and (2.11)), respectively; $\dot{q}_c$, $\dot{m}_{abs}$, and L are the transferred heat from the liquid falling film to the cooling fluid, the absorbed mass of the vapor refrigerant into the liquid falling film, and the length of the absorber,

$$\Delta T_{lm} = \frac{(T_{l,i} - T_{c,o}) - (T_{l,o} - T_{c,i})}{\ln\left(\frac{T_{l,i} - T_{c,o}}{T_{l,o} - T_{c,i}}\right)} \tag{2.10}$$

where, T_l and T_c are the liquid falling film temperature and the cooling fluid temperature (both i -inlet and o -outlet), respectively; x_{eq} is the interfacial equilibrium concentration in T_l.

$$\Delta x_{lm} = \frac{(x_{i,eq} - x_i) - (x_{o,eq} - x_o)}{\ln\left(\frac{x_{i,eq}-x_i}{x_{o,eq}-x_o}\right)} \tag{2.11}$$

Another way to evaluate the heat or mass transfer coefficient is by employing a heat and mass transfer analogy, in which both transport mechanisms are considered merely diffusional through the liquid falling film (e.g. rectification process). For that, the heat (j_H) and mass (j_D) transfer factors (Chilton; Colburn, 1934) (or dimensionless (Treybal, 1981)) are defined by Eqs. (2.12) and (2.13); h (W/m^2 °C) is the heat transfer coefficient, G (mol/m^2 s) is the mass velocity, c_p (J/kg °C) is specific heat, μ (Pa s) dynamic viscosity, k (W/m K) is the thermal conductivity, k_m (mol/m^2 s) is the mass transfer coefficient, D_{aw} (m^2/s) is the mass diffusivity,

$$j_H = \left(\frac{h}{M_m G c_p}\right)\left(\frac{c_p \mu}{k}\right)^{2/3} = \mathrm{St}\ \mathrm{Pr}^{2/3} \tag{2.12}$$

$$j_D = \left(\frac{k_m}{G}\right)\left(\frac{\mu}{\rho D_{aw}}\right)^{2/3} = \mathrm{St}\ \mathrm{Sc}^{2/3} \tag{2.13}$$

in which, these factors are equals at the liquid-vapor interface for the absorption process ($j_H = j_D$), obtaining Eq. (2.14) (Chilton; Colburn, 1934), where M_m (kg/mol), Sc and Pr are the molecular weight, Schmidt number (0.6-2500) and the Prandtl number (0.6-2500), respectively. It cannot be adopted in pool boiling because there is a low mass resistance between the bubble region and the liquid, easing the mass transfer in which the analogy underestimates the liquid mass transfer (Staedter; Garimella, 2018b).

$$\frac{h_l}{k_m} = c_p\ M_m\ \left(\frac{\mathrm{Sc}}{\mathrm{Pr}}\right)^{2/3} \tag{2.14}$$

Also, for simultaneous heat and mass transfer processes, Treybal (1981), (Bird, 2002) and Taylor and Krishna (1993) proposed to work with a corrected heat transfer coefficient (${h_l}^*$), in which the effect of mass transfer on heat transfer is taken into account (Eqs. (2.15) and (2.16)). Note that the effect of mass transfer on heat transfer can improve or deteriorate the heat transfer coefficient depending on both process directions, while $\dot{m}_i$ is the mass flow rate for the i^{th} component (Bird, 2002).

$${h_l}^* = h_l\ \frac{c}{e^c - 1} \tag{2.15}$$

$$c = \frac{\dot{m}''_A\ c_{p,A} + \dot{m}''_B\ c_{p,B}}{h_l} \tag{2.16}$$

According to the vapor mass transfer coefficient $k_{m,v}$ (m/s), it may be computed in a molar basis by using Colburn and Drew (1937) definition - Eq. (2.17), in which it assumes the vapor is stagnated, and the heat and mass transfer occurs only over a laminar boundary layer adjoin to the liquid-vapor interface under thermodynamic equilibrium, for instance, Nagavarapu and Garimella (2011), and Staedter and Garimella (2018b) carried out this formulation applied in the generator mass transfer calculations. Also, Bohra (2007) analyzed the mass transfer in the ammonia-water absorption process over a horizontal tube bundle. $\dot{n}_t''$ (mol/m^2 s) is the net molar flux, y (mol$_a$/mol$_t$) is the vapor concentration in molar basis given at the liquid-vapor interface x_{int} and for the vapor bulk concentration y_b, and z (mol$_a$/mol$_t$) is the condensing flux concentration. The z value is a function of the kind of sorption process in which $z < 1$ when the absorption process occurs and $z > 1$ for the desorption process. Sieres and Fernández-Seara (2007) presented a generalized method to analyze the simultaneous heat and mass transfer in sorption processes, mapping the possible concentration profiles and showing the typical z values.

$$\dot{n}_t'' = k_{m,v}\, c_t\, \ln\left(\frac{z - y_{int}}{z - y_b}\right) \tag{2.17}$$

Assuming ammonia vapor behaves as an ideal gas $P\,V = n \cdot \Re \cdot T$, being $n = m/M$, $P\,v = \Re\,T/M$. c_t is the molar density $c_t = \rho/M$, so, c_t may be written as $c_t = P/\Re \cdot T$. Eq.(2.17) may be rewritten as Eq. 2.18. P (Pa) is the pressure, V (m^3) is the total volume, n is the number of moles, $\Re = 8314$ (J/mol K) is the universal gas constant, T is the temperature (K), ρ (kg/m^3) and m (kg) is the mass. It is worthwhile to mention that the experimental average temperature is usually used to find it.

$$\dot{n}_t'' = k_{m,v}\, \frac{P}{\Re\,T} \ln\left(\frac{z - y_{int}}{z - y_b}\right) \tag{2.18}$$

or,

$$\dot{n}_t'' = k_{m,v}\, \frac{\rho}{M} \ln\left(\frac{z - y_{int}}{z - y_b}\right) \tag{2.19}$$

Moreover, the mass transfer for a single phase can be expressed as a function of several ways to define the driving force (Kessler; Greenkorn, 1999), e.g. species mass density as defined in Eq. (2.20), $\dot{m}_a''$ (kg/m^2 s) is the mass flux of ammonia component, $k_{m,L}$ (m/s) is the liquid mass transfer coefficient, $\rho_{a,int}$ and ρ_{bulk} is the density of ammonia species at the interface and the bulk solution, respectively,

$$\dot{m}_a'' = k_{m,L}\ (\rho_{int} - \rho_b) = \dot{n}_a''\, M_a \tag{2.20}$$

similarly, the molar flux $\dot{n}_a''$ (mol/m^2 s) is given by Eq. (2.21). z_{int} and z_b (mol$_a$/mol$_t$) is the mole fraction of ammonia species at the interface and the bulk solution, respectively. z_b corresponds with x_b for the liquid solution,

$$\dot{n}_a'' = k_{m,L}^{*}\ (z_{int} - x_b) \tag{2.21}$$

density of the ammonia ρ_a (kg/m^3) is given by $\rho_a = z_a\ M_a\ c_t$, in which c_t (mol/m^3) is the total molar concentration, so,

$$\dot{m}''_a = k_{m,L}\ \left(z_{int}\ \rho_{int} - x_b\ \rho_b\right) \tag{2.22}$$

Eq. (2.22) was used by Bohra (2007) to calculate the mass transferred by diffusion and convection through the liquid film. It is assumed that there is no resistance to mass transfer at the liquid-vapor interface. $k_{m,L}$ is given in (m/s).

Thus, from an experimental work, the link between measured quantities and a relevant definition for transfer coefficients must be established carefully. Consequently, the resulting correlation has to be compared with other studies, as already done in many previous works

2.4.2 Dimensionless numbers definition, Nu, Sh and Re

Nusselt (1916) analyzed the isothermal condensation phenomenon on a flat plate for a pure substance, assuming: laminar regime, Newtonian fluid, constant properties, and no inertial forces from the vapor acting at the interface. It was obtained a correlation of the average heat transfer coefficient as a function of the acceleration of gravity, g, the Reynolds number, Re, and the fluid properties; dynamic viscosity, μ, density, ρ, and the liquid thermal conductivity, k,

$$\frac{\overline{h}_l}{k}\left(\frac{\mu_l^2}{g\rho_l(\rho_l-\rho_v)}\right)^{1/3} = 1.467\mathrm{Re}^{-1/3} \tag{2.23}$$

Neglecting the vapor density (ρ_v), and by the definition of kinematic viscosity ($\nu = \mu/\rho$), Eq. (2.23) yields,

$$\mathrm{Nu} = \frac{\overline{h}_l}{k}\left(\frac{\nu_l^2}{g}\right)^{1/3} = \frac{\overline{h}_l L_c}{k} = 1.467\mathrm{Re}^{-1/3} \tag{2.24}$$

in which, $L_c = (\nu^2/g)^{1/3}$ is known as the characteristic length or viscous length scale. Also, the Nusselt number (Nu_δ) can be expressed (see e.g. (Karami; Farhanieh, 2009; Karami; Farhanieh, 2011) as a function of the film thickness, δ, given by:

$$\mathrm{Nu}_\delta = \frac{\overline{h}_l\delta}{k} \tag{2.25}$$

where δ may be used for the Nusselt film thickness, δ_{Nu}, in which, Γ represents the mass flow rate per unit length on each tube side, and θ the tube angle from the top or the wettability of the tube,

$$\delta_{\mathrm{Nu}} = \left(\frac{3\mu\Gamma}{g\rho_l(\rho_l-\rho_v)\sin\theta}\right)^{1/3} \cong \left(\frac{3\nu\Gamma}{\rho_l g\sin\theta}\right)^{1/3} \tag{2.26}$$

Many correlations are based on Nu (Eq. (2.24)), while others are based on Nu_δ (Eq. 2.25). In order to carry out a comparison between correlations, a common base must be established. Fortunately, both correlations are linked by the following correlation:

$$\mathrm{Nu}_\delta = (0.75\mathrm{Re})^{1/3}\,\mathrm{Nu} \tag{2.27}$$

In the same way, the Sherwood number, Sh, is defined as:

$$\mathrm{Sh} = \frac{k_m}{D_m}\left(\frac{\nu^2}{g}\right)^{1/3} \tag{2.28}$$

and by

$$\mathrm{Sh}_\delta = \frac{k_m \delta}{D_{aw}} \tag{2.29}$$

thus, the relations are linked by:

$$\mathrm{Sh}_\delta = (0.75\mathrm{Re})^{1/3}\,\mathrm{Sh} \tag{2.30}$$

In the same way, the Reynolds number involves the hydraulic diameter, D_h as the typical length for horizontal tubes;

$$\mathrm{Re} = \frac{\rho \overline{V} D_h}{\mu} = \frac{4\rho V \delta W}{\mu W} = \frac{4\dot{m}}{\mu W} = \frac{4\Gamma}{\mu} \tag{2.31}$$

or the typical length can be taken as the film thickness, δ (see e.g. (Yüksel; Schlünder, 1987a; Yüksel; Schlünder, 1987b; Nosoko et al., 2002))

$$\mathrm{Re}_\delta = \frac{\rho \overline{V} \delta}{\mu}\frac{W}{W} = \frac{\dot{m}}{\mu W} = \frac{\Gamma}{\mu} \tag{2.32}$$

the relation between these two correlations for the Reynolds number reads:

$$\mathrm{Re} = 4\mathrm{Re}_\delta \tag{2.33}$$

where, $\overline{V}$ represents the average fluid velocity, W the width or depth, $\dot{m}$ the mass flow rate. The ratio $\Gamma = \dot{m}/P_{wet}$ between the mass flow and the wet perimeter, is summarized in Table 2.1,

Table 2.1 – *Definition of the mass flow rate per unit length for different falling film geometries*

Γ, kg/m s	**Geometry**
$\frac{\dot{m}}{2W}$	Horizontal tube or flat plate (both sides wet)
$\frac{\dot{m}}{W}$	Flat plate (one side wet)
$\frac{\dot{m}}{\pi D}$	Vertical tube

2.4.3 Classical hypothesis

In order to establish correlations for heat and mass transfer coefficient in sorption processes involving the falling film technology, standard hypotheses are assumed, such as steady-state, incompressible fluid, Newtonian fluid, thermodynamic equilibrium at the liquid-vapor interface, thermal physical properties are constant, non-condensable gases in mixture, and no chemical reactions. However, some additional specific assumptions are commonly encountered in the literature:

- Fluid flow assumptions;
  - Laminar flow regime (Yüksel; Schlünder, 1987a; Castro et al., 2009; Kwon; Jeong, 2004; Karami; Farhanieh, 2009; Karami; Farhanieh, 2011; Yüksel; Schlünder, 1987b;

  Nosoko et al., 2002; Ferreira et al., 1984; Kang et al., 1999; Patnaik; Perez-blanco, 1996; Takamatsu et al., 2003; Jani et al., 2003; Bohra, 2007; Kim; Infante Ferreira, 2008; Cerezo et al., 2009; Shi et al., 2009; Shi et al., 2010; Zavaleta-Aguilar; Simões-Moreira, 2015; Lee, 2007; Narváez-Romo et al., 2020)
  - Turbulent flow regime (Yüksel; Schlünder, 1987a)
  - No wave generation at the liquid-vapor interface or smooth falling film. (Waves -known as wavy laminar- improve the heat and mass transfer in the liquid falling film due the transport process. The capillary effects are significant in low Reynolds numbers ($Re \leq 200$), and the inertial effects are relevant in higher Reynolds number ($Re \geq 200$)(Patnaik; Perez-blanco, 1996). However, a complete analysis of the simultaneous heat and mass transfer integrated to wave generation onto the interface is complex) (Castro et al., 2009; Karami; Farhanieh, 2009; Karami; Farhanieh, 2011; Shi et al., 2009; Shi et al., 2010; Zavaleta-Aguilar; Simões-Moreira, 2015)
  - Wavy flow (Patnaik; Perez-blanco, 1996)
  - No interfacial shear or stagnated vapor at constant pressure (Yüksel; Schlünder, 1987a; Castro et al., 2009; Karami; Farhanieh, 2009; Karami; Farhanieh, 2011; Kang et al., 1999; Jani et al., 2003; Bohra, 2007)
  - Shear stress acting at the interface (Kwon; Jeong, 2004; Yüksel; Schlünder, 1987b)
  - Wall friction term is negligible (Yüksel; Schlünder, 1987a; Yüksel; Schlünder, 1987b; Ferreira et al., 1984)
  - Vapor and liquid flows are homogeneous (Ferreira et al., 1984)
  - No viscous dissipation (in low Reynolds number, this implies low flow velocities and, therefore, viscous dissipation can be neglected) (Karami; Farhanieh, 2011; Patnaik; Perez-blanco, 1996)
  - No pressure or velocity gradient in the main flow direction (Castro et al., 2009; Kwon; Jeong, 2004; Karami; Farhanieh, 2011)
  - Transport governed by the convective-diffusion (Patnaik; Perez-blanco, 1996)
  - 2-D Model (Patnaik; Perez-blanco, 1996)

- Thermal transfer assumptions;
  - No nucleate flow boiling regime (Karami; Farhanieh, 2011; Shi et al., 2009; Shi et al., 2010; Zavaleta-Aguilar; Simões-Moreira, 2015)
  - No heat transfer at the vapor phase (Karami; Farhanieh, 2009; Karami; Farhanieh, 2011; Yüksel; Schlünder, 1987b; Kang et al., 1999; Patnaik; Perez-blanco, 1996; Jani et al., 2003; Lee, 2007)
  - Thermal resistance of tube wall is negligible (Karami; Farhanieh, 2009; Karami; Farhanieh, 2011; Shi et al., 2009; Shi et al., 2010; Zavaleta-Aguilar; Simões-Moreira, 2015)

- Heat and mass transfer coefficients constants along the absorber tube (Yüksel; Schlünder, 1987b; Ferreira et al., 1984)
- Vapor pressure driving equal to 0 at the inlet. No thermal entrance effects (Yüksel; Schlünder, 1987a; Karami; Farhanieh, 2009; Karami; Farhanieh, 2011).Nakoryakov et al. (2011) carried out an analysis of these effects in absorption/desorption processes. Cerro and Whitaker (1971) did for general transport processes
- Cross-streamwise diffusion. No diffusion in the flow direction (Karami; Farhanieh, 2009; Karami; Farhanieh, 2011; Yüksel; Schlünder, 1987b; Patnaik; Perez-blanco, 1996; Jani et al., 2003; Shi et al., 2009)
- Wall temperature along the tube length changes in a linear fashion (Karami; Farhanieh, 2011)
- Constant wall tube temperature (Nosoko et al., 2002; Jani et al., 2003)
- No isothermal absorption (Yüksel; Schlünder, 1987a; Yüksel; Schlünder, 1987b)
- Saturation temperature in the inlet condition (Jani et al., 2003; Kim; Infante Ferreira, 2008; Patnaik; Perez-blanco, 1996)
- Subcooling temperature in the inlet condition (Kang et al., 1999; Kim; Infante Ferreira, 2008; Peng et al., 1995)

2.5 Transfer correlations involving ammonia-water solution

ARC driven by the ammonia-water working fluid can be used in applications of temperature ranging from subzero Celsius degree owing to the ammonia thermodynamic properties. Most studies on transfer correlations in the literature focus on the absorber. Currently, there is not a heat transfer correlation for ammonia-water falling film in absorption processes using nanoparticles (Abed et al., 2015)

2.5.1 Absorber

The most frequent devices involving falling film are horizontal tubes, vertical plate surfaces and helical coil tubes.

2.5.1.1 Horizontal tubes

Bohra (2007) carried out an experimental study on an ammonia-water ARC using falling film technology, in which 24 tubes (4x6) of 9.5×10^{-3}m OD and 0.29m length were used. Flow patterns and transport processes were analyzed in his test bench, segmenting the absorber into six distinct parts. The lowest tubes of the array (where the cooling fluid enters in counter-current configuration) had obtained higher ammonia absorption rates, similarly to Lee (2007) and Lee et al. (2002b). In addition, the increase of the solution mass flow rate promoted an upgrade of the heat transfer coefficient because the liquid falling film reached a higher wettability on the tube wall. On the other hand, the heat transfer coefficient decreased as the absorber pressure (P_{abs}) and the weak solution concentration (x_{ws}) were also decreased. The overall heat transfer coefficient (U) ranged from 753 to 1853 W/m^2 °C, the film heat transfer coefficient ranged (h_l) from 923 to 2857 W/m^2 °C, the vapor mass transfer coefficient ($k_{m,v}$) ranged from 2.6×10^{-3} to 0.25 m/s, and the liquid mass transfer coefficient ($k_{m,l}$) ranged from 5.51×10^{-6} to 3.31×10^{-5} m/s. The following correlations represent the heat and mass transfer coefficients experimentally obtained by Bohra (2007), Nusselt number in the segmented liquid falling film, $\mathrm{Nu}_{seg,\delta}$

$$\mathrm{Nu}_{seg,\delta} = 7.589 \times 10^{-3}\mathrm{Re}^{1.04}\mathrm{Pr}^{0.45}\left(\frac{P_{abs}}{345}\right)^{-0.145} \tag{2.34}$$

Sherwood number in the segmented liquid falling film, $\mathrm{Sh}_{seg,\delta}$

$$\mathrm{Sh}_{seg,\delta} = 1.298 \times 10^{-4}\mathrm{Re}^{0.57}\mathrm{Sc}^{1.32}\left(\frac{P_{abs}}{345}\right)^{0.644} \tag{2.35}$$

Lee (2007) studied the absorption process in the same test rig as Bohra (2007), focusing on the analysis of the overall absorption process, in which both vapor and liquid phase correlations are obtained. Also, the same correlations were defined in Bohra et al. (2019).

Nusselt number in the liquid falling film, Nu_δ

$$\mathrm{Nu}_\delta = 3.22 \times 10^{-3}\mathrm{Re}^{0.945}\mathrm{Pr}^{0.743}\left(\frac{P_{abs}}{345}\right)^{-0.269} \tag{2.36}$$

Sherwood number in the vapor phase, Sh_v

$$\mathrm{Sh}_v = 2.708 \times 10^{-11}\left(\frac{\mathrm{Gr}_v\mathrm{Sc}_v}{\mathrm{Ja}_v}\right)^{1.256}\left(\frac{\mathrm{Pr}_l}{\mathrm{Sc}_l}\right)^{-1.681}\left(\frac{\mu_l - \mu_v}{\mu_v}\right)^{1.426} \tag{2.37}$$

while Gr and Ja are the Grashof number and the Jakob number, respectively. Sherwood number in the liquid falling film, Sh_δ, where, P_{abs} is given in kPa.

$$\mathrm{Sh}_\delta = 7.437 \times 10^{-4}\mathrm{Re}^{0.397}\mathrm{Sc}^{1.04}\left(\frac{P_{abs}}{345}\right)^{0.8841} \tag{2.38}$$

Lee et al. (2012) carried out a study focused on the absorption rates over horizontal falling film absorbers, using the same test rig and covering the influence of the operational effects over the heat and mass transfer rates. In addition, they compared their results with Wilke (1962), Hu and Jacobi (1996b), Kwon and Jeong (2004), and Meacham and Garimella (2004a). Daguenet-Frick et al. (2017) used that work to compare the heat transfer coefficient in water vapor absorption in aqueous sodium hydroxide process. However, the Reynolds number was not over the validation range (Lee et al., 2012).

2.5.1.2 Vertical surface

Kang et al. (1999) conducted an experimental work on ammonia-water falling film absorption process using a vertical surface ($0.11 \times 0.130 \times 0.034$ m^3) with offset strip fins (OSF). The simultaneous heat and mass transfer coefficients were analyzed and computed for different operation conditions such as (a) inlet temperatures of the weak liquid solution ($T_{ws} = 17 - 37.2$ °C) and the ammonia vapor ($T_v = 54.5 - 66.5$ °C), (b) mass flow rate of weak liquid solution ($\dot{m}_{ws} = 4 \times 10^{-3} - 1 \times 10^{-2}$ kg/s) and the ammonia vapor ($\dot{m}_v = 6.2 \times 10^{-4} - 9 \times 10^{-4}$ kg/s, and (c) weak liquid solution concentration ($x_{ws} = 5, 10$, and 15 %). In the absorber, it was used water as secondary cooling circuit ($\dot{m}_c = (64.7 - 79.7) \times 10^{-3}$ kg/s), circulating in a counter flow configuration to the liquid falling film. A rectification process of the wet ammonia vapor was reached before being absorbed by the liquid falling film in the absorption process due to the deeply low level of ammonia vapor purity ($y = 64.7 - 79.7$ %) and to the inlet subcooling conditions.

As a result, the heat and mass transfer ranged from 500 to 2100 W/m^2 °C and from 1.0 to 55×10^{-5} m/s, respectively. The increase of the falling film Reynolds number and the mass flow rate of ammonia vapor enhanced the Nusselt and the Sherwood number. However, the Nusselt number was more affected by the liquid mass flow rate than the mass flow of ammonia vapor, while the Sherwood number was more affected by the Reynolds number of ammonia vapor than the Reynolds number of the liquid solution. On the other hand, the Sherwood number values were higher than the Nusselt number owing to the Lewis number, meaning that the effective thickness of the thermal boundary layer is thicker than that of the diffusion boundary layer (Kang et al., 1999). i is the inlet condition. The following Nusselt and Sherwood number correlations were obtained, Nusselt number in the liquid falling film, Nu

$$\mathrm{Nu} = 8.530 \times 10^{-2} \mathrm{Re}_l^{1.518} \mathrm{Re}_v^{0.1759} \left(\frac{T_v - T_l}{T_l}\right)_i^{1.8790} \left(\frac{x_v - x_l}{x_l}\right)_i^{-0.5756} \tag{2.39}$$

Sherwood number in the liquid falling film, Sh

$$\mathrm{Sh} = 6.996 \times 10^{-6} \mathrm{Re}_l^{0.8874} \mathrm{Re}_v^{1.265} \left(\frac{T_v - T_l}{T_l}\right)_i^{0.8844} \left(\frac{x_v - x_l}{x_l}\right)_i^{0.5304} \tag{2.40}$$

Lee et al. (2002a) compared the performance of falling film and bubble absorbers for the same operation conditions. Bubble absorbers reached a better performance than falling film for low liquid Reynolds numbers and high vapor Reynolds numbers because there was a partial wettability of the tube in the falling film technology (Castro et al., 2009). However, the bubble mode may transfer less heat to the cooling fluid than the falling film for a high liquid solution and low ammonia vapor, resulting in a higher heat generation than of the falling film. Nusselt number in the liquid falling film, Nu

$$\mathrm{Nu} = 136.9 \times 10^{-4} \mathrm{Re}_l^{0.5103} \mathrm{Re}_v^{0.02461} \left(\frac{T_v - T_l}{T_l}\right)_i^{0.2977} \left(\frac{x_v - x_l}{x_l}\right)_i^{0.1438} \tag{2.41}$$

Sherwood number in the liquid falling film, Sh

$$\mathrm{Sh} = 658.46 \mathrm{Re}_l^{0.0195} \mathrm{Re}_v^{0.9571} \left(\frac{x_v - x_l}{x_l}\right)_i^{-0.0639} \tag{2.42}$$

2.5.1.3 Helical coil

The helical geometry may be an alternative to obtain a more compact machine because the heat transfer area per unit volume increases At the literature, Jeong et al. (1998) experimentally investigated the performance of the heat transfer coefficient without mass transport in a coiled tube absorber for various operation conditions such as (a) solution flow rate ($\dot{m}_{ws}$), which was up to 6×10^{-2} kg/s, (b) ammonia vapor ($\dot{m}_v$) ranged from 9×10^{-5} to 4.2×10^{-4} kg/s, and (c) inlet concentration (x_l) between 1.2 to 2.2 %. The tests were carried out with and without the ammonia absorption process, using a counter-flow absorption in which density (ρ_l), temperature (T), and pressure (P) were used to find ammonia concentration.

The heat transfer coefficient (h_l) was enhanced when the solution flow rate ($\dot{m}_l$) increased (for both with and without the absorption process). However, the heat transfer coefficient (h_l) associated with the absorption process was lower than the heat transfer obtained for pure water at the same mass flow rate because the ammonia vapor feeding in a counter-flow to the falling film caused an uneven distribution or stagnation of the liquid falling film (Jeong et al., 1998). Nevertheless, the mass transfer (k_m) behavior was not studied on the test rig. Finally, it was proposed a Nusselt number as a function only of the Reynolds number for ammonia-water, as shown in Eq. (2.43)

$$\mathrm{Nu} = 2.2 \times 10^{-4}\mathrm{Re} \quad 50 \leq \mathrm{Re} \leq 300 \tag{2.43}$$

Kim et al. (1998) also investigated the ammonia-water absorption process over shell-coil type absorber. A 1/2” O.D tube forming a coil exchanger was used as absorber, in which the solution flows over it. The internal heat transfer for the water coolant was computed through the Dittus-Boelter’s correlation (Dittus, 1930), and the heat rate was estimated between the temperature difference (inlet and outlet of the absorber) and the coolant mass flow rate. Thus, the average heat transfer coefficient in the falling film is defined. The empirical correlations (Eqs. (2.44) and (2.45)) were obtained. The heat transfer coefficient improved as the ammonia-water solution increased, presenting high dependence from the temperature ratio between the inlet coolant temperature and the solution inlet temperature.

$$\mathrm{Nu}_\delta = 2.316 \cdot 10^{-4} \cdot \mathrm{Re}_L^{0.837} \cdot \mathrm{Pr}^{0.780} \cdot \left(\frac{T_{L,i}}{T_{c,i}}\right)^{3.965} \tag{2.44}$$

$$\mathrm{Sh}_\delta = 5.364 \cdot 10^{-6} \cdot \mathrm{Re}_L^{0.744} \cdot \mathrm{Sc}^{0.411} \cdot \left(\frac{T_{L,i}}{T_{c,i}}\right)^{1.709} \tag{2.45}$$

Kwon and Jeong (2004) experimentally analyzed the effect of vapor flow direction over the heat transfer coefficient (h_l) for the absorption process at three different concentrations ($3, 14$, and 30 %) in a helical coil configuration. The effect of mass flow rate ($\dot{m}_l$) and the temperature of the weak liquid solution (T_{ws}) were investigated in the laminar regime (Re=10-250). A $0.6m$ tube length and $12.7 \times 10^{-3}m$ OD was manufactured as a helical coil heat exchanger at $82.7 \times 10^{-3}m$ and $8.0 \times 10^{-2}m$ of an average diameter of a coil and the header height, respectively. For balance equations of the absorption process, the heat transferred from the absorber to the cooling fluid circuit was expressed for both absorption processes (heat latent transfer) and change in the solution temperature (sensible heat transfer).

The effects of vapor flow over the heat transfer coefficient (h_l) were prominent when there was a counter-flow absorption and a low ammonia concentration (3%) because, in small concentrations, the vapor has high specific volume. Moreover, the liquid falling film flow pattern may be affected by a high velocity of the vapor flow. The Nusselt number was higher in the co-current absorption than in the counter-flow absorption. However, at a higher ammonia concentration (30 %), the behavior of the Nusselt number was similar for both co-current and counter-flow absorption processes. In addition, the increase in the liquid solution mass flow rate improved the heat transfer coefficient. On the other hand, the effect of the weak liquid solution temperature over the heat transfer was negligible when compared to other operational parameters.The Nusselt number for the liquid falling film for co-current absorption is given by Eq. (2.46), where τ_v^* is a non-dimensional shear stress detailed by Kwon and Jeong (2004),

$$\mathrm{Nu} = 1.975 \times 10^{-3} \mathrm{Re}_l^{0.6895} \tau_v^{*-0.0249} \tag{2.46}$$

Nusselt number in the liquid falling film for counter-current absorption

$$\mathrm{Nu} = 1.683 \times 10^{-4} \mathrm{Re}_l^{0.8672} \tau_v^{*-0.3018} \tag{2.47}$$

2.5.2 Generator

Zavaleta-Aguilar and Simões-Moreira (2012) and Zavaleta-Aguilar and Simões-Moreira (2015) analyzed a falling film generator (distiller) to optimize the concentration (y) and the mass flow rate of distilled ($\dot{m}_y$) when the ammonia vapor is separated from the ammonia-water solution, researching some mean parameters such as strong solution concentration (x_{ss}), strong solution mass flow rate($\dot{m}_{ss}$), rectifier temperature (T_{rec}), wall temperature (T_w) and strong solution temperature of the inlet (T_{ss}). A horizontal tube bundle geometry was used as a generator and rectifier, analyzing the hydraulic behavior of the liquid film and the distillation degree of purity. In the first one, a total wettability on the tubes was reached due to the small intertube distance, ($S - D = 2$ mm), homogeneous liquid distribution and a superficial treatment by sandblasting over the wall tube.

A distilled ammonia concentration (y) up to 99.74% was obtained for an ammonia-water concentration of $x_{ss} = 49\%$. In addition, the purity of distilled ammonia (y) was enhanced when the strong solution mass flow ($\dot{m}_{ss}$) and the strong solution concentration (x_{ss}) were increased, or when the average rectifier temperature (T_{rec}), wall temperature (T_w) in the generator, and the strong solution temperature (T_{ss}) were reduced. The experimental work was carried out for a strong solution mass flow of 1.6×10^{-2} to 2.76×10^{-2} kg/s equivalent to Reynolds numbers of 108 to 246. They employed two ammonia concentrations (0.37 and 0.49). The concentration of ammonia distilled (y) was increased, and the distilled mass flow rate ($\dot{m}_y$) was diminished with the increase of the mass flow rate ($\dot{m}_{ss}$) when the wall temperature and the rectifier temperature were kept constant, because the heat transfer coefficient diminishes due to the thickening of the liquid film, increasing the thermal resistance throughout the liquid film. According to the rectifier temperature, higher ammonia distilled concentration was obtained at the cooler temperatures since it rejected more water of the wet ammonia vapor (Zavaleta-Aguilar; Simões-Moreira, 2015).

Regarding the wall temperature (T_w), the distilled mass flow ($\dot{m}_y$) improved for the highest wall temperature (T_w) in the generator, however, the distilled concentration diminished (y), because a higher wall temperature promoted the evaporation of more wet vapor (Zavaleta-Aguilar; Simões-Moreira, 2015). The following correlation was derived for the heat transfer on the liquid film:

$$\mathrm{Nu} = 0.75\mathrm{Re}^{-0.27}\mathrm{Pr}^{0.4} \tag{2.48}$$

Staedter and Garimella (2018b) investigated the heat and mass transfer process in microchannel geometries for the ammonia-water mixture for generation and rectification processes. The electrical resistance of the desorber and the strong solution pump are modulated, controlling the heat rate in the generator and the mass flow rate, respectively. Also, the expansion valves are modulated. The small-capacity ARC was carried out in the following conditions; $0.004 - 0.00115$ kg/s strong solution mass flow rate, $13 - 26$ bar condensation pressure and $0.37 - 0.52$ strong solution concentration. They investigated a new generator configuration, in which it is characterized by pool boiling heat transfer. Heat and mass transfer correlations previously presented are summarized as follows.

2.5.3 Summary of transfer correlations

In Tab. 2.2, the application range of properties and dimensionless numbers applied to the ammonia-water solution is summarized. Most of the correlations are devoted to the absorption machine. To our knowledge, there exists only one work in the open literature proposing a correlation for a generator using ammonia-water solution (Zavaleta-Aguilar; Simões-Moreira, 2015). The first and second column shows the authors and their correlations, respectively; Next, Prandtl, Reynolds, and Schmidt numbers are shown; while temperature and pressure of application are shown in next two columns. The two last columns present the concentration of the liquid solution (x) and the vapor (y), and the remarks for each correlation. In Tab. 2.3, configurations of the experimental set up are summarized. The first column presents the author, the second column shows geometrical configurations; next column associates other studies that they have been used for comparing. Finally, some comments were carried out in the last column

Other studies focused on falling film technology are shown in Appx. (C), in which some of those empirical correlations have been used in the absorption process. Also, studies of lithium bromide-water absorption have been raised and they are shown in Appx. (B). Finally, some relevant studies of the bubble absorption refrigeration cycle is shown in Appx. (D).

Table 2.2 – *Summarized table of the ammonia-water working fluid studies in which it describes the application range for each correlations carried out in falling film*

Author	Correlation	Pr	Re	Sc	T, °C	P, kPa	x, % y, %	Remarks
Falling film absorber using ammonia-water working fluid								
Bohra (2007)	2.34, 2.35	2.2-10.4 $0.5 - 0.93$	$26 - 157$ -	$45.4 - 588.1$ $0.5 - 0.53$	$14.8 - 105.4$ $(-10.5) - 28.2$	$169 - 520$	$5; 15; 25; 40$ -	
Jeong et al. (1998)	2.43	$2.4 - 3.9$ -	$20 - 300$ -	-	$45 - 54$ $66 - 69$	$67 - 117$	$1.2; 3.7$ $63; 77$	
Kang et al. (1999)	2.39, 2.40	$3.8 - 5.8$ -	$17 - 24$ -	$33.8 - 39.2$ -	$17.0 - 37.2$ $54.5 - 66.5$	101.3	$5; 10; 15$ $64.7 - 79.7$	
Kwon and Jeong (2004)	2.46, 2.47	$2.1 - 3.8$ -	$10 - 250$ -	-	$45 - 60$ -	$17 - 193$	$3; 14; 30$ $45.6; 84.4; 96.5$	
Lee (2007)	2.36, 2.37, 2.38	$2.2 - 8.2$ $0.5 - 0.93$	$29.7 - 169.2$ -	$43.6 - 362.7$ $0.5 - 0.53$	$14.8 - 105.4$ $(-10.5) - 28.2$	$169 - 520$	$5; 15; 25; 40$ -	$\mathrm{Gr}_v = (4.22 - 59.89) \times 10^3$ $\mathrm{Ja}_v = (9.8 - 38.7) \times 10^{-3}$
Lee et al. (2002a)	2.41, 2.42	$3.8 - 5.8$ $-$	$50 - 700$ $25 - 200$		$15.5 - 20$ $-$	101.3	$0.1 - 0.3$ $-$	
Other works using ammonia-water working fluid								
Zavaleta-Aguilar and Simões-Moreira (2015)	2.48	$1.68 - 2.65$	$108 - 246$	-	$87 - 103$	$1460 - 1611$	$37; 49$	Generator

Table 2.3 – *Summarized table of the ammonia-water working fluid studies showing the author, geometrical aspects, its comparison with the literature review and highlights*

Experimental works using Ammonia Water: Configuration of study			
Author	Geometrical specifications	Compared	Comments
Bohra (2007)	Horizontal tube bundle 4 Col x 6 Row. O.D= 9.5×10^{-3}m, $L = 0.29$m, $S = 2 \times 10^{-2}$m $\delta_w = 7 \times 10^{-4}$m $A_{total} = 0.210$m^2	Wilke (1962), Dorokhov and Bochagov (1983), Hu and Jacobi (1996a), Kwon and Jeong (2004), Meacham and Garimella (2002), Meacham and Garimella (2004b)	Water counter-current cooling and counter-current absorption
Jeong et al. (1998)	Coiled tube O.D= 12.7×10^{-3}mm, I.D=10.7×10^{-3}mm $\overline{D}_{coil} = 82.7 \times 10^{-3}$m		Water co-current cooling and Counter-current absorption
Kang et al. (1999)	Surfaces as offset strip fin stainless steel $0.1 \times 0.13 \times 3.4 \times 10^{-2}$ mm^3 Fin pitch = 1.95mm, $\delta_w = 2 \times 10^{-4}$m Fin height = 4.8×10^{-3}mm $A_{total} = 14.3 \times 10^{-3}$m^2		Water counter-cross cooling and co-current absorption
Kwon and Jeong (2004)	Coiled tube O.D= 12.7×10^{-3}mm, I.D= 10.7×10^{-3}mm, $L = 0.6$m $A_{total} = 2.4 \times 10^{-2}$m^2		Water co-current cooling and co/counter-current absorption It took into account the shear stress at the vapor-liquid interface It used the same test rig as Jeong et al. (1998)
Lee et al. (2002b)	Three surface types smooth plate, hair lined plated treated by laser, and plate treated by sand paper (higher wettability) $0.112 \times 0.264 \times 3 \times 10^{-4}$m^3, and $A_{total} = 29.6 \times 10^{-3}$m^2		Bubble, water counter-current cooling Counter-current absorption
Lee et al. (2002a)	Three surface types smooth plate, hair lined plated treated by laser, and plate treated by sand paper (higher wettability) $0.112 \times 0.264 \times 3 \times 10^{-4}$ m^3, and $A_{total} = 29.6 \times 10^{-3}$ m^2	Lee et al. (2002a): bubble technology	Bubble water counter-current cooling Counter-current absorption
Zavaleta-Aguilar and Simões-Moreira (2015)	Horizontal stainless steel tube bundle 7 Col x10Row $\delta_w = 1 \times 10^{-3}$m, O.D= 8×10^{-3}m, $L = 0.15$m $A_T = 26.4 \times 10^{-2}$m^2	Hu and Jacobi (1996a), Wilke (1962), Chun and Seban (1971), Mitrovic (1986), Owens (1978), Fujita and Tsutsui (1998)	Generator-Rectifier Heating by thermal oil-Generator Water cooling-Rectifier Ammonia water. A 100 % surface wettability was achieved for Re above 100 up to nearly 250 Properties by *EES* and Conde (2006)

Chapter 3

ABSORPTION REFRIGERATION CYCLES OPERATIONAL PRINCIPLES

The current section focuses on the operating principles of the main ARC components that are affected by the equilibrium conditions of the ammonia-water mixture. The next paragraphs defines the definition of molar concentration, highlighting the mass transfer analysis approached from the molar basis, an explanation of the binary diagram for the ammonia water mixture by establishing relations from temperature-concentration, and enthalpy-concentration diagrams; consequently a schematic representation of the distillation and absorption processes is displayed and finally, the current study determines the heat and mass transfer operating range regarding the experimental correlations disused in Chap. (2).

3.1 Molar and weight concentration

The concentration can be defined from the molar x or mass basis w ($\mathrm{kg}_a/\mathrm{kg}_t$), thus Eq. (3.1) defines the concentration regarding molar terms ($\mathrm{mol}_a/\mathrm{mol}_t$). In addition, Eq. (3.2) converts the concentration from the molar to weight basis, in consequence, Jennings (1935) presented the concentration curve conversion displayed in Fig. (3.1). For instance, for $x = 0.4$ is the equivalent difference value $x - w = 0.0136$, following the red dashed line, thereby, $w = 0.4 - 0.0136 = 0.386$. Now, for $w = 0.4$, $x = 0.4138$ by using the green line.

$$x = \frac{\frac{\text{mass NH}_3}{\text{MW=17}}}{\frac{\text{mass NH}_3}{\text{MW=17}} + \frac{\text{mass H}_2\text{O}}{\text{MW=18}}} \tag{3.1}$$

$$x - w = \frac{1-x}{18-x}x = \frac{1-w}{w+17}w \tag{3.2}$$

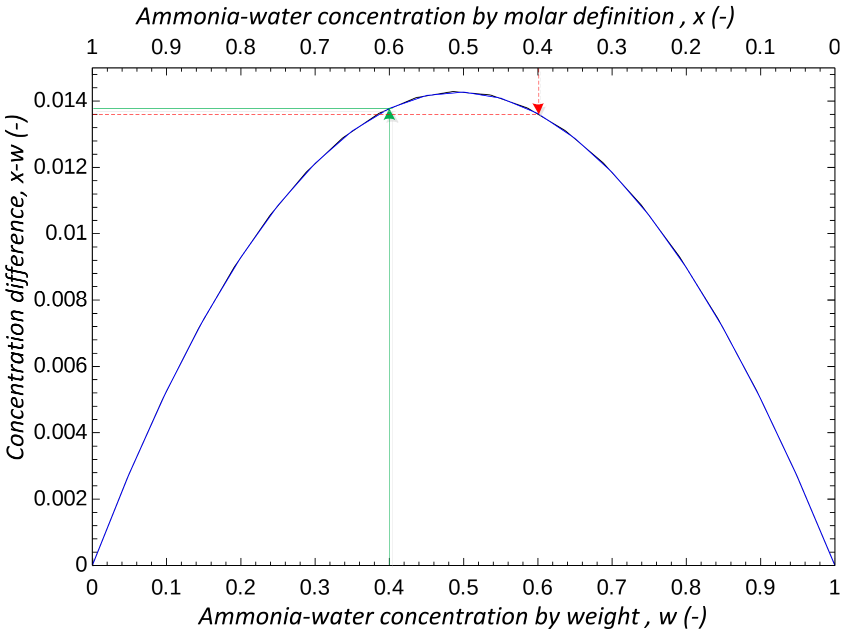

Figure 3.1 – *Concentration curve conversion used to graphically convert between the molar basis concentration and the weight concentration*

3.2 Binary diagram in sorption process for ammonia-water

Ammonia-water diagrams are determined under the macroscopic equilibrium state conditions, which means that the average rate of the mass transfer through the interface is equal in both vapor and liquid phases. Therefore, the ammonia-water solution is in equilibrium with the ammonia vapor, and three thermodynamic properties such as pressure, temperature and concentration define thermodynamic state of the ammonia-water mixture. Next, the temperature - ammonia-water mass fraction diagram, and the specific enthalpy - ammonia-water mass fraction diagram are discussed.

3.2.1 Temperature - ammonia-water mass fraction diagram

Fig. (3.2) displays a binary diagram of temperature and mass fraction for an ammonia-water mixture and also presents the variation of the temperature as a function of the pressure and mass fraction. The bubble point curve (blue lines) and the dew point curve (red lines) represent the limiting values at which bubbles and droplets appear spontaneously. The solution is in liquid state below the bubble point curve, whereas, above the dew point curve, the solution is in super-heated vapor phase. The values between both curves comprise the liquid-vapor equilibrium state. The curve moves upwards by increasing the pressure, in which these two pressure values represent the high and low pressure level of ammonia-water absorption refrigeration cycle; 15.6 bar for the generation and 2.5 bar for the absorption processes.

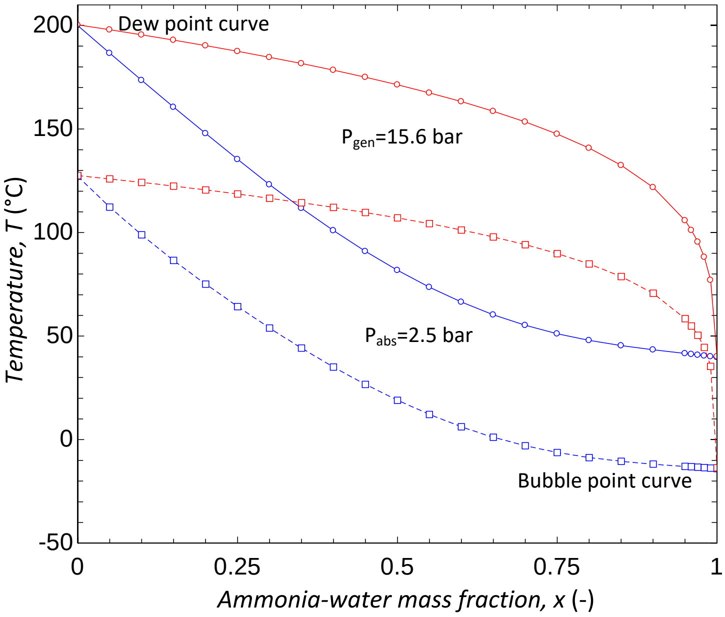

Figure 3.2 – *Binary diagram of the temperature as a function of the ammonia-water mass fraction for both absorption and generation processes under equilibrium state in which blue lines and red lines are the bubble curve and dew curve, respectively.*

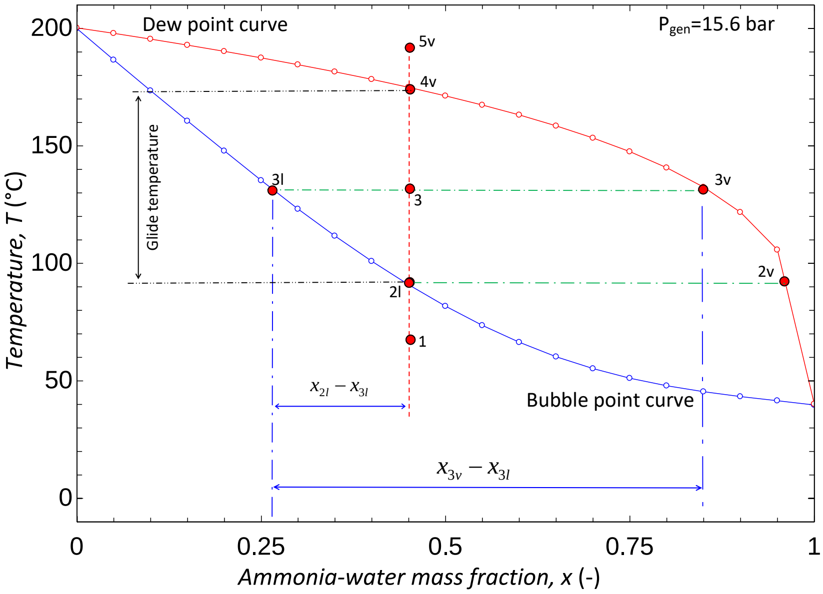

Figure 3.3 – *Total evaporation process at constant pressure represented over the binary diagram of the temperature as a function of the ammonia-water mass fraction under equilibrium state*

Fig. (3.3) shows a binary diagram of a total evaporation process at constant pressure. When, the concentration is equal to 1, the ammonia water solution is in sub-cooled liquid state. If the ammonia-water mixture is heated, it would reach the point $2l$, reaching the bubble point curve in which the first vapor formation occurs. The liquid mass fraction corresponds to $x_{2l} \approx x_1$ value, and vapor mass fraction corresponds to de x_{2v}, due to ammonia vapor pressure is higher than water vapor pressure at the same temperature (Herold et al., 2000). If the heat remains constant, the solutions attains the state 3, in which it is in the liquid-vapor phase equilibrium between the vapor mass fraction(x_{3v}) and the liquid mass fraction (x_{3l}), and these fractions can be calculated by using the lever rule (Eq. 3.3). In Fig. (3.3) the point x_{3v} has a lower ammonia concentration than x_{2v} point because higher temperatures imply higher rates of water evaporation, affecting the final ammonia-water vapor concentration. If the heating process is kept yet, the point x_{4v} is reached, (dew point curve), and an additional heat carries on the solution to point $5v$, representing the super-heated vapor state.

$$x = \frac{x_{2l} - x_{3l}}{x_{2v} - x_{3v}} \tag{3.3}$$

3.2.2 Enthalpy - ammonia-water mass fraction diagram

Ammonia-water strong solution at the saturated state (3) is enriched by adding saturated ammonia vapor with high purity degree (2) into the ammonia-water weak solution (1) through an adiabatic mixing chamber as shown in Fig. (3.4). For an ideal mixture, the curve would connect to pure states which means a lineal curve corresponding to the isothermal curve. So, the ammonia-water mixture is given by exothermic reaction in which the *mixture enthalpy* would increase as the consequence of its reaction. So, by using the energy and mass conservation equations, the mixture enthalpy definition is given by Eq. (3.4); i is the specific enthalpy and x is the ammonia-water concentration. Enthalpy behavior as a function of the mass fraction for two operational pressure values is shown in Fig. (3.5). As previously mentioned, the enriched solution achieves a new temperature value, passing from temperature T_2 to T_1,

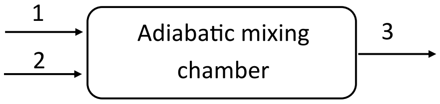

Figure 3.4 – *Schematic representation of the adiabatic mixing chamber*

$$i_3 = i_1 x_1 + i_2 x_2 \tag{3.4}$$

In Fig. (3.5), red lines are the dew point curves, blue lines are the bubble point curves and green dashed lines represents isothermal lines; Dashed lines display the diagram for 2.5 bar pressure, and continuous lines describe for 15.6 bar pressure system. Also, in the same figure may be described the energy rate consumed in the evaporation process, e.g, the vertical difference between 2 and 1 may be understood as the latent heat to produce ammonia vapor at the generator.

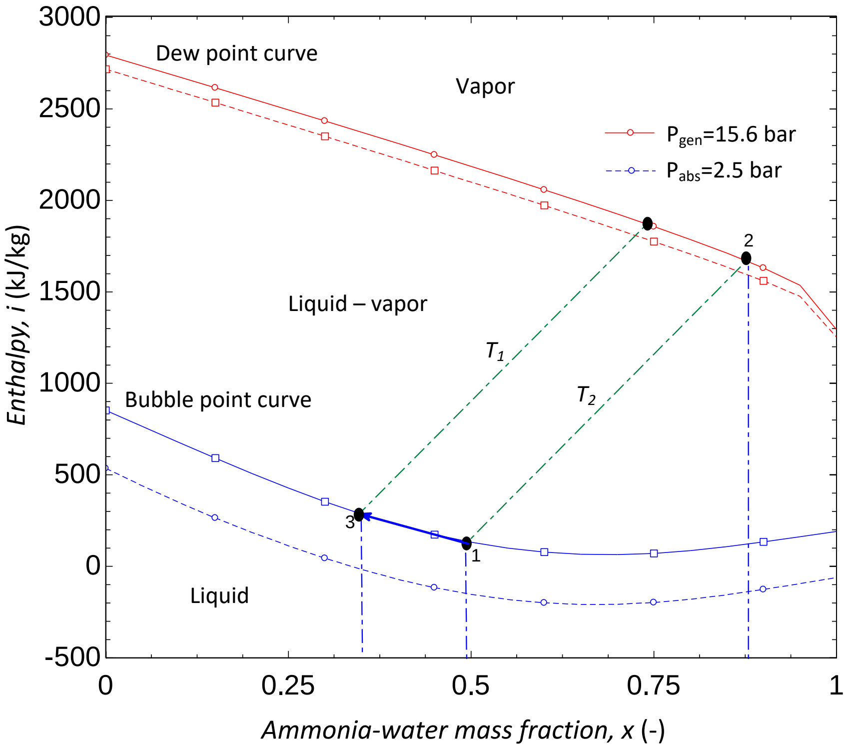

Figure 3.5 – *Binary diagram of the enthalpy as a function of the ammonia-water mass fraction for the mixture enthalpy representation*

3.2.3 Absorption refrigeration sub-processes

A focus on the operational behavior over the binary diagram are showed, being the absorption and distillation processes are the most important processes.

3.2.3.1 Distillation process

Desorption process is known as the separation process of a component diluted into two or more components. In ammonia-water mixture case, wet ammonia vapor is produced by heat adding ($\dot{Q}_{gen}$) to the ammonia-water solution. Both volatile components are separated during the vaporization process and a part of water vapor also evaporates with that ammonia vapor and demanding the rectification process. To a better explanation, Fig. (3.6) is presented; y-axis represents temperature and x-axis the ammonia mass fraction, that diagram is taken and amplified from Fig. (3.2), representing the area of interest for a typical desorption process at a constant pressure, 15.6 bar. The mixture is heated until it reaches point 1, bubble point curve. The mixture enters to the generator and ammonia separation is represented by point 2. The ammonia-water solution at the generator exit reaches state 3 at equilibrium with point 2. In the rectification process, wet ammonia vapor is purified until it reaches the point 5.

The rectification process is required because the high content of water in the vapor may cause problems at the evaporator, decreasing the cycle efficiency due to the water minimizes the refrigerant fluid quantity circulating into the evaporator. Also, water forms ice for vaporization temperature below 0 °C, acting as a thermal insulation. Moreover, the water presence at the

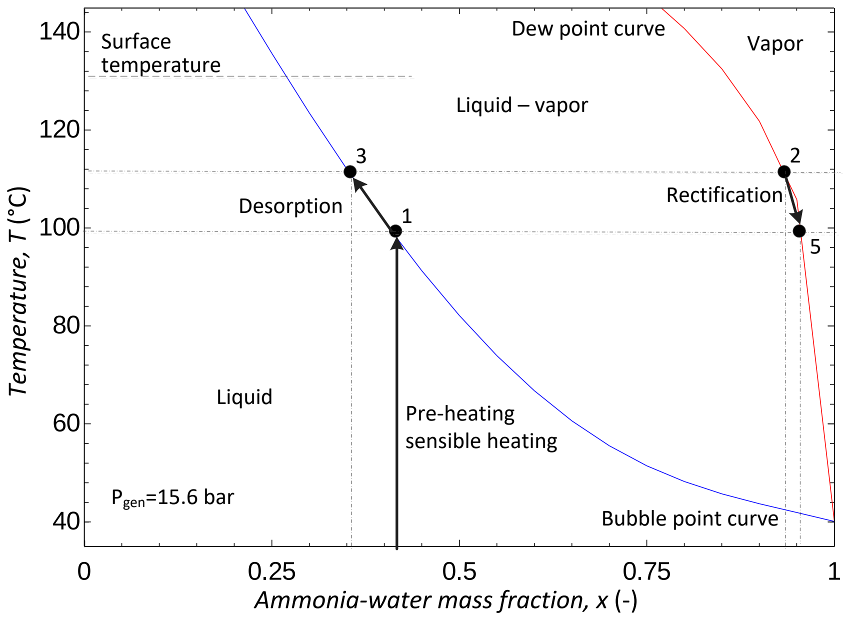

Figure 3.6 – *Schematic representation of the generation and rectification processes in the binary diagram under equilibrium*

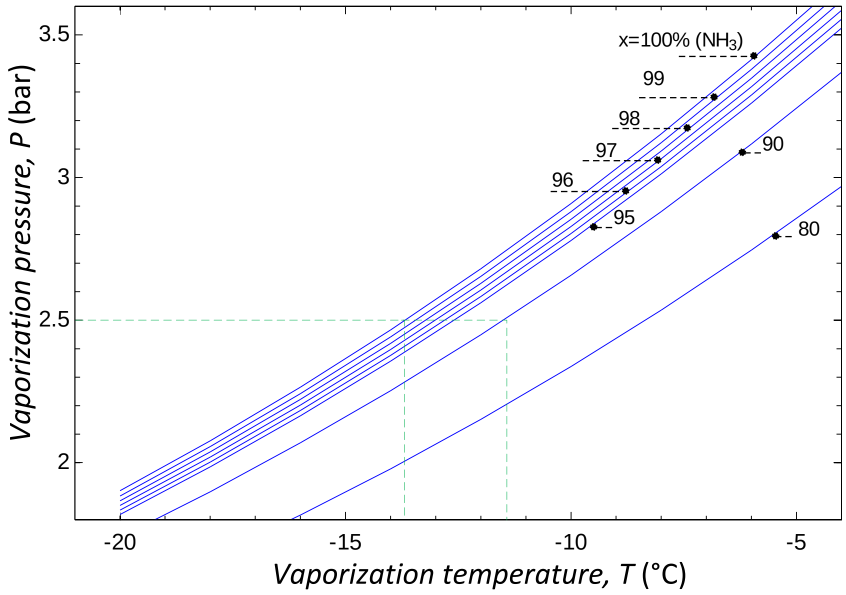

Figure 3.7 – *Set of several saturation curves for different ammonia-water concentration in which the vaporization pressure is a function of the vaporization temperature (adapted from (Jennings, 1935))*

evaporator changes the vaporization temperature, for instance, in Fig. (3.7) shows as ammonia with high purity degree (about 99.96 %) achieves about -14°C as operational temperature at the evaporator, but 90 % of purity converges to -11.4°C for the same absorption pressure, 2.5 bar.

3.2.3.2 Absorption process

In the absorption process a simultaneous heat and mass transfer occurs, where vapor which comes from evaporator (point 8) is absorbed by the weak solution that comes from the generator. In that way, the solution is enriched in ammonia (point 9) as shown in Fig. (3.8). Absorption can be analog to condensation process because a change phase exists, however, absorption process implies there is a phase condensed in the absorber entry (Herold et al., 2016). So, the rejected heat of absorption is transferred to the secondary fluid, in which it has a surface temperature lower than the ammonia-water solution.

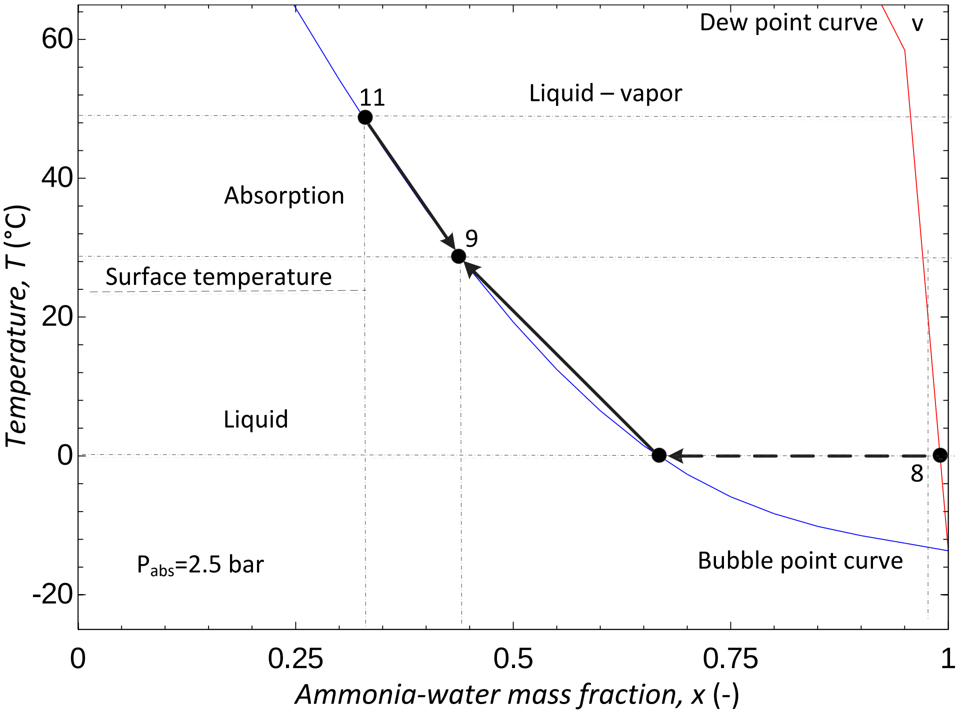

Figure 3.8 – *Schematic representation of the absorption processes in the binary diagram under the equilibrium*

3.2.4 Overall operational principles

It is of interest to note that in the experimental ARC all these operational parameters are changing, demanding an automatic control system to achieve the steady-state regime. Fig. (3.9) shows theoretical kg strong solution per kg of NH_3 that it should pumped to the generator in various pressure values, keeping constant the 2.5 bar absorption pressure and the 105°C weak solution temperature as a function of the strong solution temperature leaving the absorber. Each curve is obtained by developing the energy and mass balance at the absorber and given by Eq. (3.5). Jennings (1935) plotted the same set of curves using the weak solution temperature; subscripts ss and ws refer to strong and weak solution, respectively. x is the ammonia-water concentration and $\dot{m}$ is the mass flow rate.

$$\mathrm{SR} = \frac{\dot{m}_{ss}}{\dot{m}_{\mathrm{NH_3}}} = \frac{1 - x_{ws}}{x_{ss} - x_{ws}} \tag{3.5}$$

By means of these set of curves, it can be noted that an increase of the generation pressure from 9 bar to 12 bar implies an increase of about 6 to 9 $\mathrm{kg_{ss}/kg_{NH_3}}$, fixing the weak solution temperature leaving the generator in $T_{gen} = 105$°C, absolute absorption pressure in $P_{abs} = 2.5$ bar and keeping the same strong solution temperature leaving the absorber. By decreasing the strong solution temperature helps to decrease the theoretical strong solution rate (SR) circulating the system. It may valid as a part of the automatic control when the absorption unit operates in the full cooling capacity. However, in partial thermal loads, Goyal et al. (2015) used the evaporator temperature glide control $\Delta T = T_{eva,out} - T_{eva,in}$ as a first loop control, allowing to improve the properly phase change of the mixture at the evaporator by adjusting the expansion valve. Also, the control is completed by using a second loop, controlling the desorption process and its combustion module. The proposed control enhanced the COP by 8 %.

The same Fig. (3.9) may be used in other operational conditions by using the equivalent conditions for the absorption and generation system. For instance, in $T_{ws} = 100^\circ\mathrm{C}$, $P_{gen} = 12$ bar, $P_{abs} = 3$ bar and $T_{ss} = 40^\circ\mathrm{C}$ and by using Fig. (3.10) and (3.11) find the equivalent generation pressure and weak solution temperature, respectively. These values can be read in Fig. (3.12), whose strong solution rate (SR) is about 12 $\mathrm{kg_{ss}/kg_{NH_3}}$

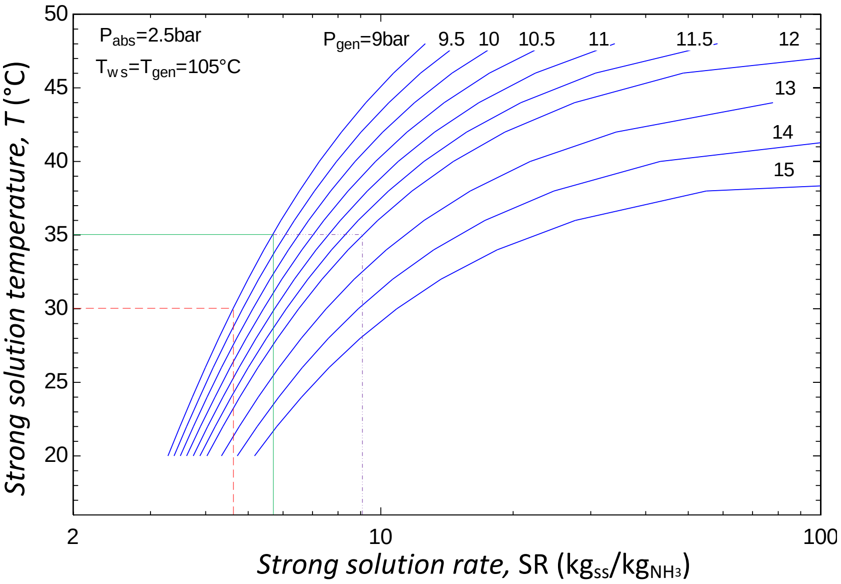

Figure 3.9 – *Strong solution pumped as a function of the strong solution temperature leaving the absorber for different generation pressures*

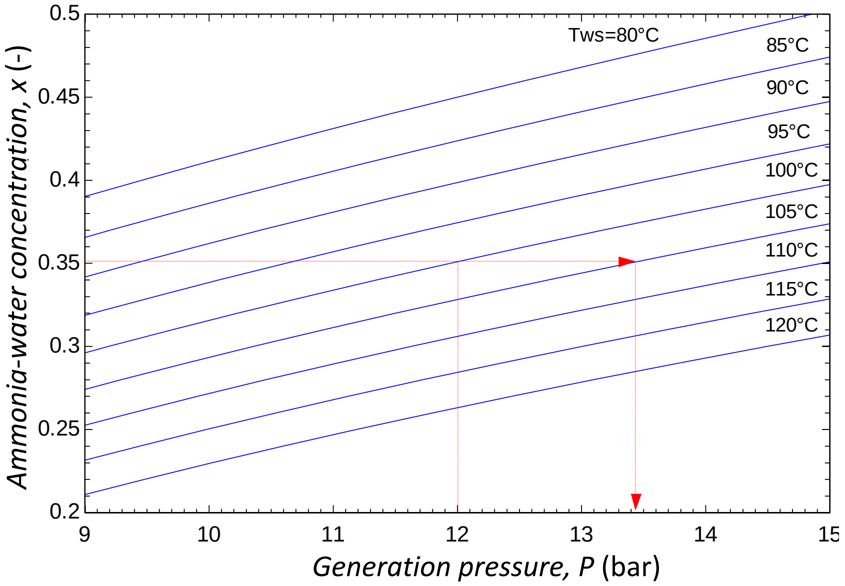

Figure 3.10 – *Bubble temperature curves: ammonia-water concentration as a function of generation pressure for different weak solution temperatures*

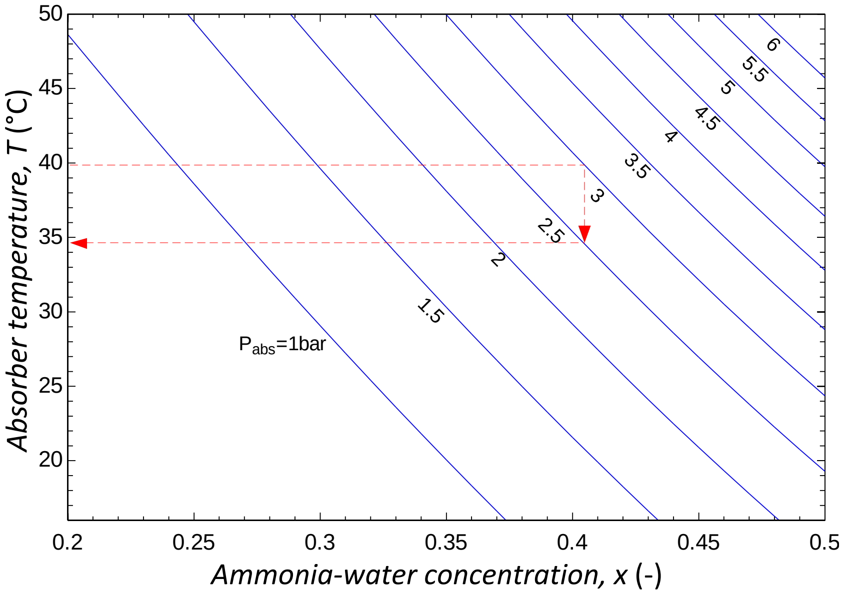

Figure 3.11 – *Bubble temperature curves: ammonia-water concentration as a function of absorber temperature for different absorption pressures*

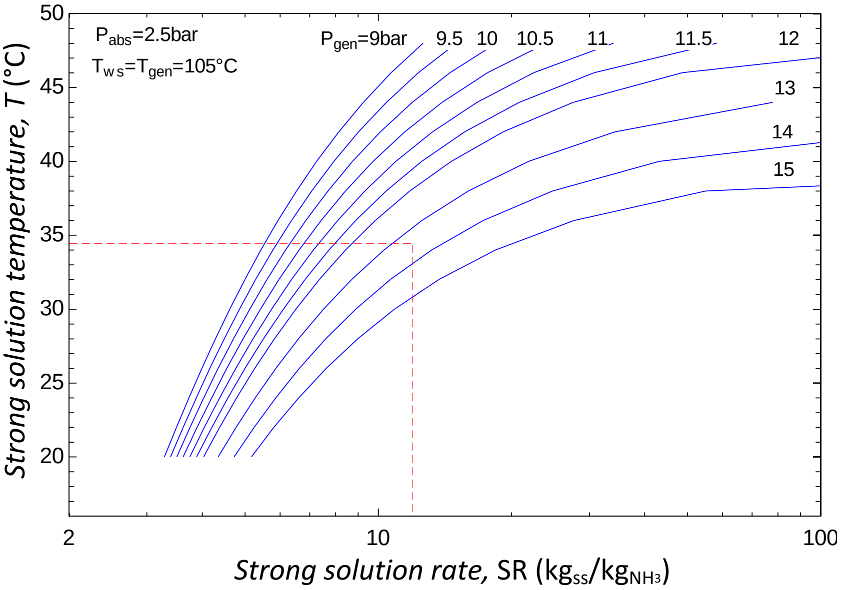

Figure 3.12 – *Example: kg strong solution pumped per* kg_{NH_3} *as a function of the strong solution temperature leaving the absorber for different generation pressure*

3.2.5 Heat and mass transfer operational range

Based on the ARC modeling defined in Appx. (E), it is detailed the possible heat and mass transfer operational range that the ARC components may achieve. In Appx. (F) is shown the same analysis for lithium bromide-water working fluid. The heat and mass transfer mapping of these correlations from the literature review are analyzed in a realistic operational conditions of an ARC for refrigeration (−20°C) and air-conditioning (7°C) applications. So, Figs. (3.13), (3.14a) and (3.14b) show the expected values of the heat and mass transfer for both absorption and generation process.

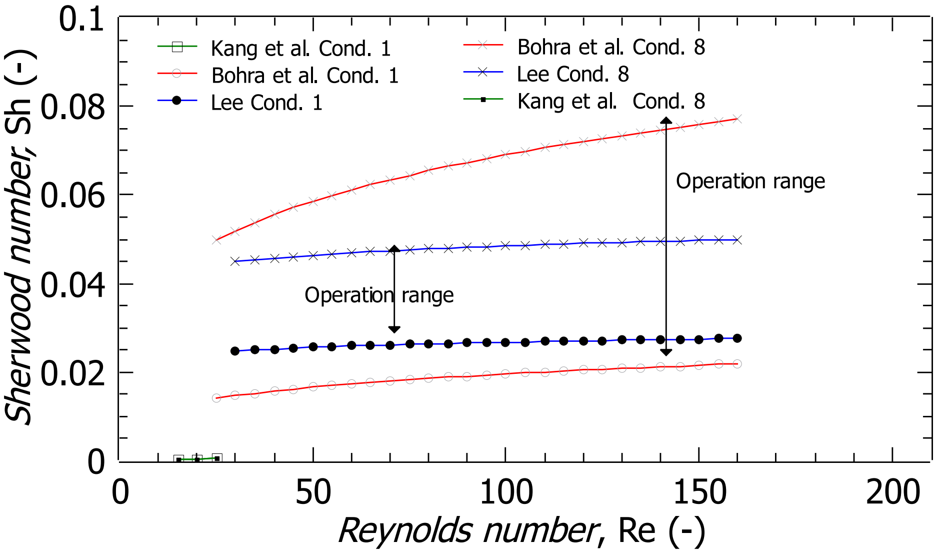

Figure 3.13 – *Sherwood number as a function of the Reynolds number for the ammonia-water solution. Cond 1 and 8 mean the operational conditions of the ARC defined in Appx. (E)*

Fig. (3.13) shows the Sherwood number as a function of the Reynolds number, which mass transfer is enhanced as the Reynolds number is increased. The mass transfer coefficient strongly enhances as the absorption refrigeration cycle achieves vaporization temperatures below 0°C. Moreover, Fig. (3.13) displays the possible mass transfer mapping for the ARC for the whole operational conditions given in Tabs. (2.2), and (E.1). The mass transfer mapping from Bohra (2007) agree with Lee (2007). However, Kang et al. (1999) underestimates these values, probably due to the fact that the conditions that the experiments are carried out at the test rig had low purity degree of ammonia vapor. Therefore, the Sherwood number may vary from 0.015 to 0.08 for the Reynolds numbers ranged from 10 to 150 in NH_3-H_2O ARC in refrigeration/air conditioning applications. The operational conditions 2 to 7 from Appx. (E) are not shown in Fig. (3.13), as these values are found within these ranges.

Fig. (3.14) shows the Nusselt number as a function of the Reynolds number. Fig. (3.14a) displays the correlations employed in the falling film technology using ammonia-water and other working fluids for evaporation process, in which correlations such as Zavaleta-Aguilar and Simões-Moreira (2015), Wilke (1962), Chun and Seban (1971), Alhusseini et al. (1998), and Narváez-Romo and Simões-Moreira (2017) show similar heat transfer values from Bohra (2007) (absorption process) for the Reynolds numbers between 100 and 150. However, the trend of these processes are in opposition to each other.

Fig. (3.14b) displays a comparison between Kwon and Jeong (2004), Jeong et al. (1998), Kang et al. (1999), Lee (2007), Lee et al. (2002b) and Hu and Jacobi (1996a), showing that these correlations present similar results to each other, i.e., Kwong and Jeong's correlation (Kwon; Jeong, 2004) found to fall within the operating range of Lee et al. (2002b) and Hu and Jacobi's (Hu; Jacobi, 1996a). Hu and Jacobi's correlation (Hu; Jacobi, 1996a) may be used to design the absorption process (droplet-column pattern flow). However, Jeong et al. (1998) and Kang et al. (1999) underestimate the heat transfer, as the first neglects the effects of Prandtl number, and the second carried out the experimental work for absorption processes for a low degree of ammonia vapor purity.

Fig. (3.14) shows that the Nusselt number may vary between 0.001 and 0.2 for the Reynolds number ranged from 10 to 250 (with an exception of Bohra (2007)) for NH_3-H_2O ARC in refrigeration/air conditioning applications. It is worthwhile to mention that the best performance of the heat transfer is achieved at the lowest vaporization temperature ($T_{eva} = -20°C$) for all the correlations.

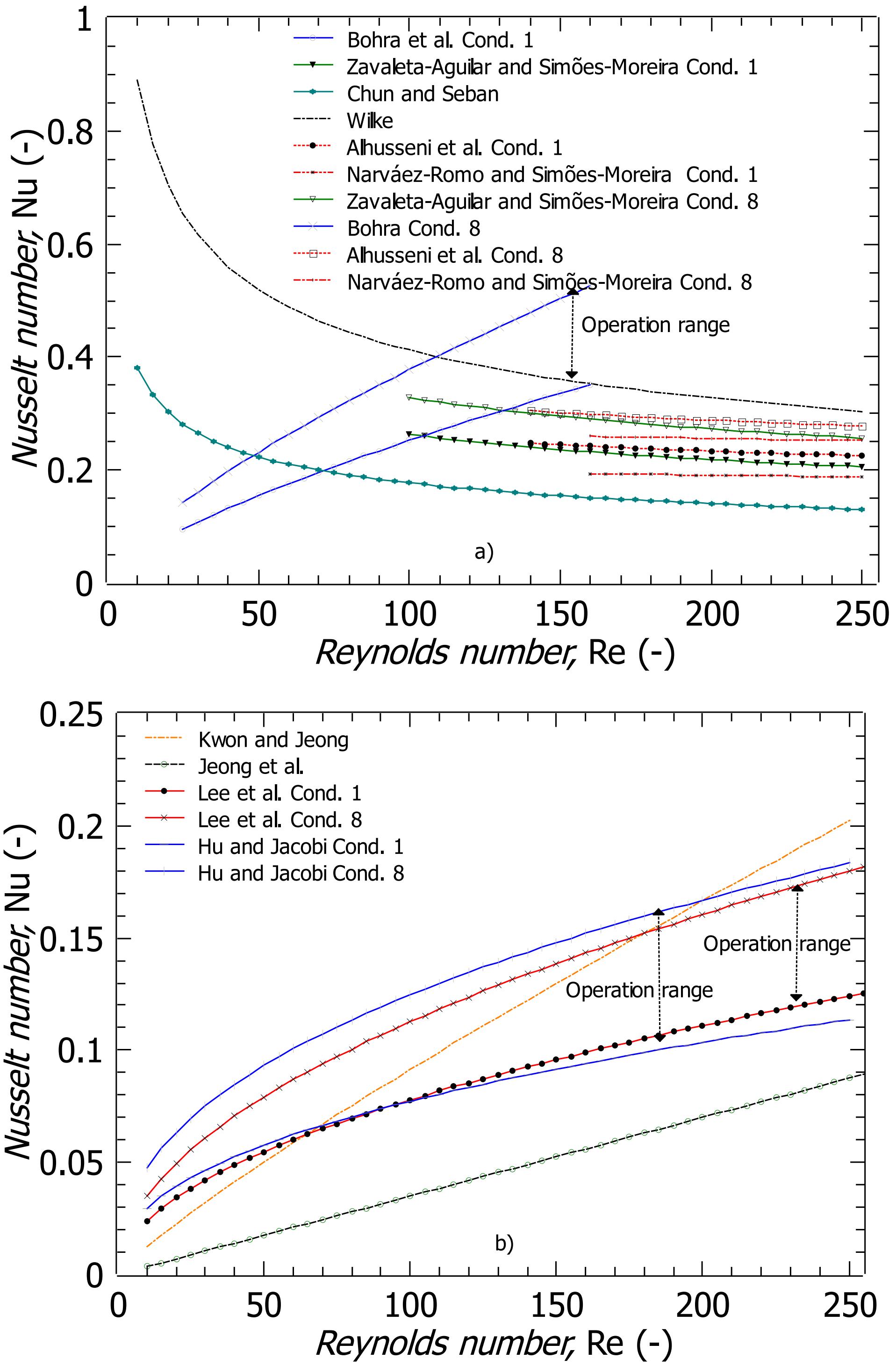

Figure 3.14 – *Nusselt number as a function of the Reynolds number for the ammonia-water solution in which a) shows all the available correlations used in falling film technology, and b) shows the correlations led for ammonia-water falling film except (Hu; Jacobi, 1996b). Cond 1 and 8 mean the operational conditions of the ARC defined in Appx. (E)*

.

Chapter 4

ABSORPTION PROCESS MODELING

In order to carry out the absorption process modeling the following main simplifications have been assumed: a) 1-D heat and mass transfer model in which the absorption occurs in a constant pressure, b) ammonia-water absorption is a physical reaction and all the heat of absorption is rejected at the liquid-vapor interface, c) the mass transfer between the liquid and vapor phase occurs as the consequence of the simultaneous effect of molecular diffusion and bulk transport of the ammonia across the interface (Bird, 2002), d) other energy forms in the energy conservation equation are neglected, e) the absorption process happens in steady-state, f) heat and mass transfer processes are given in the perpendicular direction to the interface (Taylor; Krishna, 1993), g) heat transfer by radiation is neglected, h) the circular plate is assumed to be developed as a flat plate kepping the equivalent geometrical relation, i) ammonia vapor at the saturated condition enters in the absorber, and j) ammonia-water thermodynamic properties are defined by using the Ibrahim (1993) routines implemented in the *Engineering Equation Solver* (EES) software (Klein, 2015).

Typical operational conditions are obtained from ARC modeling (Appendix E). The correlations of the transports properties for ammonia-water are defined in Appendix (H). These parameters have been used to study the absorption process in the horizontal liquid film configuration for ammonia-water mixtures. ARC has been analyzed for the following parameters; thermal load of 1 TR, vaporization temperature of $-13°$ C, condensation temperature of 40°C. These values established the range of operational conditions for the absorption process such as;

- liquid phase inlet mass flow: 0.020 kg/s or liquid flow rate per unit of plate width:$\Gamma_L =$ 0.010 kg/m s ;
- inlet liquid phase ammonia mass fraction: 0.405;
- inlet liquid phase temperature: 39.6°C (saturation temperature for $x = 0.408$ and $P = 2.5$ bar);
- inlet vapor phase mass flow: 0.0033 kg/s;

- inlet vapor phase ammonia mass fraction: 1.0;
- inlet vapor phase temperature: −13 °C;
- circular plate wall temperature: 25 °C;
- OD circular plate: 0.18 m;

The new absorber proposal is shown in Fig. (4.1), in which it has six plates for the real configuration; weak solution is display as blue color arrow entering on the absorber top, and ammonia vapor is the red dashed arrow, representing a counter-current absorption. At the end of the absorber, the strong solution is obtained and it is shown as green color arrow. A particular plate is located on the top; its shape allows it to work as a liquid solution distributor. On the bottom, the mechanism has a hole for ammonia vapor entrance. The circular plate are installed inside a quartz cylinder. The special configuration of the mechanism allows liquid solution to run from top to bottom in a zigzag way, same as vapor but in opposite direction.

As a typical absorber, it must have an entrance and an exit for the coolant substance, an entrance for the weak solution, an entrance for the ammonia vapor and an exit for the strong solution. The main place where the phenomenon occurs is the plate, which is composed by a spiral tube where the coolant flows, the shape of the plate allows the ammonia liquid solution to behave as a flooding substance which in contact with ammonia vapor absorption happens, has a particular profile which allows to form an specific one millimeter film and a total wettability of the tube as shown in Fig. (4.2)

Fig. (4.2) represents the horizontal liquid film absorption process. An spiral heat exchanger is used as coolant secondary circuit, and it is mounted over a circular plate. The weak solution

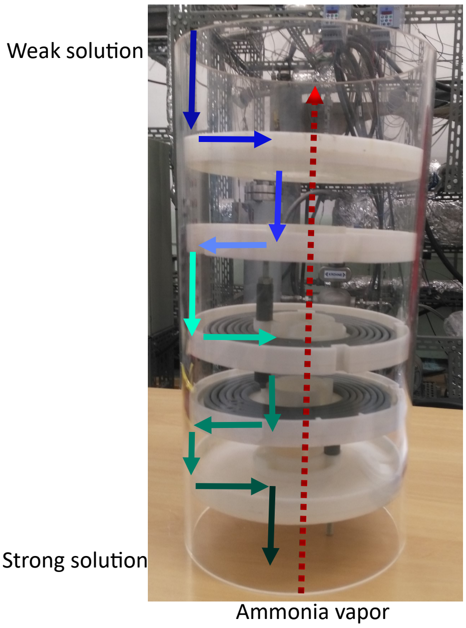

Figure 4.1 – *Still picture of a physical model of the new absorber: horizontal liquid film absorber*

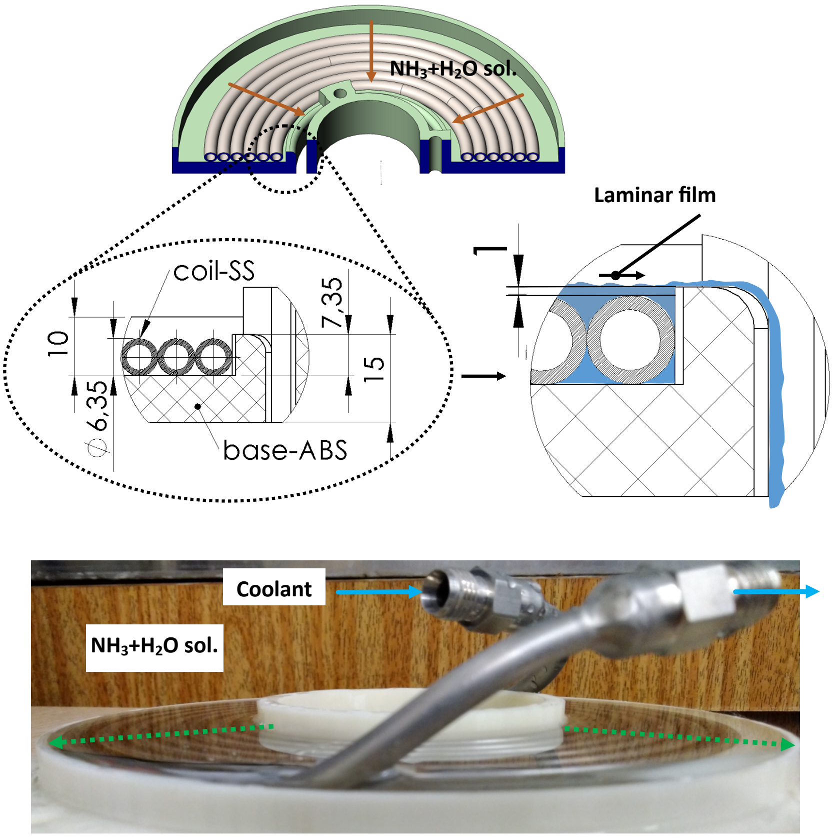

Figure 4.2 – *Schematic representation of the horizontal liquid film absorption process*

moves over the heat exchanger, allowing the contact between the ammonia vapor and the solution over it, having the total wettability. As absorption process occurs, heat of absorption is transferred to the coolant fluid.

4.1 Discretized governing equations

It is used the Leite's model (Leite, 2015) and all the results are well detailed in Narváez-Romo et al. (2020), in which the current studied is adapted for the horizontal liquid film. Concerning the discretized equations in ammonia-water absorption process using falling film technology, Fernández-Seara et al. (2005) performed one of the first thermal modeling studies including the vapor phase property variation. They used the finite difference technique, applying the laws of conservation of mass, species of ammonia, and energy for each discrete control volume: liquid, vapor, and linked by the interface. Also, Du and Wang (2018) carried out a numerical studied through a finite differential method in a novel falling film configuration. They used the Chilton and Colburn analogy to calculate the mass transfer coefficient at the vapor phase and the heat transfer coefficient at the liquid side.

In this section it is discussed the discretized equations. Given the importance, first the liquid-vapor interfacial phenomenon is discussed. The liquid-vapor interface can be represented as a control volume in which both phases coexist in thermodynamic equilibrium (Fig. 4.3). As the ammonia and water mass flux across the interface must be conserved, they can be calculated by using Colburn and Drew (Colburn; Drew, 1937) equations relating the mass transfer coefficients with the interfacial properties.

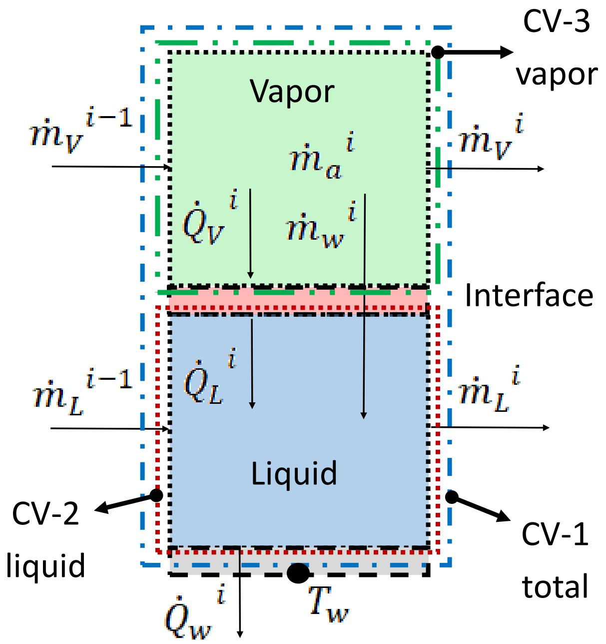

Figure 4.3 – *Schematic representation of the heat and mass transfers processes over the horizontal liquid film absorber. Blue color is the liquid phase, pink color is the liquid-vapor interface, and green color is the vapor phase. Control volume 1 (CV-1) is the blue dashed line (liquid + vapor), CV-2 is the red dashed line (liquid), and CV-3 is the green line (vapor)*

By species mass conservation, the ammonia mass flux $\dot{m}''_a$ (kg/m^2 s) becoming from the vapor and going through the interface is the same that the ammonia entering to the liquid phase, being positive when the ammonia vapor enters to the liquid phase (Treybal, 1981). It can be calculated by Eq. (2.18),

$$\dot{m}''_a = z \cdot k_{m,v} \cdot \rho_V \cdot \ln\left(\frac{z - y_{int}}{z - y}\right) \tag{4.1}$$

For the liquid phase side is given by Eq. (4.2).

$$\dot{m}''_a = z \cdot k_{m,L} \cdot \rho_L \cdot \ln\left(\frac{z - x}{z - x_{int}}\right) \tag{4.2}$$

$k_{m,v}, k_{m,L}$ (m/s) is the mass transfer coefficient for the vapor and liquid phase, respectively;ρ (kg/m^3) is the density, in which v and L denotes the vapor and liquid phase; y and x represent the concentration for the vapor and liquid phase, respectively, highlighting that the subscript $_{int}$ refers to the interface; z is the condensing flux and it is given by Eq. (4.3), in which $\dot{m}''_w$ (kg/m^2 s) is the water flux at the interface. The mass transfer can be determined through Chilton and Colburn (1934) analogy already defined in Eq. (2.14),

$$z = \frac{\dot{m}''_a}{\dot{m}''_a + \dot{m}''_w} \tag{4.3}$$

Energy balances across the interface are used to determinate the temperature profiles and energy heat rate (Taylor; Krishna, 1993) in which the heat flow across the interface by convection on either side of the interface as well as the condensation or vaporization enthalpy must be taken into account. These energy heat rate across the interface must be equals $\dot{E}_V = \dot{E}_L$. The energy balance are given in Eq (4.4 and 4.5), $\dot{Q}''_L$ and $\dot{Q}''_V$ (J/kg m^2) is the flux of heat rate between the liquid and vapor phase, i J/kg is the specific enthalpy

$$\dot{Q}''_v + \left(\dot{m}''_a + \dot{m}''_w\right) i_{v,int} = \dot{E}''_v \tag{4.4}$$

$$\dot{Q}''_L + \left(\dot{m}''_a + \dot{m}''_w\right) i_{L,int} = \dot{E}''_L \tag{4.5}$$

The heat flux to each or from each phase is given by convection alone. Eqs. (4.6−4.7) give the heat flow to the liquid and vapor phase, respectively.

$$\dot{Q}''_L = h^*_L \cdot (T_{int} - T_L) \tag{4.6}$$

$$\dot{Q}''_v = h^*_v \cdot (T_v - T_{int}) \tag{4.7}$$

In previous expressions, the superscript * indicates that the heat transfer coefficient is corrected for simultaneous heat and mass transfer by the expression mentioned by Treybal (Treybal, 1981) in which it recommends the Ackermann correction factor (Ackermann; Gnam, 1937). It is assumed that the interface area A_{int} is the same area of the heat rate transfer through the wall.The convective heat flow to the surface $\dot{Q}_w$ is given by Eq. (4.8), h_L is the convective heat transfer in the liquid side, T_L is the average liquid temperature, and T_w is the surface temperature,

$$\dot{Q}_w = h_L \cdot A_{int} \cdot (T_L - T_w) \tag{4.8}$$

while several studies (Du; Wang, 2018; Goel; Goswami, 2005b) estimate the liquid heat transfer coefficient through the work developed by Wilke (1962) or Nusselt theory (Nusselt, 1916) such as (Fernández-Seara et al., 2005), the current work estimates the heat transfer coefficient by Churchill and Ozoe's correlation (Eqs. 4.9) (Churchill; Ozoe, 1973) because that correlation is developed for natural convection over a flat plate and thus the Nusselt number Nu_δ is given as follows,

$$\mathrm{Nu}_\delta = \frac{h_L \cdot \delta}{k_l} = \frac{0.3387\mathrm{Pr}_L^{1/3}\mathrm{Re}_L^{0.5}}{\left(1 + \left(\frac{0.0468}{\mathrm{Pr}_L}\right)^{2/3}\right)^{0.5}} \tag{4.9}$$

Pr_L is the Prandtl number, k_L is the liquid thermal conductivity, δ is the horizontal liquid film and Re_L is the Reynolds number given by Eq. (4.10); μ_L is the dynamic viscosity and Γ_L is the mass flow rate per length, $\Gamma_L = \dot{m}_L/\pi \cdot D_{plate}$, D_{plate} is the diameter of the flat plate.

$$\mathrm{Re}_L = \frac{4\Gamma_L}{\mu_L} \tag{4.10}$$

It is worthwhile to mention that in falling liquid film it is generally defined as the Nusselt definition Eq. (2.26) but the current study defines the film thickness as the result of the geometrical aspect due to the high of the plate defines this value as shown in Fig. (4.3). For this work, the liquid film thickness was of 0.001 m.

The above equations are now applied to a 1-D cell. First, an individual cell is split into three control volumes as depicted in Fig. (4.3). Control volume 1 (CV-1) is the whole volume of the cell, including both liquid and vapor phases; control volume 2 (CV-2) envelopes only the liquid phase (liquid film); and control volume 3 (CV-3) encompasses the vapor phase alone. The balances of total mass, ammonia mass, and energy in CV-1 are given by the set of Eqs. (4.11−4.13).

$$\dot{m}_L^{i-1} + \dot{m}_v^{i-1} = \dot{m}_L^i + \dot{m}_v^i \tag{4.11}$$

$$\dot{m}_L^{i-1} x^{i-1} + \dot{m}_v^{i-1} y^{i-1} = \dot{m}_L^i x^i + \dot{m}_v^i y^i \tag{4.12}$$

$$\dot{m}_L^{i-1} i_L^{i-1} + \dot{m}_v^{i-1} i_v^{i-1} = \dot{m}_L^i i_L^i + \dot{m}_v^i i_v^i + \dot{Q}_w^i \tag{4.13}$$

The balances of total mass, ammonia mass, and energy in CV-2 are given by the set of Eqs. (4.14−4.16).

$$\dot{m}_L^{i-1} + \dot{m}_a^i + \dot{m}_w^i = \dot{m}_L^i \tag{4.14}$$

$$\dot{m}_L^{i-1} x^{i-1} + \dot{m}_a^i = \dot{m}_L^i x^i \tag{4.15}$$

$$\dot{m}_L^{i-1} i_L^{i-1} + (\dot{m}_a^i + \dot{m}_w^i) i_{L,int}^{i-1} + \dot{Q}_L^i = \dot{m}_L^i i_L^i + \dot{Q}_w^i \tag{4.16}$$

The energy balance at the liquid-vapor interface is given by Eq.(4.17).

$$\dot{Q}_v^i + \left(\dot{m}_a^i + \dot{m}_w^i\right) i_{v,int}^i = \dot{Q}_L^i + \left(\dot{m}_a^i + \dot{m}_w^i\right) i_{L,int}^i \tag{4.17}$$

The heat flow on the surface is given by Eq. (4.18).

$$\dot{Q}_w^i = h_L \cdot A_{int} \cdot \left(T_L^i - T_w^i\right) \tag{4.18}$$

The heat flows across the interface are given by Eqs. (4.19−4.20) for liquid and vapor sides, respectively.

$$\dot{Q}_L^i = h_L^* \cdot A_{int} \cdot \left(T_{int}^i - T_L^i\right) \tag{4.19}$$

$$\dot{Q}_v^i = h_v^* \cdot A_{int} \cdot \left(T_v^i - T_{int}^i\right) \tag{4.20}$$

The ammonia mass flow across the interface is given by the set of Eqs. (4.21−4.23).

$$\dot{m}_a^i = z^i \cdot k_{m,v} \cdot \rho_v \cdot A_{int} \cdot \ln\left(\frac{z^i - y_{int}^i}{z^i - y^i}\right) \tag{4.21}$$

$$\dot{m}_a^i = z^i \cdot k_{m,L} \cdot \rho_L \cdot A_{int} \cdot \ln\left(\frac{z^i - x_{int}^i}{z^i - x^i}\right) \tag{4.22}$$

$$z^i = \frac{\dot{m}_a^i}{\dot{m}_a^i + \dot{m}_w^i} \tag{4.23}$$

4.2 Results to calculate the absorption process area

Some of these results are shown in Narváez-Romo and Simões-Moreira (2019) and Narváez-Romo et al. (2020). Fig. (4.4) shows the heat flux along the plate length to or from each phase and to the plate surface. It is clearly shown that the heat flow in the liquid phase is larger than the heat flow in the vapor phase. That can be explained because a higher thermal resistance occurs on the vapor phase. The negative flow in the vapor phase indicates that the direction is from the interface to the vapor phase, because there is a range in which the interface temperature is higher than the temperature of the vapor phase. For a 1 TR, the absorber test rig should has a area of 0.108 m^2, allowing to reach an outlet temperature of $T_{ss} = 26.4$°C and an outlet concentration of 0.452. The temperature of the liquid phase reached 91.1 % from the surface temperature, and 77.4 % from the required concentration at the outlet for 0.6m length. The plate length should be 0.76m to achieve 90 % from the required concentration at the outlet. It is worthwhile to mention that the saturated concentration allowed for 25°C is 0.4895.

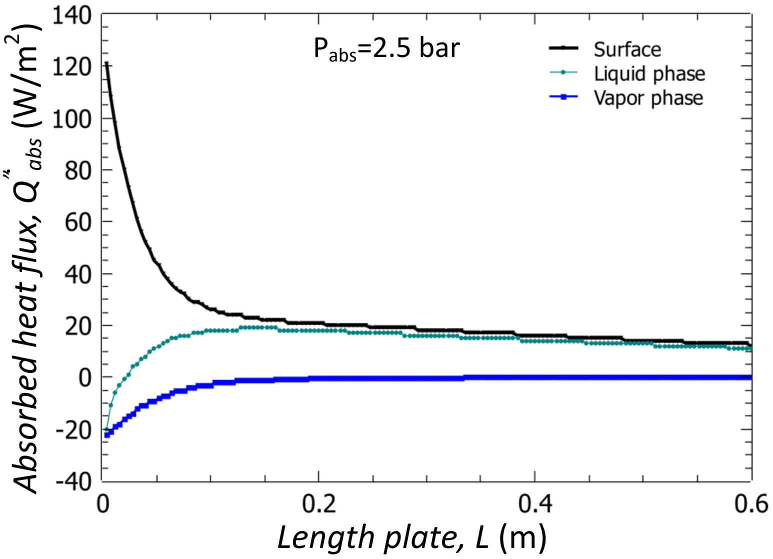

Figure 4.4 – *Heat flux along plate length for the absorption process in which the blue color line shows the vapor phase, green color line is the liquid phase, and black color line is the surface*

4.3 Individual plate heat exchanger

It's worthwhile to mention the absorbed heat rate of each plate is different although the surface temperature is kept constant. Heat and mass transfer processes are prominent in the beginning of the absorber. In Fig. 4.5, plate heat exchanger labeled with "1" is referenced to the first position and "6" as the lowest plate into the absorber. That figure also shows the absorption heat rejection decreases as a function of the position into the absorber, whose first plate absorbed about 30% of the total heat of absorption.

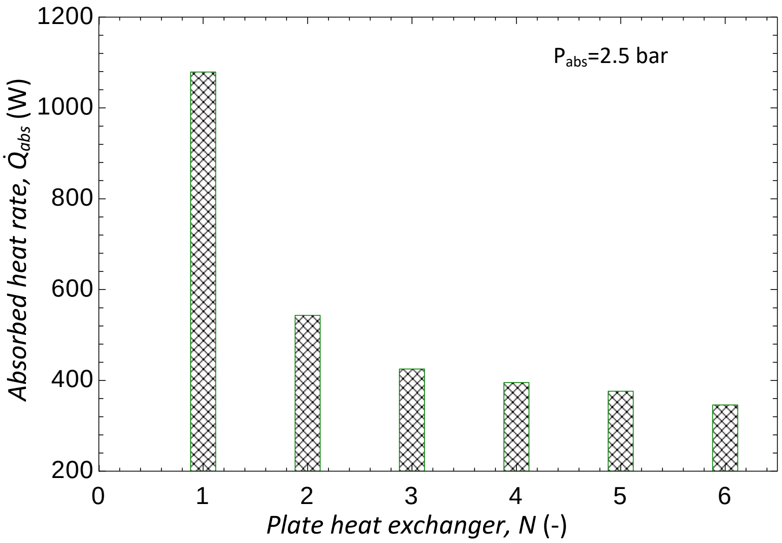

Figure 4.5 – *Absorbed heat rate as a function of the plate position into the absorber; 1 is the highest position and 7 the lowest position*

4.4 Liquid film thickness and surface temperature

The first plate is fixed to analyze the heat and mass transfer behavior as function of the liquid film thickness and the surface temperature. Also, operating conditions in the first plate were fixed: weak ammonia-water solution $m_L = 0.020$ kg/s, ammonia concentration $x = 0.358$, ammonia vapor $m_v = 0.0033$ kg/s, vapor concentration $y = 0.9997$ and vapor temperature $T_v = -13$°C. Fig. (4.6) shows the heat of the absorption as a function of the surface temperature (lower axis) and the liquid film thickness (upper axis). Green and blue color lines are the liquid film thickness and the surface temperature, respectively. Higher heat absorption rates are obtained in lower surface temperatures and lower liquid film thickness. A film thickening increases the thermal resistance.

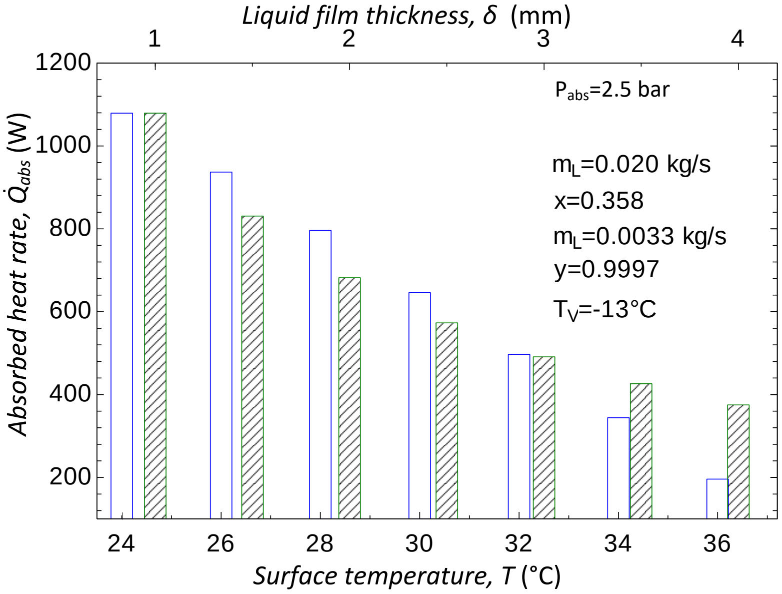

Figure 4.6 – *Absorbed heat rate as a function of the surface temperature and the liquid film thickness in which the blue color lines is the surface temperature, and the green color lines is the liquid film thickness. $\delta = 1$ mm is fixed when the surface temperature is changed. T_w=25° C is fixed when the liquid film thickness is studied.*

Chapter 5

EXPERIMENTAL TEST RIG

This chapter describes the experimental proposal to study the ammonia-water absorption refrigeration cycle and the heat and mass transfer coefficient over a modified horizontal liquid film absorber, detailing the ammonia-water ARC and its three different liquid circuits. Also, it delineates the heat exchanger absorber manufacturing, the safety conditions and procedures about the ARC. Finaly, the instrumentation, data acquisition and automation machine is defined for the new test rig supported by Thematic Project - FAPESP N $2016/09509-1$.

5.1 Ammonia-water absorption refrigeration cycle

The absorption refrigeration cycle testing bench or GAX single-stage cycle is focused to study the ammonia-water absorption process as a function of the real operational conditions of an ARC, in which it recreates a different range of parameters such as various absorption pressure or vaporization temperature, ammonia-water concentration, weak mass flow rate, strong mass flow rate, co-current/contra-current absorption process, and various inlet weak solution temperature. Also, the test rig allows to study the generation process for different surface temperature or for subcooled or saturated strong solution entering to generator. Fig. (5.1) shows the test rig assembly, in which 50x50 aluminum profiles over wheels were used to the structure building (1.6x1.4x1.6)m^3. All the assembly was carried out in the *Renewable and Alternative Energy Systems Laboratory - SISEA*. Absorber and generator were mounted by using a manual oil hydraulic lift system. Fig. (5.2) is shown the overall view of the test rig fo ammonia-water absorption refrigeration cycle.

Fig. (5.3) shows the principal circuit of the ammonia-water absorption refrigeration cycle, in which all the components are defined. It is observed three different line colors (red, green and light green). Red line is defined as the liquid refrigerant flow (ammonia with high purity degree), whose dashed and continuous line denotes the vapor and liquid conditions, respectively. The green color line defines the strong solution going from the absorber to the generator. Finally, the weak solution is shown as the light green color line.

Figure 5.1 – *Sequence of ammonia-water ARC mounting assembly*

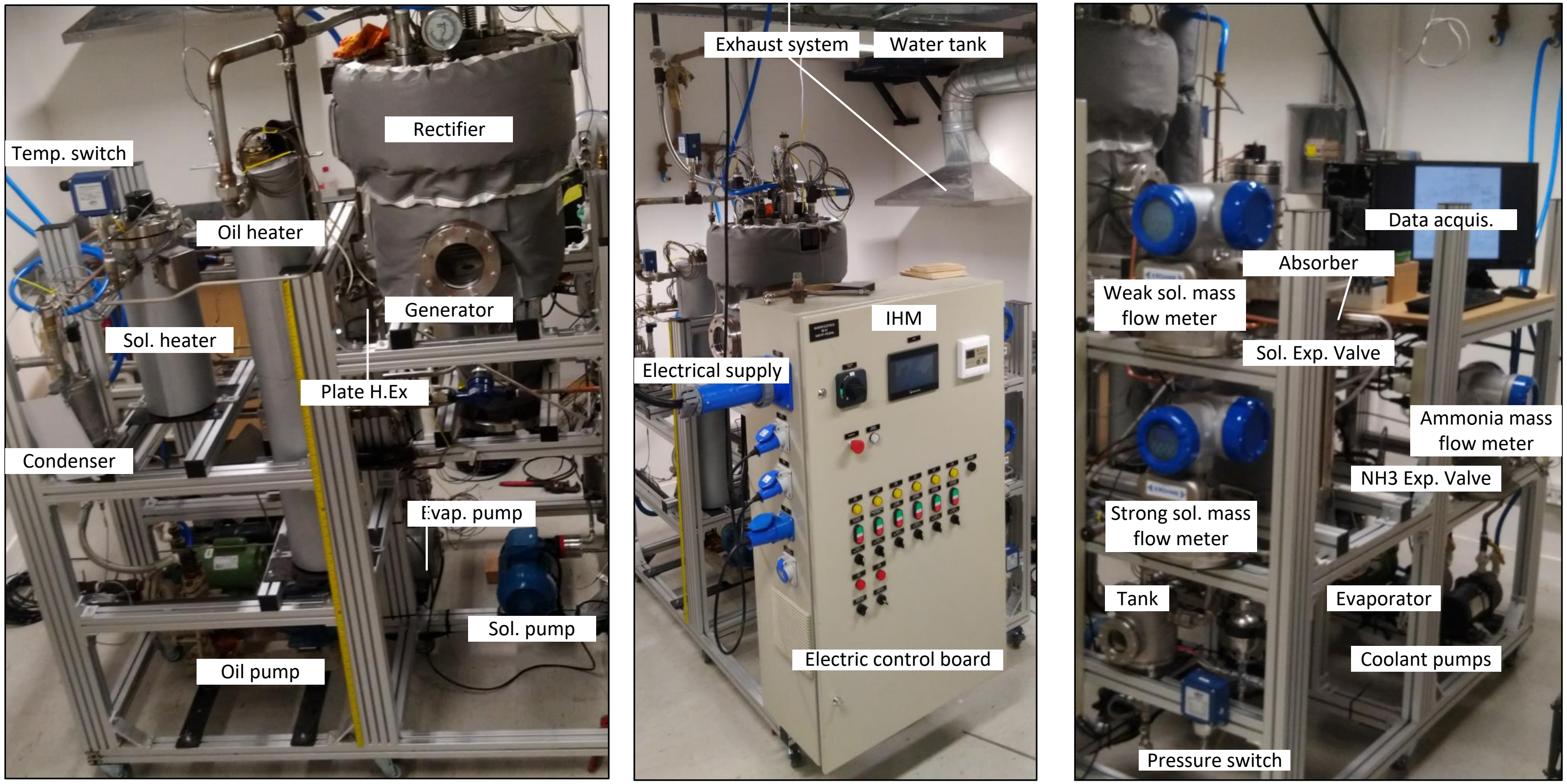

Figure 5.2 – *Overall view of the test rig of ammonia-water absorption refrigeration cycle*

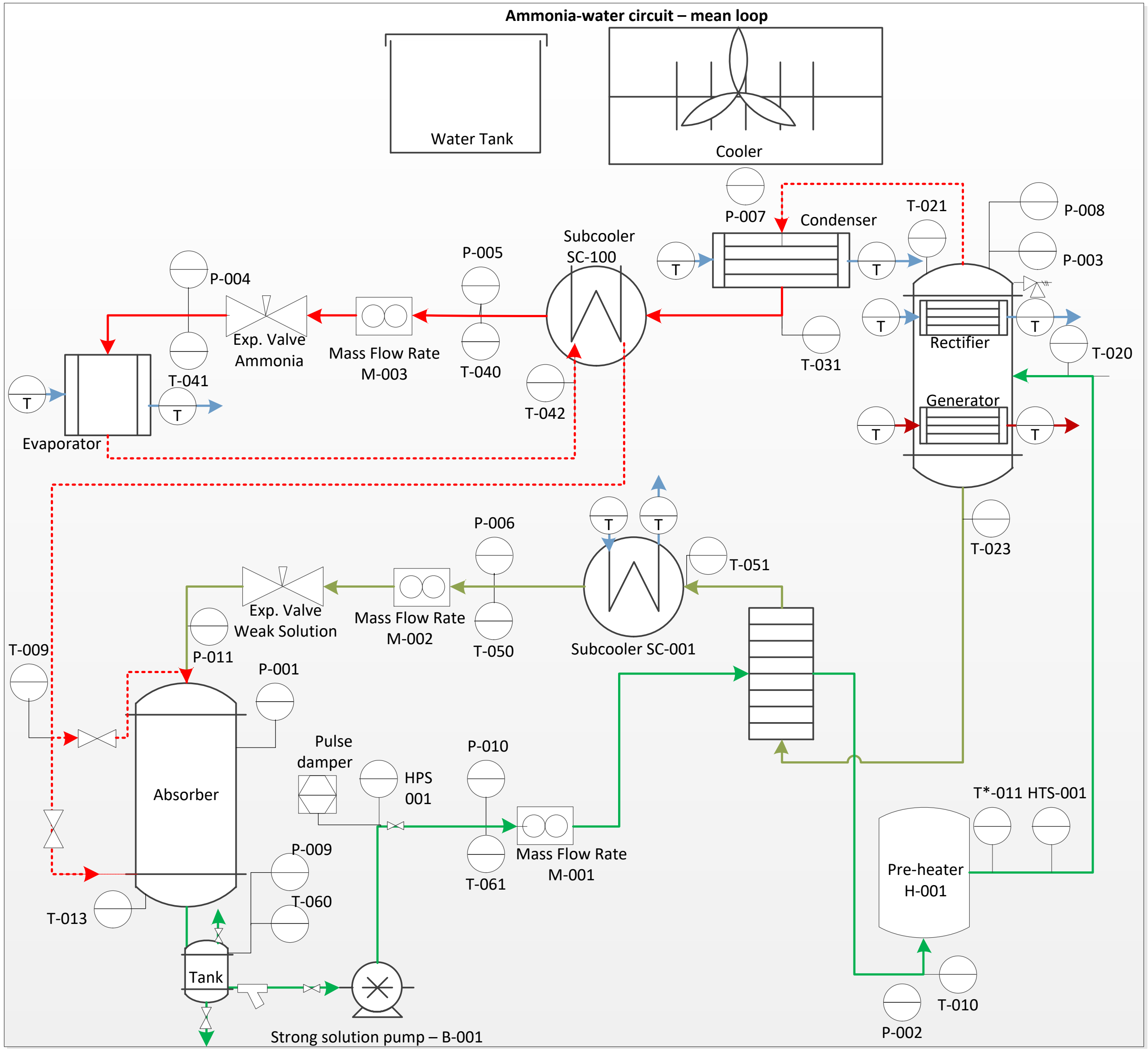

Figure 5.3 – *Diagram of the test rig of ammonia-water absorption refrigeration cycle*

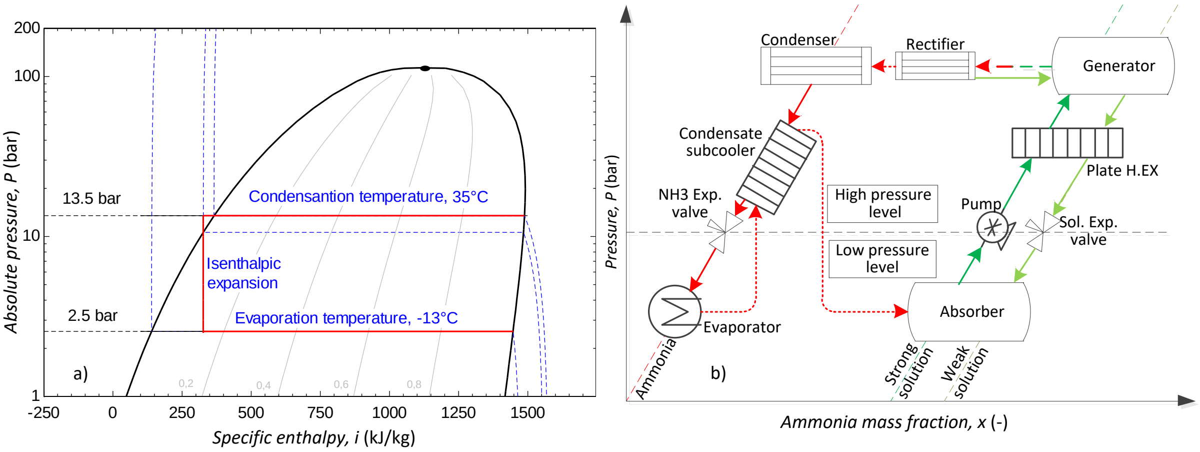

Figure 5.4 – *Schematic representation of the a) P-h diagram for ammonia refrigerant and b) the ARC on the $P-x$ diagram*

Wet ammonia vapor (red color line) is produced as consequence of the simultaneous heat and mass transfer mechanism in the generation process as the strong liquid ammonia-water solution enters in the falling film generator, whose input energy comes from an external heat source. Ammonia vapor is purified in the tube bundle rectifier under a constant pressure process. Water is condensed and it returns into the weak solution circuit. Thus, high purity degree vapor is condensed by using a water-cooled condenser. Liquid refrigerant flows to the evaporator as a conventional compression refrigeration cycle as shown in Fig. (5.4a), in which the ammonia expansion valve is installed for pressure drop and consequently the Joule-Thomson effect decreases the temperature. A micrometer needle valve is adjusted to fix the evaporation pressure. A condensate subcooler (SC-100) is installed to improve the coefficient of performance of the ARC. Thus, ammonia vapor at the saturated conditions is always guaranteed at the absorber inlet.

Weak ammonia-water solution (light green color line) comes from the generator, and then it passes through a plate heat recovery exchanger. The pressure is reduced by using an expansion valve, which operates in the same pressure range of the evaporator. The solution absorbs the ammonia vapor into the absorber and the heat of absorption is rejected to the coolant water. At the bottom of the absorber, the strong ammonia-water solution is achieved. A stainless steel tank is used as storing tank. It is worthwhile to mention that the subcooler (SC-001) is installed to control the weak solution temperature at the absorber inlet, recreating various operational conditions.

Strong ammonia-water solution (green color line) is driven from storing tank to the generator by using a positive displacement, in which a pulsation damper is included to reduce the oscillations of the mass flow rate. The circuit receives energy from the heat recovery, heating the solution before it enters to the generator. The pre-heater (H-001) is coupled to fix the solution temperature, recreating a subcooling degree or saturated condition at the generator temperature. T^*_{011} is used to control such temperature. A variable frequency drive (VFD) is installed to control the mass flow rate of the strong solution, whose "true" value is given by using the coriolis mass flow rate M_{001}. In Fig. (5.4b) is shown the $P-x$ diagram of the ARC,

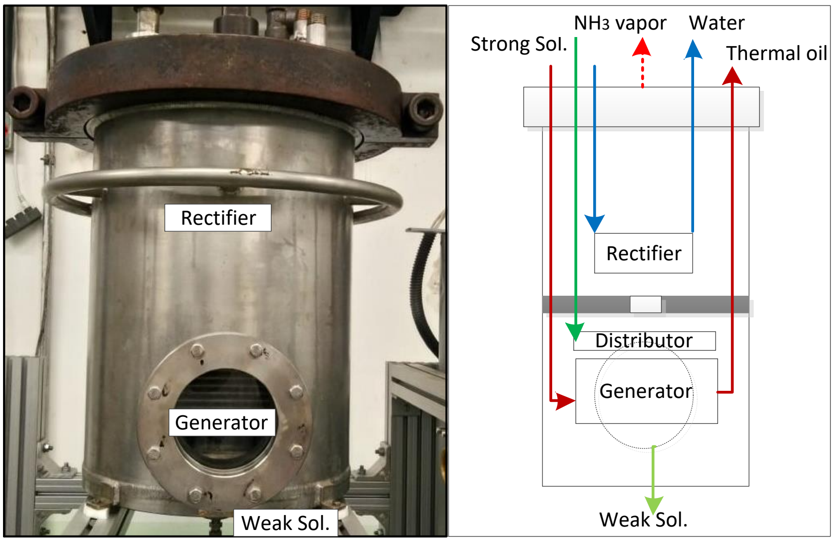

Figure 5.5 – *Ammonia distillation by using a generator connected with rectifier system*

in which it allows identifying each component.

5.1.1 Ammonia distillation system

Fig. (5.5) shows the ammonia distillation system developed by Zavaleta-Aguilar (2015), in which the falling liquid film technology was employed. The generator is connected with the rectifier system at the same pressure vessel. A plate is installed to divide the two chambers. The same author carried out an experimental study over the distiller under various operating conditions. The present work projected a new distribution system of the liquid falling film, improving the surface wettability of the heat exchanger. Also, all the tubing connections were changed, aiming to reduce the tubing size. It allows changing the welded connections by threaded connections.

For the heat transfer coefficient at the liquid film, Zavaleta-Aguilar (2015) obtained an experimental correlation to estimate the average Nusselt number as a function of the Reynolds and Prandtl number: $\mathrm{Nu} = 0.75\mathrm{Re}^{-0.27}\mathrm{Pr}^{0.4}$, whose Nu is given by Eq. (2.24). Based on the operating conditions in the generator, it estimates a $4500 - 5500$ W/m^2 °C range heat transfer coefficient at the liquid film side for Reynolds number until $\mathrm{Re} = 320$ (Eq. (2.32)). Nominal oil temperature and volume flow rate is about 130°C and 60 l/h.

Reynolds number is given by Eq. (2.31), and ammonia-water thermophysical and transport properties were computed by using Conde (2006). A maximum strong solution mass flow rate entering to the generator is about 0.026 kg/s, whose value is controlled by a VFD. The total area of the generator is $A_{gen} = 0.2639$ m^2, consisting by 70 - (7x10) horizontal tubes of 8 mm outlet diameter stainless steel tube, 0.150 m length and 2 mm thickness tube.

Fig. (5.6) shows the new ammonia-water distributor system over the bundle tubes. Distributor was built in aluminum by using milling machine. Dimensions of each tube position were obtained *in situ*, improving the distribution along each row of tubes. Also, an alignment over the center line on the first tube was carried out.

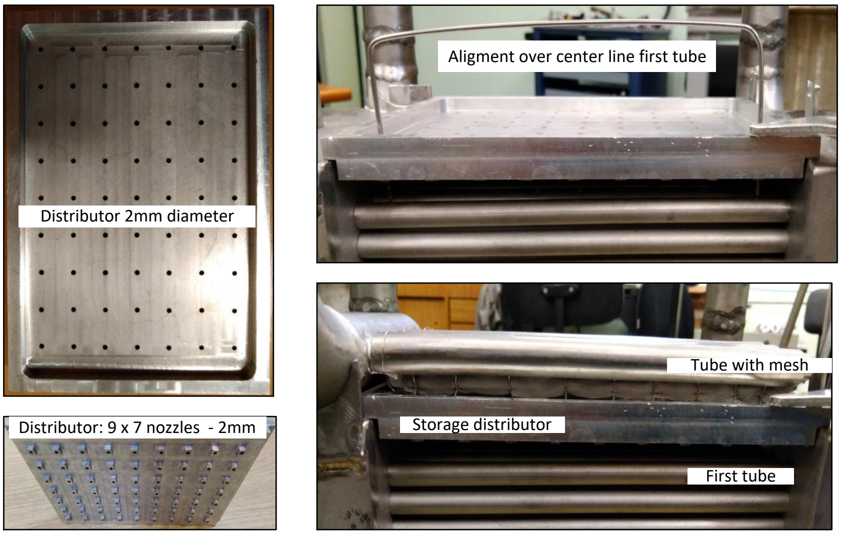

Figure 5.6 – *Distributor of the strong ammonia-water solution*

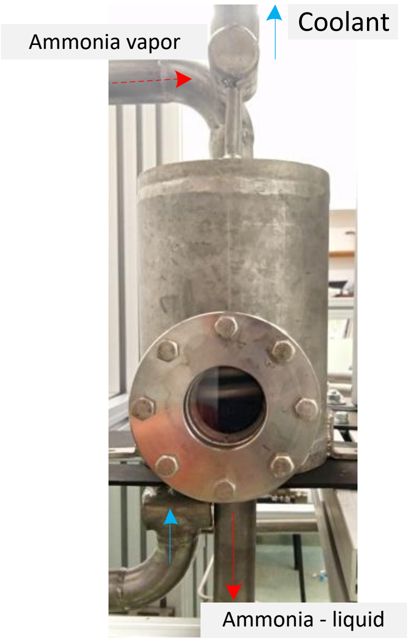

Figure 5.7 – *Condenser using water coolant as secondary flow*

5.1.2 Condenser and condensate subcooler

Air-cooled condenser are less compact as compared water-cooled heat exchanger for the same heat exchanger rate, being that the first usually operates in highest surface temperature by consequence of the low heat transfer coefficient. Water-cooled condenser was used in the current

Figure 5.8 – *Subcooler for ammonia liquid subcooling*

project, whose heat removed is transferred to the water circuit; $Q_{con} = Q_{water}$. The inlet water temperature at the condenser was fixed around 29°C, whose value usually is employed in the cooling tower. 3 tube numbers with $d_i = 6$mm, $d_o = 8$mm was defined, in which the total mass flow rate is given by $m_{total} = 3 * m_{tube}$. Reynolds number inside each tube is computed by $\mathrm{Re}_{in} = (4 \cdot m_{tube})/(\pi d_i \cdot \mu_{water})$.

Condenser rejects the heat at the high pressure level. Fig. (5.7) shows the flow directions, whose ammonia vapor enters at the condenser top, and ammonia liquid is obtained at the down part. Secondary flow absorbs the heat of condensation and it is driven to the cooler. After, the condensate subcoler is installed to improve the coefficient of performance, thus, liquid-vapor coming from evaporator is engaged to subcool the ammonia liquid entering to the evaporator as shown in Fig. (5.8). An enthalpy decreasing at the inlet of the expansion valve rises the cooling capacity using the same mass flow rate as shown in Fig. (5.9), being useful in partial thermal loads.

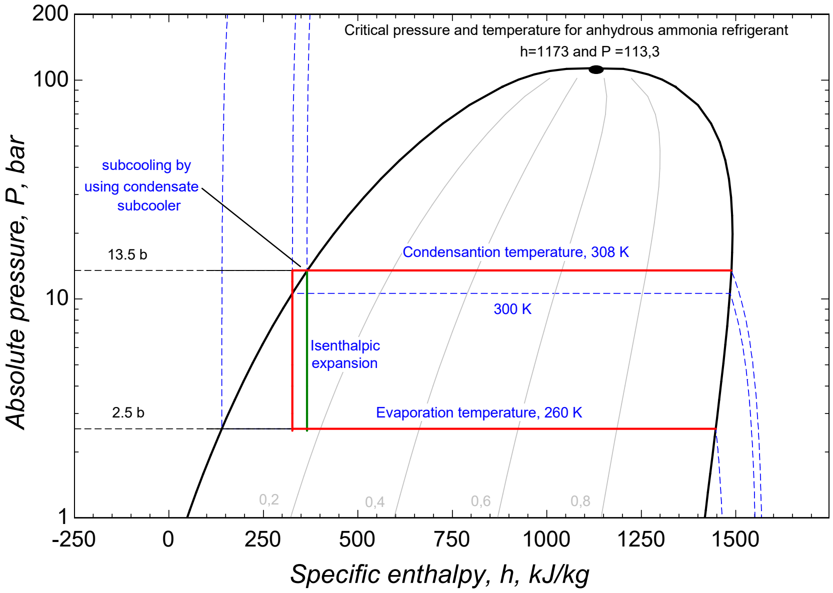

Figure 5.9 – *Schematic representation of the liquid refrigerant subcooling by using a condensate subcooler*

5.1.3 Expansion valves

In conventional compression refrigeration cycles, a thermostatic expansion valve or an electronic expansion valve is commonly installed in order to control the cooling capacity by changing the mass flow rate. Compressor follows that instructions by using a discrete or continuous control. However, needle expansion valve for ammonia-water solution and for ammonia liquid circuit are installed in ARC, whose manual set will command the absorption pressure. Fig. (5.10) shows the expansion valve for the ammonia-water solution. Coefficient flow for the ammonia refrigerant valve (31-Series Swagelok) and the ammonia-water solution valve (1315G4Y-Hoke) is 0.024 and 0.04, respectively.

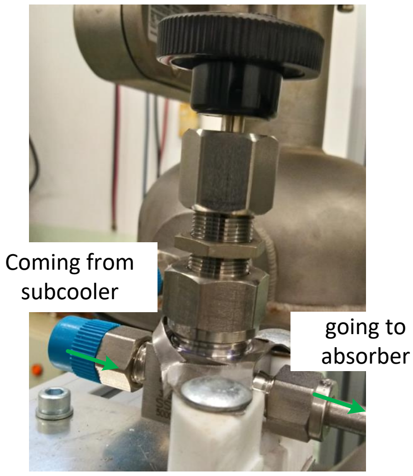

Figure 5.10 – *Expansion valve for ammonia-water weak solution*

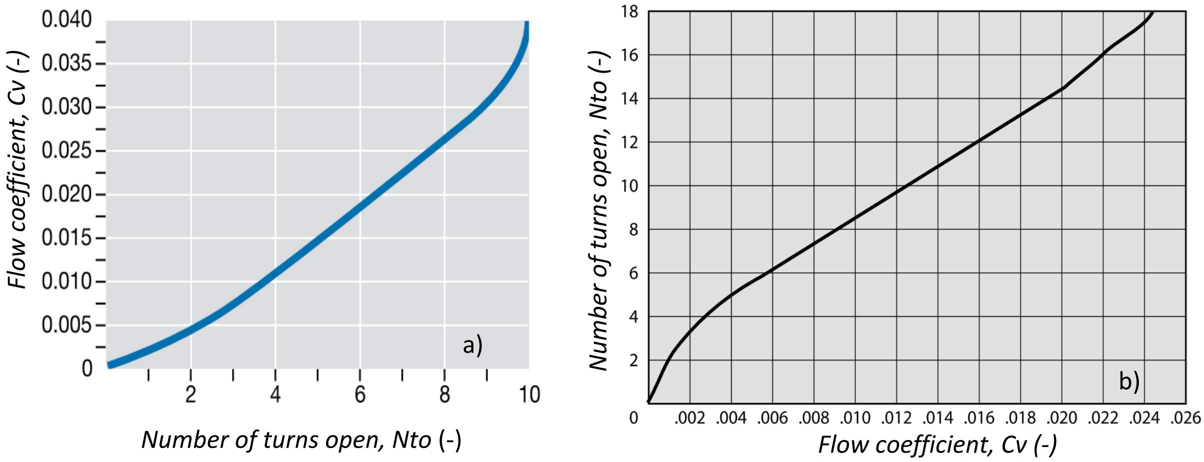

Figure 5.11 – *Cv as a function of number of turns open for solution expansion valve for a) ammonia-water solution and b) ammonia refrigerant flow*

5.1.4 Strong solution pump

A positive displacement pump with EPDM membrane was installed in the absorption refrigeration cycle, in which a 1200 rpm electrical motor with variable speed-drive (VFD) was coupled. Pump is built to work up to 121°C operating temperature and 69 bar discharge operating pressure. A pulsation damper is included to regulate the mass flow rate. Table 5.1 and Fig. (5.12) show several operational conditions as a function of the concentration x_{ss}, temperature T and cooling capacities $\dot{Q}_{eva}$.

Table 5.1 – *Operational conditions for several cooling capacities*

x_{ss}	T_{ss}, °C	$\dot{V}_{ss}$ @2000W, l/h	$\dot{V}_{ss}$ @5000 W, l/h
0.45	25	98.07	247.1
0.42	30	97.13	244.8
0.39	35	96.19	242.4
0.36	40	95.25	240
0.33	45	94.31	237.7
0.31	45	94.07	237.1

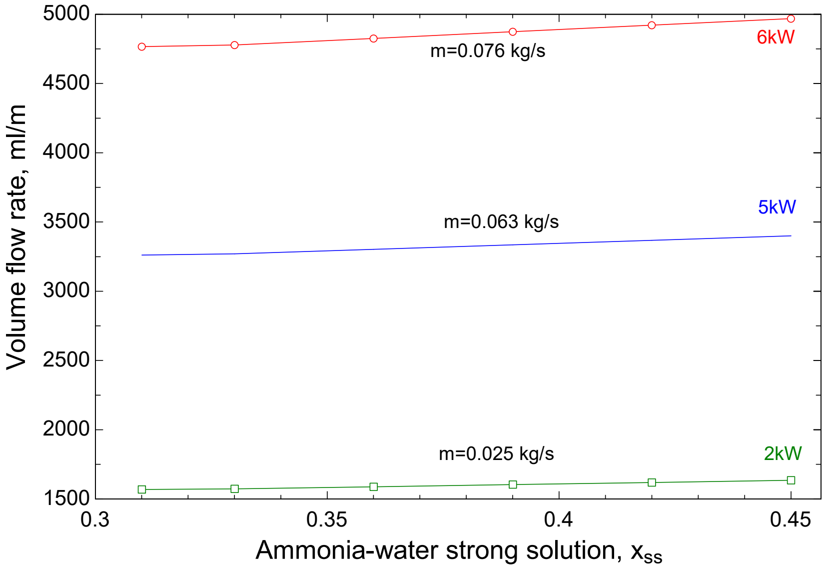

Figure 5.12 – *Different volume flow rate of the ammonia-water strong solution as a function of various cooling capacities*

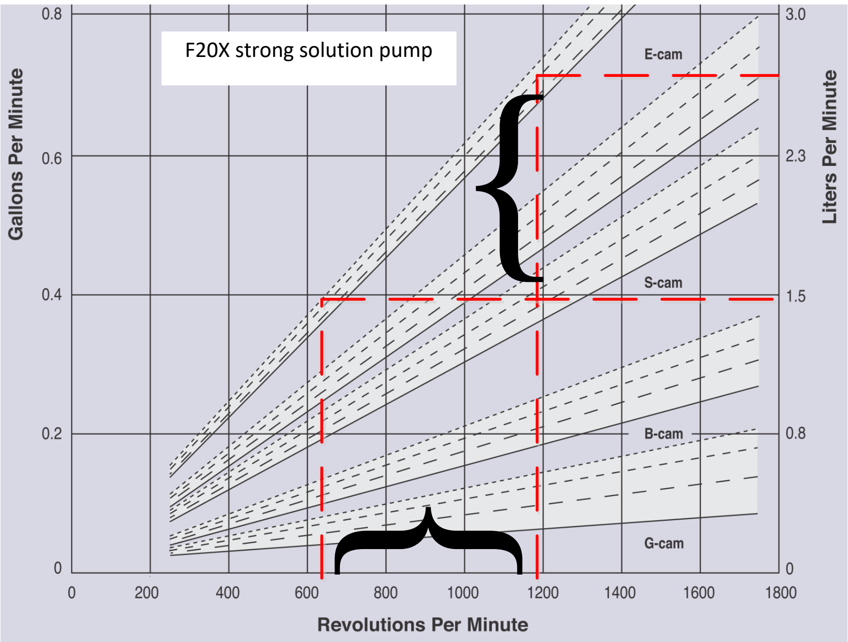

Figure 5.13 – *Operational conditions for strong solution pump. Source: Hydra-cell*

5.1.5 Subcooler (SC-001) - Weak solution

A subcooler (SC-001) is installed to control the weak solution temperature at the absorber inlet as shown in Fig.(5.14), recreating a set of temperature operating range. Also, a decrease of the sensible heat of the solution entering the absorber allows achieving low evaporation temperatures or absorption pressure. The lowest solution temperature reduces the partial vapor pressure of the ammonia because the ammonia solubility increases into the ammonia-water solution.

Heat exchanger consists of an 19.05 mm OD external tube and an 12.7 mm OD internal tube. 1 mm wall thickness and 5 m length characterizes both stainless steel tubes. Ammonia-water weak solution flows inside internal tube, and coolant water goes between both tubes. The heat

Figure 5.14 – *Still picture of the subcooler for weak solution temperature control*

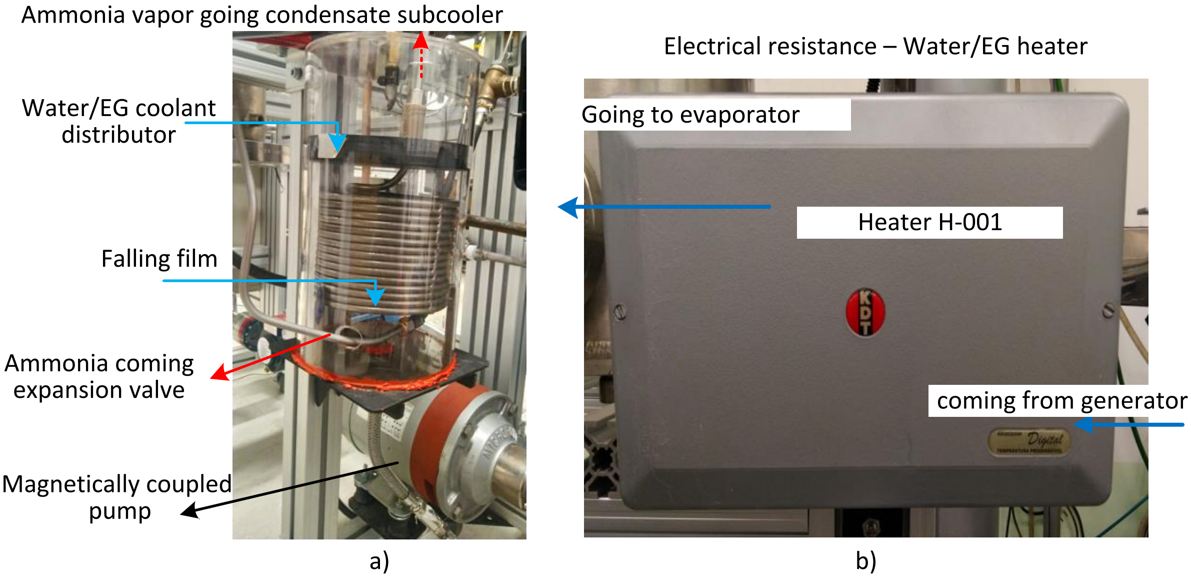

Figure 5.15 – *a) Falling film evaporator and b) electrical resistance for thermal load*

transfer coefficient inside internal tube is computed by using $\mathrm{Nu}_i = 5.74$ (Hewitt et al., 1994), in which an about Reynolds number $\mathrm{Re} = 560$ defines the laminar regime. In contrast, highest Reynolds number in the water coolant ($\mathrm{Re} = 1000$) define the Dittus-Boelter's correlation to calculate the water coolant heat transfer coefficient. An 0.00175 m^2 °C /W fouling factor is assumed as thermal resistance for both sides.

5.1.6 Evaporator and thermal load

Evaporator is projected by using falling film technology as shown in Fig (5.15), in which an 6.35 OD and 1 mm wall thickness stainless tube is employed. An 6 m length helical tube heat exchanger is manufactured in the lathe machine. Two 1/4 Swagelok tubing connections are welded at the tube ending. The liquid film distributor is built by using a 3D printer, whose dimensions were obtained *in situ*, allowing to correct geometrical manufacturing changes for better liquid distribution over the evaporator. An $9500W$ electrical resistance with PID controller is installed as thermal load.

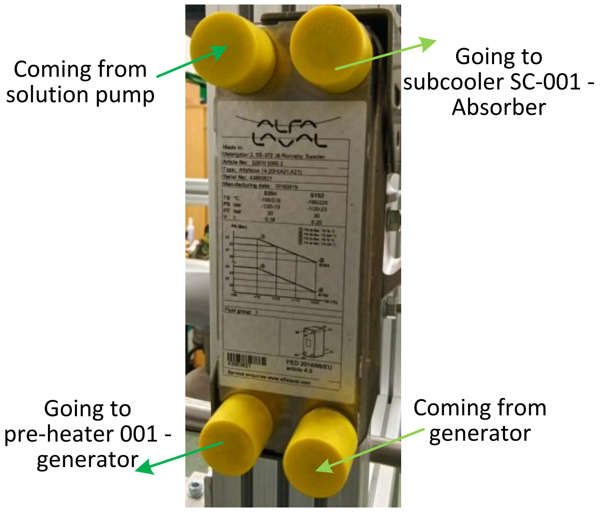

Figure 5.16 – *Plate heat recovery exchanger*

5.1.7 Recovery heat exchanger

A plate heat recovery exchanger is installed between the strong and weak solution lines, in which the first recovers energy from the weak solution going to the absorber. The AlfaNova 14 – 20H heat exchanger consists of flat 316 stainless steel plates fusion-bounded together on the edge. Four 3/4 ISO 228/1-G1 threaded connections allows connecting the counter-current flow between both the streamlines as shown in Fig. (5.16).

Heat transfer coefficient are computed under laminar regime in which the Nusselt number is given by $\mathrm{Nu} = 7.54$ (Incropera et al., 2007). The hydraulic diameter is defined as two times the wall thickness $D_h = 2 \cdot \delta_w = 0.0049\mathrm{m}$, totalizing an $0.2875\mathrm{m}^2$ heat transfer area. The weak and strong ammonia-water solution is 0.0226kg/s and 0.0278kg/s. The project estimated a 430 $\mathrm{W/m^2 °C}$ global heat transfer coefficient, resulting in a configuration of 19 plates. Therefore, the AlfaNova 14 – 20H plate heat exchanger is selected.

5.1.8 Strong solution pre-heater

A strong solution pre-heater is installed before the ammonia-water solution enters to the generator. The 3kW electrical resistance allows recreating the subcooled and saturated condition at the generator inlet.

5.2 Horizontal liquid film absorber

Based on the bibliographic literature review shown in Section (2), there are two typical absorption configurations; bubble absorber or falling film absorber. The current work shows a new absorber configuration based on the falling film technology and its wettability problems. In the absorber, ammonia vapor coming from falling film evaporator is absorbed by the weak solution coming from the generator, releasing an exothermic reaction. The heat of absorption

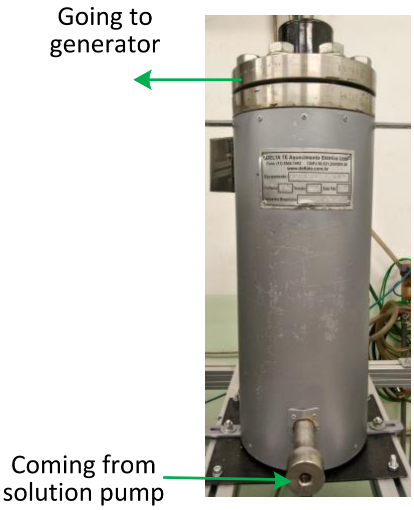

Figure 5.17 – *Electrical pre-heater for the strong ammonia-water solution*

is rejected to the water coolant that circulates through each spiral plate heat exchanger, achieving a strong solution at the ending of the ammonia-water absorber.

The absorber consists of several plates placed in the vertical position. Each one of these plates consists of a spiral cooling tube as shown in Fig.(5.18a), in which the water coolant flows inside tube and the ammonia-water solution flows over spiral tube. Each plate is placed inside the absorber. 1/4 NPT connections are installed over the wall absorber, linking the water coolant between both external and internal side as shown in Fig.(5.18b). The ABS plate barrier guarantees an one-millimeter horizontal liquid film of the ammonia-water solution. Fig.(5.18c) presents the horizontal film absorber going over the spiral at the radial direction. It is worthwhile to mention that the wettability problems over the heat exchanger are overcome. Moreover, the residence time of the ammonia-water in contact over the heat exchanger increases, whereas the heat transfer coefficient may reduce as the consequence of low velocities and high liquid film thickness as compared with the conventional falling film technology.

As can be observed, Fig. (5.18) configuration is not commercially available. The heat exchanger was built at the *SISEA Laboratory*. A low-budged heat exchanger is projected and built as shown in Fig. (5.19). An 1/4 stainless steel tube is mounted over a cylinder fixed on the lathe machine, allowing to curve over it and producing an spiral form. Two lateral supports are installed to guaranty the Z alignment direction. A cylindrical wedge is mounted over the cylinder, avoiding the uncontrolled deformation in the first turning. Welding process is carried out before it will be dismounted of the cylinder, fixing all the tubing coils.

According to the absorber vessel project, Fig. (5.20) shows the absorber manufacturing in which the absorber is built by using a 8$''$ - 40 Sch 304 stainless steel tube, with two 150 class flanges, 600 length, 16 1/4 NPT connections and two inspection window (0.380 m x 0.01 m). Connections are employed in the water coolant circuit, driven heat of absorption from each plate (6 plates) to the environment.

In the 40 Sch tube, 16 equidistant 19.05 mm OD holes are drilled to install the water coolant connections as shown in Fig. (5.20a). The tube is rectangularly cut in both side to install the

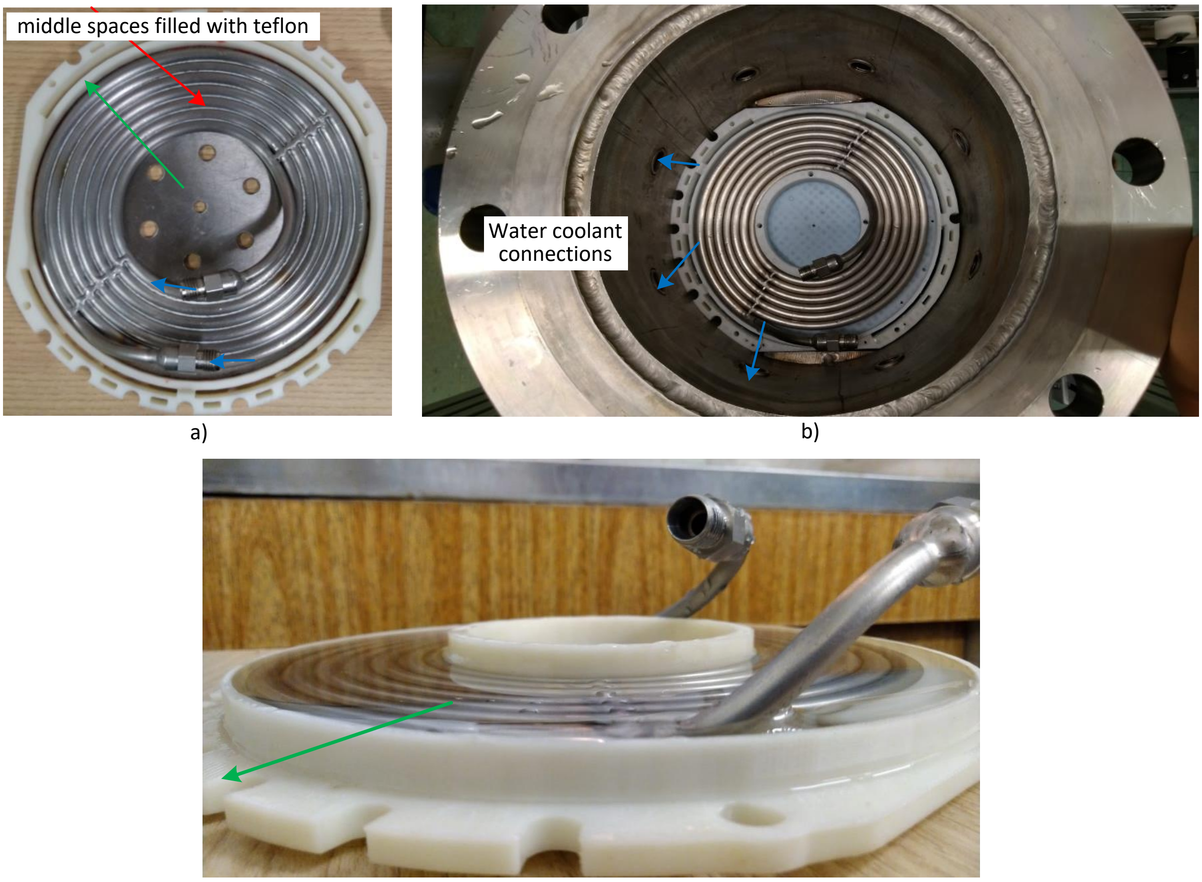

a)

b)

c)

Figure 5.18 – *a)spiral plate, b)spiral plate inside absorber and c)horizontal liquid film over the spiral plate exchanger*

Figure 5.19 – *Spiral heat exchanger manufacture by shape-lathe process*

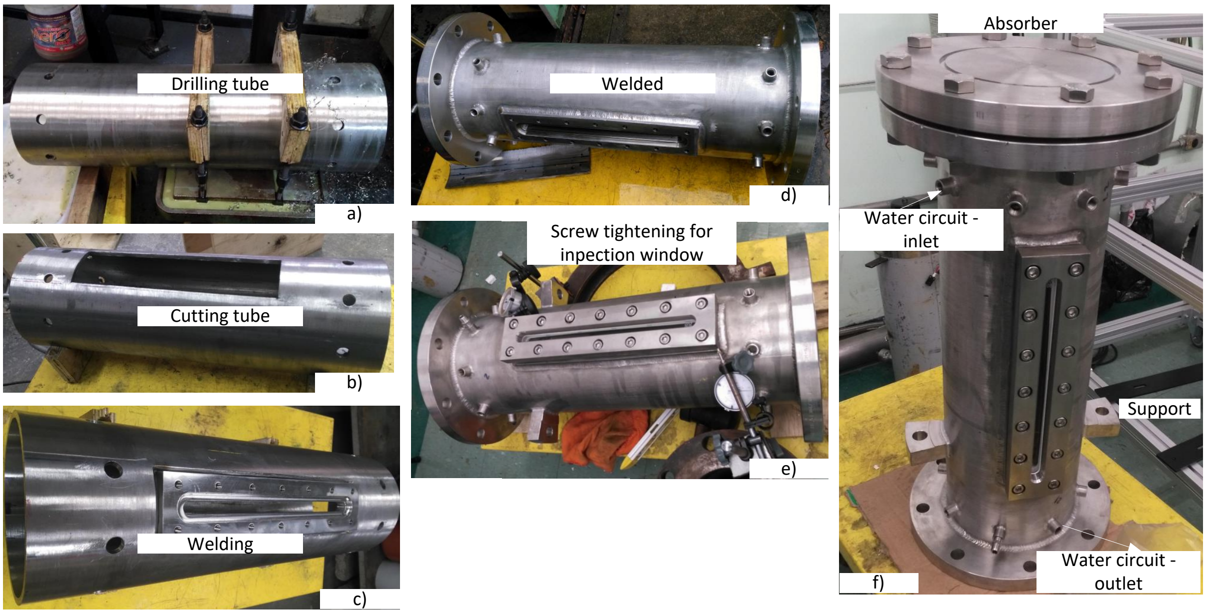

Figure 5.20 – *Absorber for ammonia-water absorption a) drilling tube, b) cutting tube, c) welding tube, d) welded tube, e) inspection window and f) final absorber*

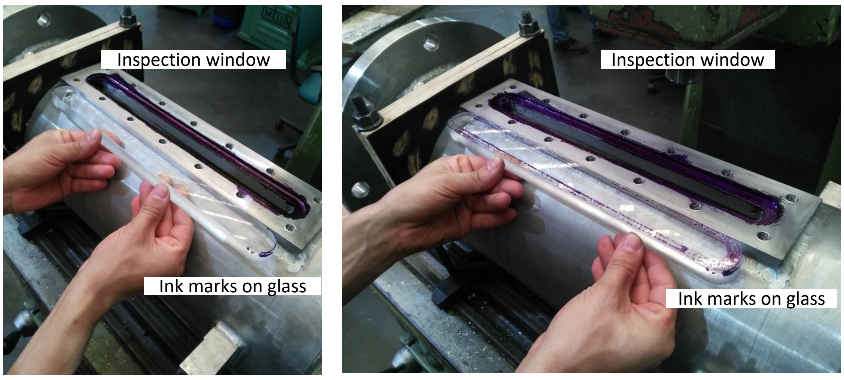

a) b)

Figure 5.21 – *Ink marks on glass to evidence leaks being a) before and b) after the new machined*

inspection windows. Then, they are welded and placed in the absorber (Fig. 5.20b,c,d,e). Fig. (5.20f) shows the final version of the absorber vessel. Leaks were detected at the inspection windows as the consequence of welding process, whose ink marks on glass shows that problem (Fig. (5.21)a). It deformed the window's seat damaging the correct seal. To avoid any risk of leaks, the tube windows were machined and a new inn mark over the seal was carried out and shown in Fig. (5.21b). Then, the windows with the teflon seals were installed correctly.

After this, the six spiral plates are placed in a vertical position forming a plate column as shown in Fig. (5.22). Water coolant connections between plates are given by using a 1/4 OD 316L stainless steel tubing together with Swagelok threaded connections. All the spiral plate heat exchangers are mounted inside tube forming the ammonia-water absorber. Both flanges are mounted, in which the description of these flanges are represented as represented in Fig. (5.23). Weak solution and ammonia vapor enters at the upper flange for a current absorption process. Nevertheless, the counter-current absorption is fixed by employing the lower vapor inlet, whose project avoids the pre-absortion when a small amount of strong solution is stored. The ammonia

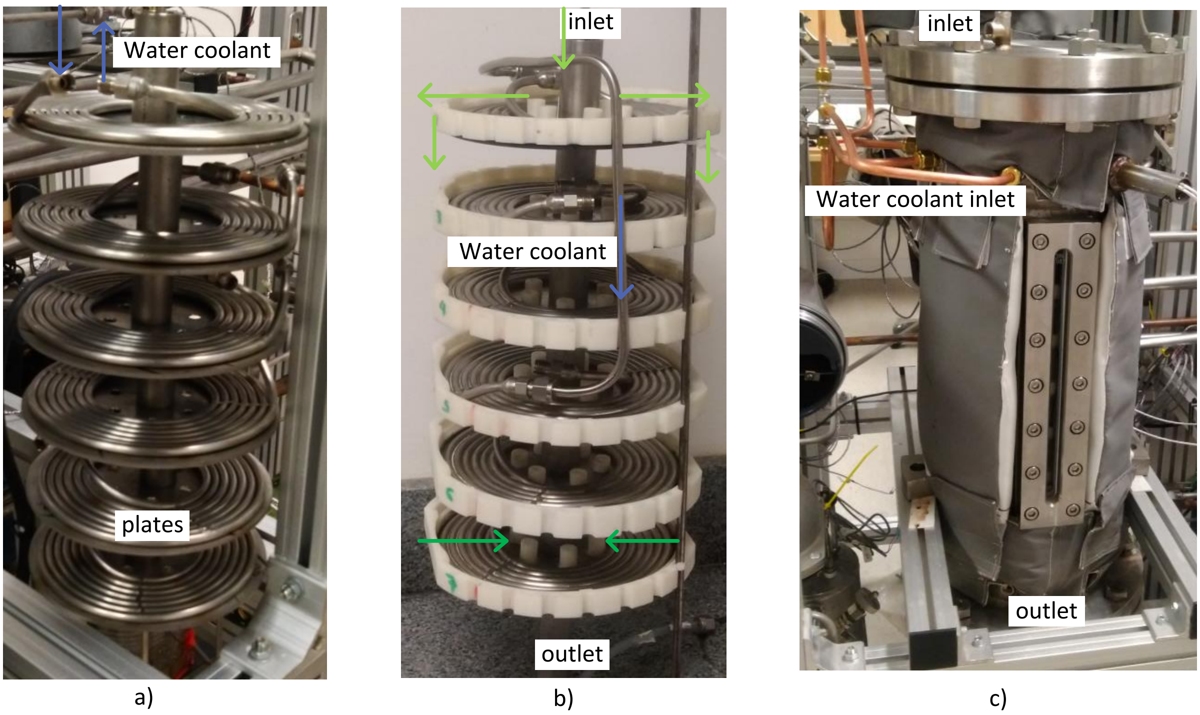

Figure 5.22 – *Horizontal liquid film absorber and a)its six plates, b)water cooling connections, and c) absorber installed in the cycle*

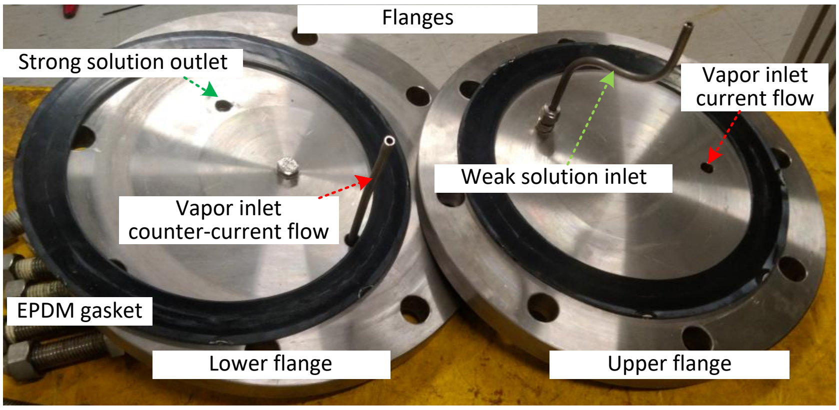

Figure 5.23 – *Description of the upper and lower flange of the ammonia-water absorber*

vapor circuit is presented in Fig. (5.3). Strong solution goes to the solution tank in the lower flange.

For better understanding about the ammonia-water and water coolant circuits, the Fig.(5.24) is shown. Fig. (5.24a) shows the ammonia-water circuit in which the red dashed and green continuous lines correspond to the ammonia-vapor and weak-solution paths, respectively, while the gray blocks to the absorber plates. The weak solution is distributed over the first plate N1, forming a zig-zag pattern in the next plates (from outside to inside at first plate and from inside to outside at the second one) until the sixth plate (N6). The temperature of ammonia vapor entering in the absorber is measured using T-type thermocouple T_{009}. At the top of the absorber, the ammonia vapor temperature is measured by employing the T_{008} and T_{005} PT-100 thermoresistances. Pt-100 sensors are also employed to measure the horizontal liquid film in

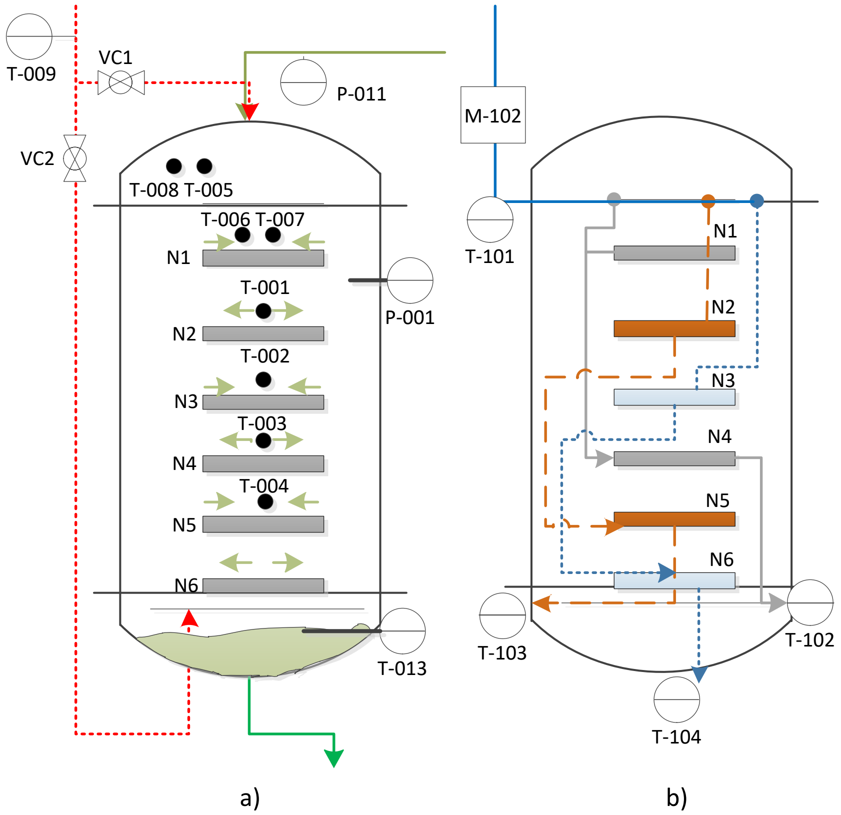

Figure 5.24 – *Schematic representation of the ammonia-water and water coolant circuit in the absorber*

each plate. A T-type thermocouple T_{013} measures strong solution temperature at the bottom of the absorber, while manometric pressure is measured using piezo-resistive pressure transducer P_{001} and P_{011}. Finally, $VC - 1$ ball valve open and $VC - 2$ ball valve closed fix the co-current absorption process and vice-versa for the contra-current absorption.

Further, the configuration and distribution of the coolant circuit in the absorber is displayed in Fig. (5.24b). Water coolant is distributed towards the plates from the main pipe, whose temperature and volume rate is monitored using a T-type thermocouple (T_{101}) and a hydrometer (M_{102}), respectively. Then, the three sub-circuits are connected to the plates; the first one goes from the N1 to the N4 plates, the second one: from N2 to N5 plates and the last one connects to the N3 and N6 plates. This distribution configuration is adopted due to the high absorption rate that occurs in the first three plates, improving the temperature measurement in the T-type thermocouples T_{102}, T_{103} and T_{104}.

Fig. (5.25) shows the temperature disposal for temperature measurements at each plate heat exchanger for the ammonia-water absorption process. Epoxy resin araldite is put-upon into the stainless steel to seal it from possible leaks, and 1/4 NPT connection is defined to fix it over the absorber. Eight PT100 3-wire temperature probes are installed into the absorber measuring the ammonia-water solution temperature as a function as absorption process is taking place.

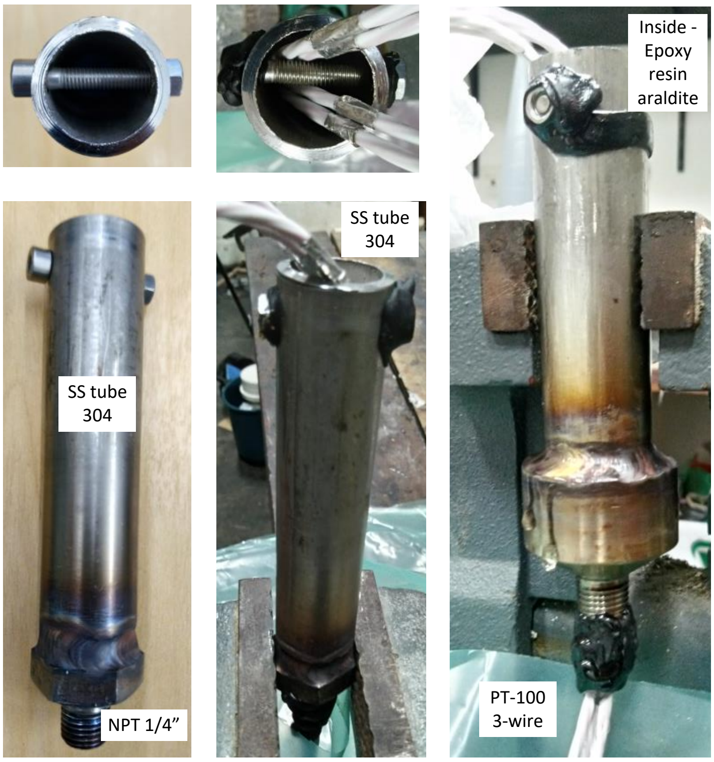

Figure 5.25 – *Temperature measurement into the absorber*

5.3 Secondary circuits of the ARC

5.3.1 Water coolant circuit and water/ethylene-glycol circuit

A water coolant circuit is installed to control the ammonia-water absorption refrigeration processes as shown in Fig. (5.26). The rectifier, condenser, absorber and subcooler (SC-001) must reject heat to environment. Firstly, the $B-101$ centrifugal pump is employed to absorb the heat of condensation. Then, the same water coolant circuit rectifies the wet ammonia vapor on the rectifier. Volume average flow rate is compute by using the $M-101$ turbine hydrometer. Next, the heat of absorption is transfered to the water coolant circuit driven by the $B-102$ centrifugal pump. The $M-102$ hydrometer measures the volume average flow rate. An independent centrifugal pump $B-104$ drives the water coolant through subcooler $SC-001$, cooling the weak solution entering at the absorber. $M-104$ estimates the volume rate. The $F-001$ industrial air cooler cools all the water coolant circuits and then, it is stored in a $500l$ water tank.

The $B-103$ magnetically coupled centrifugal pump drives the water/ethylene-glycol (EG) into a closed loop, in which the $H-100$ electrical resistance simulates the thermal load in the evaporator. The volume flow rate is controlled by using a variable frequency drive (VFD). A PID controller fixes the water/EG inlet temperature in the evaporator.

5.3.2 Thermal oil circuit

Thermal input is given in the generation process in which for a typical operation a heat recovery or solar energy is employed. For this disposal, a thermal oil circuit was defined, engaging the electrical resistance $H - 200$ with the $B - 200$ centrifugal pump to drive the thermal energy from the Therminol 59 oil to the generator as shown (5.27). It is worthwhile to mention that expansion tank and high temperature switch ($HTS - 200$) are installed in order to ensure its safety operation.

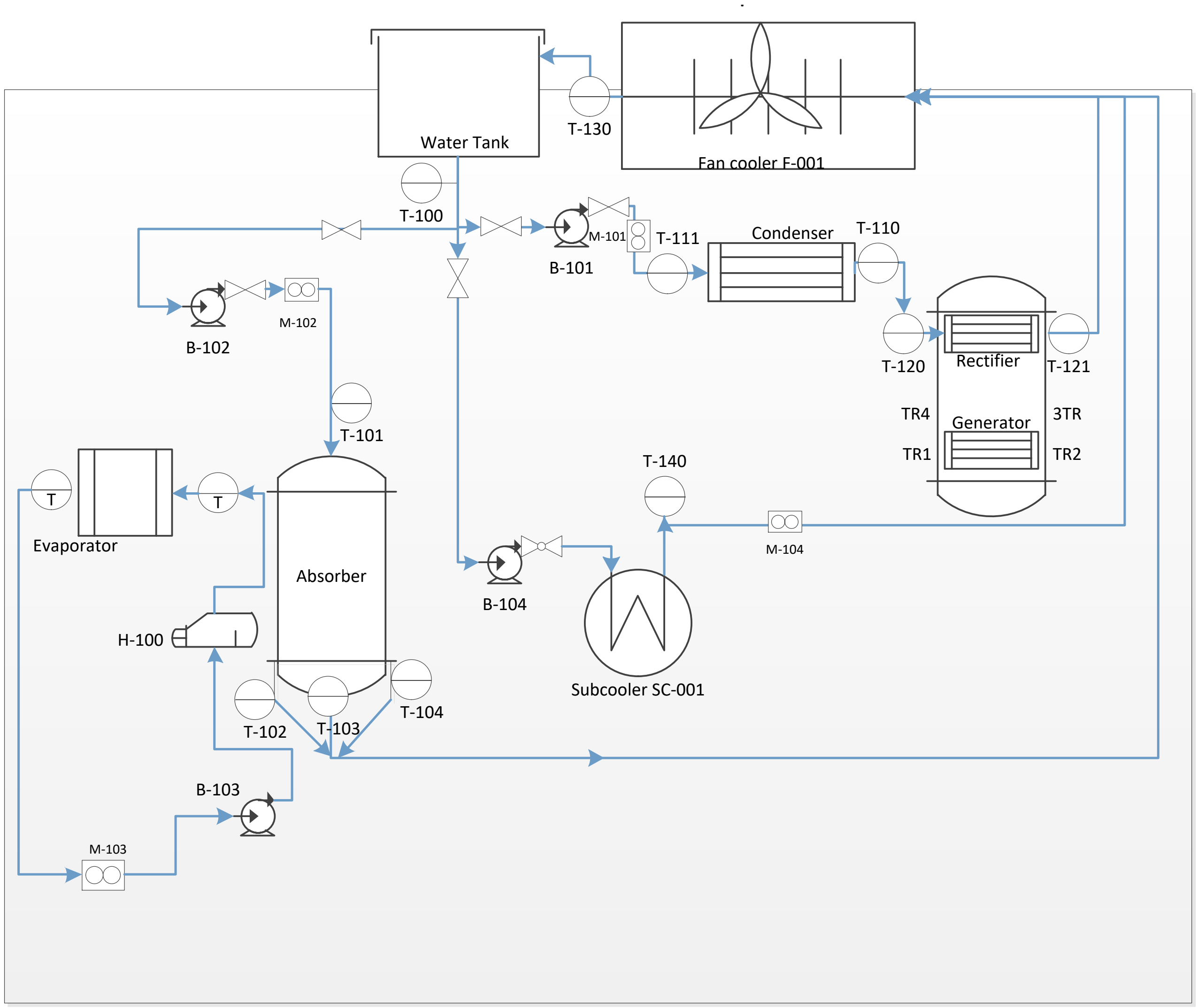

Figure 5.26 – *Schematic representation of the water coolant for ARC*

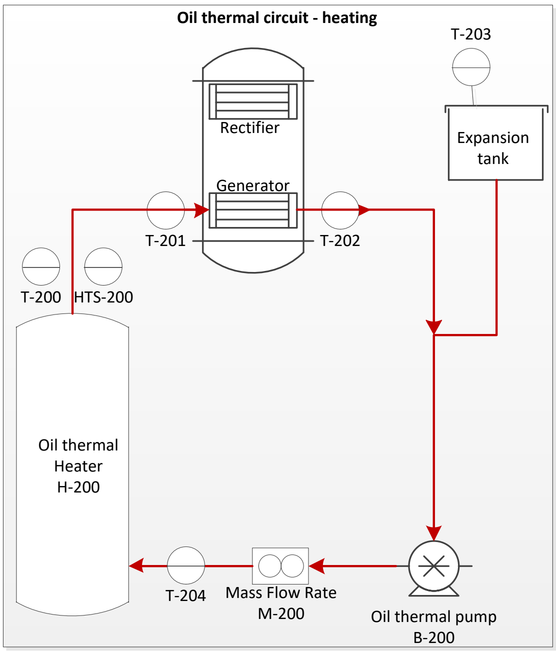

Figure 5.27 – *Heating circuit by using thermal oil*

5.4 Instrumentation, data acquisition and automation

5.4.1 Instrumentation

Temperature and mass flow rate instruments are strategically introduced in the test rig used for the calculating energy balance of the ARC. For instance, T_{201} and T_{202} T-type thermocouples together with M_{200} volume flow rate define the thermal energy supplied to the generation process. Each variable is described as follows,

Temperature: a detailed description of the temperature measurement in the absorber is carried out in Subsec. (5.2). 40 T, K and J-Type thermocouples (±0.1°C) are installed around the circuit, (37) collecting and (3) controlling ammonia-water circuit, water coolant circuit, and thermal oil circuit. It is worthwhile to mention that all these sensors has been calibrated. Calibration procedure is detail in Appx.(I.1).

Mass/volume flow rate: in the water coolant circuit, four hydrometer are installed (±2 %), while three Coriolis mass flow meters measure the ammonia-water loop as shown in Fig. (5.28a). $\dot{m}_{001}$, $\dot{m}_{002}$ and $\dot{m}_{003}$ measure weak solution, strong solution and refrigerant flow, respectively. Also, flow meters allow measuring the temperature (±1°C), mass flow rate (±0.1 % for liquids and ±0.5 % for gas) and density of the fluid (±2 kg/m^3) (Fig. (5.28b)). Also, a TURL-32 turbine flow meter (12 – 120 L/min) is used to measure the volume flow rate of the thermal oil circuit (±1.2 L/min). Maximum operational conditions are 150°C and 20 barg for temperature and pressure.

Pressure: in particular, ammonia-water loop demands pressure transducers because three thermophysical properties define the thermodynamic state when a binary solution is employed;


a) b)

Figure 5.28 – *a) Optimass 3000 Coriolis mass flow meter to mass flow and density measurements of ammonia-water circuit. Maximum operational conditions:* 130 *kg/s flow rates,* $150°\,C$ *process temperature and* 150 *barg process pressure b) IHM*

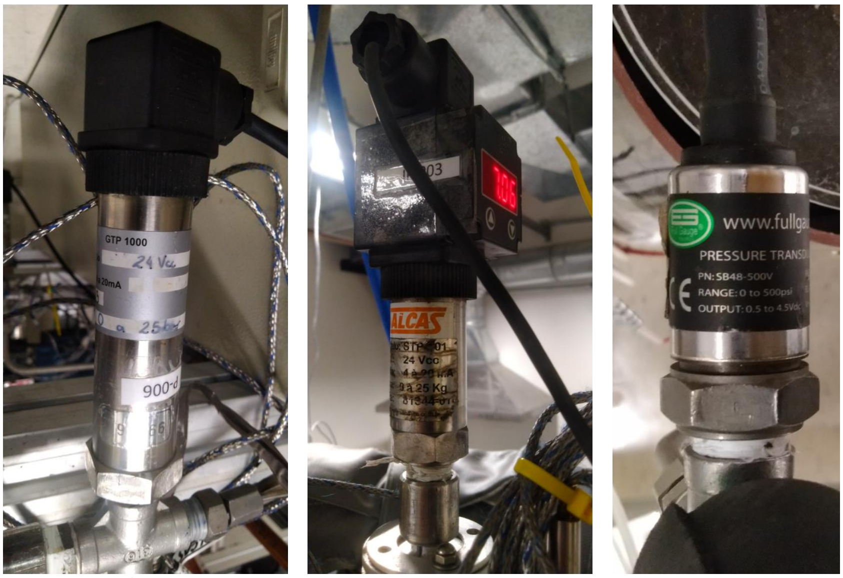
a) b) c)

Figure 5.29 – *Pressure transducer installed in the ammonia-water circuit in which a) GTP100 model +* $4 - 20mAmp$ *outlet +* $0 - 25bar$ *range pressure b) GTP100 model +* $4 - 20mAmp$ *outlet +* $0 - 25kgf/cm^2$ *range pressure and c)* $SB48 - 500V$ *model +* $0.5 - 4.5Vdc$ *outlet +* $0 - 500psi$ *range pressure*

being temperature (T), density (ρ) and pressure (P). Eleven (11) pressure transducer (±0.01 bar) are installed in the whole test rig, in which the Fig. (5.3) shows the position of each one of them. In Fig. (5.29) is shown the pressure transducers in which 1/4 NPT connections and $4 - 20$ mAmp and $0.5 - 4.5$ Vdc outlets are commonly used. See Appx.(I.2) for more detail.

5.4.2 Data acquisition

Fig. (5.30) shows the data acquisition system of absorption process test rig. All sensors are connected with three devices, according to each output demand: Agilent U2355A (Modular data

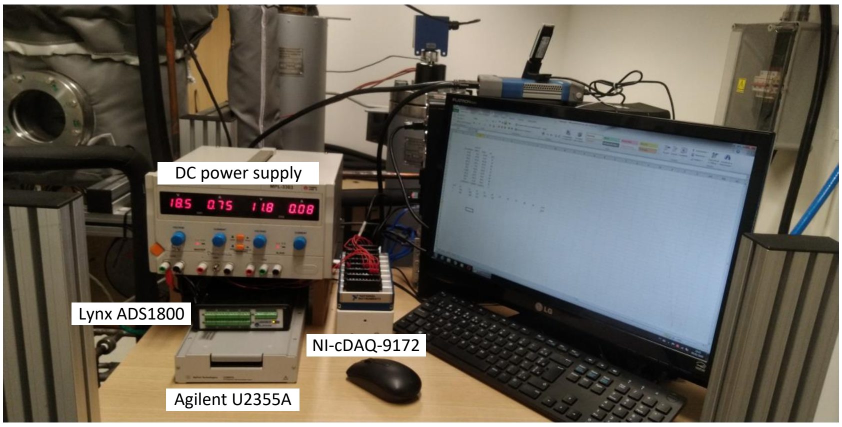

Figure 5.30 – *Data acquisition system used to temperature, pressure and mass flow rate measurement in the ARC test rig*

acquisition) + U2802A (signal conditioner), Lynx ADS-1800 and National Instruments cDAQ-9172 chassis coupled with eight (8) modules. Agilent U2355A has 31 input channels dedicated to temperature measurements (J, K, R, S, T, N, E, and B-Type thermocouples), sampling rate of 500 kSamples/s for all channels. Lynx ADS-1800 has eight universal channels (PT-100, thermocouple sensors, current, voltage, etc.), sampling rate of 96 kSamples/s per channel. Finally, NI cDAQ-9172 chassis is available for whichever sensor through the 8 independent modules; 5 (NI-9211) modules for temperature signal - 20 temperature sensors, 1 (NI-9203) module for current signal - 8 inputs and 2 (NI-9201) for voltage signal - 8 inputs per module.

5.4.3 Uncertainty propagation

Uncertainties are calculated by using Taylor and Kuyatt (1994) according to *Engineering Equation Solver* (EES) (Klein, 2015).

5.4.4 Automation system and Human-Interface Machine -HIM

A Free AVC-12600CLU programmable logic controller (PLC) and a EVE-4200 Schneider extension are installed. The automation is summarized as follows;

Water coolant circuit: the cooling circuit is started when the test rig is operating in auto mode, turning on the water pump to cool the condenser B_{101} and the absorber B_{102}. The thermal load over falling film evaporator is initialized through the B_{103} pump, setting the operating frequency in the variable frequency drive. Moreover, the water temperature is controlled by using F_{001} fan as cooler. In Fig. (5.31) is shown the logical sequence of the auxiliary circuit. It is worthwhile to mention that the HIM allows setting all these parameters. The heating circuit is the next step and it is detailed as follows.

Heating circuit: First, P_{003} pressure value and H_{200} status is checked as shown in Fig. (5.32). B_{200} turns on when there is neither a electrical motor failure nor a pending reset alarm showed at the HIM, making available the PID controller. Thus, it allows checking the high temperature switch (HTS_{200}), turning on the electrical resistance to control oil temperature at the generator

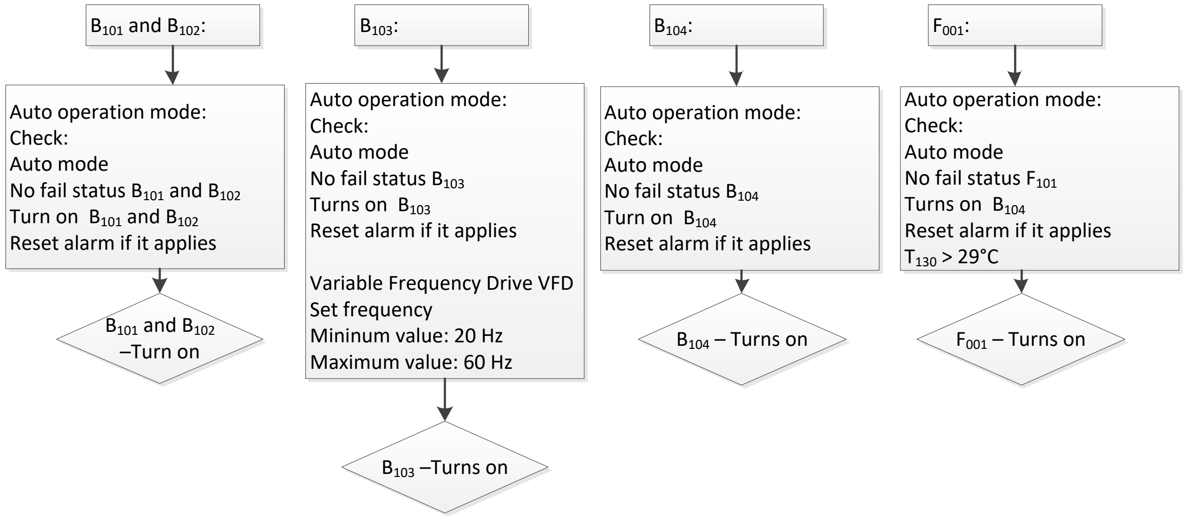

Figure 5.31 – *Cooling water control system: B_{101} and B_{102} is condensation and absorption circuit pump, respectively; B_{103} evaporation circuit pump; B_{104} subcoling solution pump and F_{001} water cooler fan*

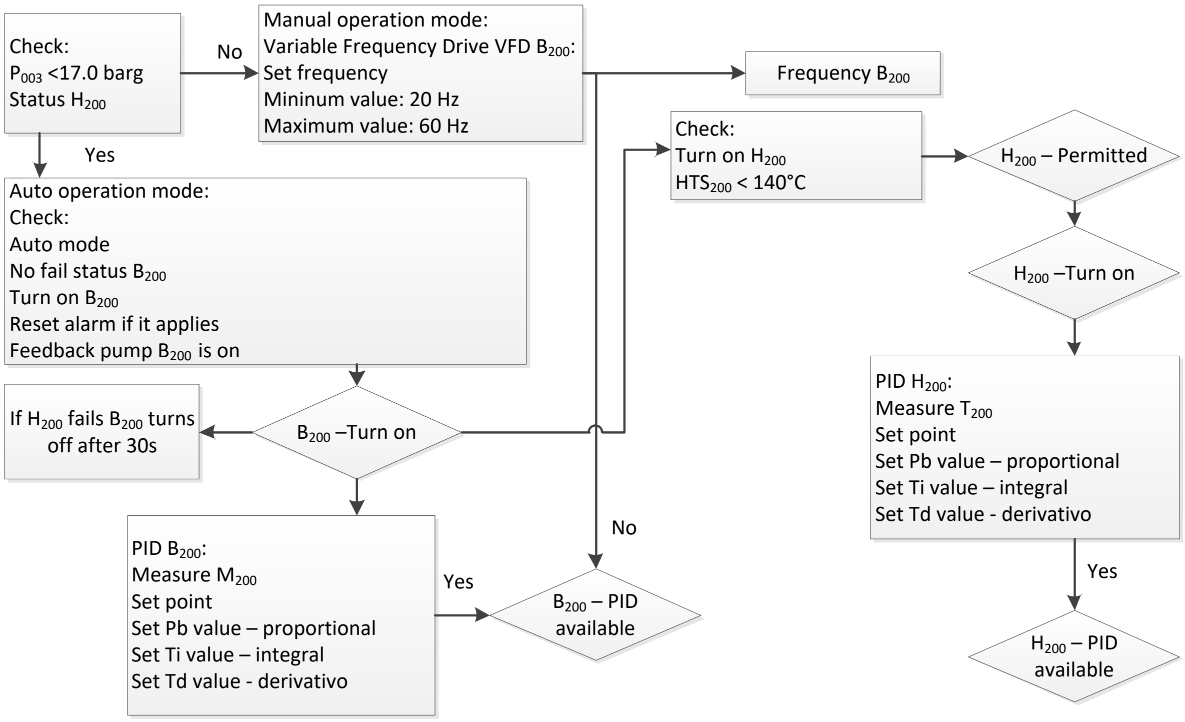

Figure 5.32 – *Heating control system; B_{200} is the oil pump, H_{200} is the electrical resistance for the oil heating*

inlet. Auto mode controls oil temperature by using the PID controller. When the test rig is operating in manual mode, pump is handly turned on, but the temperature control of the H_{200} always is kept. Finally, for safety, H_{001} is turned off when B_{200} pump stops.

Ammonia-water solution circuit: B_{001} pumps ammonia-water solution when the auxiliary circuits are running. First, auto mode checks the P_{003} generation pressure, H_{001} electrical resistance status, $T_{130} < 35$°C and high pressure switch installed at the B_{001} pump discharge. It checks an electrical motor failure or a pending alarm that it needs to be restarted. Then, B_{001} solution

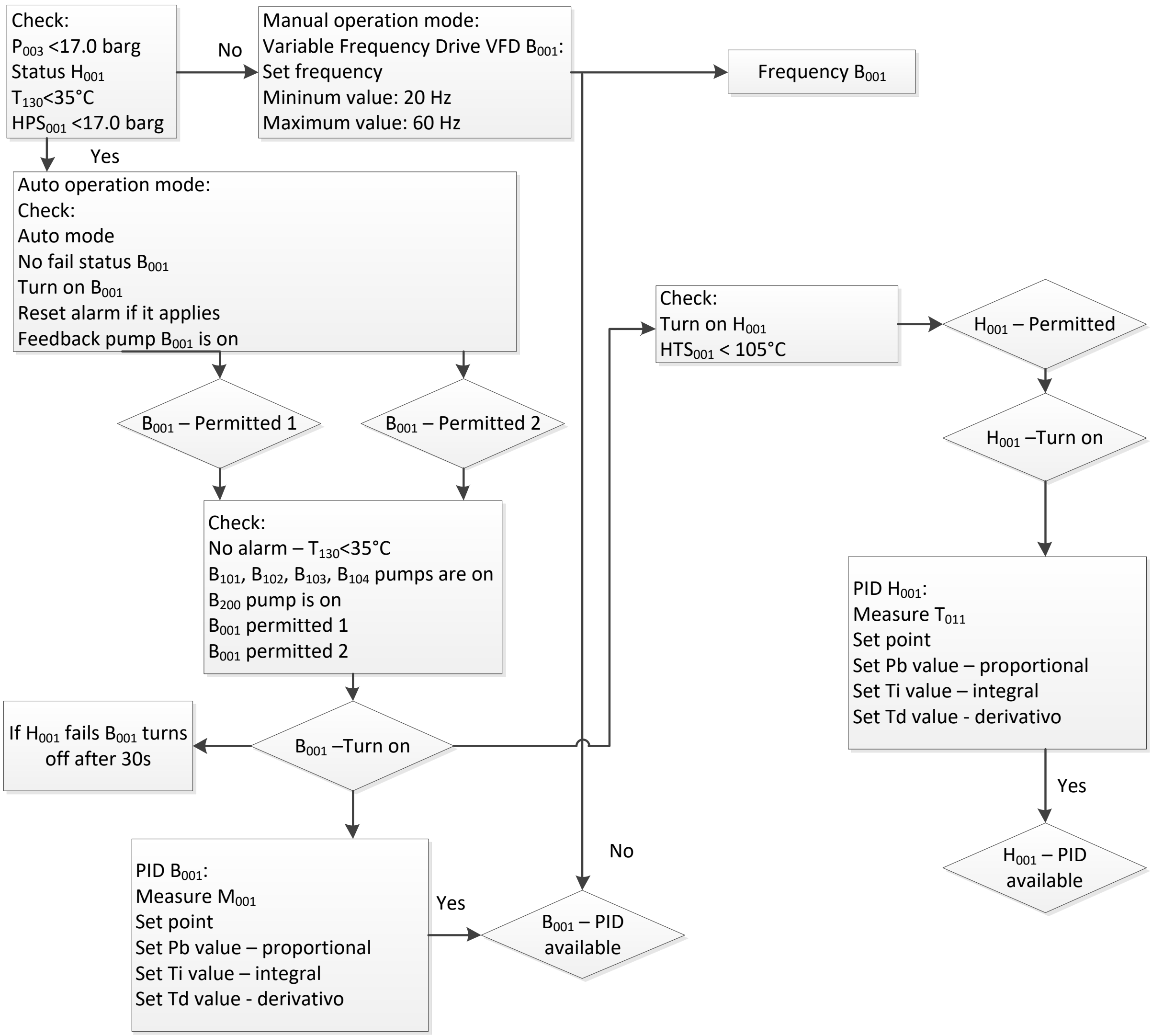

Figure 5.33 – *Ammonia-water solution control system;B_{001} is solution pump and H_{001} is the solution heater, in which the they are avaliable when the heating circuit and water coolant circuit are checked*

pump becomes available. The third checklist is based on the confirmation of B_{101}, B_{102}, B_{103}, B_{104} and B_{200}. Finally, B_{001} is turned on and the PID controller runs. Electrical resistance is turned on when the HTS_{001} high temperature switch is $\mathrm{HTS}_{001} < 105°\mathrm{C}$ and when the desorption process demands thermal energy. The comparison between the set point and the measured temperature value controls the heater, and H_{001} PID controller modules the electrical power as shown in Fig. (5.33)

For more detail, it is attached all the logical programming, electrical and control drawing (B-Annex). Also, the programming code is avaliable in C-Annex.

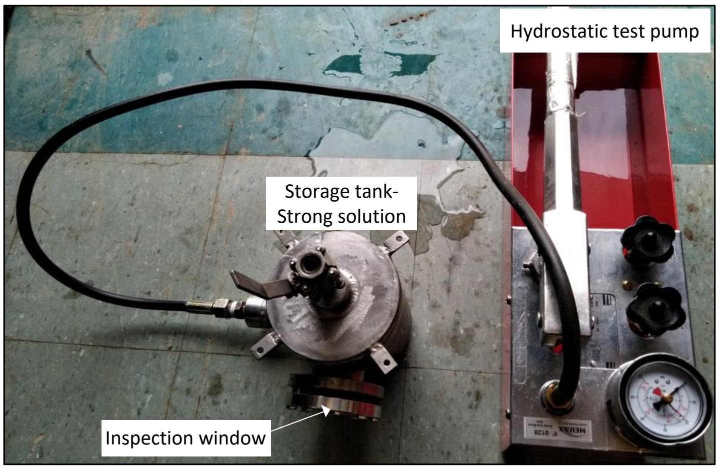

Figure 5.34 – *Hydrostatic pressure test for solution tank by using hydrostatic test pump*

5.5 Operating procedures and start-up

5.5.1 Hydrostatic test procedure

All components were tested under a hydrostatic pressure test by using a hydrostatic test pump as shown in Fig.(5.34). High and low pressure components were tested in $21bar$. Firstly, the test is carried out in each component and then all the system is evaluated as shown in Fig. (5.35). It is worthwhile to mention that the safety valve is isolated during all the time (about 2 hours).

5.5.2 Pneumatic test procedure

The layout of the pneumatic test is presented in Fig. (5.36). Nitrogen was employed to pressurize the system at 21 bar and the nitrogen got into the ARC through valve Vg1. System pressure was monitored employing the P_{003} piezoresistive transducer, whose pressure was maintained during two hours and a few leaks were registered and fixed. Valve Vg2 was employed to isolate the ARC from the safety valve Vrel.

5.5.3 Vacuum procedure

The vacuum procedure is carried out with an Edwards 18 pump as it is displayed in Fig. (5.37). The cold trap with liquid nitrogen is used to retain the condensable gases, as water vapor may damage vacuum pump. The vacuum system is connected to the ARC by the Va1 valve and the vacuometer connects to the ARC by using the Va2 valve. The positive displacement pump is isolated when the vacuum procedure is occurring by moving the Vp1 and Vp2 valves. The final value reached 630.0 microns of Hg.

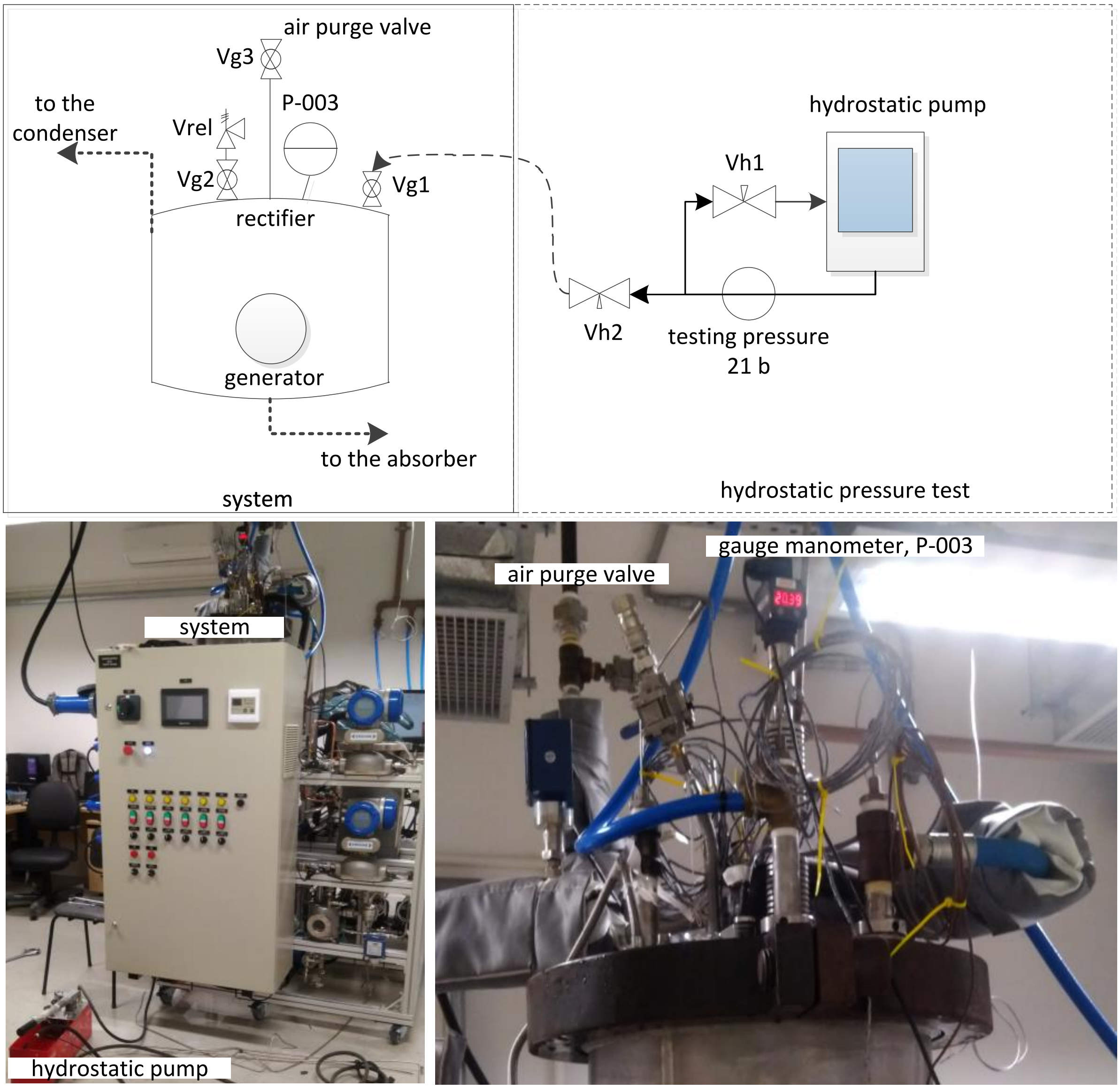

Figure 5.35 – *Hydrostatic testing of the whole ammonia-water absorption refrigeration system*

5.5.4 Leakage test procedure

Ammonia is deeply toxic in low concentration and the leak test is carried out in all the components. First, air pressured at 2 bar was used to verify the greatest leaks, whose analyses found leaks at the inspection windows of the absorber as shown in Fig.(5.21). Second, a new test was developed, in which all the ammonia-water circuit was filled by using 5 % hydrogen - 95 % nitrogen. The system was kept pressurized while the hydrogen detector was used to locate leaks on the ammonia-water absorption system. So, the experimental test of the leak detection (Fig. 5.38) found that the system must be pressurized in 9 bar although manual suggested only 5 bar of pressure. Detector may find 3 g/year leaks over all the connection.

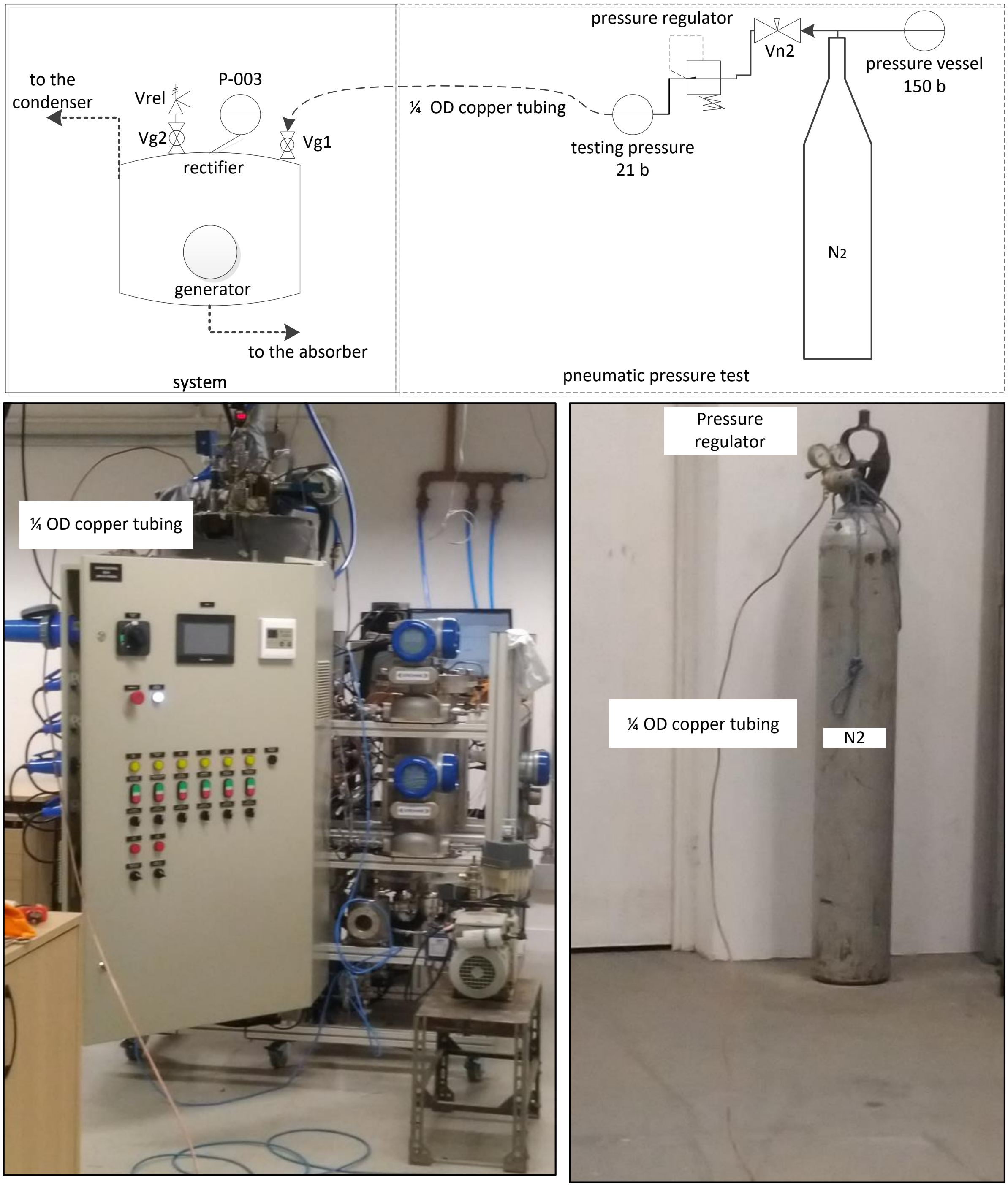

Figure 5.36 – *Pneumatic testing of the whole ammonia-water absorption refrigeration system*

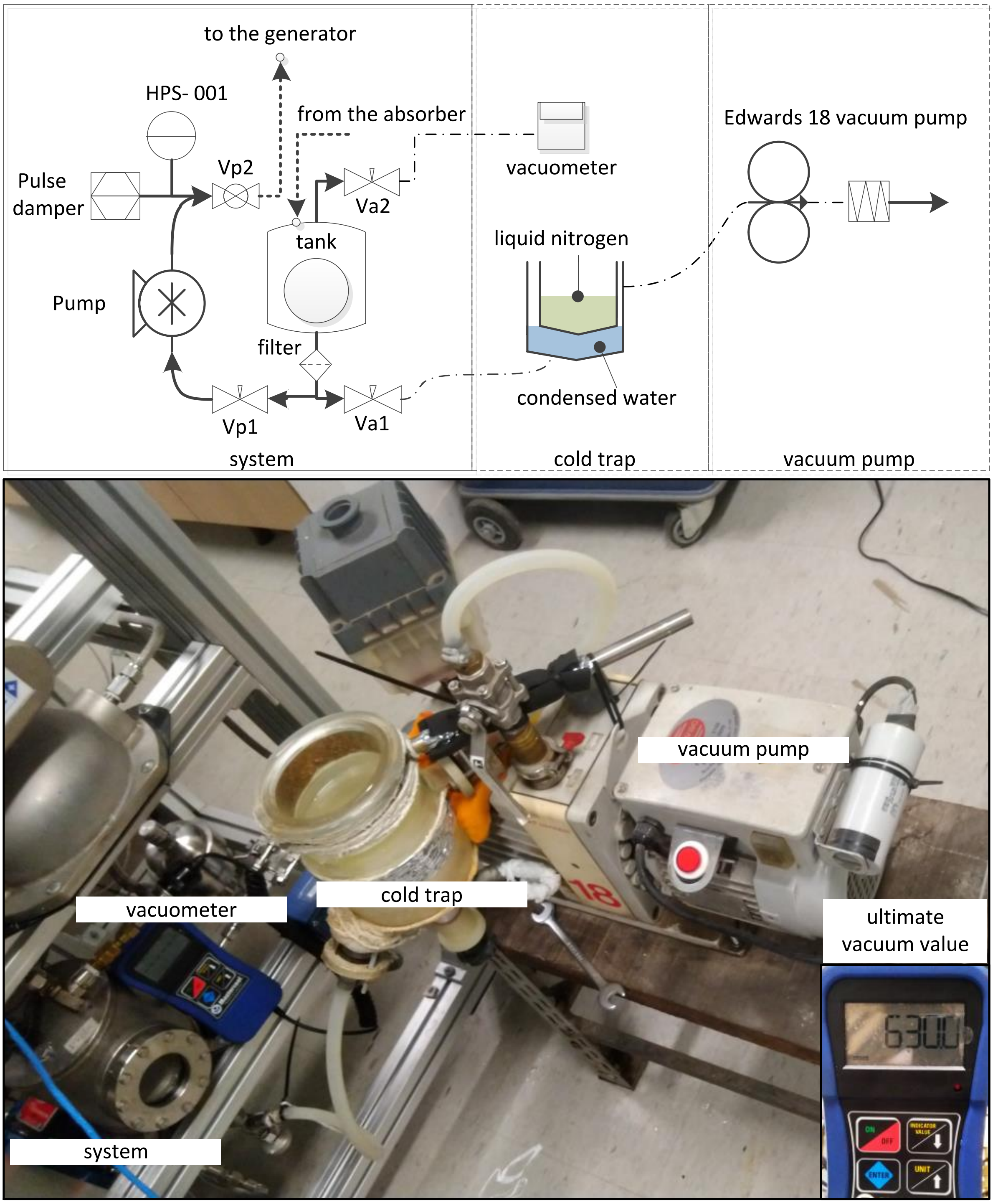

Figure 5.37 – *Vacuum procedure of the whole ammonia-water absorption system*

5.5.5 Ammonia charging procedure

The vacuum of the absorption refrigeration system allows charging the ammonium hydroxide solution in about 28 % of ammonia concentration as shown in Fig. (5.39). An 1/4 silicone tubing is used to transport the solution into the system, putting 7.74 kg solution at 28 %. Ammonia pure is charged through a stainless steel flexible hose as displayed in Fig. (5.39), being connected between the ammonia cylinder and the system. The electronic balance is used to control the

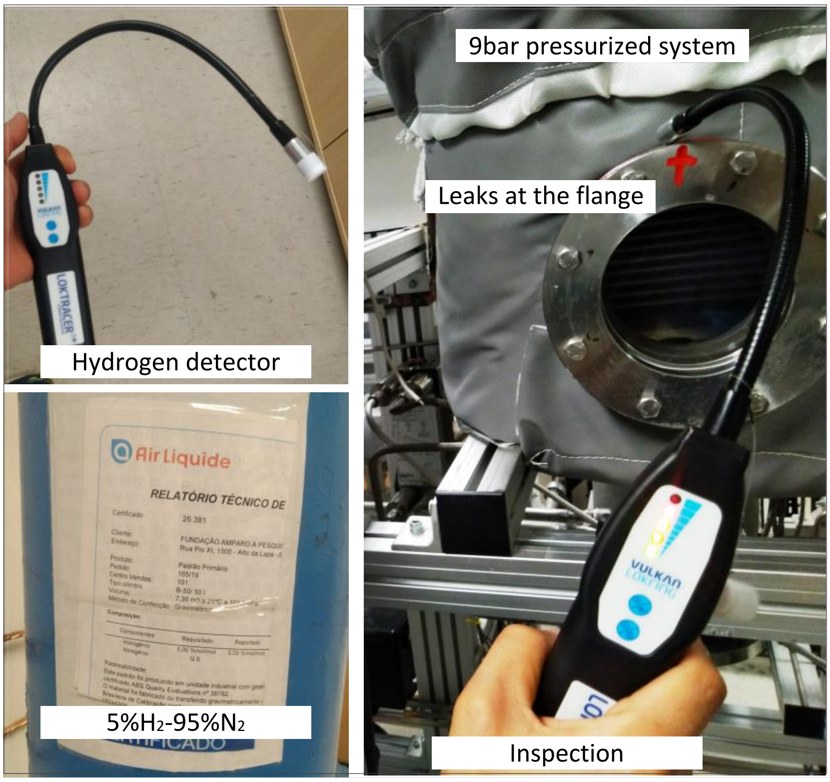

Figure 5.38 – *Leak detection by using H_2 and N_2 gas mixture and hydrogen detector*

mass flow rate going to the system. The charge was carried out in the vapor state, for better control of the ammonia mass. Thus, 1.62 kg was added to the solution reaching a final mass concentration of $x = 41.16$ % by *wt.*.

5.6 Safety conditions

Several procedures were developed for safety, as summarized next:

- An electrical interlock between the pumping system and the electrical resistance to disconnect the heater when the pump is turned off. It applies for the oil heater (H−200), for the ammonia-water pre-heater (H−001) and for the heater (H−100).
- The positive displacement pump of piston may achieve 69 bar discharge pressure, putting in danger the system. A high pressure switch (HPS_{001}) is immediately installed after the pump discharge (Fig. (5.40)), whose calibration report tested and calibrated in 17.0 bar pressure. Therefore, the maximum operating pressure is limited using this switch.
- High temperature switches limit an overheating in the ammonia-water circuit (HTS_{001}) and in the thermal oil circuit (HTS_{200}) as shown in (Fig. (5.40)). HTS_{001} and HTS_{200} are tested and calibrated at 105°C and 140°C.

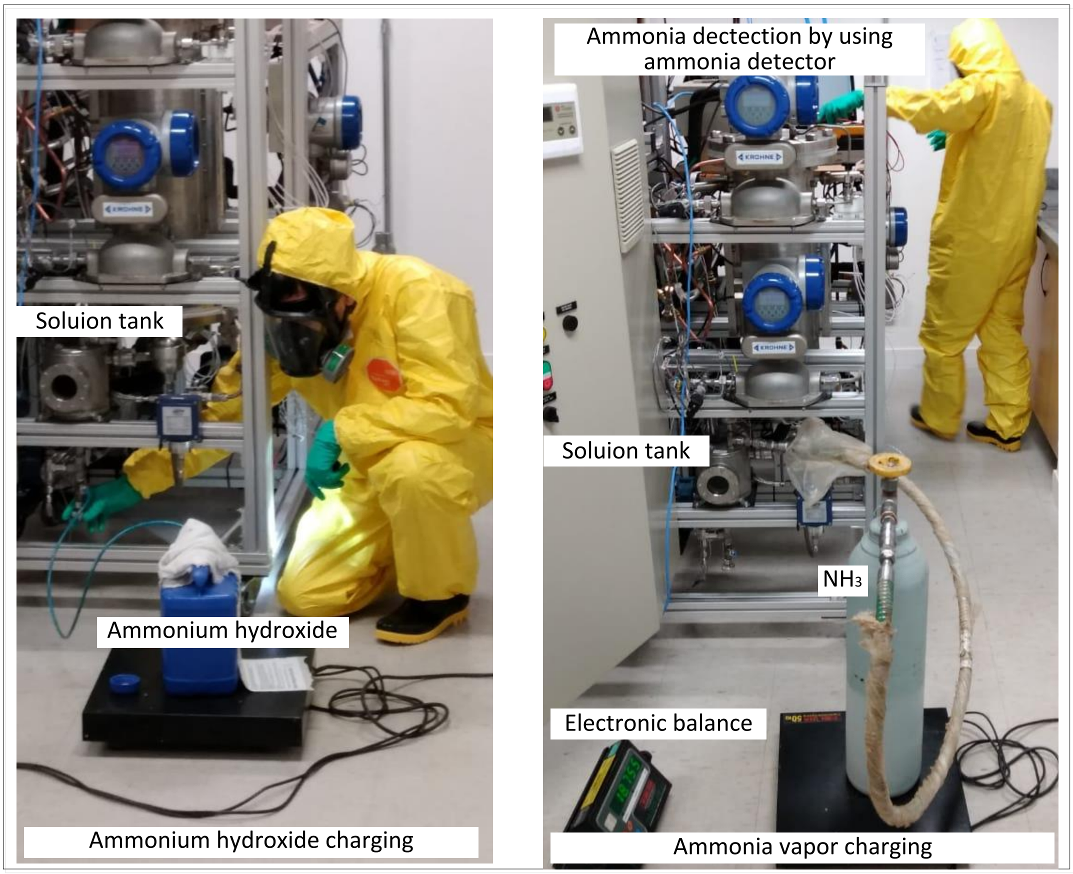

Figure 5.39 – *Ammonia-water charging in the absorption refrigeration system*

- A high pressure relief valve control is installed over the generator as shown in Fig. 5.41. The calibration report tested and calibrated in 17.5 bar, in which the ammonia vapor is released to the atmosphere through exhaust ducts.
- An 21 bar pneumatic and hydrostatic pressure test for all the test rig was carried out.
- An atmospheric expansion tank for the thermal oil circuit is installed in the pumping system to absorb thermal fluid expansion as oil temperature increases.
- The air exhaustion system was installed to remove possible ammonia leaks. A $0 - 50$ ppm ammonia gas detector will be installed in the future associated with the air exhaustion system.
- The ammonia charging was carried out by using all personal security elements: gloves, overalls, boots, mask and glasses.
- Finally, a logical automation was developed.

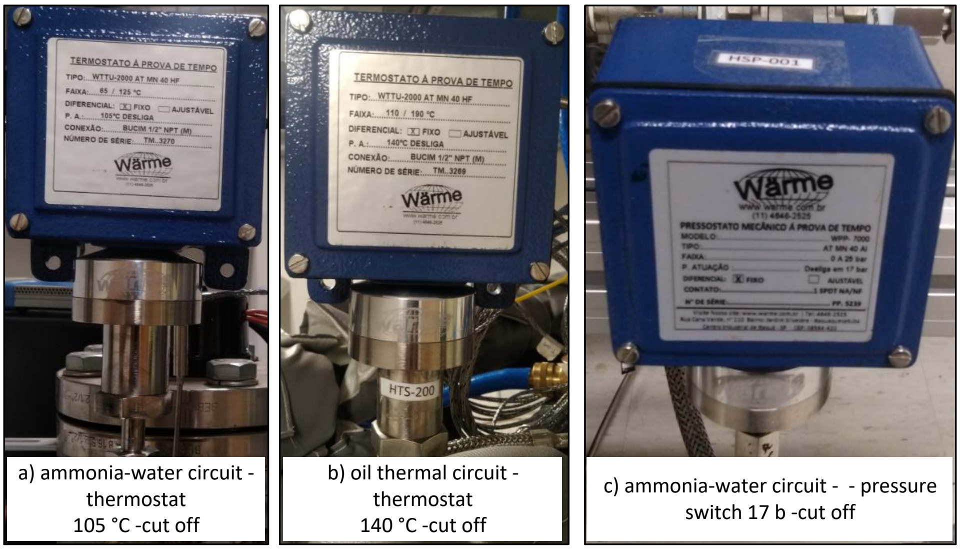

a) ammonia-water circuit - thermostat 105 °C -cut off

b) oil thermal circuit - thermostat 140 °C -cut off

c) ammonia-water circuit - - pressure switch 17 b -cut off

Figure 5.40 – *Temperature and pressure switches for ammonia-water absorption refrigeration cycle*


Certif. N 1796/2020
Set presure: 17.5b
Data:31/01/2020

Pressure relief valve

Figure 5.41 – *Pressure relief valve control*

Table 5.2 – *Summary of absorption refrigeration cycle components*

Details of the absorption refrigeration cycle components	
Component	*Specifications*
Generator	Falling film technology - bundle tube 7 x 10; $D_o = 8$ mm x $L = 150$ mm, $S = 2$ mm 304 stainless steel with two borosilicate inspection window; Heat transfer area, $A = 0.26$ m^2; Secondary fluid: thermal oil fluid; Operation pressure: 14 bar, Safety pressure: 17.5 bar; Test pressure: 50 bar **Ammonia-water strong solution**: Generation pressure, 14.7 bar; Solution mass flow rate, $0.016 - 0.022$ kg/s; Heat rate 2500 W; Inlet temperature $100 - 120$ °C. **Thermal oil**: Inlet temperature, $100 - 140$ °C; volume flow rate, 35 l/h.
Rectifier	Falling film technology - bundle tube 7 x 4 $D_o = 8$ mm x $L = 150$ mm 304 stainless steel Heat transfer area, $A = 0.18$ m^2 Nusselt average: 0.16 Secondary fluid: water **Coolant**: rectification pressure, 14.7 bar; Inlet temperature 40 °C; mass flow rate, 0.3 kg/s; Heat rate 760 W.
Plate heat exchanger	AlfaNova $14 - 20H$ Fusion-bonded plate heat exchanger; Alloy 316 Stainless steel; project pressure $@75C = 23$ bar Dimensions: 82 mm x 77 mm x 207 mm Connection: 3/4" ISSO $228/1 - G1$ Heat rate: 1000W - counter-current
Expansion valve - Weak solution	SS-31RS4 -Swagelok 31-Series; $cv = 0.040$; Body: 316L Stainless steel $ASTMA - 182$ Connection: 1/4" **Pressure range**:Inlet pressure, 14.7 bar; Outlet pressure, $2.5 - 6.0$ bar
Expansion valve - ammonia	1315G4Y-Hoke, $cv = 0.024$ Body: 316 Stainless steel $ASTMA-182$; Seal: Ethyl propylene Pressure: up 137 bar; Temperature: -54 to 232 °C; Connection: 1/4" **Pressure range**:Inlet pressure, 14.7 bar; Outlet pressure, $2.5 - 6.0$ bar
Condenser	Falling film technology - 3 coils x 7.5 spirals; $Do = 8$ mm; Pitch 0.012 m; Height: 0.1 m; Total length: 5.1 m Heat transfer area, $A = 0.13$ m^2; Secondary fluid: water **Ammonia**: Mass flow rate 0.0011 kg/s, Outlet temperature: 38 °C, Condensation heat rate: 1250 W, Pressure: 14.7 bar **Coolant fluid**: Mass flow rate: 0.3 kg/s; Inlet temperature 34 °C; Outlet temperature: 35 °C; Reynolds number 30.000; Vol. Flow rate: 1086 l/h
Evaporator	Falling film technology - coil $D_o = 6.3$ mm $D_i = 4.2$ mm, $L = 6$ m; Heat transfer area, $A = 0.11$ m^2; Secondary fluid: ethyl glycol-water **Ammonia**: Heat rate: 1200 W; Mass flow rate: 0.0011 kg/s; Inlet temperature: -13 ° C; Inlet pressure: 2.5 bar **Secondary fluid - thermal load**: 0.7 water/0.3 ethyl-glycol; Inlet temperature: 38 ° C; Outlet temperature: 30 ° C; water/EG mass flow rate: 0.02 kg/s
Absorber	Horizontal liquid film - 6 spiral plates; Spiral plates: $D_o = 6.35$ mm, $L = 3$ m; 304 stainless steel vessel - Sch 40 with two o-blong window; Vessel: 8" x $L = 0.7$ m; Heat transfer area, $A_{plate} = 0.04783$ m^2, $A_{total} = 0.2869$ m^2 **Absorption process**: Absorption pressure: $2.5 - 6.0$ bar; Solution mass flow rate:$0.016 - 0.022$ kg/s; Ammonia vapor mass flow rate: $0.0011 - 0.0020$ kg/s; Solution inlet temperature: $40 - 60$ °C; Heat rate 2500 W **Coolant fluid**: Water mass flow rate - 100 to 300 l/h; Inlet water temperature: $25 - 40$ °C

Chapter 6

EXPERIMENTAL RESULTS AND DATA REDUCTION

The current Chapter presents a detailed description about the data reduction of the first experimental results, whose operation is carried out using a 39.0%wt. ammonia-water solution charge. Fig. (6.1) shows the *Human-Machine interface* HMI of the ammonia-water absorption refrigeration AARC when it is operating. P_{003} is the generation pressure, P_{002} is the discharge pressure of the pump, P_{001} is the absorption pressure, T_{011} is the strong solution temperature entering to the generator. Fig. (6.1) shows the pressure in the generator process, achieving about 11 bar, and 2 bar for absorption pressure. The weak solution temperature entering to the generator is fixed in 95.4°C. Also, in Fig. (6.2a) is shown when ammonia vapor is condensed and it going to the evaporator after it passes the expansion valve, achieving the −8°C minimum temperature as shown in Fig. (6.2b).

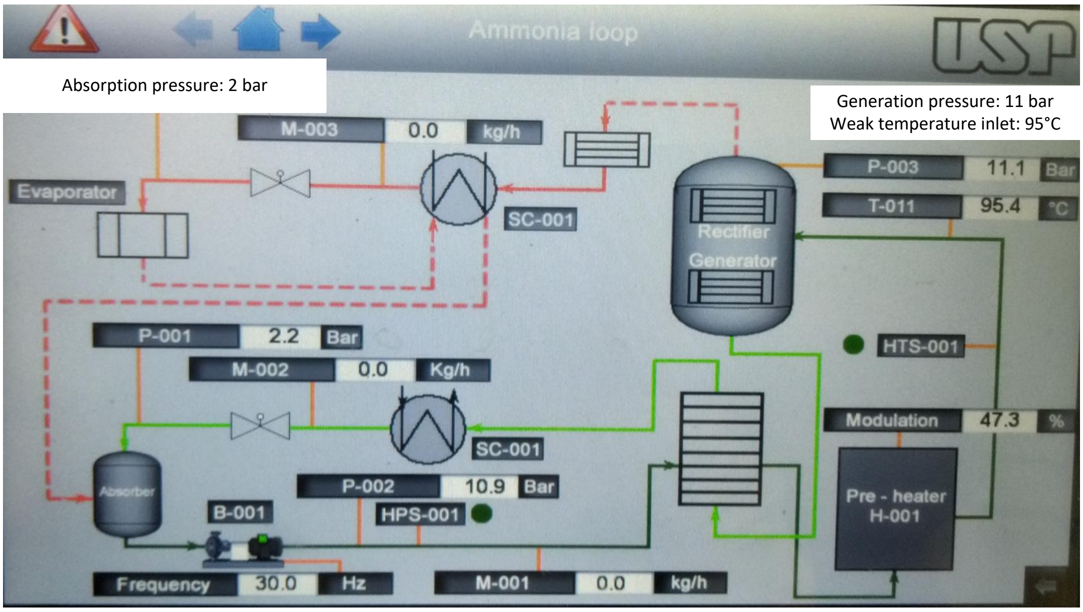

Absorption pressure: 2 bar

Generation pressure: 11 bar
Weak temperature inlet: 95°C

M-003 0.0 kg/h
P-003 11.1 Bar
T-011 95.4 °C
P-001 2.2 Bar
M-002 0.0 Kg/h
Modulation 47.3 %
P-002 10.9 Bar
Frequency 30.0 Hz
M-001 0.0 kg/h

Figure 6.1 – *Human-Machine interface HMI of the ammonia-water ARC test rig*

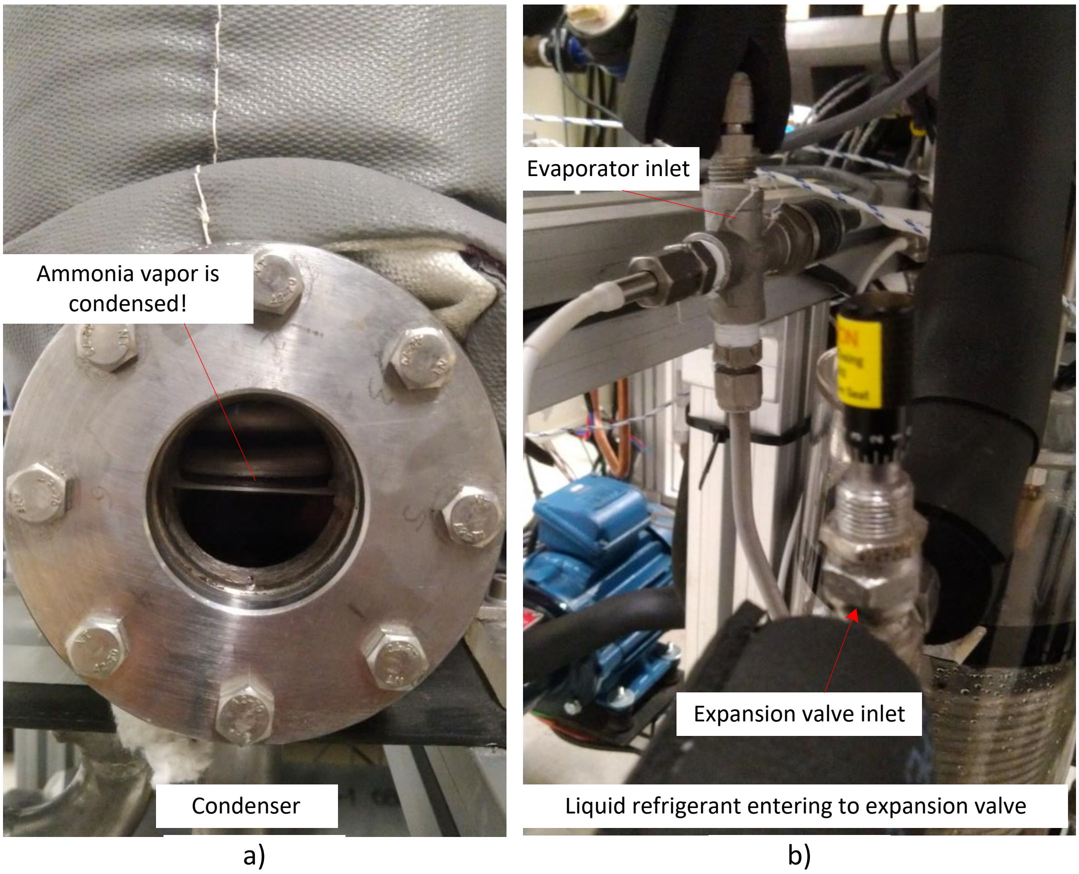

Figure 6.2 – *Experimental results at the a) condenser and b) ammonia expansion valve*

Nevertheless, the steady-state regime has not been totally achieved yet. Exist two main possible explanation, the first one refers to the hand-operated expansion valves, in which the same discharge pressure level must be guaranteed for both expansion valves. Different pressure levels mean that the lowest pressure circuit may be blocked. Although pressure transducers are installed at the valve discharge, it is not a trivial task. The second problem is the manual operation of the positive displacement pump due to the fact that *programmable logic controller* PLC had electrical problem and it will be replaced in the future. In spite of that, some experimental data were obtained. Based on the best obtained results, a focus on the new absorber proposal follows.

6.1 Horizontal liquid film absorption process

According to the absorption process, in Subsec. (2.4) has been introduced some heat and mass transfer correlations, and the behavior of the thermodynamic equilibrium for the binary ammonia-water mixture - Sec. (3). Also, in Sec. (4) the absorption modeling based on the new proposal; horizontal liquid film has been well detailed. In this way, the current subsection shows a focus on the ammonia-water absorption process by using the experimental results. As highlighted in Sec. (2), the installation of the heat recovery (HR) between the weak solution and strong solution improves the cycle performance. Moreover, the HR keeps the subcooled

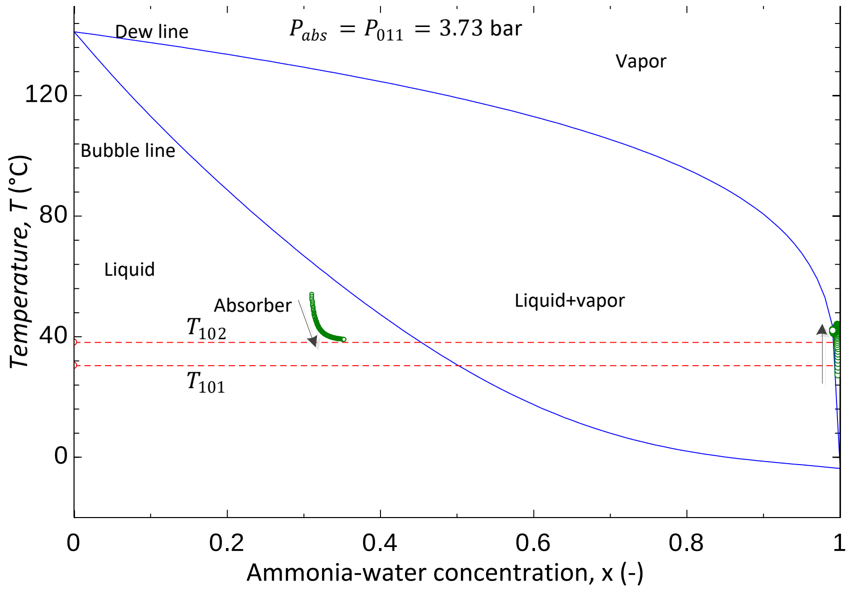

Figure 6.3 – *Schematic representation of the ammonia-water mixture in the absorption process on the temperature-concentration diagram*

condition at the absorber inlet as shown in Fig. (6.3) in which the green lines indicate the absorption process happening in the six heat plates of the absorber. T_{101} and T_{102} is the water coolant entering to the absorber, and the maximum water coolant temperature value leaving the absorber, respectively. Wet ammonia vapor is moving over the dew line, whose vapor is coming from evaporator.

Fig. (6.4) shows a schematic representation of the measured variables; temperature, pressure and mass flow rate it employed to analyze the absorber behavior. The concentration is found by using the saturated condition, i.e; in the absorber, the vapor concentration y_v is defined as a function of the temperature, pressure and saturated condition $y = f(T_{008}, P_{011}, \text{saturated vapor}) = f(55.7°\text{C}, 3.73 \text{ bar}, 1)$, thus $y = 0.9761$. The weak solution entering to the absorber is the same weak solution coming from the generator, in which the saturated condition at the generator outlet allows defining the weak solution concentration, being $x_{ws} = f(T_{023}, P_{008}, \text{saturated liquid}) = f(103.2°\text{C}, 10.3 \text{ bar}, 0) = 0.3069$. Also, concentrations are defined by using the Coriolis mass flow rate, in which the three thermophysical properties define the thermodynamic state (T, P, ρ). Vapor temperature coming from evaporator is measured by using $T_{009} = 27.2°\text{C}$. The inlet temperature T_{ws} is defined in T_{008}, being $T_{008} = 55.7°\text{C}$.

The wall absorber temperature T_w is defined as the average temperature between the temperatures $T_{101}, T_{102}, T_{103}$ and T_{104}, being $T_{avg,101} = 0.25 \cdot (30.4 + 38.1 + 36.2 + 34.9)°\text{C}$ $T_{avg,101} = 34.5°\text{C}$. The average volume flow rate is computed by using the hydrometer $(\dot{m}_{102})$, in which the measurements is carried out during 1540 s obtaining a 160 l water total volume; $\dot{V}_{101} = 160/1540 = 104 \cdot 10^{-6} \text{ m}^3/s$. Properties as density and specific heat capacity are found at the average temperature, $\rho_{101} = 994.2 \text{ kg/m}^3$, defining the total mass flow rate $\dot{m}_{101} = (0.10329 \pm 0.00206)$ kg/s (See Fig. (5.26) and (5.24). In the absorber, three water coolant circuits are defined, in which the mass flow rate per each one is defined as

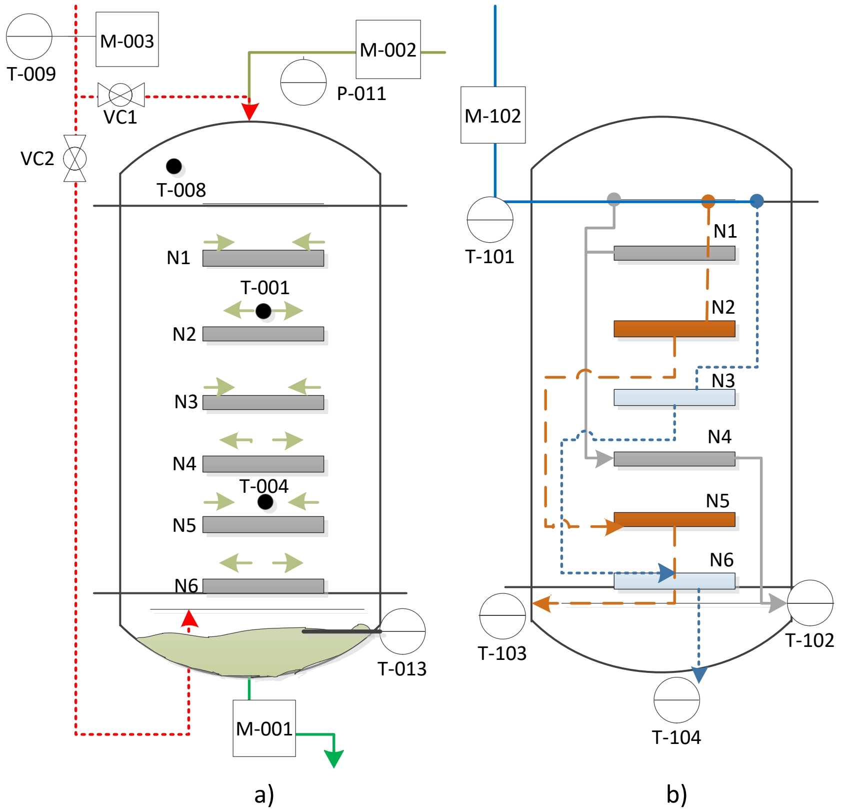

Figure 6.4 – *Measured variables in the ammonia-water absorber by using the horizontal liquid film for the a) ammonia-water circuit and b) water coolant circuit*

Table 6.1 – *Experimental results for the first test in the ammonia-water absorption process*

Ammonia-water circuit							
P_{011}, bar	T_{008},°C	T_{009},°C	T_{001},°C	T_{004},°C	T_{013},°C	$\dot{m}_{001}$, kg/s	$\dot{m}_{002}$, kg/s
3.76 ± 0.01	55.7 ± 0.1	27.2 ± 0.1	54.0 ± 0.1	42.2 ± 0.1	40.0 ± 0.1	0.0193 ± 0.0006	0.0187 ± 0.0006
Water coolant circuit							
$\dot{m}_{102}$, kg/s	T_{101},°C	T_{102},°C	T_{103},°C	T_{104},°C			
0.10329 ± 0.00206	30.4 ± 0.1	38.1 ± 0.1	36.2 ± 0.1	34.9 ± 0.1			

$\dot{m}_{102,c} = \dot{m}_{102}/3 = (0.03443 \pm 0.00068)$ kg/s. It is valid because each circuit has the same loss pressure value. All these results are summarized in Tab. (6.1).

6.1.1 Heat transfer calculations

Water coolant circuit:

The total heat of absorption $\dot{Q}_{abs}$ absorbed by the water coolant is given by Eq. (6.1), in which $\dot{Q}_{102}$ is the absorbed heat duty by the $N1$ and $N4$ plates, $\dot{Q}_{103}$ is the absorbed heat duty by the $N2$ and $N5$ plates and $\dot{Q}_{104}$ is the absorbed heat rate by the last plates $N3$ and $N6$,

$$\begin{aligned}\dot{Q}_{abs} &= \dot{m}_{101,c} \cdot cp_{101} \cdot [(T_{102} - T_{101}) + (T_{103} - T_{101}) + (T_{104} - T_{101})] \\ \dot{Q}_{abs} = 0.03443 \text{ kg/s} \cdot 4179 \text{ J/kg}^{\circ}\text{C} &\cdot [(38.1 - 30.1) + (36.2 - 30.1) + (34.9 - 30.1)]^{\circ}\,\text{C} \\ &\rightarrow \dot{Q}_{abs} = (2590 \pm 72) \text{ W} \\ &\rightarrow \dot{Q}_{102} = (1108 \pm 30) \text{ W} \\ &\rightarrow \dot{Q}_{103} = (834.5 \pm 26.3) \text{ W} \\ &\rightarrow \dot{Q}_{104} = (647.4 \pm 24.1) \text{ W}\end{aligned} \tag{6.1}$$

or, it is expressed as a function of the total mass flow rate and its average outlet temperature,

$$\begin{aligned}\dot{Q}_{abs} &= \dot{m}_{101} \cdot c_{p,101} \cdot (T_{avg,out} - T_{101}) \\ \dot{Q}_{abs} = 0.10329 \text{ kg/s} \cdot 4179 \text{ J/kg}^{\circ}\text{C} &\cdot (1/3 \cdot (38.1 + 36.2 + 34.97) - 30.4)^{\circ}\text{C} \\ &\rightarrow \dot{Q}_{abs} = (2590 \pm 72)\,\text{W}\end{aligned} \tag{6.2}$$

The heat transfer coefficient of the water coolant side is found by using the Dittus-Boelter's correlation (Dittus, 1930), in which it achieves the turbulent regime, $\text{Re}_{101} = 4\dot{m}_{101,c}/(\pi \cdot d_{101} \cdot \mu_{101}) = 4 \cdot 0.03443 \text{ kg/s}/(\pi \cdot 0.004 \text{ m} \cdot 72.08 \cdot 10^{-5} \text{ Pa s}) = 15204 \pm 487$. Prandtl number is defined as a function of the average properties, $\text{Pr}_{101} = 4.846 \pm 0.005$.

$$\begin{aligned}\text{Nu}_{101} &= 0.023 \cdot \text{Re}_{101}^{0.8} \cdot \text{Pr}_{101}^{0.4} = 0.023 \cdot 15204^{0.8} \cdot 4.846^{0.4} \\ \text{Nu}_{101} &= 95.82 \pm 2.45 = \frac{h_{101} \cdot d_{101}}{k_{101}} = \frac{h_{101} \cdot 0.004 \text{ m}}{0.6216 \text{ W/m}^{\circ}\text{C}} \\ &\rightarrow h_{101} = (14890 \pm 711) \text{ W/m}^2\,^{\circ}\text{C}\end{aligned} \tag{6.3}$$

Also, the Gnielinski correlation (Gnielinski, 1976) may be used in turbulent flow, having a 6% accuracy for $\text{Pr}_{101} < 200$ (Lienhard, 2019) and it is given by Eq. (6.4), where f is the friction factor $f_f = (1.82 \cdot \text{Log}_{10}(\text{Re}_{101} - 1.64))^{-2} = 0.0281$. The heat transfer correlation of the Dittus-Boelter correlation present less than 5% of the Gnielinski correlation, whose difference is approximately the absolute error of the heat transfer coefficient.

$$\begin{aligned}\text{Nu}_{101} &= \frac{(f_f/8) \cdot \text{Pr}_{101} \cdot (\cdot\text{Re}_{101} - 1000)}{1 + 12.7 \cdot \sqrt{f_f/8} \cdot (\text{Pr}_{101}^{2/3} - 1)} \\ \text{Nu}_{101} &= 100.5 \pm 2.8 = \frac{h_{101} \cdot d_{101}}{k_{101}} = \frac{h_{101} \cdot 0.004 \text{ m}}{0.6216 \text{ W/m}^{\circ}\text{C}} \\ &\rightarrow h_{101} = (15616 \pm 785) \text{ W/m}^2\,^{\circ}\text{C}\end{aligned} \tag{6.4}$$

Ammonia-water solution circuit:

The absorption heat rate is computed by using the energy balance in the absorber, in which a steady-state is assumed. Neglecting changes in potential energy and kinetic energy, it is given as follows,

$$\begin{aligned}\dot{m}_{002}\cdot i_{ws}+\dot{m}_{003}\cdot i_{av}&=\dot{m}_{001}\cdot i_{ss}+\dot{Q}_{abs}\\ 0.0187\text{ kg/s}\cdot 47451\text{ J/kg}+(0.0193-0.0187)\text{ kg/s}\cdot 1342\cdot 10^{3}\text{ J/kg}&\\ =0.0193\text{ kg/s}\cdot -37630\text{ J/kg}+\dot{Q}_{abs}&\\ \rightarrow \dot{Q}_{abs}=(2354\pm 180)\text{ W}&\end{aligned} \tag{6.5}$$

Also, $\dot{Q}_{abs}$ is defined as a function of the global heat transfer coefficient U_{abs}, heat transfer area A_{abs} and the log mean temperature difference ΔT_{LM} whose ΔT_{LM} can be defined as shown in (6.5), in which the weak ammonia-water solution enters to the absorber $T_{ws} = 55.7°\text{C}$. The three first plates are parallelly connected, keeping the same water coolant temperature $T_{ws} = 40.0°\text{C}$. The estimation of a global ΔT_{LM} for the total absorber is incorrect due to it doesn't represent the physical phenomena (i.e; the dashed black line in Fig. (6.5), and probably, it should exist an average value ΔT_{LM} as shown in dashed red line. However, a local ΔT_{LM} is defined for each heat exchanger plate (blue, orange and green lines), in which the first plates present the highest heat and mass transfer rates.

$$\overline{Q}_{abs} = U_{abs}\cdot A_{abs}\cdot \Delta T_{LM} \tag{6.6}$$

Unfortunately, the temperature sensors T_{002}, T_{003} and T_{005} were unavailable for the first test (red points in Fig. (6.5)). Thus, it employed an average water coolant temperature at the absorber outlet $T_{wc,avg}$, highlighting that the mass flow rate per each circuit is the same. So, $T_{wc,avg} = 1/3\cdot(38.1+36.2+34.9)°\text{C} = 36.4°\text{C}$. The individual area heat transfer is $A_{1,abs} = \pi\cdot d_o\cdot L_{abs}$ $A_{1,abs} = \pi\cdot 0.00635\text{ m}\cdot 2.4\text{ m} = (0.0478\pm 0.0007)\text{ m}^2$. So, $A_{abs} = 6\cdot A_{1,abs} \rightarrow A_{abs} = (0.2873\pm 0.0045)\text{ m}^2$.

$$\begin{aligned}\Delta T_{LM} &= \frac{\Delta T_1-\Delta T_2}{\ln\left(\frac{\Delta T_1}{\Delta T_2}\right)}\\ \Delta T_1 &= (55.7-30.4)°\text{C} = 25.3°\text{C}\\ \Delta T_2 &= (40-36.4)°\text{C} = 3.6°\text{C}\\ \Delta T_{LM} &= \frac{(25.3-3.6)°\text{C}}{\ln\left(\frac{25.3}{3.6}\right)}\\ \rightarrow \Delta T_{LM} &= (11.1\pm 0.1)°\text{C}\end{aligned} \tag{6.7}$$

so, the overall heat transfer coefficient is defined by Eq. (6.8. It is worthwhile to mention that the heat transfer area is a half of the total area due to the horizontal liquid film $A_{f,abs}$ is only over the plate. However, the average heat transfer coefficient should be define as a function A_{abs}. The overall heat transfer coefficient may reach $U_{abs} = 1548\text{ W/m}^2\ °\text{C}$ for a hypothetical configuration in which the absorber takes into account all heat transfer area.

$$\begin{aligned}U_{abs} = \frac{\overline{Q}_{abs}}{A_{abs}\cdot\Delta T_{LM}} = \frac{0.5\,(\cdot Q_{abs}(Eq.(6.2)) + Q_{abs}(Eq.(6.5)))}{A_{abs}\cdot\Delta T_{LM}} &= \frac{2472\text{ W}}{0.2873\text{ m}^2\cdot 11.1°\text{C}}\\ \rightarrow U_{abs} &= (773.8\pm 34.5)\text{ W/m}^2\ °\text{C}\end{aligned} \tag{6.8}$$

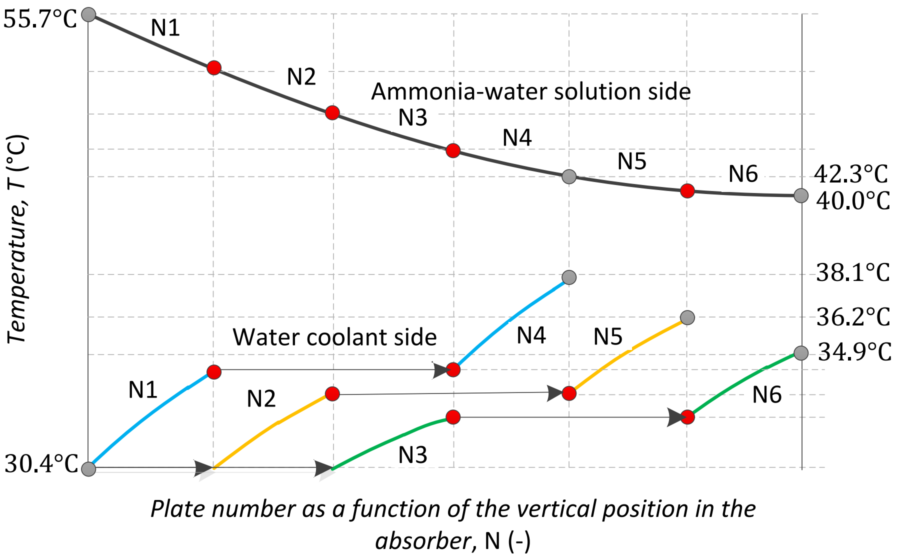

Figure 6.5 – *Log mean temperature difference for the horizontal liquid film absorber. N1-N6 are the flat plates. Blue line is the coolant circuit for the N1 and N4 plates, yellow color for the N2 and N5, and green color for the N3 and N6 plates*

In future tests, all the unknown temperatures (red dots) will be measured by using PT-100 already installed. However, the intermediate temperature can be estimated by using the absorption process modeling. Basically, the liquid solution temperature lost about 10°C when it flowed over the first plate. These results can be checked through the water coolant energy balance for the N1 and N4 plates.

The heat transfer coefficient over the horizontal liquid film is computed by using the thermal resistance network. The A_{101} is the internal heat transfer area $A_{101} = \pi \cdot d_{101} \cdot L_{abs} \cdot N_{plates} = \pi \cdot 0.004\ \mathrm{m} \cdot 2.4\ \mathrm{m} \cdot 6 = (0.1810 \pm 0.0045)\ \mathrm{m}^2$.

$$Rt_{101} = \frac{1}{h_{101} A_{101}} = \frac{1}{14890\ \mathrm{W}/\ {}^{\circ}\mathrm{C} \cdot 0.5 \cdot 0.1810\ \mathrm{m}^2} \\ \rightarrow Rt_{101} = (742.3 \pm 19.1) \cdot 10^{-6} \cdot {}^{\circ}\ \mathrm{C/W} \tag{6.9}$$

in the same way, the thermal resistance over the horizontal film Rt_f can be defined by Eq. (6.10). The global heat transfer coefficient is given by Eq. (6.12). Thus, the heat transfer coefficient in the ammonia-water absorption process for a horizontal liquid film is computed.

$$Rt_f = \frac{1}{h_f \cdot 0.5 \cdot A_f} = \frac{1}{h_f \cdot 0.5 \cdot 0.1810\ \mathrm{m}^2} \tag{6.10}$$

$$Rt_{total} = Rt_{101} + Rt_f = 742.3 \cdot 10^{-6}\ {}^{\circ}\mathrm{C/W} + Rt_f \tag{6.11}$$

$$
\begin{aligned}
\frac{1}{U_{abs}\cdot A_f} = \sum Rt_{total} \rightarrow \frac{1}{U_{abs}} &= \frac{1}{h_f} + \left(\frac{d_o}{d_i}\right)\frac{1}{h_{101}} \\
\frac{1}{U_{abs}\cdot A_f} &= 742.3\cdot 10^{-6}\ °\mathrm{C/W} + Rt_f \\
\frac{1}{773.8\mathrm{W/m^2\ °C}\cdot 0.5\cdot 0.1810\ \mathrm{m^2}} &= 742.3\cdot 10^{-6}\ °\mathrm{C/W} + Rt_f \\
\rightarrow Rt_f &= (825.5 \pm 37.3)\cdot 10^{-5}\ °\mathrm{C/W} \\
825.5\cdot 10^{-5}\ °\mathrm{C/W} &= \frac{1}{h_f\cdot 0.5\cdot 0.1810\ \mathrm{m^2}} \\
\rightarrow h_f &= (843.4 \pm 40.3)\ \mathrm{W/m^2\ °C}
\end{aligned}
\tag{6.12}
$$

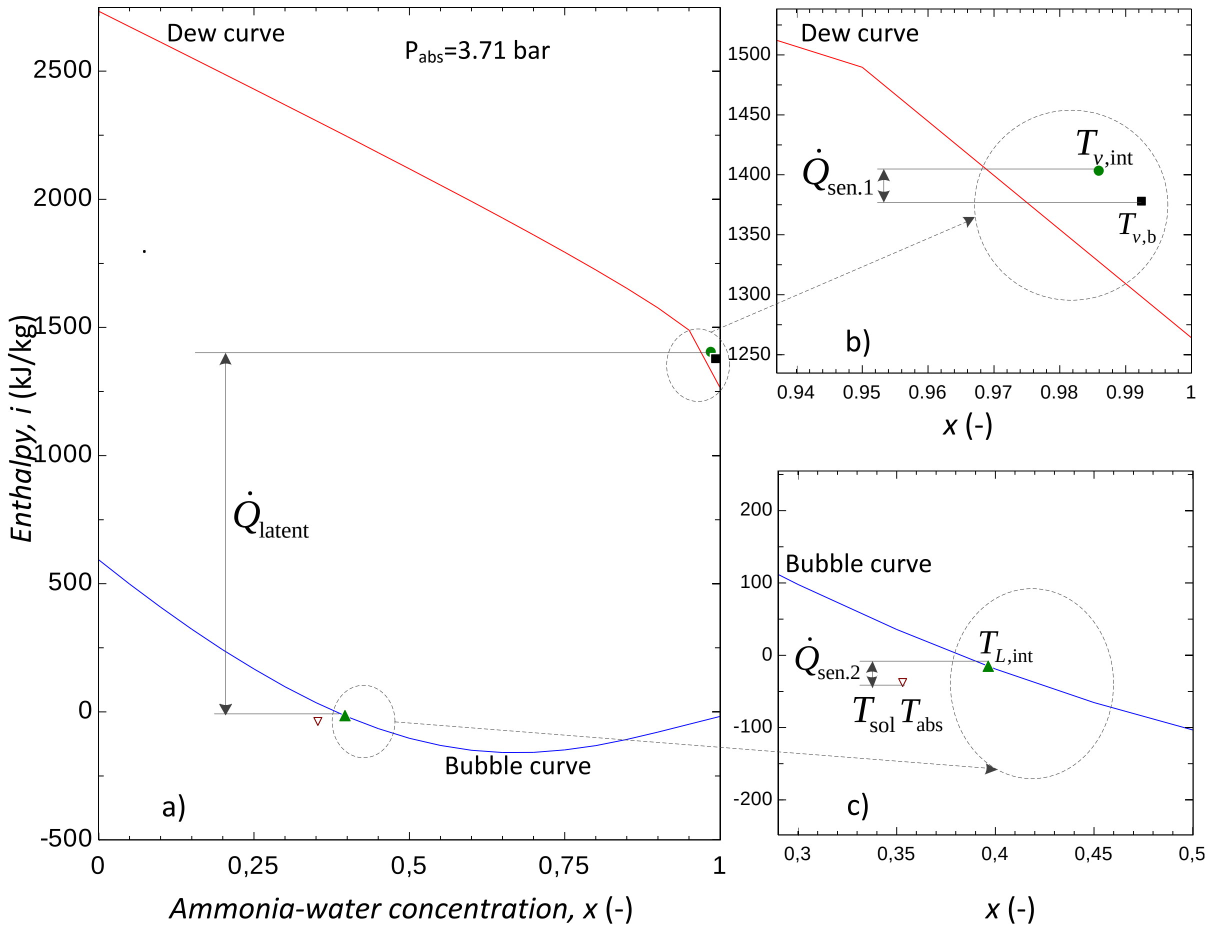

Figure 6.6 – *Schematic representation of the latent and sensible heat transfer rate for the ammonia-water absorption process by using the enthalpy - ammonia-water concentration diagram under the equilibrium condition.*

Fig. (6.6) shows the sensible and latent heat transfer process when the weak solution absorbs the wet ammonia vapor. First, $\dot{Q}_{\text{sen. }1}$ is the heat transfer rate from the vapor interface towards the vapor bulk due to the vapor interface temperature ($T_{v,int}$) may be higher than the vapor bulk temperature ($T_{v,b}$). Second, $\dot{Q}_{\text{latent}}$ is the latent heat transfer rate from the interface to the solution. Finally, $\dot{Q}_{\text{sen. }2}$ refers the sensible heat transfer rate for the liquid phase, in which it goes from the saturated condition ($T_{L,int}$) to the subcooled condition (T_{abs}) (Bohra, 2007). T_{int} is defined as the average temperature between the inlet solution temperature (T_{008}) and the outlet solution temperature (T_{013}), being $T_{int} = 0.5 \cdot (T_{008} + T_{013})$; $T_{int} = 0.5 \cdot (55.7 + 40.0)$°C $\rightarrow T_{int} = 47.9$°C. $i_{v,int}$ is the interface enthalpy for the vapor phase, $i_{v,b}$ is the bulk enthalpy for the vapor phase, $i_{L,int}$ is the interface enthalpy for the liquid phase, and $i_{L,b}$ is the bulk enthalpy for the liquid phase. Enthalpies are defined as follows,

- $i_{v,int} = f(T_{int}, P_{011}, 1)$; $i_{v,int} = f(47.9°\text{C}, 3.71 \text{ bar}; 1) \rightarrow i_{v,int} = 1430 \cdot 10^3$ J/kg
- $i_{v,b} = f(T_{013}, P_{011}, 1)$; $i_{v,int} = f(40.0°\text{C}, 3.71 \text{ bar}; 1) \rightarrow i_{v,b} = 1378 \cdot 10^3$ J/kg
- $i_{L,int} = f(T_{int}, P_{011}, 0)$; $i_{L,int} = f(47.9°\text{C}, 3.71 \text{ bar}; 0) \rightarrow i_{L,int} = -15.27 \cdot 10^3$ J/kg
- $i_{L,b} = f(T_{013}, P_{011}; x_{ss})$; $i_{L,b} = f(40.0°\text{C}, 3.71 \text{ bar}; 0.353) \rightarrow i_{L,b} = -37.63 \cdot 10^3$ J/kg

so, the heat rate may be computed as follows,

$$\begin{aligned} \dot{Q}_{\text{sen. 1}} &= (\dot{m}_{002} - \dot{m}_{001}) \cdot (i_{v,b} - i_{v,int}) \\ \dot{Q}_{\text{sen. 1}} &= (0.0193 - 0.0187)\text{kg/s} \cdot (1378 - 1430) \cdot 10^3\text{J/kg} \\ &\rightarrow \dot{Q}_{\text{sen. 1}} = (-13.9 \pm 3.4)\text{W} \end{aligned} \tag{6.13}$$

$$\begin{aligned} \dot{Q}_{\text{latent}} &= (\dot{m}_{002} - \dot{m}_{001}) \cdot (i_{v,int} - i_{L,int}) \\ \dot{Q}_{\text{latent}} &= (0.0193 - 0.0187)\text{kg/s} \cdot (1430 - \; -15.27) \cdot 10^3\text{J/kg} \\ &\rightarrow \dot{Q}_{\text{latent}} = (780.2 \pm 190.9)\text{W} \end{aligned} \tag{6.14}$$

$\dot{Q}_{\text{sen. 2}}$ refers to the total solution subcooling, in which it takes into account the weak solution subcooling $\dot{Q}_{\text{sen. 2-Sol}}$ and the subcooling degree of the ammonia vapor absorbed into the ammonia-water solution $\dot{Q}_{\text{sen. 2-Con}}$,

$$\dot{Q}_{\text{sen. 2}} = \dot{Q}_{\text{sen. 2-Con}} + \dot{Q}_{\text{sen. 2-Sol}} \tag{6.15}$$

so, the condensed subcooling is defined as follows,

$$\begin{aligned} \dot{Q}_{\text{sen. 2-Con}} &= (\dot{m}_{002} - \dot{m}_{001}) \cdot (i_{L,int} - i_{L,b}) \\ \dot{Q}_{\text{sen. 2-Con}} &= (0.0193 - 0.0187)\text{kg/s} \cdot (-15.27 - \; -37.63) \cdot 10^3\text{J/kg} \\ &\rightarrow \dot{Q}_{\text{sen. 2-Con}} = (12.3 \pm 3.1)\text{W} \end{aligned} \tag{6.16}$$

the average total absorber heat rate is defined by using the Eq. (6.17,)

$$\begin{aligned} \dot{Q}_{abs} &= \dot{Q}_{\text{sen. 1}} + \dot{Q}_{\text{latent}} + \dot{Q}_{\text{sen. 2}} \\ \dot{Q}_{abs} &= \dot{Q}_{\text{sen. 1}} + \dot{Q}_{\text{latent}} + \dot{Q}_{\text{sen. 2-Con}} + \dot{Q}_{\text{sen. 2-Sol}} \\ 2472\text{W} &= -13.9\text{W} + 780.2\text{W} + 12.3\text{W} + \dot{Q}_{\text{sen. 2-Sol}} \\ &\rightarrow \dot{Q}_{\text{sen. 2-Sol}} = (1693 \pm 108)\, W \end{aligned} \tag{6.17}$$

the condensing flux concentration z is given by Eq. (6.18),

$$\begin{aligned} i_{v,\text{total}} &= z \cdot i_{Lv,\text{NH}_3} + (1-z) \cdot i_{Lv,\text{H}_2\text{O}} \\ 1419 \cdot 10^3\text{J/kg} &= z \cdot 1276 \cdot 10^3\text{J/kg} + (1-z) \cdot 2142 \cdot 10^3\text{J/kg} \\ &\rightarrow z = 0.8352 \end{aligned} \tag{6.18}$$

6.1.2 Mass transfer calculations - vapor phase

In Sec. (2) is detailed the procedure to compute de mass transfer coefficients. Total molar flux across the liquid-vapor interface is shown in Eq. (6.19)

$$\begin{aligned} \dot{n}_T &= \frac{\dot{m}_v}{A_{in} \cdot (z \cdot M_{NH_3} + (1-z) \cdot M_{H_2O})} \\ \dot{n}_T &= \frac{0.0006 \text{ kg/s}}{0.0905 \text{ m}^2 \cdot (0.8352 \cdot 17.03 \text{ kg/kmol} + (1 - 0.8352 \cdot 18.02 \text{ kg/kmol})} \\ &\rightarrow \dot{n}_T = (-222.7 \pm 54.6) \cdot 10^{-6}\text{kmol/m}^2\text{s} \end{aligned} \tag{6.19}$$

based on Bohra (2007) the mass transfer coefficient for the vapor phase $k_{m,v}$ is given in Eq. (6.20)

$$\begin{aligned} k_{m,v} &= \frac{\dot{n}_T}{C_{T,v} \cdot \ln\left(\frac{z-y_{int}}{z-y_b}\right)} \\ k_{m,v} &= \frac{\dot{n}_T}{P_{abs}/8314 \cdot \overline{T}_f \cdot \ln\left(\frac{\tilde{z}-y_v}{\tilde{z}-y_{int}}\right)} \\ k_{m,v} &= \frac{-222.7 \cdot 10^{-6}\text{kmol/m}^2\text{s}}{371000 \text{ m}/8314 \text{ J/kmol K} \cdot 313.2 \text{ K} \cdot \ln\left(\frac{0.8352-0.986}{0.8352-0.9924}\right)} \\ &\rightarrow k_{m,v} = (0.038 \pm 0.009) \text{ m/s} \end{aligned} \tag{6.20}$$

6.1.3 Mass transfer calculations - Liquid phase

Staedter and Garimella (2018b) defined the bulk concentration as the average between the weak and strong solution, and the interface concentration is given where it is evaluated at the saturated condition for the average temperature; $x_{int} = 39.64$. M_L is the molecular mass. Bohra (2007) computed the liquid mass transfer as follows,

$$\begin{aligned} \dot{m}_v &= k_{m,L} \cdot 0.5 \cdot A_{in} \cdot (z \cdot \rho_{int,L} - x_{avg,L} \cdot \rho_{avg,L}) \\ 0.0006 \text{ kg/s} &= k_{m,L} \cdot 0.2873 \text{ m}^2 \cdot \left(0.8352 \cdot 846.8 \text{ kg/m}^3 - 0.3964 \cdot 846.8 \text{ kg/m}^3\right) \\ &\rightarrow k_{m,L} = (10.3 \pm 2.5) \cdot 10^{-6} \text{ m/s} \end{aligned} \tag{6.21}$$

6.2 Distillation process

The distillation process has already been introduced in Sec. (2). However, a schematic representation is shown in Fig. (6.7) where experimental results are defined and drawn over the temperature-concentration diagram for a constant pressure in which the liquid solution is in thermodynamic equilibrium with the vapor leaving from generator. The strong ammonia-water solution entering in the generator achieves the weak ammonia-water solution in the generator outlet as represented in red circles. As desorption is happening, the solution temperature is increasing and weakening the ammonia-water solution following the bubble line. Wet ammonia vapor is shown over the dew line. In red dashed line is highlighted the oil temperature, supplying the thermal energy to the desorption process. Purification is carried out after the generation process using the water coolant and represented in green dashed line. The drips of ammonia-water return to the generator in about $30 - 45\%$ concentration. Next, the experimental results over the distiller are shown;

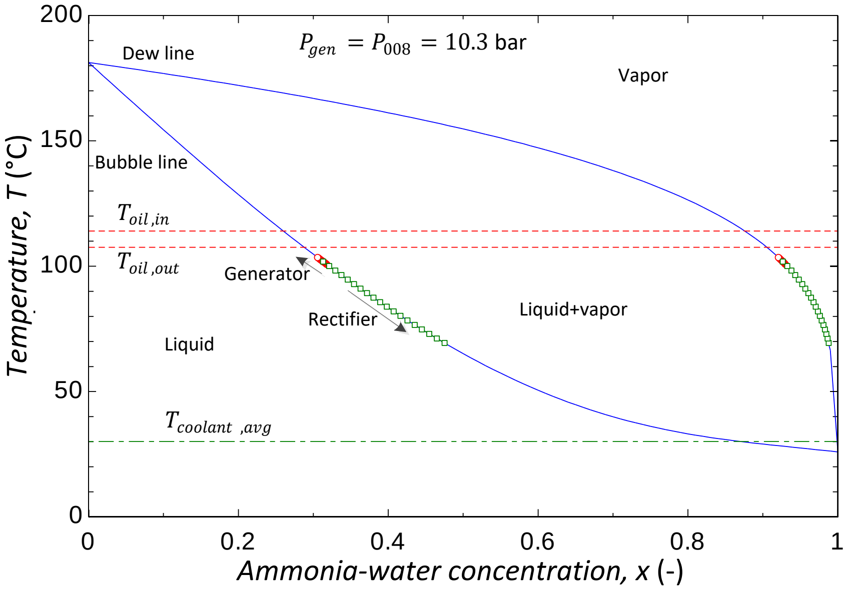

Figure 6.7 – *Temperature-concentration diagram for the ammonia-water mixture in the generation and purification processes*

- therminol 59 oil: $T_{201} = T_{oil,in} = 112.6°C$ and $T_{202} = T_{oil,out} = 109.1°C$, (see Fig. (5.27))
- ammonia-water solution: $T_{020} = T_{ss} = 100.5°C$, $T_{023} = T_{ws} = 103.2°C$, $T_{021} = T_{coolant,avg} = 67.5°C$ and $P_{gen} = P_{008} = 10.3$ bar (see Fig. (5.3))
- water coolant: $T_{120} = T_{rect,in} = T_{coolant,avg} = 30.5°C$ (see Fig. (5.26))

T_{201}, T_{202} is the oil temperature at the inlet and outlet of the generator, respectively. T_{020} is the strong solution temperature, T_{023} is the weak solution temperature and T_{021} is the average distilled ammonia vapor temperature. T_{120} is the average water coolant. P_{gen} is the measured absolute pressure in the generator.x and y is the ammonia-water concentration for the liquid and vapor phase, respectively.

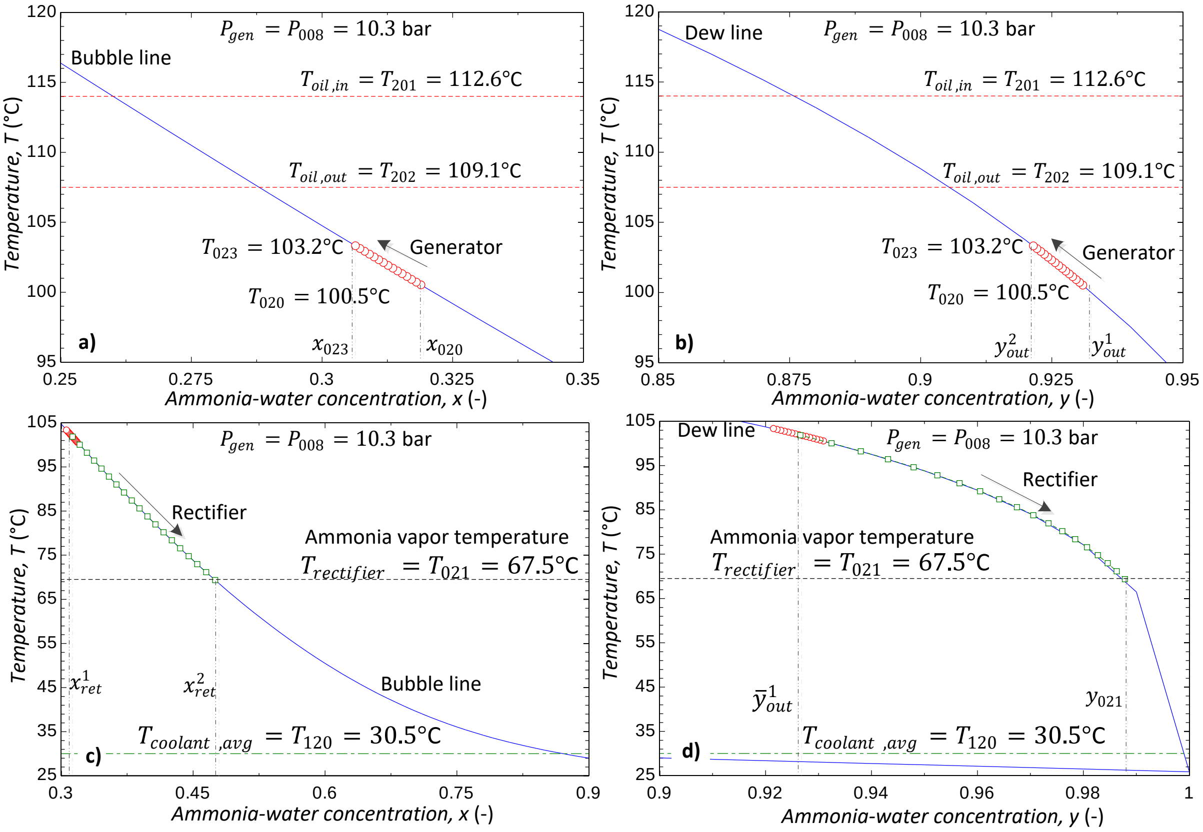

Figure 6.8 – *Schematic representation of the generation and rectification process; a) - c) over the bubble line (saturated liquid), and b) - d) over the dew line (saturated vapor)*

Fig. (6.8) shows a detailed representation of the both generation and purification processes over the temperature-concentration diagram. Fig. (6.8a) and (6.8c) define the process on the bubble line, representing the saturated liquid solution condition. Fig. (6.8b) and (6.8d) display the ammonia-water vapor over the dew line. In Fig. (6.8a) 38.3% strong solution enters to generator and following the bubble line until it achieves a 30.69% and 103.2°C weak solution. Simultaneously, ammonia vapor is produced with a low degree of purity (between $y^1_{out} - y^2_{out}$, about 92.66%) as shown in Fig. (6.8b). The purification allows achieving a 98.93% ammonia vapor as displayed in Fig. (6.8d), while the drips of the liquid solution returns in 48.58% ammonia concentration (Fig. (6.8c)). Also, Staedter and Garimella (2018b) assumed the weak solution, wet ammonia vapor leaving from generator and purified ammonia vapor leaving from rectifier as saturated condition. A focus on the heat and mass transfers follows;

6.2.1 Heat transfer calculations

The falling film technology is employed in the generator, having the temperature and concentration profile shown in Fig. (6.9). $\overline{T}_{b,oil}$ is the bulk temperature of the therminol 59 oil, $\overline{T}_{b,oil} = 0.5 \cdot (T_{oil,in} + T_{oil,out})$. $\overline{T}_f$ is the bulk temperature of the ammonia-water solution liquid film, $\overline{T}_f = 0.5 \cdot (T_{ss} + T_{ws})$. $\overline{T}_{w,vessel}$ is the surface temperature on the external generator vessel, and it is measured and given by $0.25 \cdot (TR_1 + TR_2 + TR_3 + TR_4)$ (See Fig. (5.26)). $\overline{T}_{v,vessel}$ is the internal vapor temperature and due to the low thermal conductivity resistance,

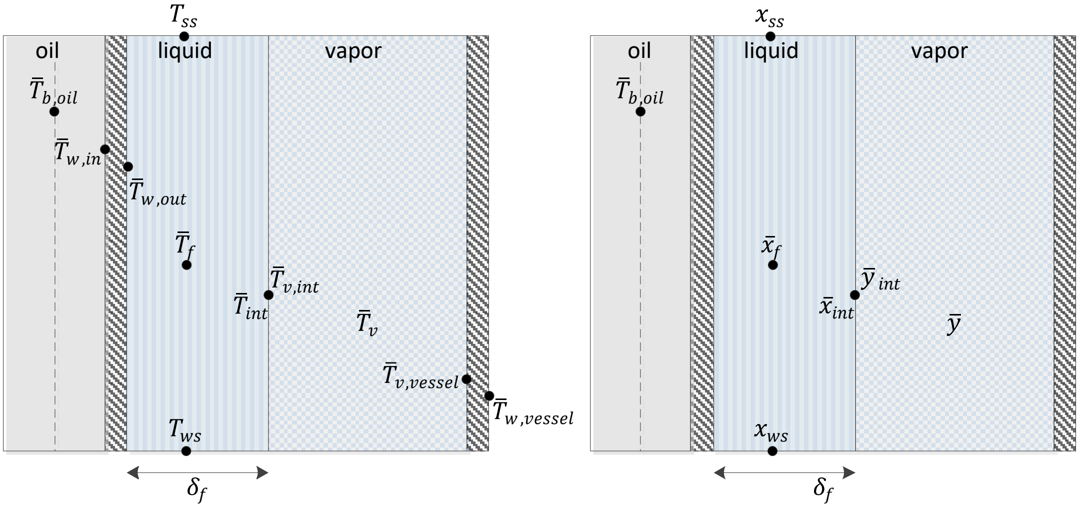

Figure 6.9 – *Temperature and concentration profiles in the liquid falling film generator*

Table 6.2 – *Estimated values of the temperature and concentration in the falling film generator*

$\overline{T}_{b,oil}$	$\overline{T}_f$	$\overline{T}_{int}$	$\overline{T}_{v,int}$	$\overline{T}_{w,vessel}$
110.8°C	99.9°C	99.9°C	99.9°C	97.9°C
$\overline{x}_{ss}$	$\overline{x}_{ws}$	$\overline{x}_f$	$\overline{y}_{int}$	$\overline{y}$
31.9	30.69	31.3	93.1	92.66

Table 6.3 – *Calculated values of the transport and thermal properties*

Properties	Therminol 59	Liquid film, f	Vapor, v
ρ– kg/m^3	907.9	820.8	5.977
c_p– J/kg°C	1977	3648	2593
μ– Pa s	$11.5 \cdot 10^{-6}$	$128.2 \cdot 10^{-6}$	$15.3 \cdot 10^{-6}$
k– W/m°C	0.1138	0.4691	0.04028

it is assumed as $\overline{T}_{v,vessel} = \overline{T}_{w,vessel}$. In the same way, $\overline{T}_{w,in} = \overline{T}_{w,out}$. Thermal conductivity resistance is about 2% of the total thermal resistance as shown further. $\overline{T}_v$, $\overline{T}_{v,int}$ and $\overline{T}_{int}$ is the bulk vapor temperature, interface vapor temperature and interface temperature, respectively, in which $\overline{T}_{v,int} = \overline{T}_{int}$. δ_f is the average liquid film and it is given by Eq. (2.26). $\overline{x}_f = 0.5 \cdot (x_{ws} + x_{ss})$ is the bulk concentration of the liquid film (Also it was assumed by (Staedter; Garimella, 2018b)), $\overline{x}_{int}, \overline{x}_{int}$ and $\overline{y}_{int}$ is the liquid concentration at the interface, vapor concentration at the interface and the average vapor concentration, respectively. These values are summarized in Tab. (6.2);

By assuming that the strong solution enters to the generator at the saturated conditions, it may estimate the $\overline{T}_{int} = \overline{T}_f$. Thus, Tab. (6.3) shows the properties for the Therminol 59, ammonia-water liquid film and the wet ammonia vapor.

The generation pressure is measured, being $P_{gen} = 10.3$ bar, but it may be estimated as $P_{con} = f(\text{saturated liquid}, \overline{T}_{con})$. Thus, all the conditions are defined at the interface of the falling film generator. General dimensions of the generator are defined in Subsection (5.1.1). Next, the heat transfer calculations are carried out;

Ammonia-water solution - External side: Non-dimensional number are computed at the liquid film by using the properties of ammonia-water mixture from the EES routine. Prandtl number Pr_f, mass flow rate per each side Γ_f and Reynolds number Re_f are defined in Eqs. $(6.22-6.24)$. L_t, N_t is the length of the generator horizontal tube and the number of tubes.

$$\mathrm{Pr}_f = \frac{c_{p,f} \cdot \mu_f}{k_f} = \frac{3648 \text{ J/kg}^\circ\text{C} \cdot 128.2 \cdot 10^{-6} \text{ Pa s}}{0.4691 \text{ W/m}^\circ\text{C}} = 0.997 \pm 0.0003 \tag{6.22}$$

$$\Gamma_f = \frac{\dot{m}_{ss}}{2 \cdot L_t \cdot N_t} = \frac{0.0193 \text{ kg/s}}{2 \cdot 0.150 \text{ m} \cdot 70} = (91.9 \pm 0.7) \cdot 10^{-4} \text{ kg/m s} \tag{6.23}$$

$$\mathrm{Re}_f = \frac{4 \cdot \Gamma_f}{\mu_f} = \frac{4 \cdot 91.9 \cdot 10^{-4} \text{ kg/m s}}{128.2 \cdot 10^{-6} \text{ Pa s}} = 286.8 \pm 2.4 \tag{6.24}$$

Zavaleta-Aguilar (2015) defined the Nusselt number Nu_f by Eq. (6.25). $\overline{h}_f$ is the average convective heat transfer coefficient of the liquid film over the external tube and ν is the cinematic viscosity $(\nu = \mu/\rho)$.

$$\begin{aligned} \mathrm{Nu}_f = 0.75 \cdot \mathrm{Re}_f^{-0.27} \cdot \mathrm{Pr}_f^{0.4} &= \frac{\overline{h}_f}{k_f} \cdot \left(\frac{\nu^2}{g}\right)^{1/3} \\ = 0.75 \cdot 286.8^{-0.27} \cdot 0.9971^{0.4} &= 0.1626 \pm 0.0004 \\ &= \frac{\overline{h}_f}{0.4691 \text{ W/m}^\circ\text{C}} \cdot \left(\frac{(\frac{128.2 \cdot 10^{-6} \text{ Pa s}}{820.8 \text{ kg/m}^3})^2}{9.81 \text{ m/s}^2}\right)^{1/3} \\ &\rightarrow h_f = (5628 \pm 13) \text{ W/m}^2\ {}^\circ\text{C} \end{aligned} \tag{6.25}$$

Therminol 59 oil - Internal side: Similarly, the mass flow rate $m_{oil,1t}$ of the Therminol 59 oil per each tube is define in Eq. (6.26), whose total volume flow rate $V_{oil,1t}$ is measured by M_{200} (see Fig. (5.27). Thus, the Reynolds number (Re_{oil}) is estimated by Eq. (6.27), in which d_{gi} is the internal diameter of the horizontal tube. Prandtl number is defined in Eq. (6.28);

$$\dot{m}_{oil,1t} = \frac{\dot{m}_{oil,1t}}{N_t} = \frac{\rho_{oil} \cdot V_{oil,t}}{N_t} = \frac{907.9 \text{ kg/m}^3 \cdot (\frac{20 \text{ l/min}}{6 \cdot 10^4 \text{ s/m}^3}) \cdot}{70} = (43.23 \pm 2.6) \cdot 10^{-4} \text{ kg/s} \tag{6.26}$$

$$\mathrm{Re}_{oil} = \frac{4\dot{m}_{oil,1t}}{\pi \cdot d_{gi} \cdot \mu_{oil}} = \frac{4 \cdot 43.23 \cdot 10^{-4} \text{ kg/s}}{\pi \cdot 0.006 \text{ m} \cdot 11.5 \cdot 10^{-6} \text{ Pa s}} = 798.7 \pm 82.1 \tag{6.27}$$

$$\mathrm{Pr}_{oil} = \frac{c_{p,oil} \cdot \mu_{oil}}{k_{oil}} = \frac{1977 \text{ J/kg}^\circ\text{C} \cdot 11.5 \cdot 10^{-6} \text{ Pa s}}{0.1138 \text{ W/m}^\circ\text{C}} = 19.950 \pm 0.014 \tag{6.28}$$

Nusselt inside tube for the entry region is defined in Eq. (6.29);

$$\begin{aligned} \mathrm{Nu}_{oil} = 1.953 \cdot \left(\frac{\frac{L_t}{d_{gi}}}{\mathrm{Re}_{oil} \cdot \mathrm{Pr}_{oil}} \right)^{-1/3} &= \frac{h_{oil} \cdot d_{gi}}{k_{oil}} \\ = 1.953 \cdot \left(\frac{\frac{0.150 \text{ m}\cdot}{0.006 \text{ m}}}{798.7 \cdot 19.95} \right)^{-1/3} &= 16.81 \pm 0.34 \\ &= \frac{h_{oil} \cdot 0.006 \text{ m}}{0.1138 \text{ W/m°C}} \\ \rightarrow h_{oil} &= (318.9 \pm 27.4) \text{ W/m}^2 \text{ °C} \end{aligned} \tag{6.29}$$

Global heat transfer coefficient, U_g:

The global heat transfer coefficient is defined by using the thermal resistance analysis in which all resistances are computed in Eqs. (6.30- 6.32). Thermal resistance by conduction Rt_w is about 2% of the total thermal resistance. The thermal conductivity of the 304 stainless steel tube-wall k_w is defined in the average temperature, $k_w = 16.08$ W/m°C. d_{go} is the outlet diameter of the horizontal tube. The oil thermal resistance (Rt_{oil}) is the main problem in this project as compared with the thermal resistance due to the liquid film Rt_f, in which Rt_{oil} is about 90% of the total thermal resistance Rt_{total}. Results will be studied in more detail.

$$\begin{aligned} Rt_w = \frac{\ln\left(\frac{d_{go}}{d_{gi}}\right)}{2\pi \cdot k_w \cdot L_t \cdot N_t} &= \frac{\ln\left(\frac{0.008 \text{ m}}{0.006 \text{ m}}\right)}{2\pi \cdot 16.08 \text{ W/m°C} \cdot 0.150 \text{ m} \cdot 70} \\ &\rightarrow Rt_w = (267.1 \pm 96.8) \cdot 10^{-6} \text{ °C/W} \end{aligned} \tag{6.30}$$

$$\begin{aligned} Rt_{oil} = \frac{1}{h_{oil}\pi \cdot d_{gi} \cdot L_t \cdot N_t} &= \frac{1}{318.9 \text{ W/m}^2 \text{ °C} \cdot 0.006 \text{ m} \cdot 0.150 \text{ m} \cdot 70} \\ &\rightarrow Rt_{oil} = (15.85 \pm 0.32) \cdot 10^{-3} \text{ °C/W} \end{aligned} \tag{6.31}$$

$$\begin{aligned} Rt_f = \frac{1}{h_f\pi \cdot d_{go} \cdot L_t \cdot N_t} &= \frac{1}{5628 \text{ W/°C}\pi \cdot 0.008 \text{ m} \cdot 0.150 \text{ m} \cdot 70} \\ &\rightarrow Rt_f = (673 \pm 42) \cdot 10^{-6} \text{ °C/W} \end{aligned} \tag{6.32}$$

$$\begin{aligned} Rt_{total} = Rt_w + Rt_{oil} + Rt_f &= (267.1 \cdot 10^{-6} + 15.85 \cdot 10^{-3} + 673 \cdot 10^{-6}) \text{ °C/W} \\ &\rightarrow Rt_{total} = (16.79 \pm 0.33) \cdot 10^{-3} \text{ °C/W} \end{aligned} \tag{6.33}$$

The global heat transfer coefficient is given by Eq. (6.34). A_g is the generator area, being $A_g = \pi \cdot d_{go} \cdot L_t \cdot N_t {=} \pi \cdot 0.008 \text{ m} \cdot 0.150 \text{ m} \cdot 70 = (0.2639 \pm 0.0165) \text{ m}^2$.

$$\begin{aligned} \frac{1}{U_g A_g} = \sum Rt_{total} \rightarrow \frac{1}{U_g} = \left(\frac{d_{go}}{d_{gi}}\right) \frac{1}{h_{oil}} + \left(\frac{d_{go}}{2\pi \cdot k_w}\right) ln \left(\frac{d_{go}}{d_{gi}}\right) + \frac{1}{h_f} \\ \frac{1}{U_g \cdot 0.2639 \text{ m}^2} = 16.78 \cdot 10^{-3} \text{ °C/W} \rightarrow U_g = (225.8 \pm 15.0) \text{ W/m}^2 \text{ °C} \end{aligned} \tag{6.34}$$

the log mean temperature difference ΔT_{LMg} is

$$\begin{gathered}\Delta T_{LMg} = \frac{(T_{oil,in} - T_{ws}) - (T_{oil,out} - T_{ss})}{\left(\frac{T_{oil,in} - T_{ws}}{T_{oil,out} - T_{ss}}\right)} \\ \Delta T_{LMg} = \frac{(112.6 - 103)^{\circ}\mathrm{C} - (109.1 - 100.5)^{\circ}\mathrm{C}}{\left(\frac{(112.6-103)^{\circ}\mathrm{C}}{(109.1-100.5)^{\circ}\mathrm{C}}\right)} = (8.9 \pm 0.1)^{\circ}\mathrm{C}\end{gathered} \tag{6.35}$$

<u>Heat transfer rate in the generator, $\dot{Q}_{gen}$:</u> The heat transfer rate is defined by Eq. (6.36):

$$\begin{aligned}\dot{Q}_{gen} = U_g \cdot A_g \cdot \Delta T_{LMg} = 225.8\ \mathrm{W/m^2\ ^{\circ}C} \cdot 0.2639\ \mathrm{m^2} \cdot 8.9^{\circ}\mathrm{C} \\ \rightarrow \dot{Q}_{gen} = (535.8 \pm 12.3) W\end{aligned} \tag{6.36}$$

then, the wet ammonia vapor $\dot{m}_v$ produced in the generator is given by Eq. (6.37). i_v i_f is the vapor enthalpy and the liquid film enthalpy, as a function of the P_{gen}, temperatures and the saturated conditions. $i_v = 1570 \cdot 10^3$ J/kg and $i_f = 257 \cdot 10^3$ J/kg. $i_v - i_f = \Delta i_{fv} = 1320 \cdot 10^3$ J/kg being the latent heat of generation.

$$\begin{aligned}\dot{Q}_{gen} = \dot{m}_v \cdot (i_v - i_f) = 535.9\ \mathrm{W} = \dot{m}_v \cdot (1570 \cdot 10^3 - 257 \cdot 10^3)\ \mathrm{J/kg} \\ \rightarrow \dot{m}_v = (4.058 \pm 0.092) \cdot 10^{-4}\ \mathrm{kg/s}\end{aligned} \tag{6.37}$$

<u>Total heat rate in the generator, $\dot{Q}_{gen,in}$:</u>

Heat of generation supplied to the generator by heating the electrical resistance of the thermal oil circuit must be equal to the sum of the latent heat of generation $\dot{Q}_{gen}$ plus the sensible heat rate $\dot{Q}_{sen}$ plus the heat transfer losses into the generator $\dot{Q}_{loss}$. $\dot{Q}_{gen}$ was already defined, thus, it may estimates $\dot{Q}_{sen}$ when solution enters to the generator. Also, $\dot{Q}_{loss}$ should be taking into account, and it is comprised of convection and radiation losses.

$$\dot{Q}_{gen,in} = \dot{Q}_{gen} + \dot{Q}_{sen} + \dot{Q}_{loss} \tag{6.38}$$

The generator thermal energy $\dot{Q}_{gen,in}$ is defined as follows;

$$\begin{aligned}\dot{Q}_{gen,in} = \dot{m}_{oil} \cdot cp_{oil} \cdot (T_{oil,in} - T_{oil,out}) \\ \rightarrow \dot{Q}_{gen,in} = 30.26 \cdot 10^{-2}\ \mathrm{kg/s} \cdot 1977\ \mathrm{J/kg^{\circ}C} \cdot (112.6 - 109.1)^{\circ}\mathrm{C} = (2094 \pm 151)\ \mathrm{W}\end{aligned} \tag{6.39}$$

so, $\dot{Q}_{sen}$ is;

$$\begin{aligned}\dot{Q}_{sen} = \dot{Q}_{gen,in} - \dot{Q}_{gen} - \dot{Q}_{loss} \\ \dot{Q}_{sen} = \dot{2}094\ \mathrm{W} - 535.8\ \mathrm{W} - 27.0\ \mathrm{W} - 18.4\ \mathrm{W} \\ \rightarrow \dot{Q}_{sen} = (1515 \pm 143)\ \mathrm{W}\end{aligned} \tag{6.40}$$

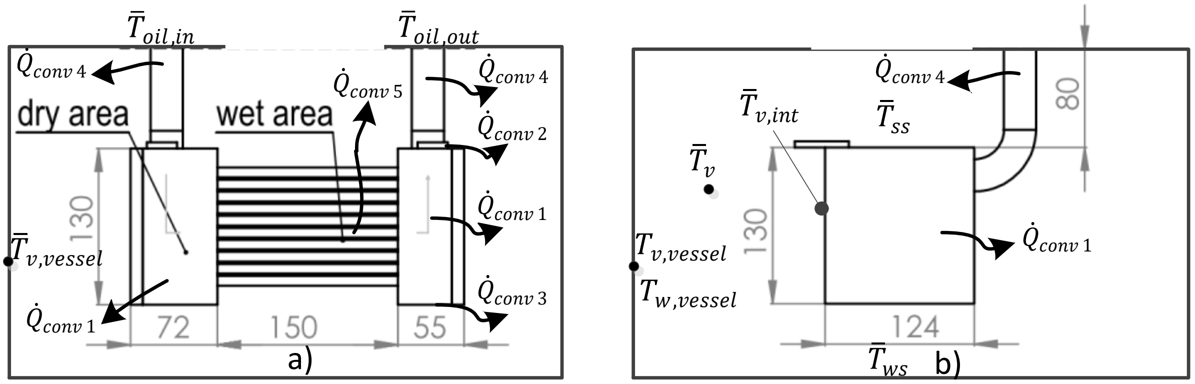

Figure 6.10 – *Heat transfer losses by natural convection inside generator a)plan view b)profile view*

6.2.2 Heat losses by convection

$$\dot{Q}_{loss,conv} = \dot{Q}_{conv1} + \dot{Q}_{conv2} + \dot{Q}_{conv3} + \dot{Q}_{conv4} + \dot{Q}_{conv5} \tag{6.41}$$

The generator is composed by dry and wet areas, in which the dry zones achieve the average oil temperature $\overline{T}_{w,out}$. The wet area references the ammonia-water solution over the lateral horizontal tubes that it is defined as the average solution temperature between the inlet and outlet from the generator $T_{s,gen}$. The external wall temperature of the generator vessel $T_{w,vessel}$ is measured by using four T-type thermocouples. $A1$-$A4$ are dry areas of the generator, and $A5$ are wet areas of the generator in which the complete wettability over the tubes is assumed. Also, the natural convection over the $d_ot = 0.0254$ m and $L_t = 0.060$ m vertical tube of thermal oil feeding is computed. Areas are computed as follows;

- $A1 = 2 \cdot 0.124\text{ m} \cdot 0.130\text{ m} + 2 \cdot 0.055\text{ m} \cdot 0.124\text{ m} + 2 \cdot 0.072\text{ m} \cdot 0.124\text{ m} = 0.06374\text{ m}^2$ (vertical surfaces)
- $A2 = 0.124\text{ m} \cdot 0.055\text{ m} + 0.124\text{ m} \cdot 0.72\text{ m} = 0.01618\text{ m}^2$ (horizontal upper surface)
- $A3 = 0.124\text{ m} \cdot 0.055\text{ m} + 0.124\text{ m} \cdot 0.72\text{ m} = 0.01618\text{ m}^2$ (horizontal lower surface)
- $A4 = 2 \cdot \pi \cdot 0.0254\text{ m} \cdot 0.060\text{ m} = 0.004788\text{ m}^2$ (vertical tubes of thermal oil)
- $A5 = 2 \cdot 0.150\text{ m} \cdot 0.130\text{ m} = 0.039\text{ m}^2$ (wet area- solution)

For computing the convection heat transfer losses $\dot{Q}_{conv}$ inside generator, it was divided in five regions that they are characterized as a function of different orientations of each plate. Thus, each heat transfer loss $\dot{Q}_{conv,i=1...5}$ is correctly computed. For instance, Eq. (6.42) is defined for vertical plates, Eq. (6.43) for horizontal plates with the upper surface heated, Eq. (6.44) for horizontal plates with the lower surface heated, Eq. (6.45) for natural convection in vertical cylinder and Eq. (6.46) for vertical plates but it defines the solution liquid temperature as average temperature. $h_{v,i=1...5}$ is the heat transfer coefficient in the ammonia-water vapor phase.

$$\dot{Q}_{conv1} = h_{v1} \cdot A_1 \cdot (\overline{T}_{w,out} - T_{w,vessel}) \tag{6.42}$$

$$\dot{Q}_{conv2} = h_{v2} \cdot A_2 \cdot (\overline{T}_{w,out} - T_{w,vessel}) \tag{6.43}$$

$$\dot{Q}_{conv3} = h_{v3} \cdot A_3 \cdot (\overline{T}_{w,out} - T_{w,vessel}) \tag{6.44}$$

$$\dot{Q}_{conv4} = h_{v4} \cdot A_4 \cdot (\overline{T}_{w,out} - T_{w,vessel}) \tag{6.45}$$

$$\dot{Q}_{conv5} = h_{v5} \cdot A_5 \cdot (\overline{T}_{s,gen} - T_{w,vessel}) \tag{6.46}$$

The Nusselt number is define to calculate the heat transfer coefficient of the ammonia-water vapor phase, in which vertical and horizontal flat plates are computed by using the experimental correlations showed in Eqs. (6.47-6.50), being the Eq. (6.47) is employed for natural convection in vertical plates, Eq. (6.48) applies to horizontal plate with the heating plate at the upper surface. In contrast, Eq. (6.49) is referenced when the lower surface of the plate is heated. Finally, the heat transfer losses through vertical thermal oil tube inside the vessel should be taken into account. The 0.025m OD tube d_{ot} doesn't satisfy the criteria to the vertical cylinder can be treated as the vertical plate $d_ot > 35 \cdot L_t/Gr^{0.25}$ (Cengel, 2014). Thus, Cebeci (1974) defined the average Nusselt number for natural convention in a isothermal vertical cylinder Nu_v, and it is given by Eq. (6.50), in which the Nu_{fp} references the natural convection in flat plate applications that it may be employed the Churchill and Chu's correlation (Eq. (6.47)) - (Churchill; Chu, 1975) as mentioned by Day et al. (2013).

$$\mathrm{Nu}_1 = \mathrm{Nu}_{fp} = \frac{h_{v1} \cdot L_1}{k_v} = 0.68 + \frac{0.670 \cdot Ra^{0.25}}{(1 + (0.492/Pr)^{9/16})^{4/9}} \tag{6.47}$$

$$\mathrm{Nu}_2 = \frac{h_{v2} \cdot L_2}{k_v} = 0.15 \cdot Ra^{1/3} \tag{6.48}$$

$$\mathrm{Nu}_3 = \frac{h_{v3} \cdot L_3}{k_v} = 0.52 \cdot Ra^{1/5} \tag{6.49}$$

$$\mathrm{Nu}_4/\mathrm{Nu}_{fp} = \frac{h_{v4} \cdot L_1}{k_v} = 1 + 0.3(32^{0.5} \cdot Gr^{-0.25} \cdot L_t/d_{ot}) \tag{6.50}$$

$$\mathrm{Nu}_5 = \mathrm{Nu}_1 = \frac{h_{v5} \cdot L_5}{k_v} \tag{6.51}$$

$L_i = 1...5$ is the length of the cylinder, k_v is the thermal vapor conductivity, Ra is the Rayleigh number (Eq. (6.52)) , Pr is the Prandtl number, Gr is the Grashof number (Eq. (6.53)), and L_t is the height of the cylinder.

$$Ra = \frac{9.81 \cdot \beta_v \cdot (T_{w,out} - T_{w,vessel}) \cdot L_c*^3}{\nu_v \cdot \alpha_v} \tag{6.52}$$

$$Gr = \frac{9.81 \cdot \beta_v \cdot (T_{w,out} - T_{w,vessel}) \cdot L_c*^3}{\nu_v} \tag{6.53}$$

in which $\alpha_v = k_v/(cp_v \cdot \rho_v)$, $\nu_v = \mu_v/\rho_v$ and L_c* is the characteristic length $\beta_v = 1/T_v$

$$Gr = \frac{9.81\ \text{m/s}^2 \cdot (1/383.9)\ \text{K} \cdot (383.9 - 371.2)\ \text{K} \cdot 0.130^3\ \text{m}^3}{\frac{14.75 \cdot 10^{-6}\ \text{Pa s}}{7.127\ \text{kg/m}^3}} = 1.670 \cdot 10^8 [-] \tag{6.54}$$

$$Ra = \frac{9.81\ \text{m/s}^2 \cdot (1/383.9\ \text{K}) \cdot (383.9 - 371.2)\ \text{K} \cdot 0.130^3\ \text{m}^3}{\frac{14.75 \cdot 10^{-6}\ \text{Pa s}}{7.127\ \text{kg/m}^3} \cdot \frac{39.25 \cdot 10^{-3}\ \text{W/m K}}{2618\ \text{J/kg K} \cdot 7.127\ \text{kg/m}^3}} = 1.643 \cdot 10^8 [-] \tag{6.55}$$

$$\begin{aligned} \text{Nu}_1 &= 0.68 + \frac{0.670 \cdot (1.643 \cdot 10^8)^{0.25}}{(1 + (0.492/0.984)^{9/16})^{4/9}} \\ &= \frac{h_{v1} \cdot 0.13\ \text{m}}{0.03925\ \text{W/m K}} \rightarrow h_{v1} = 18.41\ \text{W/m}^2\text{K} \end{aligned} \tag{6.56}$$

$$\text{Nu}_2 = 0.15 \cdot (1.643 \cdot 10^8)^{1/3} = \frac{h_{v2} \cdot 0.124\ \text{m}}{0.03925\ \text{W/m K}} \rightarrow h_{v2} = 26.01\ \text{W/m}^2\text{K} \tag{6.57}$$

$$\text{Nu}_3 = 0.52 \cdot (1.643 \cdot 10^8)^{1/5} = \frac{h_{v3} \cdot 0.124\ \text{m}}{0.03925\ \text{W/m K}} \rightarrow h_{v3} = 7.24\ \text{W/m}^2\text{K} \tag{6.58}$$

$$\begin{aligned} \text{Nu}_4/60.96 &= 1 + 0.3(32^{0.5} \cdot (1.670 \cdot 10^8)^{-0.25} \cdot 0.06\ \text{m}/0.0254\ \text{m}) \\ &= \frac{h_{v4} \cdot 0.060\ \text{m}}{0.03925\ \text{W/m K}} \rightarrow h_{v4} = 41.59\ \text{W/m}^2\text{K} \end{aligned} \tag{6.59}$$

$$\text{Nu}_5 = \text{Nu}_1 = \frac{h_{v5} \cdot 0.13m}{0.03925\ \text{W/m K}} \rightarrow h_{v5} = 18.41\ \text{W/m}^2\text{K} \tag{6.60}$$

Therefore, convection heat losses are defined;

$$\dot{Q}_{conv1} = 18.41\ \text{W/m}^2\text{K} \cdot 0.06374\ \text{m}^2 \cdot (110.8°\text{C} - 97.9°\text{C}) = 14.96\ \text{W} \tag{6.61}$$

$$\dot{Q}_{conv2} = 26.01\ \text{W/m}^2\text{K} \cdot 0.01618\ \text{m}^2 \cdot (110.8°\text{C} - 97.9°\text{C}) = 5.36\ \text{W} \tag{6.62}$$

$$\dot{Q}_{conv3} = 7.24\ \text{W/m}^2\text{K} \cdot 0.01618\ \text{m}^2 \cdot (110.8°\text{C} - 97.9°\text{C}) = 1.43\ \text{W} \tag{6.63}$$

$$\dot{Q}_{conv4} = 43.19\ \text{W/m}^2\text{K} \cdot 0.004788\ \text{m}^2 \cdot (110.8°\text{C} - 97.9°\text{C}) = 5.27\ \text{W} \tag{6.64}$$

$$\dot{Q}_{conv5} = 18.41\ \text{W/m}^2\text{K} \cdot 0.039\ \text{m}^2 \cdot (101.8°\text{C} - 97.9°\text{C}) = 3.24\ \text{W} \tag{6.65}$$

finding the total heat transfer by convection;

$$\dot{Q}_{loss,conv} = 14.96\ \text{W} + 5.36\ \text{W} + 1.43\ \text{W} + 5.27\ \text{W} + 3.24\ \text{W} = 27\ \text{W} \tag{6.66}$$

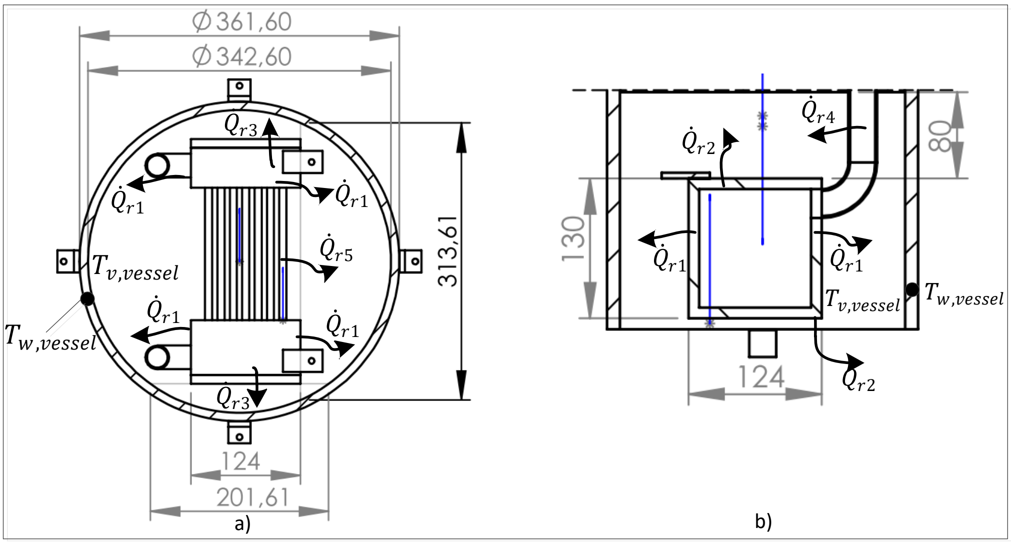

Figure 6.11 – *Heat transfer losses by radiation inside generator a)plan view b)profile view*

6.2.3 Heat losses by radiation

Fig. (6.11) details the heat transfer losses by radiation between the heat transfer area of the generator and vessel. It may be expressed as given in Eq. (6.67); $\dot{Q}_{r1}$ is the heat transfer loss at the vertical face. It is assumed that all the surface has the same distribution temperature at the $T_{w,gen}$ and that the internal wall vessel is at the $T_{w,vessel}$ temperature; σ is the Stefan-Boltzman constant $\sigma = 5.67 \cdot 10^{-8}$ W/m^2 K^4, ϵ_{gen} is the emissivity $\epsilon_{gen} = 0.85$, A_1 is the heat exchanger area $A_1 = 0.1434$ m^2, A_2 is the internal area of the generator $A_2 = 0.66$ m^2.

$$\dot{Q}_{rad} = \sigma \cdot \frac{T^4_{w,gen} - T^4_{w,vessel}}{\frac{1-\epsilon_{gen}}{\epsilon_{gen} \cdot A_1} + \frac{1}{A_1 \cdot Ff_{oil}} + \frac{1-\epsilon_{gen}}{\epsilon_{gen} \cdot A_2}} \tag{6.67}$$

$$\dot{Q}_{rad} = 5.67 \cdot 10^{-8} W/\text{m}^2\text{K}^4 \cdot \frac{(384.0^4 - 371.2^4)\text{K}}{\frac{1-0.85}{0.85 \cdot 0.1434\text{m}^2} + \frac{1}{0.1434\text{m}^2 \cdot 1} + \frac{1-0.85}{0.85 \cdot 0.66\text{m}^2}} \tag{6.68}$$

$$\rightarrow \dot{Q}_{rad} = 18.5 \text{ W} \tag{6.69}$$

6.2.4 Mass transfer calculations - Vapor phase

By the energy balance and isolating z, the condensing flux concentration is computed in Eq. (6.70);

$$\Delta i_{lv} = z \cdot i_{v,\text{NH}_3} + (1-z) \cdot i_{v,\text{H}_2\text{O}} \tag{6.70}$$

$$\tilde{z} = \frac{\Delta i_{lv} - i_{v,\text{H}_2\text{O}}}{i_{v,\text{NH}_3} - i_{v,\text{H}_2\text{O}}} = \frac{(1320 - 2679) \cdot 10^3 \text{ J/kg}}{(1431 - 2679) \cdot 10^3 \text{ J/kg}} \rightarrow z = 1.089 \tag{6.71}$$

so, the total molar flux across the liquid-vapor is shown in Eq. (6.72)

$$\begin{gathered}
\dot{n}_T = \frac{\dot{m}_v}{A_{in} \cdot (\tilde{z} \cdot M_{\mathrm{NH_3}} + (1 - \tilde{z}) \cdot M_{\mathrm{H_2O}})} \\
\dot{n}_T = \frac{0.00040 \ \mathrm{kg/s}}{0.2639 \ \mathrm{m}^2 \cdot (1.089 \cdot 17,031 \ \mathrm{kg/kmol} + (1 - 1.089 \cdot 18,015 \ \mathrm{kg/kmol})} \\
\rightarrow \dot{n}_T = (90.7 \pm 6.1) \cdot 10^{-6} \ \mathrm{kmol/m^2s}
\end{gathered} \tag{6.72}$$

based on Bohra (2007) the heat transfer coefficient for the vapor phase $k_{m,v}$ is given in Eq. (6.73)

$$\begin{gathered}
k_{m,v} = \frac{\dot{n}_T}{C_{T,v} \cdot \left(\ln \frac{\tilde{z} - y_v}{\tilde{z} - y_{int}} \right)} \\
k_{m,v} = \frac{\dot{n}_T}{P_{gen}/8314 \cdot \overline{T}_f \cdot \left(\ln \frac{\tilde{z} - y_v}{\tilde{z} - y_{int}} \right)} \\
k_{m,v} = \frac{90.7 \cdot 10^{-6} \ \mathrm{kmol/m^2s}}{1030000 Pa/8314 J/kMol \cdot K \cdot 375 K \cdot \left(\ln \frac{1.089 - 0.9266}{1.089 - 0.9331} \right)} \\
\rightarrow k_{m,v} = (0.0099 \pm 0.0008) \ \mathrm{m/s}
\end{gathered} \tag{6.73}$$

6.2.5 Mass transfer calculations - Liquid phase

As already previously defined, the mass transfer through the liquid phase may be computed as follows,

$$\begin{gathered}
\dot{m}_v = k_{m,L} \cdot A_{in} \cdot (z \cdot \rho_{int,L} - x_{avg,L} \cdot \rho_{avg,L}) \\
0.00040 kg/s = k_{m,L} \cdot 0.2639 \ \mathrm{m}^2 \cdot \left(1.089 \cdot 820.8 \ \mathrm{kg/m^3} - 0.313 \cdot 820.7 \ \mathrm{kg/m^3} \right) \\
\rightarrow k_{m,L} = (2.41 \pm 0.16) \cdot 10^{-6} \ \mathrm{m/s}
\end{gathered} \tag{6.74}$$

6.3 Discussion

Tab. (6.4) shows the comparison data between the current study and Bohra (2007)'s data. $\dot{Q}$ is the heat rate, U is the overall heat transfer coefficient, h_f is the horizontal liquid film coefficient, $k_{m,v}$ and $k_{m,L}$ is the mass transfer coefficient for the vapor and liquid phase, z is representing the condensing flux concentration. The first set of columns detail the results for the absorber and generator based on the present study. The last column refers to the experimental results of Bohra (2007). The heat rate at the generator is lower than the heat rate of absorption because the solution passes through the heater H-001 before it enters the separation process, adding sensible heat to the solution. In the absorption process, z is inferior to unity, meaning that water fluxes trough condensation going from the interface towards the liquid interface. The low purity degree of ammonia vapor may explain the tiny z value, being $z = 0.8352$ for the absorption process. In contrast, z values higher than unity are found for the generation process as expected.

In the absorber, the heat transfer coefficient on the horizontal liquid film $h_f = 843.4$ W/m^2 °C is low as compared from the conventional falling film tube bundle from Bohra (2007)'s data - above $h_f = 923$ W/m^2 °C. However, the performance seems similar when the overall heat transfer coefficient is analyzed. It may be explained that although the new absorber proposal to be characterized by low heat transfer values, the total area wettability may compensate for the overall heat transfer coefficient. Also, the mass transfer coefficients for both liquid and vapor phases are at the same operational range defined by Bohra (2007). Summarizing, the thermal resistance of the horizontal liquid film thickness is about 90 % of the total thermal resistance, due to the convective heat transfer coefficient for the water coolant is high $h_{101} = 15000$ W/m^2 °C as compared from h_f. Furthermore, the heat rate of the first heat exchanger represents about 40 % of the total heat of absorption.

In the generator, a notorious high heat transfer coefficient is found at the liquid falling film, even overcoming the experimental results from Bohra (2007)'s data. However, the thermal oil convective heat transfer coefficient is extremely inferior as compared from the others, decreasing the overall heat transfer coefficient $U = 225.8$ W/m^2 °C. In opposition to the absorber behavior, the heat transfer coefficient of the falling film represents the lowest thermal resistance between both coefficients. The mass transport has similar performance from the absorption processes.

Table 6.4 – *Comparison data between the current study and Bohra (2007)*

	Current study		*Bohra (2007)*
	Absorber	Generator	Absorber
	Test 1	Test 1	Range
$\dot{Q}$ (W)	2472	2094	3260-10750.
U (W/m^2 °C)	773.8	225.8	753-1853
h_f (W/m^2 °C)	843.4	5662	923-2857
$k_{m,v}$ (m/s)	0.0380	0.0099	0.0025-0.2541
$k_{m,L}$ $\times 10^{-6}$ (m/s)	10.3	2.41	5.51-33.1
z	0.8352	1.089	0.8534

Chapter 7

CONCLUSIONS AND FUTURE WORKS

Although the technical development of such machines has reached an acceptable maturity for industrial purposes, research is still active as more experimental work and theoretical analysis are necessary. In the open-source literature, the existing correlations for designing the absorber show the evolution of each developed research, exposing that the phenomenological aspects of the absorption process applied to refrigeration cycles have not been completely developed, which means that this subject requires more attention. In this thesis, an experimental test rig of the absorption refrigeration cycle was devised, built, and tested for studying the heat and mass transport for both generation and absorption processes. Also, the new absorber configuration for the ammonia-water absorption was studied.

Main heat and mass transfer studies focused on the ammonia-water sorption processes using falling film technology have been completely detailed. Most of the empirical correlations were obtained for low Reynolds numbers (up to 700) and (100 - 520 kPa) operating pressure range. The literature review shows that Chilton and Colburn (1934)'s analogy and Colburn and Drew (1937) definition are usually employed to evaluate the heat or mass transfer coefficients. Next, the absorption refrigeration cycle operation principles have been detailed. Also, the study defined a schematic representation for both the distillation and absorption process over the binary diagram under the macroscopic thermodynamic equilibrium. Also, the theoretical strong solution flow rate circulating in the cycle was defined. Based on the same technical literature, a heat and mass transfer operational range for the absorption refrigeration cycle has been defined. For instance, Nusselt number may vary between 0.001 and 0.2 for the Reynolds numbers ranging from 10 to 250 (with an exception of Bohra (2007)) for NH_3-H_2O ARC in refrigeration/air conditioning applications, in which best heat and mass transfer performance is achieved at the lowest vaporization temperature ($T_{vap} = -20°C$) for all the correlations. Sherwood number may vary from 0.015 to 0.08 for the Reynolds numbers ranged from 10 to 150. Moreover, correlations carried out for evaporation processes did not apply directly to the absorption process, and the heat and mass transfer enhances as the Reynolds number is increased.

Furthermore, the absorption process modeling of a novel modified horizontal liquid film absorption system was developed. It employed a horizontal liquid film configuration using ammonia-water mixtures as the working fluid pair, reaching the total area wettability. The absorption modeling presents pitfalls over the liquid film thickness; i) both transport processes are quite dependent on the liquid film thickness. However, this parameter is a new unknown variable, and its definition is not only concerned with geometrical aspects, ii) the irregular plates formed by using spiral tubes deepen the problem of the liquid film thickness in which there are regions with different depths or local film thickness at the middle of tubes. It is expected because the study aim was focused on evaluating the experimental behavior of the new absorber configuration. Similar attempts occur in falling film technology, in which most of the researches adopt the Nusselt liquid film definition, underestimating the heat transfer coefficient. Despite those new challenges, the model predicts high absorption rates occurring at the first plate as the consequence of high driving forces (temperature and concentration). Also, the thermal model shows the heat of rejection decreased as a function of the vertical position into the absorber, whose first plate absorbed about 30 % of the total heat rate. Moreover, the absorber heat rate is improved by using the lowest surface temperature and lowest liquid film thickness as expected.

An apparatus to study the cycle and its main components are projected, built and tested, in which the ARC may attain a different range of parameters such as various absorption pressure or vaporization temperature, ammonia-water concentration, strong mass flow rate solution, strong solution temperature at the generator, co-current/contra-current absorption processes and various inlet weak solution temperature at the absorber. In that vein, a new proposal of the ammonia-water absorber is completely developed, beginning since the project, proposing a low-cost spiral heat exchanger, and mounting it as an absorber. It improved the wettability problems as compared with the conventional falling film technology. Moreover, it may be applied in the generation process taking advantage of the flooded evaporators due to the first does not change the boiling temperature as the consequence of the hydrostatic pressure of the liquid column.

Based on the first experimental results, the following highlights are described:

1. In the absorber, the heat transfer coefficient on the horizontal liquid film $h_f = 843.4$ W/m^2 °C is slightly low in comparison the conventional falling film tube bundle from Bohra (2007)'s data - above $h_f = 923$ W/m^2 °C. However, the performance seems similar when the overall heat transfer coefficient is analyzed. It may be explained that although the new absorber proposal to be characterized by a lower heat transfer values, the total area wettability may compensate for the overall heat transfer coefficient. Also, the mass transfer coefficients for both liquid and vapor phases are at the same operational range defined by Bohra (2007). Summarizing, the thermal resistance of the horizontal liquid film thickness is about 90 % of the total thermal resistance, due to the convective heat transfer coefficient for the water coolant is high $h_{101} = 15000$ W/m^2 °C as compared from h_f. Furthermore, the heat rate of the first heat exchanger represents about 40 % of the total heat of absorption.

2. In the generator, a notorious high heat transfer coefficient is found at the liquid falling film, even overcoming the experimental results from Bohra (2007)'s data. However, the thermal oil convective heat transfer coefficient is much lower when compared to the others, decreasing the overall heat transfer coefficient $U = 225.8$ W/m^2 °C. In opposition to the absorber behavior, the heat transfer coefficient of the falling film represents the lowest thermal resistance between both coefficients. The mass transport has a similar performance from the absorption processes.

Suggestions for future works:

More sets of tests should be carried out, evaluating a broader operating range of the ARC. The parametric analysis will allow fitting experimental correlations for the absorption process in which the heat and mass transfer behavior will be analyzed. Add more tests over a big data range to order to led a fitting $\mathrm{Nu} = a\mathrm{Re}^b\mathrm{Pr}^c$ and $Sh = e\mathrm{Re}^f\mathrm{Sc}^g$, specifically for low Reynolds number because the advantageous from the horizontal liquid film may be higher than falling film due to the dry out generation zones are dominants in this operating range.

The absorber assembly was complex as the consequence of an independent connection between the heat exchanger plate circuit. The absorber project should be improved by using a new version in which the tubes will be connected in a plenum. Also, rectangular channels forming a plate may be tested, in which the horizontal film will be formed over it. So, the new configuration should improve the assembly and the parallelism between these, enhancing the heat transfer area. Also, future works must study an alternative working fluid to improve the thermal oil convective heat transfer coefficient such as heat pipes driven by solar energy.

The cycle itself also should be studied, evaluating the COP as a function of these operational parameters. Also, individual components as the falling film evaporator should be studied. Moreover, the literature review suggests enhancing the automation to increase the COP, for instance, thermal energy supplied to the generator and expansion valve should be controlled as a function of the thermal load at the vaporization process. So, futures works might be carried out such as to evaluate the COP of ARC as a function of partial and full load.

REFERENCES

Abed, A. M.; Alghoul, M.; Yazdi, M. H.; Al-Shamani, A. N.; Sopian, K. The role of enhancement techniques on heat and mass transfer characteristics of shell and tube spray evaporator: a detailed review. *Applied Thermal Engineering*, v. 75, p. 923–940, jan 2015. ISSN 13594311.

Abed, A. M.; Sopian, K.; Alghoul, M.; Majadi, H. S.; Al-Shamani, A. N. Experimental evaluation of single stage ejector-absorption cooling cycle under different design configurations. *Solar Energy*, Elsevier, v. 155, p. 130–141, 2017.

Ackermann, G.; Gnam, E. *Wärmeübergang und molekulare Stoffübertragung im gleichen Feld bei großen Temperatur-und Partialdruckdifferenzen; Tropfenkondensation von Wasserdampf.* [S.l.]: VDI-Verlag, 1937.

Alhusseini, A. A.; Tuzla, K.; Chen, J. C. Falling film evaporation of single component liquids. *Int. J. Heat Mass Transfer*, Elsevier, v. 41, n. 12, p. 1623–1632, 1998.

Alobaid, M.; Hughes, B.; Calautit, J. K.; O'Connor, D.; Heyes, A. A review of solar driven absorption cooling with photovoltaic thermal systems. *Renewable and sustainable energy reviews*, Elsevier, v. 76, p. 728–742, 2017.

Altamirano, A.; Pierres, N. L.; Stutz, B. Review of small-capacity single-stage continuous absorption systems operating on binary working fluids for cooling: Theoretical, experimental and commercial cycles. *International Journal of Refrigeration*, Elsevier, 2019.

Babadi, F.; Farhanieh, B. Characteristics of heat and mass transfer in vapor absorption of falling film flow on a horizontal tube. *Int. Commun. Heat Mass*, v. 32, n. 9, p. 1253–1265, 2005. ISSN 07351933.

Banasiak, K.; Kozioł, J. Mathematical modelling of a LiBr–H2O absorption chiller including two-dimensional distributions of temperature and concentration fields for heat and mass exchangers. *Int. J. Thermal Sciences*, v. 48, n. 9, p. 1755–1764, sep 2009. ISSN 12900729.

Baranov, A.; Churagulov, B.; Kalina, A.; Sharikov, F. Y.; Zharov, A.; Yoroslavtsev, A. The investigation of ammonia-water gas and liquid mixture properties. In: *Report on the Workshop on Thermophysical Properties of Ammonia/Water mixtures. NISTIR.* [S.l.: s.n.], 1997. v. 5059, p. 59–67.

Bird, R. B. Transport phenomena. *Appl. Mech. Rev.*, v. 55, n. 1, p. R1–R4, 2002.

Bohra, L. K. *Analysis of binary fluid heat and mass transfer in ammonia-water absorption.* Tese (Doutorado) — Georgia Institute of Technology, 2007.

Bohra, L. K.; Lee, S.; Garimella, S. Heat and mass transfer models for horizontal-tube falling-film ammonia-water absorption. *International Journal of Refrigeration*, Elsevier, v. 107, p. 84–97, 2019.

Boman, D. B.; Hoysall, D. C.; Staedter, M. A.; Goyal, A.; Ponkala, M. J.; Garimella, S. A method for comparison of absorption heat pump working pairs. *International Journal of Refrigeration*, Elsevier, v. 77, p. 149–175, 2017.

Braune, B. Hirntumoren beim säugling. *Arch. Kinderheilk*, v. 112, p. 193–202, 1937.

Carnot, S. Réflexions sur la puissance motrice du feu et sur les machines propresa développer cette puissance. bachelier, paris, 1824. *French, Bachelier, Paris*, 1824.

Castro, J.; Oliet, C.; Rodríguez, I.; Oliva, A. Comparison of the performance of falling film and bubble absorbers for air-cooled absorption systems. *Int. J. Thermal Sciences*, v. 48, n. 7, p. 1355–1366, jul. 2009. ISSN 12900729.

Cebeci, T. Laminar-free-convective-heat transfer from the outer surface of a vertical slender circular cylinder. In: Begel House Inc. *International Heat Transfer Conference Digital Library*. [S.l.], 1974.

Cengel, Y. *Heat and mass transfer: fundamentals and applications*. [S.l.]: McGraw-Hill Higher Education, 2014.

Cengel, Y. A.; Boles, M. A. *Thermodynamics: an engineering approach, 8th edittion pp. 502-505*. [S.l.]: New York: McGraw-Hill Education, 2015.

Cerezo, J.; Bourouis, M.; Vallès, M.; Coronas, A.; Best, R. Experimental study of an ammonia–water bubble absorber using a plate heat exchanger for absorption refrigeration machines. *Appl. Thermal Eng.*, v. 29, n. 5-6, p. 1005–1011, abr. 2009. ISSN 13594311.

Cerro, R. L.; Whitaker, S. Entrance region flows with a free surface: the falling liquid film. *Chemical Engineering Science*, v. 26, n. 6, p. 785–798, 1971. ISSN 00092509.

Cheng, C.-M. Absorption refrigeration system. 1966.

Chien, L.-H.; Tsai, Y.-L. An experimental study of pool boiling and falling film vaporization on horizontal tubes in R-245fa. *Appl. Thermal Eng.*, Elsevier, v. 31, n. 17, p. 4044–4054, 2011.

Chilton, T. H.; Colburn, A. P. Mass transfer (absorption) coefficients prediction from data on heat transfer and fluid friction. *Industrial & Eng. Chemistry*, ACS Publications, v. 26, n. 11, p. 1183–1187, 1934.

Chun, K.; Seban, R. Heat transfer to evaporating liquid films. *J. Heat Transfer*, American Society of Mechanical Engineers, v. 93, n. 4, p. 391–396, 1971.

Chun, K. R.; Seban, R. Performance prediction of falling-film evaporators. *J. Heat Transfer*, American Society of Mechanical Engineers, v. 94, n. 4, p. 432–436, 1972.

Churchill, S. W.; Chu, H. H. Correlating equations for laminar and turbulent free convection from a horizontal cylinder. *International journal of heat and mass transfer*, Elsevier, v. 18, n. 9, p. 1049–1053, 1975.

Churchill, S. W.; Ozoe, H. Correlations for laminar forced convection with uniform heating in flow over a plate and in developing and fully developed flow in a tube. *Journal of Heat Transfer*, American Society of Mechanical Engineers, v. 95, n. 1, p. 78–84, 1973.

Colburn, A. P.; Drew, T. B. *The condensation of mixed vapors*. [S.l.]: American Institute of Chemical Engineers, 1937.

Conde, M. Thermo-physical properties of {NH3+H2O} mixtures for industrial design of absorption refrigeration equipment. *M. Conde Eng., Zurich*, p. 12–15, 2006.

Daguenet-Frick, X.; Gantenbein, P.; Müller, J.; Fumey, B.; Weber, R. Seasonal thermochemical energy storage: Comparison of the experimental results with the modelling of the falling film tube bundle heat and mass exchanger unit. *Renewable Energy*, Elsevier, v. 110, p. 162–173, 2017.

Day, J. C.; Zemler, M. K.; Traum, M. J.; Boetcher, S. K. Laminar natural convection from isothermal vertical cylinders: Revisting a classical subject. *Journal of heat transfer*, American Society of Mechanical Engineers Digital Collection, v. 135, n. 2, 2013.

DiGuilio, R.; Lee, R.; Jeter, S.; Teja, A. Properties of lithium bromide–water solutions at high temperatures and concentrations–i. thermal conductivity. *ASHRAE Trans*, v. 96, n. 1, p. 702–708, 1990.

Dittus, F. W. Heat transfer in automobile radiators of the tubler type. *Univ. Calif. Pubs. Eng.*, v. 2, p. 443, 1930.

Dorokhov, A.; Bochagov, V. Heat transfer to a film falling over horizontal cylinders. *Heat transfer. Soviet research*, Scripta, v. 15, n. 2, p. 96–101, 1983.

Du, S.; Wang, R. Modeling and numerical analysis of an s pattern small diameter tube bundle ammonia water falling film absorber. In: Begel House Inc. *International Heat Transfer Conference Digital Library*. [S.l.], 2018.

Elvas, M. C.; Peres, I. M.; Carvalho, S. Making science cooler: Carré's apparatus. In: Societat Catalana d'Història de la Ciència i de la Tècnica. *The Circulation of Science and Technology: Proceedings of the 4th International Conference of the European Society for the History of Science. Barcelona, 18-20 November 2010*. [S.l.], 2012. p. 441–449.

Elvas, M. C.; Perez, M. I.; Carvalho, S. Making science cooler: Carré's apparatus. In: *Int. Conference of ESHS*. [S.l.: s.n.], 2010. p. 441–449.

Fernández-Seara, J.; Sieres, J.; Rodríguez, C.; Vázquez, M. Ammonia–water absorption in vertical tubular absorbers. *International journal of thermal Sciences*, Elsevier, v. 44, n. 3, p. 277–288, 2005.

Ferreira, C.; Keizer, C.; Machielsen, C. Heat and mass transfer in vertical tubular bubble absorbers for ammonia-water absorption refrigeration systems. *Int. J. Refrigeration*, v. 7, n. 6, p. 348–357, 1984. ISSN 01407007.

Florides, G.; Kalogirou, S.; Tassou, S.; Wrobel, L. Design and construction of a libr–water absorption machine. *Energy Conversion and Management*, Elsevier, v. 44, n. 15, p. 2483–2508, 2003.

Fujita, I.; Hihara, E. Heat and mass transfer coefficients of falling-film absorption process. *Int. J. Heat Mass Transfer*, v. 48, n. 13, p. 2779 – 2786, 2005. ISSN 0017-9310.

Fujita, T. Falling liquid films in absorption machines. *Int. J. Refrigeration*, v. 16, n. 4, p. 282–294, jan. 1993. ISSN 01407007.

Fujita, Y.; Tsutsui, M. Experimental investigation of falling film evaporation on horizontal tubes. *Heat Transfer-Japanese Research*, Wiley Online Library, v. 27, n. 8, p. 609–618, 1998.

Gierow, M.; Jernqvist, A. Measurement of mass diffusivity with holographic interferometry for H2O-NaOH and H2O-LiBr working pairs. In: *Proceedings of the Int. Heat Pump Conference, AES*. [S.l.: s.n.], 1993. v. 31, p. 525–532.

Gnielinski, V. New equations for heat and mass transfer in turbulent pipe and channel flow. *Int. Chem. Eng.*, v. 16, n. 2, p. 359–368, 1976.

Goel, N.; Goswami, D. Y. Analysis of a counter-current vapor flow absorber. *Int. J. Heat and Mass Transfer*, v. 48, n. 7, p. 1283–1292, 2005. ISSN 00179310.

Goel, N.; Goswami, D. Y. A compact falling film absorber. *J. of Heat Transfer*, American Society of Mechanical Engineers, v. 127, n. 9, p. 957–965, 2005.

Goyal, A.; Rattner, A. S.; Garimella, S. Model-based feedback control of an ammonia-water absorption chiller. *Science and Technology for the Built Environment*, Taylor & Francis, v. 21, n. 3, p. 357–364, 2015.

Han, W.; Chen, Q.; Sun, L.; Ma, S.; Zhao, T.; Zheng, D.; Jin, H. Experimental studies on a combined refrigeration/power generation system activated by low-grade heat. *Energy*, Elsevier, v. 74, p. 59–66, 2014.

Herold, K.; Radermacher, R.; Klein, S. Absorption chillers and heat pumps book 329 pages. *CRS Press LLC*, 2000.

Herold, K. E.; Radermacher, R.; Klein, S. A. *Absorption chillers and heat pumps.* [S.l.]: CRC press, 2016.

Hewitt, G. F.; Shires, G. L.; Bott, T. R. *Process heat transfer.* [S.l.]: CRC press Boca Raton, FL, 1994. v. 113.

Hoffmann, L.; Greiter, I.; Wagner, A.; Weiss, V.; Alefeld, G. Experimental investigation of heat transfer in a horizontal tube falling film absorber with aqueous solutions of libr with and without surfactants. *Int. J. Refrigeration*, Elsevier, v. 19, n. 5, p. 331–341, 1996.

Holman, J. P. J. P. Book; Book/Illustrated. *Experimental methods for engineers.* 6th ed. ed. New York : McGraw-Hill, 1993. Previous ed.: J.P. Holman, in collaboration with W.J. Gajda, Jr. 1989. ISBN 0070296669 (solutions man.). Disponível em: <http://www.loc.gov/catdir/enhancements/fy0602/93023893-t.html>.

Hu, X.; Jacobi, A. The intertube falling film: Part 1—flow characteristics, mode transitions, and hysteresis. *J. Heat Transfer*, American Society of Mechanical Engineers, v. 118, n. 3, p. 616–625, 1996.

Hu, X.; Jacobi, A. The intertube falling film: Part 2—mode effects on sensible heat transfer to a falling liquid film. *J. Heat Transfer*, American Society of Mechanical Engineers, v. 118, n. 3, p. 626–633, 1996.

Ibrahim, O. Thermodynamic properties of ammonia-water mixtures. In: *ASHRAE Transactions: Symposia.* [S.l.: s.n.], 1993. v. 93, p. 1495.

Incropera, F. P.; Lavine, A. S.; Bergman, T. L.; DeWitt, D. P. *Fundamentals of heat and mass transfer.* [S.l.]: Wiley, 2007.

Islam, M. R.; Wijeysundera, N.; Ho, J. Evaluation of heat and mass transfer coefficients for falling-films on tubular absorbers. *Int. J. Refrigeration*, Elsevier, v. 26, n. 2, p. 197–204, 2003.

Jani, S. Simulation of Heat and Mass Transfer Process in Falling Film Single Tube Absorption Generator. *Int. J. of Science and Eng. Investigations*, v. 1, n. 3, p. 79–84, 2012.

Jani, S.; Saidi, M. H.; Heydari, A.; Mozaffari, A. A. Second law based optimization of falling film single tube absorption generator. In: American Society of Mechanical Engineers. *ASME 2002 Int. Mechanical Eng. Congress and Exposition.* [S.l.], 2002. p. 49–54.

Jani, S.; Saidi, M. H.; Mozaffari, a. a. Tube bundle heat and mass transfer characteristics in falling film absorption generators. *Int. Commun. Heat Mass*, v. 30, n. 4, p. 565–576, 2003. ISSN 07351933.

Jennings, B. New investigations in absorption refrigeration. *Journal of the ASRE*, v. 30, p. 87 – 93, 1935.

Jeong, S.; Lee, S. K.; Koo, K.-K.; Ziegler, F. et al. Heat transfer performance of a coiled tube absorber with working fluid of ammonia/water/discussion. *ASHRAE Transactions*, American Society of Heating, Refrigeration and Air Conditioning Engineers, Inc., v. 104, p. 1577, 1998.

Jiang, W.; Li, S.; Yang, L.; Du, K. Experimental investigation on performance of ammonia absorption refrigeration system with tio2 nanofluid. *International Journal of Refrigeration*, Elsevier, v. 98, p. 80–88, 2019.

Jones, J. C. R. L. Recent developments in large ammonia absorption systems. *Journal of the ASRE*, p. 25 – 31, 1942.

Kandlikar, S. G. *Handbook of phase change: boiling and condensation.* [S.l.]: CRC Press, 1999.

Kang, Y. T.; Akisawa, A.; Kashiwagi, T. Experimental correlation of combined heat and mass transfer for NH3-H2O falling film absorption. *Int. J. Refrigeration*, v. 22, p. 250–262, 1999.

Kang, Y. T.; Kim, J.; Jeong, J.; Park, C.; Akisawa, A.; Kashiwagi, T. Mass transfer enhancement of a binary nanofluid for absorption application. In: Begel House Inc. *International Heat Transfer Conference 13.* [S.l.], 2006.

Kanitz, A. Ueber die innere reibung von salzlösungen und ihren gemischen. *Zeitschrift für physikalische Chemie*, De Gruyter Oldenbourg, v. 22, n. 1, p. 336–357, 1897.

Karami, S.; Farhanieh, B. A numerical study on the absorption of water vapor into a film of aqueous LiBr falling along a vertical plate. *Heat and Mass Transfer/Waerme- und Stoffuebertragung*, v. 46, n. 2, p. 197–207, 2009. ISSN 09477411.

Karami, S.; Farhanieh, B. Numerical modeling of incline plate LiBr absorber. *Heat and Mass Transfer/Waerme- und Stoffuebertragung*, v. 47, n. 3, p. 259–267, 2011. ISSN 09477411.

Keinath, C. M.; Nagavarapu, A. K.; Delahanty, J. C.; Garimella, S.; Garrabrant, M. A. Experimental assessment of alternative compact configurations for ammonia-water desorption. *Applied Thermal Engineering*, Elsevier, v. 161, p. 113852, 2019.

Kessler, D. P.; Greenkorn, R. A. *Momentum, heat, and mass transfer fundamentals.* [S.l.: s.n.], 1999.

Killion, J. D.; Garimella, S. A critical review of models of coupled heat and mass transfer in falling-film absorption. *Int. J. Refrigeration*, Elsevier, v. 24, n. 8, p. 755–797, 2001.

Kim, D.; Ferreira, C. I. A gibbs energy equation for libr aqueous solutions. *Int. J. Refrigeration*, Elsevier, v. 29, n. 1, p. 36–46, 2006.

Kim, D.; Kim, M. H. Heat transfer enhancement characteristics for falling-film evaporation on horizontal enhanced tubes with aqueous libr solution. *J. Enhanced Heat Transfer*, Begel House Inc., v. 6, n. 1, p. 61–69, 1999.

Kim, D. S.; Infante Ferreira, C. a. Flow patterns and heat and mass transfer coefficients of low Reynolds number falling film flows on vertical plates: Effects of a wire screen and an additive. *Int. J. Refrigeration*, Elsevier Ltd and IIR, v. 32, n. 1, p. 138–149, 2008. ISSN 01407007.

Kim, K.; Berman, N.; Chau, D.; Wood, B. Absorption of water vapour into falling films of aqueous lithium bromide. *Int. J. Refrigeration*, Elsevier, v. 18, n. 7, p. 486–494, 1995.

Kim, K.-S.; Lee, J.-W.; Kim, J.-S.; Lee, H. Heat capacity measurement and cycle simulation of the trifluoroethanol (tfe)+ quinoline mixture as a new organic working fluid used in absorption heat pump. *Korean Journal of Chemical Engineering*, Springer, v. 20, n. 4, p. 762–767, 2003.

Kim, S.; Kim, Y. J.; Joshi, Y. K.; Fedorov, A. G.; Kohl, P. A. Absorption heat pump/refrigeration system utilizing ionic liquid and hydrofluorocarbon refrigerants. *Journal of Electronic Packaging*, American Society of Mechanical Engineers Digital Collection, v. 134, n. 3, 2012.

Kim, S.-C.; Yun, J.-H.; Oh, M.-D.; Lee, J.-H. Heat and mass transfer in a shell-coil type absorber of ammonia absorption heat pump. In: Begel House Inc. *International Heat Transfer Conference Digital Library*. [S.l.], 1998.

Kim, Y. J.; Kim, S.; Joshi, Y. K.; Fedorov, A. G.; Kohl, P. A. Thermodynamic analysis of an absorption refrigeration system with ionic-liquid/refrigerant mixture as a working fluid. *Energy*, Elsevier, v. 44, n. 1, p. 1005–1016, 2012.

Klein, S. *Engineering Equation Solver (EES) V9, F-chart software, Madison, USA*. 2015.

Klein, S. A.; Alvarado, F. Engineering equation solver. *F-Chart Software, Madison, WI*, v. 1, 2002.

Kühn, R.; Meyer, T.; Ziegler, F. Experimental investigation of ionic liquids as substitute for lithium bromide in water absorption chillers. *Energy*, Elsevier, p. 117990, 2020.

Kwon, K.; Jeong, S. Effect of vapor flow on the falling-film heat and mass transfer of the ammonia/water absorber. *Int. J. Refrigeration*, v. 27, n. 8, p. 955–964, 2004. ISSN 01407007.

Lee, K. B.; Chun, B. H.; Lee, J. C.; Hyun, J. C.; Kim, S. H. Comparison of heat and mass transfer in falling film and bubble absorbers of ammonia water. n. September 2001, p. 191–205, 2002.

Lee, K. B.; Chun, B. H.; Lee, J. C.; Lee, C. H.; Kim, S. H. Experimental analysis of bubble mode in a plate-type absorber. *Chem. Eng. Sci.*, v. 57, n. 11, p. 1923–1929, 2002. ISSN 00092509.

Lee, S. *Development of techniques for in-situ measurement of heat and mass transfer in ammonia-water absorption systems.* Tese (Doutorado) — Georgia Institute of Technology, 2007.

Lee, S.; Bohra, L. K.; Garimella, S.; Nagavarapu, A. K. Measurement of absorption rates in horizontal-tube falling-film ammonia-water absorbers. *Int. J. Refrigeration*, v. 35, n. 3, p. 613–632, 2012. ISSN 01407007.

Lees, C. H. On the thermal conductivities of single and mixed solids and liquids and their variation with temperature. *Philosophical Transactions of the Royal Society of London. Series A, Containing Papers of a Mathematical or Physical Character*, JSTOR, v. 191, p. 399–440, 1898.

Leite, B. *Modelagem do absorvedor e do gerador de ciclos de refrigeração por absorção de calor com o par NH3-H2O baseados na tecnologia de filme descendente sobre placas inclinadas, (In Portuguese)*. 163p p. — University of Sao Paulo, 2015.

Lienhard, J. H. *A heat transfer textbook*. [S.l.]: Courier Dover Publications, 2019.

Liu, Z.-H.; Zhu, Q.-Z.; Chen, Y.-M. Evaporation heat transfer of falling water film on a horizontal tube bundle. *Heat Transfer-Asian Research*, Wiley Online Library, v. 31, n. 1, p. 42–55, 2002.

McNeely LA. Thermodynamic properties of aqueous solutions of lithium bromide. *ASHRAE*, v. 85, p. 413–434, 1979.

Meacham, J.; Garimella, S. Experimental demonstration of a prototype microchannel absorber for space-conditioning systems. In: *Int. Sorption Heat Pump Conference, Shanghai, China.* [S.l.: s.n.], 2002. p. 270–276.

Meacham, J. M.; Garimella, S. Ammonia-water absorption heat and mass transfer in microchannel absorbers with visual confirmation. *ASHRAE Transactions*, v. 110, n. 1, 2004.

Meacham, J. M.; Garimella, S. Ammonia-water absorption heat and mass transfer in microchannel absorbers with visual confirmation. *ASHRAE Transactions*, v. 110, n. 1, 2004.

Medrano, M.; Bourouis, M.; Coronas, A. Absorption of water vapour in the falling film of water–lithium bromide inside a vertical tube at air-cooling thermal conditions. *Int. J. Thermal Sciences*, Elsevier, v. 41, n. 9, p. 891–898, 2002.

Mitrovic, J. Influence of tube spacing and flow rate on heat transfer from a horizontal tube to a falling liquid film. In: *Proceedings of the 8th Int. Heat Transfer Conference.* [S.l.: s.n.], 1986. v. 4, p. 1949–1956.

Nagaoka, Y.; Nishiyama, N.; Ajisaka, K.; Nakamura, M.; Inoue, N.; Yabase, H.; Hihara, E.; Saito, T. *Absorber of absorption refrigerating machine (enhancement of heat and mass transfer in falling film absorbers by surface configuration).(73).* [S.l.]: na, 1987.

Nagavarapu, A. K.; Garimella, S. Design of microscale heat and mass exchangers for absorption space conditioning applications. *Journal of Thermal Science and Engineering Applications*, American Society of Mechanical Engineers Digital Collection, v. 3, n. 2, 2011.

Nakoryakov, V. E.; Grigoryeva, N. I.; Bartashevich, M. V. Heat and mass transfer in the entrance region of the falling film: Absorption, desorption, condensation and evaporation. *Int. J. Heat and Mass Transfer*, v. 54, n. 21-22, p. 4485–4490, 2011. ISSN 00179310.

Narváez-Romo, B.; Simões-Moreira, J. R. Falling Film Evaporation: an Overview. In: *Proceeding of 22nd Int. Congress of Mechanical Eng. (COBEM), Riberão Preto.* [S.l.: s.n.], 2013. p. 1–7.

Narváez-Romo, B.; Simões-Moreira, J. R. Falling film evaporation: a qualitative analysis of the distribuition system. In: *Proceeding of the Brazilian Congress of Thermal Sciences and Eng. (ENCIT), Belém.* [S.l.: s.n.], 2014.

Narváez-Romo, B.; Simões-Moreira, J. R. Falling Liquid Film Evaporation in Subcooled and Saturated Water over Horizontal Heated Tubes. *Heat Transfer Eng.*, v. 38, p. 361–376, 2017.

Narváez-Romo, B.; Simões-Moreira, J. R. Numerical study of heat and mass transfer absorption processes using a horizontal flooded-liquid film in ammonia-water mixtures. In: *Proceeding of the 25th Int. Congress of Refrigeration (ICR), Montreal.* [S.l.: s.n.], 2019.

Narváez-Romo, B.; Chhay, M.; Zavaleta-Aguilar, E. W.; Simões-Moreira, J. R. A critical review of heat and mass transfer correlations for libr-h2o and nh3-h2o absorption refrigeration machines using falling liquid film technology. *Applied Thermal Engineering*, v. 123, p. 1079 – 1095, 2017. ISSN 1359-4311.

Narváez-Romo, B.; Leite, B. M.; Simões-Moreira, J. R. Ammonia-water absorption process on falling films at vertical and inclined plates. *Heat Transfer Research*, v. 51, n. 4, p. 297–318, 2020. ISSN 1064-2285.

Neuforn, M. R. S. von. *Kompressionswärmepumpe mit Lösungskreislauf.* Tese (Doutorado), 1986.

Nosoko, T.; Miyara, a.; Nagata, T. Characteristics of falling film flow on completely wetted horizontal tubes and the associated gas absorption. *Int. J. Heat Mass Transfer*, v. 45, n. 13, p. 2729–2738, 2002. ISSN 00179310.

Nusselt, W. Die oberflachenkondesation des wasserdamffes the surface condensation of water. *Zetrschr. Ver. Deutch. Ing.*, v. 60, p. 541–546, 1916.

Owens, W. *Correlation of thin film evaporation heat transfer coefficients for horizontal tubes.* [S.l.: s.n.], 1978.

Parken, W.; Fletcher, L.; Sernas, V.; Han, J. Heat transfer through falling film evaporation and boiling on horizontal tubes. *J. Heat Transfer*, American Society of Mechanical Engineers, v. 112, n. 3, p. 744–750, 1990.

Patnaik, V.; Perez-blanco, H. A Study of Absorption Enhancement by Wavy Film Flows. *Int. J. Heat Fluid Flow*, v. 17, n. 1996, p. 71–77, 1996.

Peng, X.; Wang, B.; Peterson, G.; Ma, H. Experimental investigation of heat transfer in flat plates with rectangular microchannels. *Int. J. Heat and Mass Transfer*, Elsevier, v. 38, n. 1, p. 127–137, 1995.

Prost, J. S.; González, M. T.; Urbicain, M. J. Determination and correlation of heat transfer coefficients in a falling film evaporator. *J. of Food Eng.*, v. 73, n. 4, p. 320–326, 2006. ISSN 02608774.

Ribatski, G.; Jacobi, A. M. Falling-film evaporation on horizontal tubes - A critical review. *Int. J. Refrigeration*, v. 28, n. 5, p. 635–653, 2005. ISSN 01407007.

Saxena, S.; Mason, E. Higher approximations for the transport properties of binary gas mixtures. iii. isotopic thermal diffusion. *The Journal of Chemical Physics*, AIP, v. 28, n. 4, p. 623–625, 1958.

Shahzada, M. W.; Ng, K. C.; Thu, K.; Myat, A.; Gee, C. W. An improved film evaporation correlation for saline water at sub-atmospheric pressures. In: *AIP Conference Proceedings.* [S.l.: s.n.], 2011.

Shi, C.; Chen, Q.; Jen, T.-C.; Yang, W. Heat transfer performance of lithium bromide solution in falling film generator. *Int. J. Heat Mass Transfer*, Elsevier Ltd, v. 53, n. 15-16, p. 3372–3376, 2010. ISSN 00179310.

Shi, C.; Xu, C.; Hu, H.; Ying, Y. Study on falling film generation heat transfer of lithium bromide solution in vertical tubes. *J. of Thermal Science*, v. 18, n. 3, p. 241–245, 2009. ISSN 10032169.

Sieres, J.; Fernández-Seara, J. Modeling of simultaneous heat and mass transfer processes in ammonia–water absorption systems from general correlations. *Heat and mass transfer*, Springer, v. 44, n. 1, p. 113–123, 2007.

Sofrata, H. Carnot and lorenz cycles for dual absorption system. *Wärme-Und Stoffübertragung*, Springer, v. 28, n. 3, p. 107–116, 1993.

Srikhirin, P.; Aphornratana, S.; Chungpaibulpatana, S. A review of absorption refrigeration technologies. *Renewable and sustainable energy reviews*, Elsevier, v. 5, n. 4, p. 343–372, 2001.

Staedter, M. A.; Garimella, S. Experimental investigation of a compact thermal compressor for an ammonia-water absorption heat pump. *Applied Thermal Engineering*, Elsevier, v. 143, p. 550–560, 2018.

Staedter, M. A.; Garimella, S. Heat and mass transfer in microscale diabatic distillation columns for ammonia–water desorption and rectification. *International Journal of Refrigeration*, Elsevier, v. 95, p. 10–20, 2018.

Takamatsu, H.; Yamashiro, H.; Takata, N.; Honda, H. Vapor absorption by LiBr aqueous solution in vertical smooth tubes. *Int. J. Refrigeration*, v. 26, n. 6, p. 659–666, 2003. ISSN 01407007.

Taylor, B. N.; Kuyatt, C. E. Guidelines for evaluating and expressing the uncertainty of nist measurement results. US Department of Commerce, Technology Administration, National Institute of . . . , 1994.

Taylor, R.; Krishna, R. *Multicomponent mass transfer*. [S.l.]: John Wiley & Sons, 1993. v. 2.

Thome, J. R. Falling film evaporation: state-of-the-art review of recent work. *J. Enhanced Heat Transfer*, GORDON & BREACH PUBLISHERS, v. 6, p. 263–278, 1999.

Thorin, E. Thermophysical properties of ammonia–water mixtures for prediction of heat transfer areas in power cycles. *International journal of thermophysics*, Springer, v. 22, n. 1, p. 201–214, 2001.

Tomforde, C.; Luke, A. Experimental Investigations on Falling-Film Absorbers with Horizontal Tubes – a Review. *Int. Refrigeration and Air Conditioning Conference at Purdue*, p. 1–10, 2012.

Treybal, R. *Mass-transfer operations*. [S.l.]: McGraw-Hill Book Company, 1981.

Triché, D.; Bonnot, S.; Perier-Muzet, M.; Boudéhenn, F.; Demasles, H.; Caney, N. Experimental and numerical study of a falling film absorber in an ammonia-water absorption chiller. *Int. J. Heat and Mass Transfer*, v. 111, p. 374 – 385, 2017. ISSN 0017-9310.

Wang, M.; Ferreira, C. A. I. Absorption heat pump cycles with nh3–ionic liquid working pairs. *Applied energy*, Elsevier, v. 204, p. 819–830, 2017.

Wassiljewa, A. Heat conduction in gaseous mixtures. *Phys. Z*, v. 5, n. 22, p. 737–742, 1904.

Wilke, C. A viscosity equation for gas mixtures. *The journal of chemical physics*, AIP, v. 18, n. 4, p. 517–519, 1950.

Wilke, C.; Chang, P. Correlation of diffusion coefficients in dilute solutions. *AIChE Journal*, Wiley Online Library, v. 1, n. 2, p. 264–270, 1955.

Wilke, W. (heat transfer to falling liquid films) warmeubertragung an rieselfilme. *VDI-Forschungsheft*, v. 490, p. 36, 1962.

Yi, Y.; Hu, T.; Xie, X.; Jiang, Y. Experimental assessment of a detachable plate falling film heat and mass exchanger couple using lithium bromide and water as working fluids. *International Journal of Refrigeration*, Elsevier, v. 113, p. 219–227, 2020.

Yih, S.-M.; Chen, K.-Y. Gas absorption into wavy and turbulent falling liquid films in a wetted-wall column. *Chem. Eng. Comm.*, Taylor & Francis, v. 17, n. 1-6, p. 123–136, 1982.

Yüksel, M.; Schlünder, E. Heat and mass transfer in non-isothermal absorption of gases in falling liquid films. *Chem. Eng. Process. Process Intensification*, v. 22, n. 4, p. 193–202, dec 1987. ISSN 02552701.

Yüksel, M.; Schlünder, E. Heat and mass transfer in non-isothermal absorption of gases in falling liquid films Part II: Theoretical description and numerical calculation of turbulent falling film heat and mass transfer. *Chem. Eng. Process: Process Intensification*, v. 22, n. 4, p. 203–213, dec 1987. ISSN 02552701.

Zavaleta-Aguilar, E.; Simões-Moreira, J. Thermal design of a tray-type distillation column of an ammonia/water absorption refrigeration cycle. *Applied thermal engineering*, Elsevier, v. 41, p. 52–60, 2012.

Zavaleta-Aguilar, E.; Simões-Moreira, J. Horizontal tube bundle falling film distiller for ammonia–water mixtures. *Int. J. Refrigeration*, Elsevier, v. 59, p. 304–316, 2015.

Zavaleta-Aguilar, E. W. *Estudo experimental de um destilador por filme descendente para um ciclo de refrigeração por absorção de amônia-água em um banco de tubos horizontais.* 197 f. p. Tese (Doutorado), 2015.

Appendix

APPENDIX A

Vapor compression refrigeration cycle modeling

A vapor compression refrigeration cycle (VCRC) was modeled using the same operational conditions of an ACR, allowing to compare the power consumption of these cycles. While an ACR consumes 10.75 W a VCRC demands 668.7 W for the same conditions: thermal load of 3517 W with condensation temperature and vaporization temperature of 40°C and 7°C, respectively; ammonia as working fluid. Therefore, the ARC (pumping system) only consumes 1.6 % from a VCRC (compression system). It is worthwhile to mention these cycles were modeled for ideal conditions: pumping and compression system as isentropic processes. Table (A.1) presents the power consumption for other working fluids.

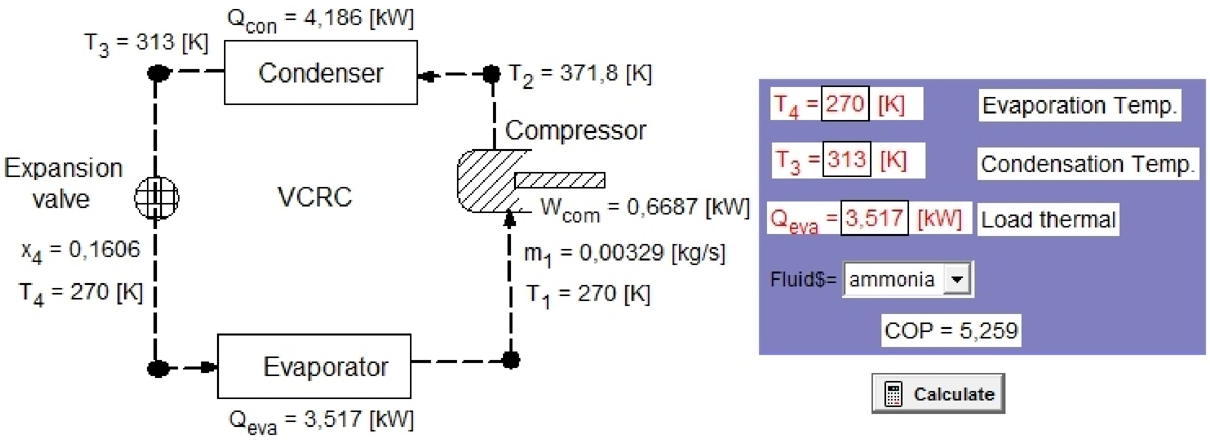

T_4 = 270 [K] Evaporation Temp.

T_3 = 313 [K] Condensation Temp.

Q_{eva} = 3,517 [kW] Load thermal

Fluid$= ammonia

COP = 5,259

Figure A.1 – *Vapor compression refrigeration cycle*

Table A.1 – *Power consumption comparison between ARC and VCRC*

Fluid	COP	Power, W	% Consumption
Ammonia	5.259	668.7	1.61
R134a	4.982	706	1.52
Propane	4.889	719.4	1.49
R22	5.03	697.9	1.54
R410a	4.65	756.3	1.42

Next, the code used in Engineering Equation Solver is shown:

```
"Operational conditions"
{T[4]=253 "Evaporation temperature"
T[3]=313 "Condensation temperature"
Fluid$='ammonia'
Q_eva=3,517 [kW]}

"Mass conservation"
m[1]=m[2]:m[2]=m[3]:m[3]=m[4]

"Energy conservation"
Q_eva=m[1]*(h[1]-h[4])
Q_con=m[2]*(h[2]-h[3])
h[3]=h[4]
W_com=m[1]*(h[2]-h[1])

"Hypothesis"
T[4]=T[1]
x[3]=0:x[1]=1
s[1]=s[2]
P[3]=P[2]: P[4]=P[1]

"Thermodynamic properties"
P[3]=Pressure(Fluid$;T=T[3];x=x[3])
h[3]=Enthalpy(Fluid$;T=T[3];x=x[3])
x[4]=Quality(Fluid$;T=T[4];h=h[4])
h[1]=Enthalpy(Fluid$;T=T[1];x=x[1])
P[1]=Pressure(Fluid$;T=T[1];x=x[1])
s[1]=Entropy(Fluid$;T=T[1];x=x[1])
h[2]=Enthalpy(Fluid$;P=P[2];s=s[2])
T[2]=Temperature(Fluid$;P=P[2];h=h[2])

"Coefficient of Performance - COP"
COP=Q_eva/W_com
```

APPENDIX B

Studies of falling film technology by using LiBr-Water working fluid

The transfer correlations involving lithium bromide-water systems are discussed, in which each one is classified by application (absorption or desorption) and geometry disposal. Additionally, these correlation are summarized in tables by application range and by test rig specifications. The sorption machine using lithium bromide solution works both at low pressure (around 1 kPa) where the LiBr solution absorbers the water vapor, and at high pressure (around 10 kPa) where the desorption process occurs. Although the absorber constitutes the critical device in the machine, many studies have also focused on the generator.

B.1 Generator

The main devices used for generators involving lithium-bromide pair are vertical tubes and horizontal tubes.

B.1.1 Vertical tubes

Shi et al. (2009) carried out a mathematical simulation and experimental work of a desorption process inside a vertical tube of 25 mm OD and 760 mm in length, analyzing the influence of the heat flux and the volume flow rate over the heat transfer coefficient for a single absorption pressure (97.25 kPa), solution concentration of 49.5 %, heat flux ranging 5-25 kW/m^2, and for Reynolds smaller than 500 [1]. In the mathematical analysis, the interfacial effects, wave generation in the liquid film, changes in film thickness, and pool boiling by superheating (only by the evaporation on the interface) were neglected. In addition, the performance of the flooded generator and the falling film evaporator were compared for the same heat flux. The heat transfer coefficient (1000-1800 W/m^2 °C was enhanced when the heat flux was increased for different volume flow solutions. However, the heat transfer rate decreased with the increases of the volume flow solution when the Reynolds number was less than $\mathrm{Re}_\delta \leq 500$ or $\mathrm{Re} \leq 2000$, and for

---

[1] Reynolds number was defined as a function of the film thickness, Re_δ

$\mathrm{Re}_\delta \geq 500$. The heat transfer behavior was the opposite when the volume flow was incremented because there was a regime transition from the laminar to the turbulent regime. Concerning numerical and experimental analysis, both results of the heat transfer coefficient were compared, having the heat transfer coefficient underestimated by the numerical study due to the simplified hypotheses previously mentioned. Finally, the falling film evaporator had the best performance of the heat transfer coefficient for heat flux lower than 12.000 W/m^2 as compared with the flooded generator. Heat transfer coefficient (±19 % maximum deviation) for the liquid-phase

$$h_l = 14 \times 10^3 {q''_w}^{0.0764} \mathrm{Re}_l^{-0.5391} \tag{B.1}$$

Later, Shi et al. (2010) built a test rig to investigate the heat transfer behavior for a vertical in-tube falling film generator, testing different heat fluxes (10-25 kW/m^2) and concentrations of lithium bromide (49.5-58 %) for a laminar regime ($\mathrm{Re} = 287 - 770$), and for other operation conditions such as (a) generation pressure of 9.725 kPa and (b) volume flow rate range of 7-14 ml/s. A 25 mm OD stainless steel tube and 760 mm length was employed, in which the lithium bromide solution was fed inside the tube top in the saturated condition. In addition, the falling film technology was compared with the flooded generator as well. According to the inlet concentration of lithium bromide solution, the change in this parameter promoted the variation in the thermophysical properties, meaning the increases of the viscosity and the surface tension when the concentration was increased, diminishing the inertial flow effects, and thus, the convection heat transfer decrease on the solution side. On the other hand, the increase of the heat flux may have modified the heat transfer mechanism from the evaporation process given at the interface to the evaporation process accompanied by nucleate boiling, which implied increase of the heat transfer coefficient, as usual. However, Shi et al. (2010) did not study these phenomena in an independent fashion. Finally, the heat transfer coefficient in the falling film technology reached higher performance (up to 4 times) than flooded tube generator, making the design of a desorption equipment more compact. Heat transfer coefficient for the liquid-phase

$$h_l = 129.7712 {x_i}^{-0.8058} q_w^{0,2422} \mathrm{Re}_l^{-0.0856} \tag{B.2}$$

where, x_i is the weak solution concentration at the inlet condition and q_w is the heat transferred by the wall.

B.1.2 Horizontal tubes

Jani et al. (2003) developed an analytical model to study the heat and mass transfer coefficient in a falling film generator over a horizontal tube bundle, in which the Reynolds numbers (in the laminar regime without wave generation), tube diameter, tube spacing, and thermophysical properties were analyzed. The model considered three regions over the horizontal tubes for different heat and mass transfer phenomena, being (a) impingement region on the top of the tubes, (b) vertical liquid sheet for the tube spacing, and (c) tube bundle for all horizontal tubes. Prandtl numbers ranged from 7 to 10, Reynolds number ranged from 100 to 500, generation pressure from 5 to 10 kPa, and lithium bromide concentration from 50 to 60 %. The average heat transfer coefficient decreased with the increase of the number of tubes in the vertical position in the bundle tube, being expressed as a function of the tube numbers (N) and the heat transfer coefficient (h) of the first tube, $hN^{-0.25}$. For low Reynolds numbers (Re $\leq$ 200), the increase in the Reynolds number improved the average heat transfer rate. However, above this value, the effects of the Reynolds number over the average heat transfer coefficient may be neglected as well as the generation pressure variations or the super-heating wall.

Nusselt number for the liquid phase for one tube

$$\mathrm{Nu} = 54.41 \times 10^{-2} \mathrm{Re}_l^{0.1597} \mathrm{Pr}_l^{0.4563} D^{*-0.3971} s^{*0.001626} P^{0.0213} e^{-0.004598x} \tag{B.3}$$

Nusselt number for bundle tube

$$\mathrm{Nu} = 54.41 \times 10^{-2} \mathrm{Re}_l^{0.1597} \mathrm{Pr}_l^{0.4563} D^{*-0.3971} s^{*0.001626} P^{0.0213} e^{-0.004598x} \cdot N^{-0.25} \tag{B.4}$$

where D^* and s^* represent the dimensionless tube diameter (D/L_c) and the dimensionless vertical tube spacing (s/L_c), respectively. L_c represents the characteristic length $(\nu^2/g)^{1/3}$.

Jani (2012) proposed correlations for the dimensionless heat and mass transfer coefficients obtained by numerical modeling. The configuration studied corresponds to a solution of LiBr falling down over a horizontal single heated tube. The model used for the hydrodynamic part corresponds to the Nusselt solution (the stream-wise component of velocity is quadratic for a given cross section of the liquid film) but varied following the angle along tube. The transport equations correspond to the steady advection-diffusion equations. An increase of absorption pressure led to an increment of the saturation temperature of the solution, reducing the viscosity of solution, and therefore, an enhancement of the heat and mass transfer coefficient. On the other hand, the viscosity could be increased with a higher inlet concentration, negatively affecting the equipment performance (Jani, 2012). The correlations obtained were Nusselt number for the liquid phase

$$\mathrm{Nu} = 78.93 \times 10^{-2} \mathrm{Re}_l^{0.16587} \mathrm{Pr}_l^{0.37275} \mathrm{Sc}_l^{-0.041769} D^{*-0.40335} \tag{B.5}$$

Sherwood number for the liquid phase

$$\mathrm{Sh} = 2 \times 10^{-3} \times \mathrm{Re}_l^{1.0023} \mathrm{Pr}_l^{-0.74049} \mathrm{Sc}_l^{1.3455} D^{*-1.0006} \tag{B.6}$$

where D^* represents the dimensionless diameter of the tube as previously defined. The range of validity holds for values of Pr between 7 and 10, values of Re between 100 and 500. The pressure values from 5 kPa to 10 kPa and the concentration of lithium bromide used was around 50 % to 60 %. According to the results, the Nu number increased as the Re_l number also increased, but seemed to be unaffected by the Sc_l number. The Sh number grew linearly with the Re_l number but remained proportionally inverse to the tube diameter. An increase of the generator pressure (or saturation temperature) and/or a reduction of the inlet concentration improved the heat transfer coefficient due to the thinning of the falling film by a decrease of the viscosity.

Table B.1 – *Constant for equations (B.7) and (B.8) ($\times 10^{-3}$)*

Configuration	a	b	c	d
Solution, Bare	24.9	69	896	-300
Solution, Screen	4.93	469	965	-343
Solution + 2-EH, Bare	25.9	247	2623	-265
Solution + 2-EH, Screen	16.6	279	886	-240

B.2 Absorber

Most of the works devoted to absorbers using lithium bromide-water solution are focused on vertical flat plate and horizontal tubes.

B.2.1 Flat plate

Kim and Infante Ferreira (2008) studied the heat and mass transfer coefficients enhancement, for vertical plate absorber, thanks to the presence of wire screen, when the Re_l number is varying (from 40 to 110). In their investigation, four different liquid films are used: pure water and a 50 % LiBr solution, with or without 100 ppm of 2-ethyl-1-hexanol (2-EH) as additive. The experimental setup uses a flat copper plate that may be covered by a wire screen. For the whole 39 data set obtained, the range used for pressure was from 0.7 to 2.9 kPa. The mass flow rate at the inlet varied from 0.6×10^{-3} to 7.7×10^{-3} kg/s. The resulting correlations are given by: Nusselt number for the liquid phase

$$\mathrm{Nu} = a \times \mathrm{Re}_l^b \mathrm{Pr}_l^{0.5} \tag{B.7}$$

Sherwood number for the liquid phase

$$\mathrm{Sh} = c \times \mathrm{Re}_l^d \mathrm{Sc}_l^{0.5} \tag{B.8}$$

where, for 4 configurations (over the 10 performed), the coefficients are presented in Table B.1.

The global result shows that the presence of the wire screen tends to decrease both heat and mass transfer coefficients of LiBr solution when mixed with the 2-EH additive. Specifically, for the heat transfer coefficient, the screened surface slightly enhances transfers by promoting the wetting surface of pure LiBr solution, in comparison with the bare surface. Yet the reciprocal occurs when 2-EH is added: the screen tends to reduce the heat transfer. For the mass transfer, the Sh number remains higher when the solution is water-cooled than for the adiabatic case. In the former configuration, the presence of the wire screen tends to weaken the mass diffusion when the 2-EH additive is used. The wire screen produces the converse effect (increasing the mass diffusion) for solutions without additive. The presence of the wire screen seems not to produce any significant effect on the Sh number for other configurations. However, the authors highlight that their analysis does not take into account incomplete wetting. Moreover, an error analysis yielding a possible error to heat transfer coefficient estimation of ±20 %, in case of water-cooled absorption.

Karami and Farhanieh (2009) carried out a numerical study of the simultaneous heat and mass transfer phenomenon in the absorption process in a vertical plate using the lithium bromide-water as the working fluid, analyzing (a) the effects of the solution mass flow ($\mathrm{Re} = 5 - 150$), (b) inlet cooling temperature, and (c) the inlet solution concentration. A fully implicit finite-difference method was used to solve the one-dimensional mass, energy and momentum equations, analyzing the grid size effects and then employed the 800×160 mesh, and the mass flux value as convergence criteria (10^{-6}). The temperature distribution across the film thickness was assumed to be linear due to the dominating heat only conduction effect, in which the lowest temperature profile was obtained in the last section of the absorber. The mass transfer rate reached a maximum value of 51.80×10^{-4} kgm^2 s. The local heat transfer coefficient changed as a function of the vertical position on the plate (up to 5 times). Nevertheless, the local mass transfer coefficient was strongly dependent on the vertical position (up to 12 times), having the highest values in the first section of the absorber (Karami; Farhanieh, 2009). The correlations based on the numerical results were, Nusselt number for the liquid phase

$$\mathrm{Nu}_\delta = 47.67 \times 10^{-2} \mathrm{Re}_l^{0.0477} \mathrm{Pr}_l^{0.334} \tag{B.9}$$

Sherwood number for the liquid phase

$$\mathrm{Sh}_\delta = 13.29 \times 10^{-2} \mathrm{Re}_l^{1.0571} \mathrm{Sc}_l^{0.334} \tag{B.10}$$

Later, Karami and Farhanieh (2011) carried out the similar numerical modeling to analyze the simultaneous heat and mass transfer behavior for different inclinations of the flat plate, covering from the quasi-horizontal position ($\beta = 10°$) up to the vertical position ($\beta = 90°$). The absorption mechanism occurring within the film was modeled by the 2D steady advection-diffusion equations, tested for the absorption pressure of $P = 1$ kPa, inlet solution temperature fixed at 45°C, whereas the inlet concentration was 60 %. The properties of the lithium bromide-water solution were taken from McNeely LA (1979).The Reynolds number ranged from 4 up to 150 for different flat plate inclinations, β, proposing the following correlations, Nusselt heat transfer for the liquid phase

$$\mathrm{Nu}_\delta = A \cdot \mathrm{Re}_l^B \mathrm{Pr}_l^{0.334} \tag{B.11}$$

Sherwood number for the liquid phase

$$\mathrm{Sh}_\delta = C \cdot \mathrm{Re}_l^D \mathrm{Sc}_l^{0.334} \tag{B.12}$$

with coefficients A, B, C and D depending on the angle and given by equations (B.13) to (B.16).

$$\begin{aligned}
A &= 6 \times 10^{-8}\beta^3 - 2 \times 10^{-5}\beta^2 + 1.4 \times 10^{-3}\beta + 1.58 \times 10^{-2} && \text{(B.13)}\\
B &= -1 \times 10^{-7}\beta^3 + 3 \times 10^{-5}\beta^2 - 3 \times 10^{-3}\beta + 5.637 \times 10^{-1} && \text{(B.14)}\\
C &= -2 \times 10^{-7}\beta^3 + 3 \times 10^{-5}\beta^2 - 2.3 \times 10^{-3}\beta + 1.31 \times 10^{-1} && \text{(B.15)}\\
D &= 3.23 \times 10^{-6}\beta^2 - 6.19 \times 10^{-4}\beta + 1.16 && \text{(B.16)}
\end{aligned}$$

Following their results, the averaged Nu does not seem to be highly affected (variations inferior to 0.07) for different inclination at $\mathrm{Re}_l = 20.5$, whereas the averaged Sh number reduces by about 42 % (from 46 to 27) when the angle goes from 10° to 90°. Moreover, the formulas performed shows that the optimal angle for the averaged Nu seems to be for an inclination around $\beta = 85°$.

Yi et al. (2020) studied a new prototype of the liquid film distributor over a detachable plate falling film film in which the solution flows by using overflow over a weir. Hydrodynamic tests were carried out under atmospheric conditions; $37 - 15.6$°C and 42 % lithium bromide - water concentration. The wetting rate over the plate is computed as a function of the proportion between the wet pixel value and the total pixel value, achieving 90 % wetting rate. Also, the influence of the distributor over the heat and mass transfer processes in the lithium-bromide cycle were analyzed. The overall heat transfer coefficient in the generator is improved as mass flow rate is increased when it ranged $1.8 - 5.8$ kW/m min.

B.2.2 Horizontal tubes

Babadi and Farhanieh (2005) developed an analytical study of the heat and mass transfer phenomena in the lithium bromide-water absorption process over a horizontal tube for operation conditions such as (a) Reynolds number ranging from 5 to 100, (b) absorption pressure of 1 kPa, (c) inlet concentration of 62 %, (d) wall temperature of 32°C, and (e) inlet temperature of 40°C. The average heat transfer coefficient ranged between 2000 and 5000 W/m^2 °C. A large temperature difference between the tube wall and the inlet solution promoted the highest value of heat transfer rate. In contrast, at the outlet region, the heat transfer decreased due to the thickening of the liquid film, increasing the thermal resistance. Moreover, the film thickness was associated with the Reynolds number changes, meaning the diminishing of the heat transfer rate with the decreasing of the Reynolds number due to the viscosity effects were more prominent than the inertial effects. In the opposite behavior, a high Reynolds number promoted convective heat transfer rate. Nevertheless, the Reynolds number influence was more dominant over the mass transfer than over the heat transfer rate (Babadi; Farhanieh, 2005). Banasiak and Kozioł (2009) used this study to compute the heat transfer coefficient,

Nusselt number for the liquid phase

$$\mathrm{Nu} = 0.45\mathrm{Re}_l^{-0,23}\mathrm{Pr}_l^{0.33} \qquad \text{for} \qquad \mathrm{Re} < 60 \tag{B.17}$$

Sherwood number for the liquid phase

$$\mathrm{Sh} = 1.03\mathrm{Re}_l^{-0.146}\left(\frac{\mathrm{Sc}_l}{1000}\right)^{1.42} \qquad \text{for} \qquad \mathrm{Re} < \left(\frac{\mathrm{Sc}_l}{5367}\right)^{-3.61} \tag{B.18}$$

$$\mathrm{Sh} = 9.4 \times 10^{-2}\mathrm{Re}_l^{0.29}\left(\frac{\mathrm{Sc}_l}{1000}\right)^{2.6} \qquad \text{for} \qquad \mathrm{Re} > \left(\frac{\mathrm{Sc}_l}{5367}\right)^{-3.61} \tag{B.19}$$

B.3 Summary of transfer correlations

Table B.2 – *Application range of the correlations using lithium bromide-water*

Author	*Correlation*	Pr	Re	T,°C	P, kPa	x	*Remarks*
Generator falling film using lithium bromide-water solution							
Jani et al. (2003)	B.3, B.4	$7-10$	$100-500$	$60-140$	$5-10$	$50-60$	
Jani (2012)	B.5, B.6	$7-10$	$100-500$	$60-140$	$5-10$	$50-60$	Sc= 268
Shi et al. (2009)	B.1	$3.8-4.7$	$\leq 500^*$	$126-150$	97.25	$49.5-58$	$q''=5-25$ kW/m^2
Shi et al. (2010)	B.2	$5.6-10.61$	$287-770$	$126-150$	9.725	$49.5-58$	$q''=10-25$ kW/m^2
Absorber falling film using lithium bromide-water solution							
Babadi and Farhanieh (2005)	B.17, B.18, B.19	28.5	$5-100$	40	1	62	
Karami and Farhanieh (2009)	B.9, B.10	17.7	$5-150$	45	1	60	
Karami and Farhanieh (2011)	B.11, B.12	17.7	$5-150$	45	1	60	Inclined plate
Kim and Infante Ferreira (2008)	B.7, B.8	$\cong 11-15$	$40-110$	$18-42$	$0.7-2.9$	50	

Table B.3 – *Summary of configuration studies on sorption process using lithium bromide-water*

Author	*Geometrical specifications*	*Compared*	*Comments*
Analytical and Numerical works using Lithium Bromide: Configuration of study			
Babadi and Farhanieh (2005)	Horizontal tube $D=20\times10^{-3}$m		Method: finite difference method. Assumes the total wettability of the tube
Jani et al. (2003)	Tube bundle $D=19.05\times10^{-3}$m, $S=3\times10^{-2}$m	Kim and Kim (1999), Jani et al. (2002)	Method: Non-linear differential equations solved by Runge-Kutta. The position tube effect on the row tube bundle is analyzed
Jani (2012)	Horizontal tube $D=19.05\times10^{-3}$m	Kim and Kim (1999), Shi et al. (2010), Nusselt (1916)	Method: implicit Crank-Nicolson method
Karami and Farhanieh (2009)	Vertical plate $L=1$m	Medrano et al. (2002)	Method: Fully implicit finite difference. Properties: Florides et al. (2003), and McNeely LA (1979). Convergence criterion: mass flux (10^{-6})
Karami and Farhanieh (2011)	Incline plate $L=1$ m	Medrano et al. (2002)	Properties: Florides et al. (2003), and McNeely LA (1979). Method: Implicit finite difference. Convergence criterion: mass flux (10^{-6})
Experimental works using Lithium Bromide: Configuration of study			
Kim and Infante Ferreira (2008)	Flat plate-smooth copper surface and copper+wire screen Screen: woven with 3.8×10^{-4} m copper wire, having 22 meshes per inch. 0.095 x 0.540 m $A_{total}=51.3\times10^{-3}$ m^2	Heat transfer: Hoffmann et al. (1996) Mass transfer: Yih and Chen (1982), Nagaoka et al. (1987), Kim et al. (1995)	Adiabatic condition are tested too. Properties: thermodynamic properties of Kim and Ferreira (2006) k,μ of DiGuilio et al. (1990), and D_m of Gierow and Jernqvist (1993)
Shi et al. (2009)	Vertical tube $L=0.760$ m, $O.D=25\times10^{-3}$ m		Study with modeling
Shi et al. (2010)	Vertical stainless steel in−tube $\delta_w=2\times10^{-3}$m, OD=25×10^{-3} m, $L=0.76$ m		Overall heat transfer in-tube falling film is 4.37 times higher than immersed generator

B.4 Other works devoted to transfer coefficient study

Some other works focus on establishing a formula for heat transfer coefficient. These works may involve the specific geometric length (whose influence has been suggested in the previous graphs), or the study is simply dedicated to fluid couples other than ammonia-water or lithium bromide-water.

Yüksel and Schlünder (1987a) carried out an experimental study of a non isothermal absorption in liquid films for the laminar and turbulent regime, in which the local and the average heat and mass transfer coefficients were analyzed. A vertical tube with variable length ($0-2.5$ m) and the counter-current absorption was configured. There was not any mass transfer resistance in the vapor phase and the film surface temperature was measured by infra-red pyrometer (± 0.3K).Two partial heat transfer coefficients were defined, being (a) from the film surface to the bulk, and (b) from the bulk to the vapor-liquid interface. For the former, the wall temperature and the bulk temperature were taken into account, and for the second, the bulk temperature and the interface were taken into account.

They found that assuming the same value for the bulk and the interface temperatures led to low Sherwood numbers. However, their results of mass transfer obtained by interface temperature measurements agreed well with the calculated by Nu/Sh analogy. In addition, for the Reynolds number in the $100-500$ range, the mass transfer is highly sensitive to the vapor phase velocity because it amplified the shear stress over the interface. The turbulent regime is less dependent on this condition because the mass transport is severe in the turbulence (Yüksel; Schlünder, 1987a). According to the Nusselt number, the Nu/Sh analogy agrees with that computed by interface temperature measurements, but when it take into account the assumption of the same temperature between bulk and interface, it overestimates the Nusselt number.

Patnaik and Perez-blanco (1996) investigated the simultaneous heat and mass transfer in the absorption process for the wavy film flow, employing an iterative finite-difference method for a transient and two-dimensional (2-D) model, testing the operation conditions such as (a) inlet concentration of 60 %, (b) absorption pressure of 0.850 kPa, (c) inlet temperature solution of 40°C, (d) surface temperature of 35°C, and (e) wavy-laminar regime $200 \leq \mathrm{Re} \leq 1000$, in which there are two types of wavy laminar. The mass transfer rate was found to be higher in wavy laminar than in smooth laminar regime due to the inertial and roll waves it promotes, enhancing the normal convective flux.

Takamatsu et al. (2003) studied the heat and mass transfer behavior in a 400 mm long falling vertical in-tube absorber, comparing the results with the previously reported 1200 mm long, in which the effect of the solution flow rate ($13 \times 10^{-3} - 25 \times 10^{-3}$ kg/s), solution subcooling temperature ($\Delta T_{sub} = 0$°C and $\Delta T_{sub} = 5$°C), and cooling water temperature ($T_{l,i} = 34; 35$°C) were tested. The experimental work found the total wettability of the tube when the Reynolds number reached $Re = 130$. Nevertheless, the film break-down may happen below this value, causing the deterioration of the average heat and mass transfer coefficient. In addition, it pointed out that the logarithmic mean difference in concentration is not always valid for the absorber, diverging from the real driving force of the absorption process. According to the absorption process, when the solution was fed at the saturated condition ($\Delta T_{sub} = 0°\text{C}$), the absorption process started after the thermal boundary layer on the cooled wall reaching the vapor-liquid interface, and for the subcooled condition, the absorption process began in the inlet of the absorber. The higher absorption process was given at the first 0.4 m ($15 - 50$ %) when compared with the last 0.8 m section, explained due to the wettability problems, such as the breaking film. This allows concluding that the absorption process was deeply influenced by the tube length (Takamatsu et al., 2003).

APPENDIX C

Studies of falling film technology by using other working fluids

A focus on the heat transfer correlations involving falling technology follows,

- Nosoko et al. (2002) carried out an experimental study of oxygen gas absorption in falling water films over horizontal tubes in the laminar regime (10 – 150). There was a complete tube wettability without additives, using copper tubes and a capillary tube of distribution. It tested various tube spacings $(2 - 15) \times 10^{-3}$ m and flow rates, in which an isothermal film was assumed due to the low heat of absorption of the oxygen. The logarithmic mean concentration difference and the equilibrium condition at the interface were used to calculate the mass transfer coefficient, in which all the tests were developed in atmospheric pressure, and the temperature ranged between 18 – 23°C.

  It was concluded that the droplet flow promotes more increase of the mass transfer than the sheet droplet because it penetrates the film depth, enhancing the mass transfer coefficient at the wall-film interface, and the mass transfer could improve up to 45%, on the Reynolds number 30 – 150. On the other hand, the Sherwood number improved when the tube spacing increased from 2×10^{-3} to 5×10^{-3} m, and it was kept constant for higher tube spacing, such as higher than 10 (Nosoko et al., 2002). The following correlations were obtained:

  $$\mathrm{Sh} = 37.77 \times 10^{-3} \mathrm{Re}_l^{0.86} \mathrm{Sc}_l^{0.5} \tag{C.1}$$

- Goel and Goswami (2005b) (Goel; Goswami, 2005a), and Triché et al. (2017) used the Wilke correlation (Wilke, 1962) to compute the heat transfer coefficient for the laminar flow regime, in which Wilke (Wilke, 1962) studied the falling film heat transfer, and Kandlikar (1999) showed the next follows, For $\mathrm{Re} \leq 2460\mathrm{Pr}^{-0.646}$

  $$\mathrm{Nu} = 1.92\mathrm{Re}^{-1/3} \tag{C.2}$$

  For $2460\mathrm{Pr}^{-0.646} \leq \mathrm{Re} \leq 1600$

  $$\mathrm{Nu} = 32.3 \times 10^{-3} \mathrm{Re}^{1/5} \mathrm{Pr}^{0.344} \tag{C.3}$$

For $1600 \leq \text{Re} \leq 3200$

$$\text{Nu} = 10.2 \times 10^{-4}\text{Re}^{2/3}\text{Pr}^{0.344} \tag{C.4}$$

For $3200 \leq \text{Re}$

$$\text{Nu} = 8.7 \times 10^{-3}\text{Re}^{2/5}\text{Pr}^{0.344} \tag{C.5}$$

- Chun and Seban (1971), (Chun; Seban, 1972) is given by; Laminar regime, $\text{Re} \leq 2.44Ka^{-1/11}$ is given by:

$$\text{Nu} = 0.822\text{Re}^{-1/3} \tag{C.6}$$

Wavy laminar regime, $2.44Ka^{-1/11} \leq \text{Re} \leq 5800\text{Pr}^{-1.06}$

$$\text{Nu} = 0.822\text{Re}^{-0.22} \tag{C.7}$$

Turbulent regime, and the departure from the wavy laminar to turbulent regime $\text{Re} = 5800\text{Pr}^{-1.06}$

$$\text{Nu} = 3.8 \times 10^{-3}\text{Re}^{0.4}\text{Pr}^{0.65} \tag{C.8}$$

- Hu and Jacobi (1996b), sheet mode

$$\text{Nu} = 2.194\text{Re}^{0.28}\text{Pr}^{0.14}Ar^{-0.20}\left(\frac{S-D}{D}\right)^{0.07} \tag{C.9}$$

Jet mode, and the departure from the jet mode to the sheet mode is $Re = 1.431Ga^{0.234}$.

$$\text{Nu} = 1.378\text{Re}^{0.242}\text{Pr}^{0.26}Ar^{-0.23}\left(\frac{S-D}{D}\right)^{0.08} \tag{C.10}$$

Droplet mode, and the departure from the droplet mode to the jet is $Re = 8.4 \times 10^{-2}Ga^{0.302}$.

$$\text{Nu} = 0.113\text{Re}^{0.85}\text{Pr}^{0.85}Ar^{-0.27}\left(\frac{S-D}{D}\right)^{0.04} \tag{C.11}$$

- Alhusseini et al. (1998), laminar regime

$$\text{Nu} = 2.65\text{Re}^{-0.158}Ka^{0.0563} \tag{C.12}$$

and turbulent regime,

$$\text{Nu} = \frac{\text{Pr}\delta^{*1/3}}{A_1\text{Pr}^{3/4} + A_2\text{Pr}^{1/2} + A_3\text{Pr}^{1/4} + C_1 + B_1Ka^{1/2}\text{Pr}^{1/2}} \tag{C.13}$$

where

- $A_1 = 9.17$
- $A_2 = 0.328\pi(130 + \delta^*)$
- $A_3 = 0.289(152100 + 2340\delta^* + 7\delta^{*2})/\delta^{*2}$;
- $B_1 = (2.51x10^6\delta^{*1/3}Ka^{-0.173})/\text{Re}^{(3.49Ka^{0.0675})}$
- $C_1 = 8.82 + 3 \times 10^{-4}\text{Re}$

  - $\delta^* = 94.6 \times 10^{-3}\mathrm{Re}^{0.8}$;

- Shahzada et al. (2011) modified the Han and Flecter's correlation, getting;

$$\mathrm{Nu} = 1.7 \times 10^{-3} \left(\frac{\nu^2}{gk^3}\right)^{-0.276} \mathrm{Re}^{-1/3}\mathrm{Pr}^{-0.75} \left[2e^{S/S_o} - 1\right]^{0.07} \left(\frac{T_{sat}}{322}\right)^{0.73} \tag{C.14}$$

  and the modified of Chun and Seban's correlation (Chun; Seban, 1971), getting;

$$\mathrm{Nu} = 0.20 \left(\frac{\nu^2}{gk^3}\right)^{0.23} \mathrm{Re}^{1.66} \left[2e^{S/S_o} - 1\right]^{0.006} \left(\frac{T_{sat}}{319}\right)^{-1.01} \tag{C.15}$$

  where, $S_o = 3 \times 10^4$ ppm, while S is the salt concentration given in ppm, T_{sat} is the saturation temperature given in K.

- Parken et al. (1990), for the 25.4×10^{-3} m diameter tube

$$\mathrm{Nu} = 4.2 \times 10^{-2}\mathrm{Re}^{0.15}\mathrm{Pr}^{0.53} \tag{C.16}$$

  for the 50.8 mm diameter tube

$$\mathrm{Nu} = 3.8 \times 10^{-2}\mathrm{Re}^{0.15}\mathrm{Pr}^{0.53} \tag{C.17}$$

- Mitrovic (1986), for $160 \leq \mathrm{Re} \leq 560$

$$\mathrm{Nu} = 13.74 \times 10^{-2}\mathrm{Re}^{0.349}\mathrm{Pr}^{0.5}\beta \tag{C.18}$$

  where, $\beta = \frac{(S/D)^{0.158}}{1+e^{0.008\mathrm{Re}^{1.32}}}$

- Liu et al. (2002) for $1.75 \leq \mathrm{Pr} \leq 7.02$; $800 \leq \mathrm{Re} \leq 5000$; $213 \leq Ar \leq 1546$; $1 \times 10^4 \leq D \leq 4 \times 10^4$ m,

$$\mathrm{Nu} = 4.1 \times 10^{-2}\mathrm{Re}^{0.3}\mathrm{Pr}^{0.66}Ar^{-0.12} \tag{C.19}$$

- Chien (Chien; Tsai, 2011) for R-245fa, $6.26 \leq Pr \leq 7.15$; $115 \leq Re \leq 372$; $16.5 \times 10^{-5} \leq We \leq 16.8 \times 10^{-5}$,

$$\mathrm{Nu} = 38.6 \times 10^{-3}\mathrm{Re}^{0.09}\mathrm{Pr}^{0.986} \tag{C.20}$$

- Narváez-Romo and Simões-Moreira (2017) for water, $0.72 \leq \mathrm{Pr} \leq 7.92$; $160 \leq \mathrm{Re} \leq 940$,

$$\mathrm{Nu} = 0.21\mathrm{Re}^{-0.067}\mathrm{Pr}^{0.528} \tag{C.21}$$

- Leite (2015) developed a numerical study of both absorber and generator, applying the finite difference method for an inclined plate, in which the mass, species and energy balances were employed. Both components were modeled for various operation conditions, testing the geometry dimensions, plate angle of inclination, wall temperature and the inlet conditions. The results confirmed that the vertical position is the best position of performance, promoting a stable operation condition. Finally a correlation between the heat and mass transfer over an inclined plate as a function of the vertical position is obtained by:

$$F_{\mathrm{Nu}}(\beta) = \frac{\mathrm{Nu}(\beta)}{\mathrm{Nu}(\pi/2)} \tag{C.22}$$

$$F_{\mathrm{Sh}}(\beta) = \frac{\mathrm{Sh}(\beta)}{\mathrm{Sh}(\pi/2)} \tag{C.23}$$

$$F_{\mathrm{Nu}}(\beta) = e^{-0.081(\beta-\pi/2)+0.054(\beta^2-\pi^2/4)-0.012(\beta^3-\pi^3/8)} \tag{C.24}$$

$$F_{\mathrm{Sh}}(\beta) = e^{-1.712(\beta-\pi/2)+1.402(\beta^2-\pi^2/4)-0.392(\beta^3-\pi^3/8)} \tag{C.25}$$

These factors were obtained by fitting the numerical results of Karami and Farhanieh (2011). In addition, the correlation of Kang et al. (1999) was used to compute the heat and mass transfer coefficient for the vertical position ($\beta = \pi/2$).

APPENDIX D

Studies of bubble absorber technology

A review of the bubble Ferreira et al. (1984) researched the behavior of the simultaneous heat and mass transfer in a vertical co-current upward absorption, and the influence of the operation conditions such as (a) tube geometry, (b) liquid and vapor mass flow rate, (c) wall heat flux, (d) ammonia concentration, (e) vapor and liquid temperature, and (f) absorption pressure. An absorption model was developed to carry out the analytical study, applying the conservation laws (mass and energy), and the heat transfer correlations of the two-phase flow. The model was fitted by the experimental results. The built test rig tested three different diameter tubes ($D = 10, 15.3$ and 20.5 mm), and various absorption lengths (limited to $L = 1$ m) for different operation parameters such as (a) ammonia mass flow ($0.000018 - 0.00048$ kg/s), (b) water solution mass flow ($0.0021 - 0.0262$ kg/s), (c) absorption pressure ($126 - 333$ kPa), (d) weak liquid solution concentration ($0.341 - 0.451$ %), (e) weak liquid solution temperature ($9.5 - 33.5$°C), and (f) ammonia vapor temperature ($8.2 - 32$°C). The absorption process in the tube obeys the two-phase phenomenon, and, therefore, the average heat transfer coefficient of the solution side was computed as a function of the local heat transfer reached for each flow pattern and the void fraction definition. Slug and froth flow patterns were analyzed as a thin liquid film, and the bubble flow pattern was analyzed as a single phase. The highest values of the local heat transfer coefficient were obtained in the slug flow pattern ($2800 - 15600$ W/m^2 °C), resulting the greatest part of the absorption process. The bubble absorber with the greatest length and the lowest diameter tube presented low volumetric mass transfer coefficients. Moreover, the increase of the absorption pressure and the liquid solution mass flow rate implied smaller absorbers. In contrast, the increase of the weak liquid concentration, of the weak liquid temperature, of the ammonia vapor temperature, and of the ammonia vapor mass flow rate required larger absorbers (Ferreira et al., 1984). Sherwood number in the liquid falling film

$$\mathrm{Sh} = e^{0.86307} \mathrm{Re}^{0.853} \mathrm{Sc}_l^{0.5} \left(\frac{D}{L} \right) \tag{D.1}$$

$$\mathrm{Re} = \frac{\rho_l v_v D}{\mu_l} \tag{D.2}$$

Absorber length as a function of the inlet conditions

$$L = 133.6x_l^{2.1}\dot{m_v}^{0.7}i_{lv}^{0.6}T_l^{0.4}P^{-1.0}D^{-0.5}\dot{m_l}^{-0.04} \tag{D.3}$$

Lee et al. (2002b) carried out an experimental study of ammonia-water bubble absorption for a plate geometry ($0.112 \cdot 0.264 \cdot 0.003\text{m}^3$) for a laminar regime. Three wall surfaces were tested (smooth plate, hair lined plate treated by laser, and plated treated by sand paper), being the plate treated by sand paper the surface with the highest wettability. For all the tests, a counter-current absorption was adopted, and several operation conditions were considered, such as (a) ammonia vapor mass flow rate ($1-9$l/min), (b) weak liquid solution mass flow rate ($0.002-0.015$ kg/s), and (c) weak liquid solution concentration ($0-30\%$), keeping the weak liquid solution constant at a temperature of 20°C. The increase of the weak liquid solution mass flow rate improves the heat transfer coefficient for a constant value of ammonia vapor mass flow or for different ammonia vapor mass flows, being the influence more prominent in the low weak liquid mass flow. It should also mentioned that, the increase of the ammonia vapor mass flow rate has remarkable influence over the mass and heat transfer performance for a given weak solution flow. In addition, the thermal boundary layer may be affected if a slug flow pattern is reached when the vapor mass flow is increased, improving the heat transfer coefficient (Lee et al., 2002b), similar to Ferreira study (Ferreira et al., 1984). Thereby, a variation in the ammonia vapor mass flow and in the weak liquid solution mass flow significantly affect the Sherwood number and the Nusselt number, respectively, agreeing with Kang et al. (1999). Nusselt number in the bubble absorber. Error between measured and calculated Nusselt number (±10 %)

$$\text{Nu} = 3.133\text{Re}_l^{0.2519}\text{Re}_v^{0.2995}\left(\frac{\Delta T_{sub,i}}{T_l}\right)^{0.06851}\left(\frac{\Delta x_i}{x_l}\right)^{0.08636} \tag{D.4}$$

Sherwood number in the bubble absorber. Deviation between two Sherwood numbers (±5%)

$$\text{Sh} = 43.57\text{Re}_l^{0.0403}\text{Re}_v^{0.2865}\left(\frac{\Delta x_i}{x_l}\right)^{0.0462} \tag{D.5}$$

$$\text{Sh} = 1.62\left(\frac{\dot{m}}{DL\rho}\right)^{1/3} \tag{D.6}$$

Kang et al. (2006) investigaed the mass transfer behavior for the bubble ammonia absorption by using nanofluids combined with surfactants such as 2−ethyl-1-hexanol 2E1H, n-octanol, and 2-octanol. The averaged absorbed mass flow rate increased when the surfactants were added into the nanafluids (Cu, CuO and Al_2O_3), in which the 2E1H (700ppm) achieve the a better perfomance of all them. Tests were carried out in atmospheric conditions in 18% ammonia-water solution.

Cerezo et al. (2009) studied the absorption process using a corrugated plated heat exchanger with three channels (effective surface area of $0.1m^2$), evaluating the mean parameters that affect the absorption performance. Tests were ranged for absorption rate flux from 0.0025 to 0.0063 kg/m^2 s, solution heat transfer coefficient from 2700 to 5400 W/m^2 $°C$, and an absorber thermal load from 0.5 to 1.3 kW. The heat transfer coefficient increased almost linearly when the solution flow rate increased due to the turbulent effect over the thermal layer on the surface (a reduction). On the other hand, the Reynolds number changes did not affect the mass absorption rate flux when the inlet concentration was 33%. Moreover, a smaller concentration (between 29% and 33%) presented higher mass absorption rate flux for the same Reynolds number (Re = 290), being an opposite behavior to the driving force definition. In addition, the heat transfer coefficient decreased when the cooling water temperature decreased. Finally, the highest heat transfer rate and mass absorption rate flux were reached for higher values of absorption pressure.

APPENDIX E

Ammonia-water absorption refrigeration cycle modeling

The current Appx. analyzes the ACR's for the ammonia-water mixture, defining the Nusselt number and the Sherwood number under several operational conditions. It allows mapping a possible operational region of these dimensionless number as a function of the Reynolds numbers in air-conditioning and refrigeration applications. For that purpose, the absorption cycle simulation is carried out, defining the possible range operational parameters, whose values are evaluated for each correlation of heat and mass transfer.

The heat and mass transfer mapping of these correlations from the literature review are analyzed in a realistic operational conditions of an ARC for refrigeration ($-20°C$) and air-conditioning ($7°C$) applications as shown in Fig. (E.1). Lithium bromide-water is analyzed in Appendix (F). Also, the study aims to compare the heat and mass transfer correlations, looking for a standardization comparison for further studies.

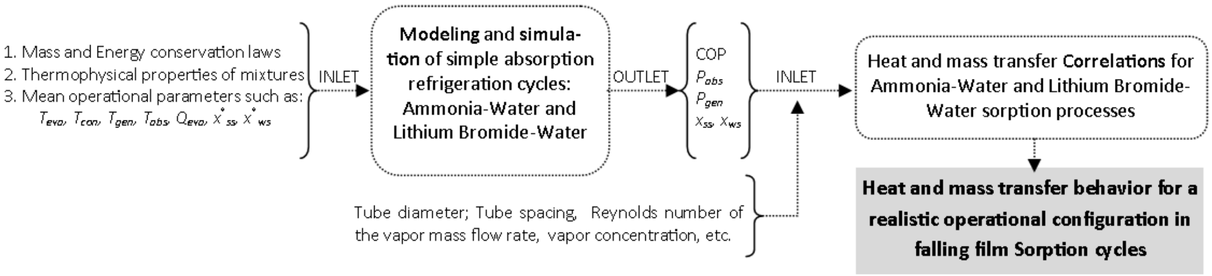

Figure E.1 – *Method to evaluate the heat and mass transfer coefficient in a realistic sorption refrigeration cycles*

E.1 Absorption refrigeration modeling

An ARC modeling is carried out, taking into account all the components of the cycle such as generator, rectifier (for $NH_3 - H_2O$ only), condenser, expansion valves, evaporator, absorber, and pump. Each one is analyzed as an independent control volume, in which the mass, species and energy equations are developed in a steady-stage regime. Thermodynamic properties are defined by using the Ibrahim (1993) routines implemented in the *Engineering Equation Solver* (EES) software ((Klein, 2015)). In the following sections, the ammonia-water ARC is analyzed.

E.1.1 First law and second law analysis

The conservation of energy for steady-state regime is given by Eq. (E.1) in which the change in the potential and kinetic energy are neglected. $\dot{Q}$ is the heat transfer rate between the system and the surroundings, $\dot{W}$ refers the work done by the system; $\dot{m}$ and i is the mass fluxes and the enthalpy, respectively.

$$\dot{Q} - \dot{W} = \sum(\dot{m} \cdot i)_{out} - \sum(\dot{m} \cdot i)_{in} \tag{E.1}$$

The second law analysis of the absorption refrigeration cycle allows defining the theoretical machine limits or the concept of perfection (Cengel; Boles, 2015) due to no cycle could be more efficient than a reversible machine (Cheng, 1966). Real processes in the absorption cycle promote entropy changes as consequence of the irreversibilities, in which each one could increase or decrease the entropy. However, the entropy of the universe must be increased. This property can be evaluated by integrating $ds = dQ/T$ along an internally reversible path between the initial and the final states;

$$\Delta S = s_2 - s_1 = \int_1^2 \frac{dQ}{T} \tag{E.2}$$

The entropy balance is given by Eq. (E.3), in which for the steady-state regime $\Delta_{stored} = 0$,

$$\sum S_{in} - S_{gen} + \int_1^2 \frac{dQ}{T} = \sum S_{out} + \Delta_{Stored} \tag{E.3}$$

Fig. (E.2) shows the heat transferred between the system and the surroundings for the simple absorption refrigeration cycle, in which T_g, T_e and T_0 is the generator temperature, evaporator temperature and environment temperature, respectively. Generator process receives heat Q_g from an external source at the generator temperature level, whose heat is used to produce wet ammonia vapor. Rectifier purifies the ammonia vapor by rejecting the heat of rectification Q_r to the environment at T_0 temperature. Also, condenser Q_c and absorber Q_a reject the heat of condensation and absorption to the environment, respectively. Finally, the evaporator absorbs heat of evaporation Q_e from the surroundings. On the other hand, the heat exchanger is considered as adiabatic. By simulating the cycle, it can be noted that generator requires the highest heat rate, and that the absorber is about 25% less than the generator when it (heat exchanger) has an infinite area. In addition, Q_c is about equal to Q_e, whose difference is due to the pumping work.

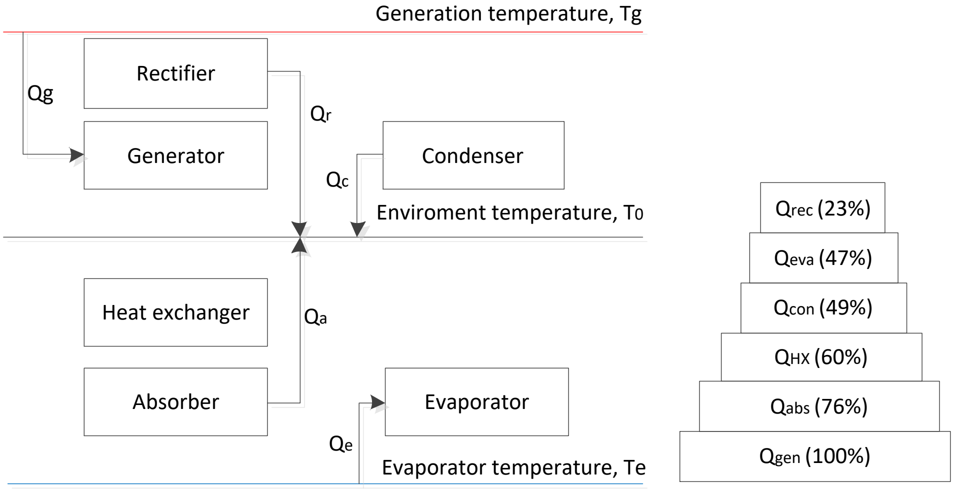

Figure E.2 – *a)Duty heat in the simple absorption refrigeration system (adopted from (Cheng, 1966)) and b)typical heat rate proportions for each component*

E.1.2 Ammonia-water ARC

ARC modeling requires attention to the most critical processes at the generator and absorber, such as generation and absorption processes due to simultaneous heat and mass transfer. The states are defining by using Gibbs phase rule in which for ammonia-water (multi components) are mandatory the definition of three thermodynamic properties. A focus on the generator and absorber is shown in Fig. (E.3).

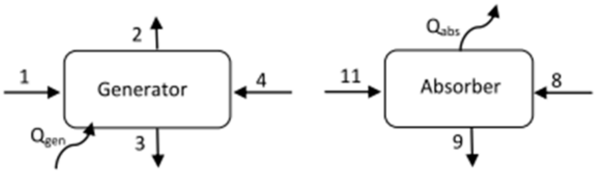

Figure E.3 – *Control volume for the generation and the absorption process*

The generator is employed to ammonia distillation the (2-label) from the ammonia-water strong solution (1-label) when a heat source is applied (Q_{gen}), in which the weak solution is the remaining solution after the separation process (3-label). The rectifier is used to purify the ammonia vapor and hence that condensed goes back to the generator (4-label). On the other hand, the falling film absorber is used to absorb the ammonia vapor coming from the evaporator (8-label) to be absorbed by the weak ammonia-water solution (11-label), whose mixture comes from the generator obtaining the strong ammonia-water solution (9-label) as shown in Fig. (E.3).

$$\dot{m}_3 + \dot{m}_2 = \dot{m}_1 + \dot{m}_4 \tag{E.4}$$

$$\dot{Q}_{gen} = \dot{m}_2 i_2 + \dot{m}_3 i_3 - \dot{m}_1 i_1 - \dot{m}_4 i_4 \tag{E.5}$$

$$\dot{m}_3 x_3 + \dot{m}_2 x_2 = \dot{m}_1 x_1 + \dot{m}_4 x_4 \tag{E.6}$$

$$S_{created,g} = \dot{m}_1 s_1 + \dot{m}_4 s_4 - \dot{m}_3 s_3 - \dot{m}_2 s_4 - \int \frac{dQ_g}{T_g} \tag{E.7}$$

The mass, ammonia mass, and energy equations are given by Eqs. (E.4-E.6) and by Eqs. (E.8-E.10) for the generation and absorption processes, respectively;

$$\dot{m}_{11} + \dot{m}_8 = \dot{m}_9 \tag{E.8}$$

$$\dot{Q}_{abs} = \dot{m}_8 i_8 + \dot{m}_{11} i_{11} - \dot{m}_9 i_9 \tag{E.9}$$

$$\dot{m}_{11} x_{11} + \dot{m}_8 x_8 = \dot{m}_9 x_9 \tag{E.10}$$

where Q_{abs} is rejected to the coolant fluid, $\dot{m}$, i and x are the mass flow rate, specific enthalpy and the ammonia mass fraction, respectively. Several simplified hypothesis are carried out to solve the equation system such as;

- condensation temperature, $T_{con} = 40°C$;
- vaporization temperature, $T_{eva} = 7°C$;
- thermal load, $\dot{Q}_{eva} = 3.517kW^1$;
- generation temperature, $T_{gen} = 100°C$;
- absorption temperature, $T_{abs} = 25°C$;
- quality equal to $q_u = 0$ - saturated liquid- at states 3, 4, 6, and 9;
- quality equal to $q_u = 1$ saturated vapor- in the 2, 5 and 8 points;
- two pressure levels only: high pressure level in the 1, 2, 3, 4, 5, 6, 11 and 12, low pressure level in the 7, 8, 9 and 10 points;
- generation process occurs in thermodynamic equilibrium, $T_3 = T_2$;
- the temperature in the point 4 is computed by the arithmetic mean, $T_4 = 0.5 * (T_2 + T_5)$ (Herold et al., 2016);
- heat exchanger with infinity area, $Q_{subcool} = Q_{pre-heat}$, $T_{11} = T_{12}$;
- isentropic pumping. Fig. (E.4) shows the numerical results of the whole operational parameters such as ammonia-mass fraction (x), absorption pressure (P_{abs}) and generation pressure (P_{gen}), mass flow rate ($\dot{m}$), just to mention a few.

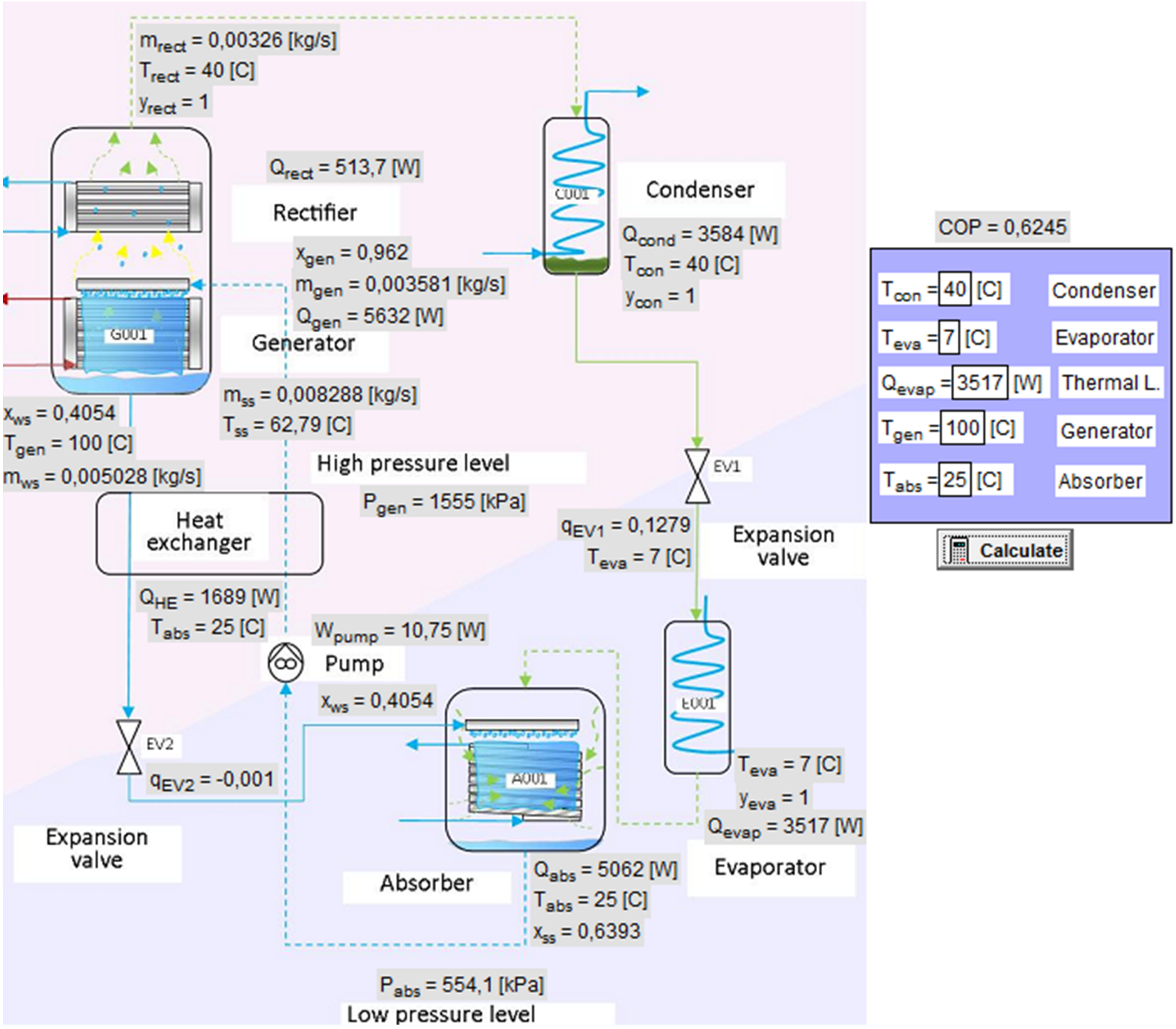

COP = 0,6245

T_{con} = 40 [C] Condenser

T_{eva} = 7 [C] Evaporator

Q_{evap} = 3517 [W] Thermal L.

T_{gen} = 100 [C] Generator

T_{abs} = 25 [C] Absorber

Figure E.4 – *Results of the simulation of the ammonia-water ARC*

Table E.1 – *Operational conditions of the ammonia-water ARC*

Cond.	$T_{con}, ^{\circ}C$	$T_{eva}, ^{\circ}C$	$T_{gen}, ^{\circ}C$	COP	P_{abs}, kPa	P_{gen}, kPa	$x_{ss}, \%$	$x_{ws}, \%$	Pr	Sc
1	40	7	100	0.6245	554.1	1555	63.72	40.52	1.64	14.4
2	40	7	110	0.5157	554.1	1555	63.72	31.41	1.91	21.5
3	40	-20	100	0.5547	190.1	1555	41.51	40.52	2.29	37.3
4	40	-20	110	0.4606	190.1	1555	41.51	31.41	2.63	52.4
5	30	7	100	0.6083	554.1	1167	63.72	34.54	1.82	18.9
6	30	7	110	0.4779	554.1	1167	63.72	25.78	2.1	27.4
7	30	-20	100	0.5407	190.1	1167	41.51	34.54	2.52	46.9
8	30	-20	110	0.4298	190.1	1167	41.51	25.78	2.87	64.2

Some parameters are adjusted to cover the operation ranges applied in refrigeration/air conditioning systems. The simulation is carried out for two vaporization temperatures; $T_{eva} = -20°C$ for refrigeration applications and $T_{eva} = 7°C$ for air condition systems, two condensation temperatures ($T_{con} = 40°C$ and $T_{con} = 30°C$), and two generation temperatures ($T_{gen} = 100°C$ and $T_{gen} = 110°C$), aiming to achieve typical operation conditions. All the simulation results are shown in Table (E.1), in which eight operation conditions had been

---

[1] Thermal load was necessary to run the model, however, the thermal load affect directly the equipment size

evaluated, as shown in the first column. The second, third and fourth columns show the condensation temperature (T_{con}), vaporization temperature (T_{eva}) and generation temperature T_{gen}; while COP, P_{abs} and P_{gen} are the coefficient of performance, absorption pressure and generation pressure, respectively; Next, x_{ss}, x_{ws} are the strong and weak solution, respectively. Finally, the last two columns show Prandtl number (Pr) and Schmidt number (Sc) for absorption conditions.

APPENDIX F

Lithium bromide-water absorption refrigeration cycle modeling and heat and mass transfer mapping

The work developed in Appx. (E) is extended for the lithium bromide-water working fluid, whose operation conditions are also set by the same analysis carried out in Sec. (E.1.2). The results are shown in Fig. (F.1), in which the lithium bromide concentrations are defined at the design specifications using the crystallization limit to define the weak solution concentration. The generator temperature is given as a function of the weak and strong liquid concentration, being a dependent variable. Evaporation temperature is only evaluated at $7°C$ due to refrigerant properties (water). Therefore, this technology is widely used in air conditioning applications. All the results are shown in Tab. (F.1), in which two operation conditions are evaluated and shown in first column, the second and third columns show the condensation temperature (T_{con}) and vaporization temperature (T_{eva}), respectively; while x_{ss}, x_{ws} are the strong and weak solution, respectively.

Table F.1 – *Operational conditions of the lithium bromide-water ARC*

Cond.	T_{con}, $°C$	T_{eva}, $°C$	x_{ss}, %	x_{ws}, %	COP	P_{abs}, kPa	P_{gen}, kPa	T_{gen}, 0°C	Pr	Sc
1	40	7	50	62.7	0.8659	1	7.38	90.29	24.17	2101
2	30	7	50	62.7	0.883	1	4.25	78.43	24.17	2101

F.1 Heat and mass transfer mapping

Fig. (F.2) shows the Sherwood number as a function of Reynolds number, in which the correlations display different behavior for the same operational conditions, i.e., Karami and Farhanieh's (Karami; Farhanieh, 2009) and Karami and Farhanieh's (Karami; Farhanieh, 2011) correlations show a strong dependence of the Sherwood number as the Reynolds number changes, enhancing the mass transfer as the Reynolds number increases. In contrast, Kim and

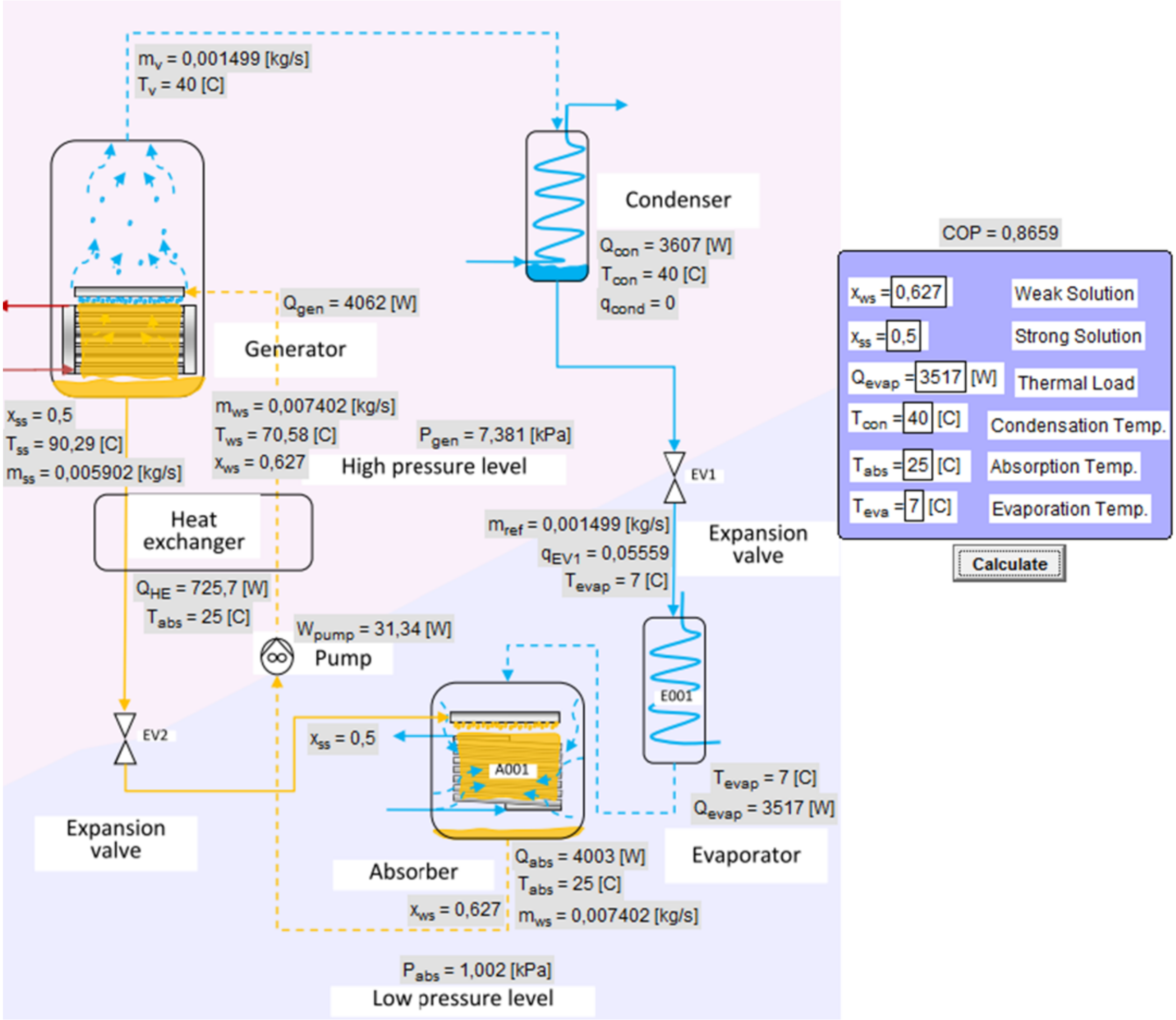

Figure F.1 – *Results of the simulation of the lithium bromide-water ARC*

Ferreira's (Kim; Infante Ferreira, 2008) show that the increase of the Reynolds number decreases the Sherwood number.

It is worthwhile to mention that the Kim and Ferreira's (Kim; Infante Ferreira, 2008) correlations were obtained experimentally. Babadi and Farhanieh (2005) underestimates the Sherwood number as compared with Kim and Infante Ferreira (2008), Karami and Farhanieh (2009), and Karami and Farhanieh (2011).Therefore, Fig. (F.2) shows that the Sherwood number may be vary between 0 and 100 for the Reynolds number ranging from 10 to 150 for $LiBr - H_2O$ ARC in air conditioning applications.

Finally, Fig. (F.3) shows the behavior of the Nusselt number as a function of the Reynolds number, in which the heat transfer improves as the Reynolds number increases. Nevertheless, the correlations of Babadi and Farhanieh (2005), and Karami and Farhanieh (2009) shows an opposite behavior. Nusselt number may vary between 0.1 and 0.8 as the Reynolds number ranged from 10 to 150 in $LiBr - H_2O$ ARC for air conditioning applications. So, the study shows some theoretical advantages of the heat and mass transfer process for air-condition applications when lithium bromide-water working fluid is used.

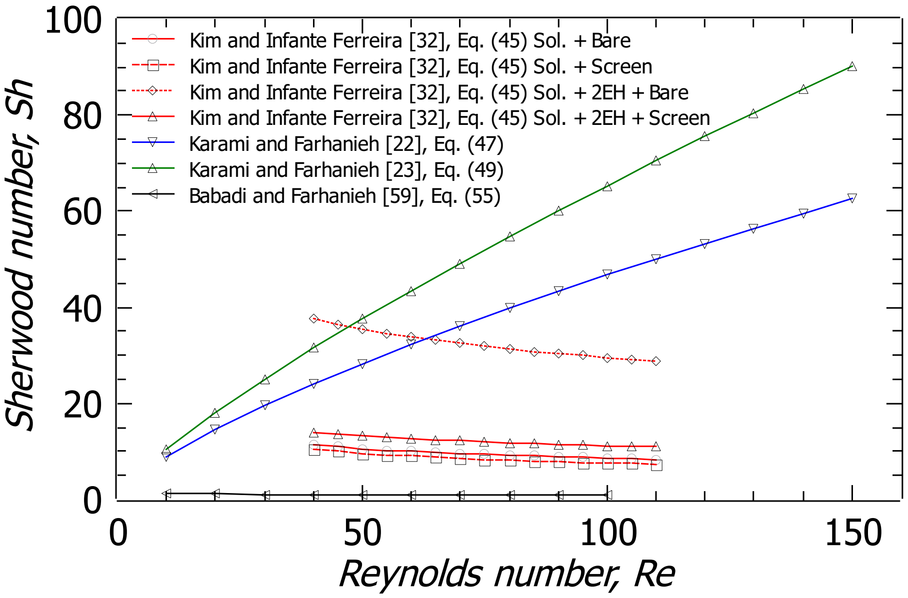

Figure F.2 – *Sherwood number as a function of the Reynolds number for the Lithium bromide-water solution*

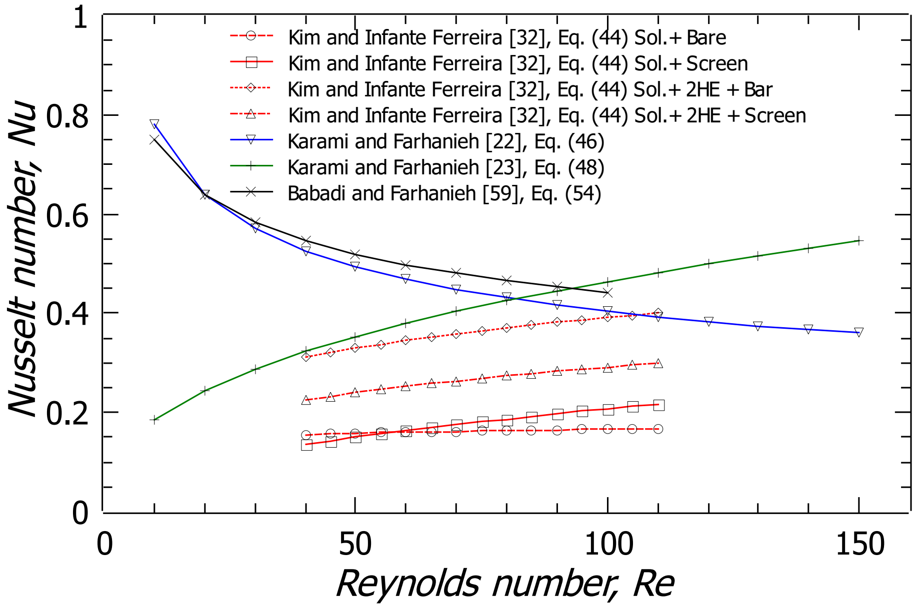

Figure F.3 – *Nusselt number as a function of the Reynolds number for the Lithium bromide-water solution*

Transfer correlations involving lithium bromide-water working fluid pair shows divergences between theoretical studies such as Kim and Infante Ferreira (2008), Karami and Farhanieh (2009), and Babadi and Farhanieh (2005); and experimental studies such as Kim and Infante Ferreira (2008). Sherwood number may vary between 0 and 100 for the Reynolds numbers ranging from 10 to 150, and Nusselt number may vary between 0.1 and 0.8 for the Reynolds number ranged from 10 to 150.

APPENDIX G

Ammonia Absorption refrigeration cycle modeling

G.1 Ammonia-water mixtures

Next, the code used in Engineering Equation Solver EES (Klein; Alvarado, 2002) is shown:

```
“Conditions"
{T[6]=40+273,15 "Condenser [K]"
T[8]=-20+273,15 "Evaporator [K]"}
{Q_eva=3,517 [kW]"Thermal load - 1TR"}
{T[9]=25+273,15 "Absorber-outlet [K]"}
{T[3]=100+273,15 "Generator-Outlet"}

"Hypothesis"
q[3]=0: q[3]=q[4]: q[3]=q[6]: q[3]=q[9]: "Saturated liquid"
q[2]=1: q[2]=q[5]: q[2]=q[8] "Saturated vapor"
P[6]=P[5]: P[6]=P[4]: P[6]=P[2]: P[6]=P[3]: P[6]=P[1]: P[6]=P[12]: P[6]=P[11] "High pressure level"
P[8]=P[7]: P[8]=P[10]: P[8]=P[9] "Low pressure level"
T[3]=T[2] "Themal equilibrium"
T[4]=0,5*(T[2]+T[5]) "Temp. [4]= average of T[2]+T[5]"
x[5]=1 "Purity=1, pure ammonia"
Q_sub=Q_aqe "Heat Ex - Infinity area"
s[9]=s[12] "Isentropic process - pump"
T[11]=T[12] "HEx - contra-current"

"Species conservation"
{m[1]*x[1]+m[4]*x[4]=m[2]*x[2]+m[3]*x[3] "Generator"}
m[2]*x[2]=m[4]*x[4]+m[5]*x[5] "Rectifier"
x[5]=x[6] "Condenser"
x[6]=x[7] "Exp. Valve  #1"
x[7]=x[8] "Evaporator"
m[8]*x[8]+m[10]*x[10]=m[9]*x[9] "Absorber"
x[10]=x[11] "Exp. Valve  #2"
x[11]=x[3] "Subcooled"
x[9]=x[12] "Pump"
x[12]=x[1] "HEx"

"Mass"
{m[1]+m[4]=m[2]+m[3] "Generator"}
m[2]=m[4]+m[5] "Rectifier"
m[5]=m[6] "Condenser"
m[6]=m[7] "Exp. Valve #1"
m[7]=m[8] "Evaporator"
m[8]+m[10]=m[9] "Absorber"
m[10]=m[11] "Exp. Valve #2"
m[11]=m[3] "Subcooled"
m[9]=m[12] "Pump"
m[12]=m[1] "HEx"

"Energy"
Q_ger=m[2]*h[2]+m[3]*h[3]-m[1]*h[1]-m[4]*h[4] "Generator"
Q_ret=m[2]*h[2]-m[5]*h[5]-m[4]*h[4] "Retifier"
Q_con=m[5]*h[5]-m[6]*h[6] "Condenser"
h[6]=h[7]  "Exp. Valve #1"
Q_eva=m[8]*h[8]-m[7]*h[7] "Evaporator"
Q_abs=m[8]*h[8]+m[10]*h[10]-m[9]*h[9] "Absorver"
h[11]=h[10]  "Exp. Valve #2"
Q_sub=m[3]*h[3]-m[11]*h[11] "Subcooled"
W_bom=m[12]*h[12]-m[9]*h[9] "Pump"
Q_aqe=m[1]*h[1]-m[12]*h[12] "HEx"

"Thermodynamic properties"
```

APPENDIX H

Ammonia-water thermodynamic properties

H.1 Thermodynamic properties for pure substances

Ammonia-water solution is a no azeotropic mixture, and both substances have similar molecular weight and good chemical affinity. Tab. (H.1) shows some properties for each other obtained by *Engineering Equation Solver*.

Table H.1 – *Thermodynamic properties*

Property	Ammonia	Water
Molar weight [kg/kmol]	17.03	18.02
Enthalpy fusion [kJ/kg]	332.4	333.6
Normal boiling point [°C]	-33.33	100
Critical pressure [kPa]	11333	22064
Critical temperature [°C]	132.3	374
Critical volume [m^3/kg]	0.0044	0.0031

H.2 Thermodynamic properties for ammonia-water working fluid pair

The ammonia-water properties are used to define the thermodynamic state, in which three properties are necessary for a binary mixture. Thorin (2001) developed an extensive review of correlations used to find the ammonia-water properties. However, in this work is used the correlations carried out by Conde (2006), whose correlations are expressed as a function of the molar fraction, $\widetilde{x}$,

$$\widetilde{x} = \frac{n \text{ mols NH}_3}{n \text{ mols Total}} \tag{H.1}$$

H.3 Transport properties

Some transport properties are defined for heat and mass transfer processes.

H.3.1 Thermal conductivity (W/m°C)

- For liquid phase: Conde (2006) showed that Lees (1898), Braune (1937) and Baranov et al. (1997) present deeply inconsistencies from the experimental results. Thus, Conde (2006) suggests to use the thermal conductivity for an ideal solution,

$$k_L = \widetilde{x} \cdot k_{a,l} + (1 - \widetilde{x}) \cdot k_{w,l} \tag{H.2}$$

- For vapor phase: is computed with the equation of Wassiljewa (1904), taking into account the considerations carried out by Saxena and Mason (1958), in which this property is affected by dynamic viscosity of the vapor phase (Conde, 2006).

$$k_v = \tilde{y}\left(\frac{k_{a,v}}{\tilde{y} + (1-\tilde{y})\phi_{12}}\right) + (1-\tilde{y})\left(\frac{k_{v,w}}{1-\tilde{y}+\tilde{y}\phi_{21}}\right) \tag{H.3}$$

$$\phi_{12} = \frac{\left[1 + \left(\frac{\mu_{a,v}}{\mu_v}\right)^{0.5}\left(\frac{M_w}{M_a}\right)^{0.25}\right]^2}{\left[8\left(1 + \frac{\mu_{a,v}}{\mu_{w,v}}\right)\right]^{0.5}} \tag{H.4}$$

$$\phi_{21} = \phi_{12}\left(\frac{\mu_{w,v}}{\mu_{a,v}}\right)\left(\frac{M_a}{M_w}\right) \tag{H.5}$$

H.3.2 Dynamic viscosity (Pa s)

- For liquid phase: in 1897, the first measurements of the dynamic viscosity ($T = 25°\mathrm{C}$) were carried out by Kanitz (1897). Neuforn (1986) developed a equation with good agreement from the experimental data. However, these results are available for high temperatures and higher ammonia concentrations. A new approximation was obtained by Conde (2006). Temperature T is given in K.

$$\ln(\mu_l) = \widetilde{x}\ln\mu_a^* + (1-\widetilde{x})\ln\mu_w^* + \Delta\mu_{T,\widetilde{x}} \tag{H.6}$$

where:

$$\Delta\mu_{T,\widetilde{x}} = \left(0.534 - 0.815\frac{T}{T_{c,w}}\right)F(\widetilde{x}) \tag{H.7}$$

$$F(\widetilde{x}) = 6.38(1-\widetilde{x})^{1.125\widetilde{x}}\left(1 - e^{-0.585\widetilde{x}(1-\widetilde{x})^{0.18}}\right)ln(\mu_a^{*0.5}\mu_w^{*0.5}) \tag{H.8}$$

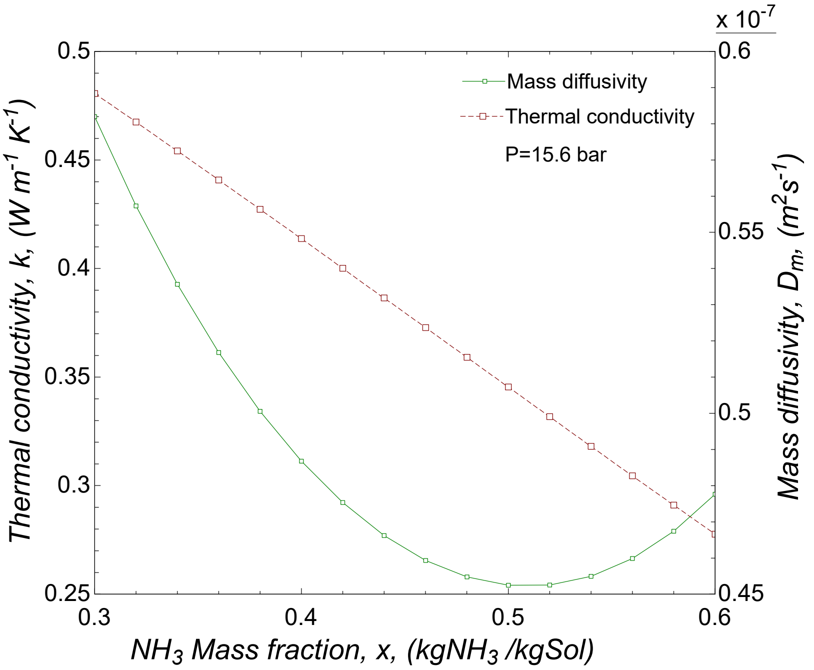

Figure H.1 – *Thermal conductivity and mass diffusivity as a function of the ammonia mass fraction*

- For vapor phase: in 1950, Wilke (1950) proposed an equation for the dynamic viscosity, being;

$$\mu_v = \tilde{y}\left(\frac{\mu_{a,v}}{\tilde{y} + (1-\tilde{y})\phi_{12}}\right) + (1-\tilde{y})\left(\frac{\mu_{w,v}}{(1-\tilde{y}) + \tilde{y}\phi_{21}}\right) \tag{H.9}$$

H.3.3 Mass diffusivity - NH_3 vapor into aqueous solutions - (m^2/s)

For the diffusion coefficient (mass diffusivity), Wilke and Chang (1955) proposed an equation for strongly associative liquids, such as ammonia-water solution.

$$D_{aw} = 117.282 \times 10^{-18} T_l \cdot \frac{\sqrt{\psi M_l}}{\mu \cdot \left(\frac{M_{a,l}}{\rho_{a,l}}\right)^{0.6}} \tag{H.10}$$

where, the associative factor ψ of water is given by:

$$\psi_l = \widetilde{x} \cdot 1.7 + (1-\widetilde{x}) \cdot 2.6 \tag{H.11}$$

Fig. (H.1) compares the thermal conductivity and the mass diffusivity as a function of the ammonia mass fraction, in which the mass diffusivity reaches a minimal value at $x = 0.5$. Concerning thermal conductivity, as ammonia mass fraction increases, thermal conductivity decreases as a linear fashion.

H.4 Thermophysical properties

H.4.1 Specific thermal capacity at constant pressure (kJ/kg °C)

- For liquid phase: this property is computed by a approximation of the solution as quasi-ideal solution (Conde, 2006).

$$c_{p,l} = \widetilde{x} c^*_{p,a} + (1 - \widetilde{x}) c^*_{p,w} \tag{H.12}$$

- For vapor phase: ammonia-water at the vapor condition is calculated as for an ideal solution (Conde, 2006).

$$c_{p,v} = y \cdot c^*_{p,a} + (1 - y) c^*_{p,w} \tag{H.13}$$

H.4.2 Surface tension (N/m)

To compute the surface tension is assumed a quasi-ideal solution, describe by:

$$\sigma_l = \widetilde{x}\sigma^*_a + (1 - \widetilde{x})\sigma^*_w + \Delta\sigma_{T,\widetilde{x}} \tag{H.14}$$

where,

$$\Delta\sigma_{T,\widetilde{x}} = -(\sigma^*_w - \sigma^*_a) F(\widetilde{x}) \tag{H.15}$$

$$F(\widetilde{x}) = 1.442(1 - \widetilde{x}) \left[1 - e^{-2.5\widetilde{x}^4}\right] - 1.106\widetilde{x} \left[1 - e^{-2.5(1-\widetilde{x})^6}\right] \tag{H.16}$$

$$\sigma^*_{subs} = \sigma_0 \left[1 + b_\sigma \left(1 - \frac{T}{T_c}\right)\right] \left(1 - \frac{T}{T_c}\right)^{u_\sigma} \tag{H.17}$$

σ_0, b_σ and u_σ from Eq. H.17 are showed in Tab. H.2.

Table H.2 – *Constants from Eq. H.17.*

subs	σ_0	b_σ	u_σ
NH_3	91.2	0.0	1.103
H_2O	235.8	-0.625	1.256

Finally, Fig. (H.1) is shown to behavior of the thermal conductivity

APPENDIX I

Calibration procedure and data: pressure and temperature

The calibration of the temperature sensors and pressure transducer is detailed. Basically, it collected several operational points and through the method of least squares is determined the best fit line of these data. The normal error σ_m is computed from the data acquisition for each measurement, in which it is defined as $\sigma_m = \sigma/\sqrt{n}$ (Holman, 1993); σ is the the sample standard deviation, and n is the sample numbers, e.g. for each pressure measurement, the normal error is neglected because it only represents 0.2% of the measured pressure value. Tab. (I.1) and (I.2) shows the summarized data of the temperature and pressure calibration.

I.1 Temperature sensors

Fig. (I.1) shows the temperature calibration procedure in which three kind of acquisition data are used Agilent, Lynx and National Instrument (NI). The temperature sensor of mercury is employed as the "true" temperature value (±0.1°C) in which the thermostatic bath defines the temperature range of calibration (up 90°C).

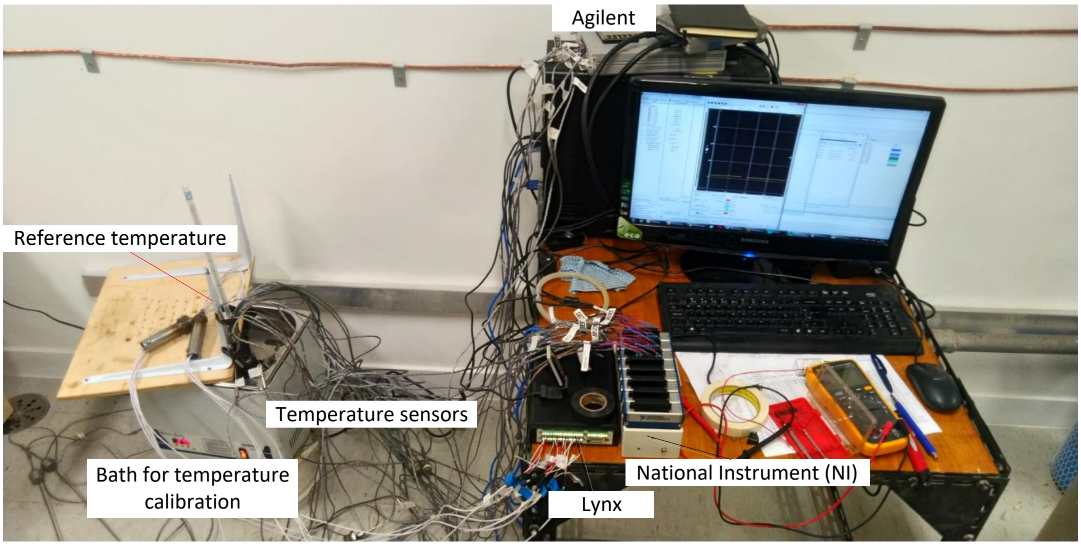

Figure I.1 – *Temperature calibration of all the temperature sensors*

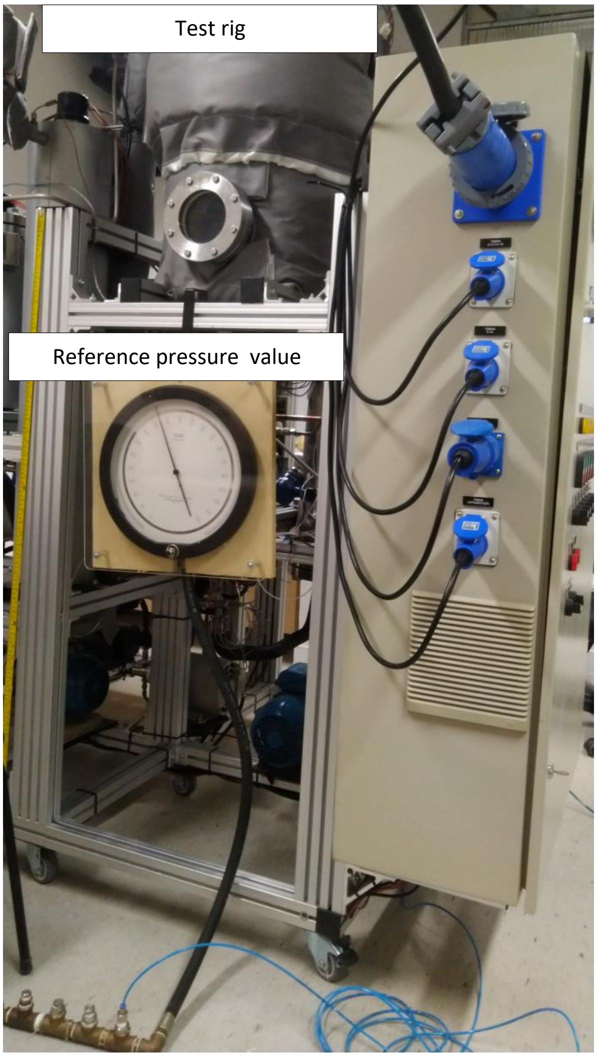

Figure I.2 – *Pressure calibration in situ of all the pressure transducer installed in the test rig*

Table I.1 – *Measured values of the temperature sensors and definition of the corrected values obtained by using the method of least squares*

Calibration of the temperature sensors installed in the absorption refrigeration cycle, temperature value given in °C												
"True"	T_{001}	T_{002}	T_{003}	T_{004}	T_{005}	T_{006}	T_{007}	T_{008}	T_{031}	T_{060}	T_{030}	T_{050}
26.9	25.18	25.82	25.02	25.86	25.51	24.98	26.10		26.48	26.32	26.25	26.41
47.4	44.62	46.13	42.47	46.18	45.91	45.37	46.49		47.14	47.22	47.36	47.32
56.7	53.45	55.16	51.05	55.38	55.21	54.54	55.70		56.60	57.00	56.99	57.02
67.5	64.34	66.34	61.69	66.13	65.99	65.45	66.56		67.34	67.89	67.85	67.96
77.3	74.81	77.00	72.51	76.20	76.30	75.38	76.69		76.97	77.59	77.58	77.79
84.4	81.19	84.18	73.53	82.98	83.22	82.37	83.50		84.07	84.79	84.77	84.77
83.0	80.44	84.03	75.72	81.71	81.98	80.99	82.21	82.30	82.80	83.22	83.19	83.42
90.9	88.21	92.19	85.25	89.66	90.00	88.97	90.14	90.27	90.75	91.40	91.31	91.29
93.0	90.58	94.70	81.88	91.83	92.18	91.20	92.34	92.44	92.78	93.26	93.46	93.35
96.2	94.16	98.42	88.24	94.83	95.09	94.05	95.22	95.31	96.50	96.27	96.36	96.22
Coefficients by using the method of least squares. m is the slope. b the intercept and R^2 is the correlation coefficient.												
m	1.002518	0.951232	1.095448	1.002447	0.991149	0.999614	0.998697	1.006847	0.995639	0.989338	0.988510	0.990565
b	2.456423	3.463810	0.320447	1.079667	1.820932	2.027811	0.927067	0.076140	0.500893	0.606654	0.649706	0.458771
R^2	0.999510	0.998887	0.991855	0.999975	0.999945	0.999976	0.999967	0.999422	0.999944	0.999910	0.999928	0.999898

T_{061}	T_{009}	T_{051}	T_{201}	T_{200}	T_{040}	T_{023}	T_{010}	T_{130}	T_{1001}	T_{1003}	T_{1004}	T_{1008}
26.36	26.32	26.46	26.31	26.31	26.25	26.33	26.17	26.14	26.12	27.66	26.51	26.43
47.25	47.38	47.07	47.31	47.39	47.29	47.23	47.06	46.92	46.06	47.84	46.49	46.40
56.94	57.01	56.57	56.89	57.07	56.75	57.02	56.79	56.59	55.44	57.21	56.01	55.87
67.69	67.77	67.54	67.74	67.83	67.71	67.99	67.63	67.24	65.69	67.84	66.48	66.41
77.41	77.33	76.98	77.29	77.43	77.46	77.74	77.19	76.73	75.15	77.61	76.12	76.07
84.59	84.66	84.12	84.69	84.83	84.42	84.96	84.48	83.88	81.53	84.45	82.81	82.85
83.08	83.10	82.64	83.09	83.33	83.26	83.44	82.91	82.44	80.47	83.09	81.63	81.56
90.95	91.09	90.29	90.97	91.06	91.41	91.47	90.78	90.31	88.62	90.94	89.73	89.73
92.80	93.24	92.20	92.73	93.32	93.22	93.42	92.53	92.24	90.38	93.17	91.60	91.61
95.85	96.29	95.39	95.99	96.52	96.04	96.54	96.26	95.39	93.59	96.09	94.97	95.06
Coefficients by using the method of least squares. m is the slope. b the intercept and R^2 is the correlation coefficient.												
0.996486	0.992147	1.005549	0.995571	0.989921	0.990307	0.986230	0.993617	1.002455	1.030005	1.011167	1.014021	1.011673
0.293485	0.479793	0.003948	0.348306	0.553172	0.650328	0.717090	0.611283	0.365533	-0.084010	-1.069953	0.096746	0.300404
0.999878	0.999929	0.999885	0.999878	0.999926	0.999904	0.999933	0.999883	0.999911	0.999887	0.999985	0.999939	0.999938

I.2 Pressure transducers

Fig. (I.2) shows the pressure calibration of all the pressure transducer, in which a absolute pressure reference is utilized (± 1 kPa). The atmospheric pressure is estimated by a mercury barometer. Tab. (I.2) shows the seven (7) pressure points that these are used to carry the pressure transducer calibration.

Table I.2 – *Measured values of the pressure transducers and definition of the corrected values obtained by using the method of least squares*

Calibration of the pressure transdutors installed in the absorption refrigeration cycle. pressure value given in bar												
	Pressure transdutores used to control					Pressure transdutores used to acquisition						
"True"	P_{001}	P_{002}	P_{003}	IP_{003}	P_{004}	P_{005}	P_{006}	P_{007}	P_{008}	P_{009}	P_{010}	P_{011}
7.10	7.23	7.23	7.13	7.20	7.26	7.34	7.29	7.34	7.36	7.28	7.30	7.28
6.14	6.23	6.23	6.13	6.19	6.24	6.32	6.30	6.33	6.37	6.28	6.32	6.26
5.44	5.53	5.63	5.43	5.49	5.54	5.70	5.65	5.69	5.63	5.63	5.66	5.56
4.30	4.43	4.43	4.23	4.30	4.34	4.51	4.48	4.50	4.46	4.43	4.50	4.37
3.49	3.53	3.53	3.33	3.38	3.42	3.63	3.55	3.59	3.50	3.55	3.62	3.43
2.28	2.43	2.43	2.23	2.28	2.30	2.56	2.53	2.55	2.39	2.42	2.54	2.33
0.94	1.13	1.13	0.93	0.93	0.93	1.27	1.23	1.24	1.02	1.10	1.27	0.95
Coefficients by using the method of least squares, m is the slope, b the intercept and R^2 is the correlation coefficient.												
m	1.010584	1.006138	0.989421	0.980925	0.972632	1.013415	1.012635	1.007686	0.968143	0.995192	1.017868	0.972486
b	-0.170053	-0.16503	0.077764	0.063049	0.06759	-0.295826	-0.248035	-0.257719	-0.011796	-0.124758	-0.299324	0.046811
R^2	0.999585	0.999418	0.99929	0.999454	0.999547	0.99929	0.999017	0.999098	0.999416	0.99964	0.999417	0.999513

APPENDIX J

Published articles and Conferences/Workshops

Published articles:

- Falling liquid film evaporation in subcooled and saturated water over horizontal heated tubes - *Heat Transfer Engineering*, 2017
- A critical review of heat and mass transfer correlations for LiBr-H_2O and NH_3-H_2O absorption refrigeration machines using falling liquid film technology - *Applied Thermal Engineering*, 2017
- Vertical and inclined plates falling film absorption process in ammonia-water mixture - *Heat Transfer Research*, 2020

Conferences and Workshops:

- A heat and mass transfer mapping for the NH_3-H_2O and LiBr-H_2O absorption refrigeration systems based on the falling film technology - JEM 2017
- Theoretical study of heat and mass transfer absorption process using a horizontal flooded film in ammonia-water mixtures - Workshop of Solar-Thermal Energy Exploitation Research - 2018
- Theoretical modeling of a new evaporator for an ammonia-water absorption refrigeration using flooded-laminar film tube - ICMF-2019
- Project and building of an experimental test rig for ammonia-water absorption refrigeration system - Workshop of Solar-Thermal Energy Exploitation Research - 2019
- An experimental study of an NH_3-H_2O absorption refrigeration cycle using a novel modified horizontal liquid film absorption system driven by solar energy -Workshop of Solar-Thermal Energy Exploitation Research - 2020

ANNEX A

Diagrams

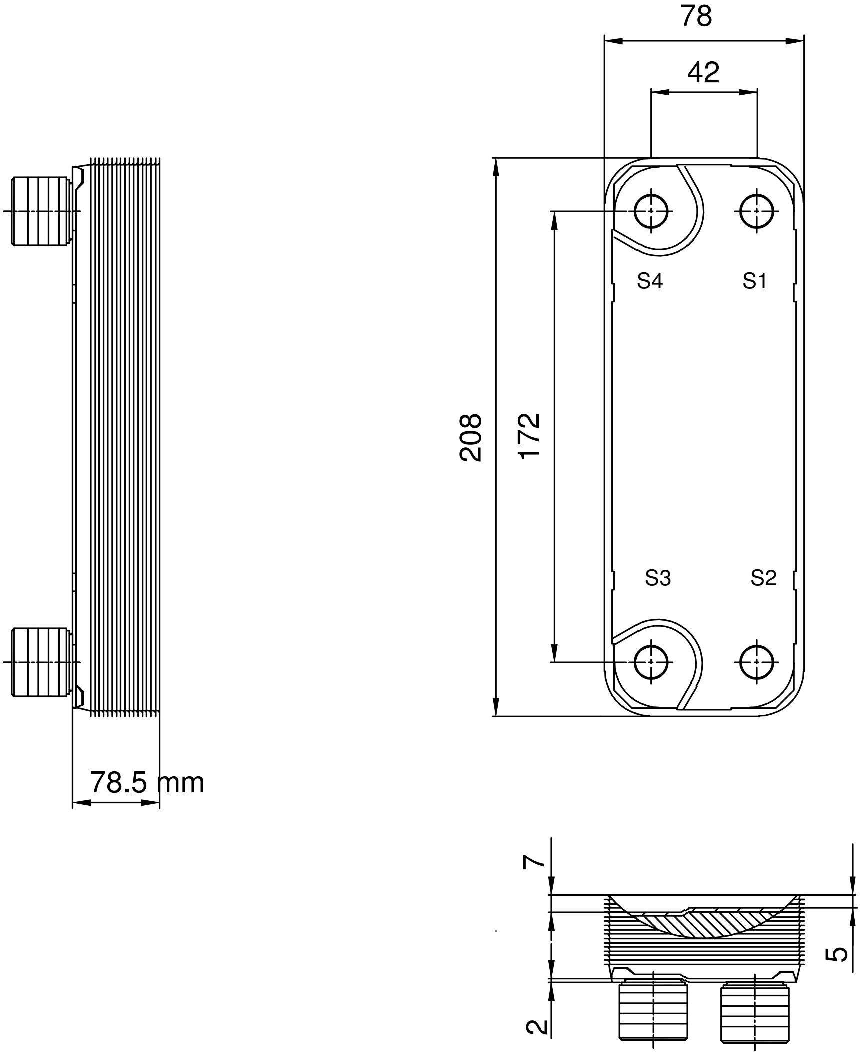

Frameplate is depressed 2 mm at connection S3/S4
Pressureplate is depressed 2 mm / even number of channel plates att connections T3/T4 / uneven number of channel plates att connections T1/T2.

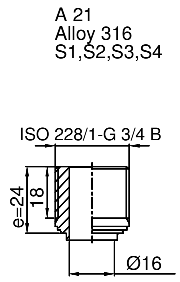

ALL DIMENSIONS IN MILLIMETERS

MEDIA	INLET	TEMP.	OUTLET	TEMP.	FLOW RATE	PRESSURE DROP	LIQUID VOL.
Water	S4	°C	S3	°C	kg/h	kPa	0.2800 dm³
Water	S2	°C	S1	°C	kg/h	kPa	0.3000 dm³

HEATING SURFACE	m²	PLATE MATERIAL	Alloy 316	TOTAL LENGTH	102.5
NETWEIGHT	2.600 kg	PLATE THICKNESS	0.3 mm	TOTAL WIDTH	77.0
OPERATING WEIGHT	3.180 kg	PLATE GROUPING	1*15H/1*14H	TOTAL HEIGHT	207.0

SUPPLIER	REF.	MP NO.	PLATE HEAT EXCHANGER
AGENT / REF.			
CUSTOMER NAME / REF. NO.			
SIGN.			

AlfaNova 14-30H(A21,A21)

PED

ITEM ID.
32870 5066 3

DATE
2009-05-15

REV
No. 0

ANNEX B

Circuit Drawings and Wiring Diagrams

REV.	DESCRIÇÃO	DATA	NOME
05	As-Built de Fábrica	20/08/2019	Diego Almeida
04	Para Aprovação	14/06/2019	Diego Almeida
03	Conforme Comentários	07/06/2019	Diego Almeida
02	Inclusão Automação	06/06/2019	Diego Almeida
01	Conforme Comentários	04/06/2019	Ray Alves
00	Emissão Inicial	28/05/2019	Ray Alves

br-SAUTER

br-Sauter Comércio e Automação Ltda Epp.

Rua Francisca de Paula, 295 - Vila Carrão
CEP: 03436-000
Tel: (11) 3294-2077
www.br-sauter.com / comercial@br-sauter.com

São Paulo - SP
Brasil

USP

SISEA
LABORATÓRIO DE SISTEMAS ENERGÉTICOS ALTERNATIVOS

CLIENTE:

USP - Universidade de São Paulo

Av. Professor Mello Moraes, 2231 - Cid. Universitária - Bl. Eng. Mec.
Sala TT003 - São Paulo - SP
Tel: (11) 3091-9671

OBRA:

Absorption Refrigeration Cycle

SISTEMA ATENDIDO:

SISEA - Alternative Energy Systems Lab./ Beethoven Narvaez

PAINEL: QE-01

PROJETISTA: Ray Alves

TENSÃO DE ALIMENTAÇÃO: 220V/3F+PE/60Hz

DATA: 20/08/2019

TENSÃO DE COMANDO: 220Vca

NÚMERO PROJETO: BZX-QE-001-R05

Índice

Coluna X: uma página gerada automaticamente foi alterada manualmente

Rev.	Desc.	Data	Nome
05	As-Built de Fábrica	20/08/2019	Diego Almeida
04	Para Aprovação	14/06/2019	Diego Almeida
03	Conforme Comentários	07/06/2019	Diego Almeida
00	Emissão Inicial	28/05/2019	Ray Alves

TAG QE: QE-01

Nº VL BZX-QE-001-R05

Índice : /1 - /33

Notas:

Cliente
USP - Universidade de São Paulo

Obra
Absorption Refrigeration Cycle

Folha 2 De 44

Índice

Coluna X: uma página gerada automaticamente foi alterada manualmente

Rev.	Desc.	Data	Nome
05	As-Built de Fábrica	20/08/2019	Diego Almeida
04	Para Aprovação	14/06/2019	Diego Almeida
03	Conforme Comentários	07/06/2019	Diego Almeida
00	Emissão Inicial	28/05/2019	Ray Alves

TAG QE:
QE-01

Índice : /34 - /44

Nº VL
BZX-QE-001-R05

Notas:

br-SAUTER

USP

Cliente
USP - Universidade de São Paulo

Obra
Absorption Refrigeration Cycle

Folha
3

De
44

CARACTERÍSTICAS DO PAINEL

1 - MODELO :

1x CS1408035 (1400 x 800 x 350 mm)

2 - FABRICANTE :

SR SENADOR

3 - GRAU DE PROTEÇÃO :

IP-65

4 - CONSTRUÇÃO :

ESTRUTURA : CHAPA DE AÇO BITOLA 18
PORTA : CHAPA DE AÇO BITOLA 18
PLACA DE MONTAGEM : CHAPA DE AÇO BITOLA 16

5 - VEDAÇÃO :

POLIURETANO INJETADO

6 - PINTURA :

ESTRUTURA E PORTA : BEGE RAL 7032
PLACA : LARANJA RAL-2004

7 - CIRCUITOS DE FORÇA E COMANDO :

IDENTIFICAÇÃO : ANILHAS

8 - ESPECIFICAÇÃO DOS CABOS :

OS CABOS DE COMANDO SERÃO DE BITOLA 1,5mm2, COR AZUL CLARO (NEUTRO) E COR VERMELHA (RESTANTE), 750V/70°C.

OS CABOS DE FORÇA SERÃO DE BITOLA CONFORME INDICADO NOS DESENHOS, NA COR PRETA ALIMENTAÇÃO DE MOTORES, 750V/70°C. COR AZUL PARA NEUTRO E VERDE PARA TERRA.

9 - TODOS OS COMPONENTES INTERNOS SERÃO IDENTIFICADOS

10 - DIMENSÕES EM MILÍMETROS

11 - BARRAMENTO EM COBRE ELETROLÍTICO, PROTEGIDO COM PLACA DE ACRÍLICO E IDENTIFICADOS NAS CORES:

FASE R : AZUL ESCURO
FASE S : BRANCA
FASE T : VIOLETA OU MARROM
TERRA : VERDE

12 - PORTA DOCUMENTOS :

A4 234 x 173 mm - PADRÃO VL

Rev.	Desc.	Data	Nome
05	As-Built de Fábrica	20/08/2019	Diego Almeida
04	Para Aprovação	14/06/2019	Diego Almeida
03	Conforme Comentários	07/06/2019	Diego Almeida
00	Emissão Inicial	28/05/2019	Ray Alves

TAG QE: QE-01
Nº VL: BZX-QE-001-R05
Características do Painel
Notas:
br-SAUTER
USP
Cliente: USP - Universidade de São Paulo
Obra: Absorption Refrigeration Cycle
Folha: 4
De: 44

SIMBOLO	SIGLA	DESCRIÇÃO
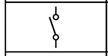	CS	CHAVE SECCIONADORA
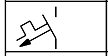	DJ	DISJUNTOR
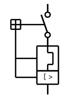	DJM	DISJUNTOR MOTOR
	F	FUSÍVEL
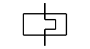	RP	RELÉ DE PROTEÇÃO
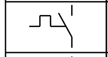	RP	RELÉ DE PROTEÇÃO CONTATO "NF"
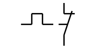	RP	RELÉ DE PROTEÇÃO CONTATO "NA"
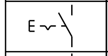	BL	BOTÃO LIGA
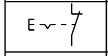	BD	BOTÃO DESLIGA
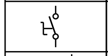	IM	INTERRUPTOR MANUAL
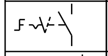	S	SELETOR 2 POSICÕES
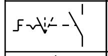	S	SELETOR 3 POSICÕES
	CNA	CONTATO NORMALMENTE ABERTO "NA"
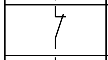	CNF	CONTATO NORMALMENTE FECHADO "NF"
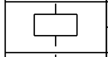	C CA	BOBINA CONTATOR BOBINA CONTATOR AUXILIAR
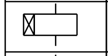	RT	RELÉ DE TEMPO RETARDADO AO TRABALHO
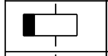	RT	RELÉ DE TEMPO RETARDADO AO REPOUSO
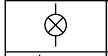	H	SINALIZADOR
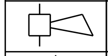	AL	ALARME SONORO
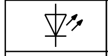	LED	DIODO EMISSOR DE LUZ
	D	DIODO RETIFICADOR

SIMBOLO	SIGLA	DESCRIÇÃO
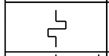	RM	RELÉ DE MERCÚRIO
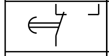	RT	CONT. RELÉ DE TEMP. RETARDADO AO TRAB.
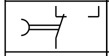	RT	CONT. RELÉ DE TEMP. RETARDADO AO REP.
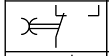	RT	CONT. RELÉ DE TEMPO DE IMPULSO
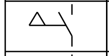	CF	CHAVE DE FLUXO "Fecha com fluxo"
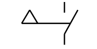	CF	CHAVE DE FLUXO "Abre com fluxo"
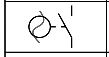	CN	CHAVE DE DE NÍVEL "Desliga c/ Nível Baixo"
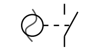	CN	CHAVE DE DE NÍVEL "Liga c/ Nível Baixo"
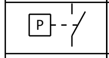	PA	PRESSOSTATO DE ALTA "Abre c/ Alta pressão"
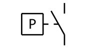	PB	PRESSÓSTATO DE ALTA "Abre c/ Baixa pressão"
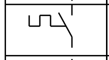	TR	TERMOSTATO DE REFRIGERAÇÃO
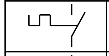	TA	TERMOSTATO DE AQUECIMENTO
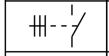	UU	UMIDOSTATO DE UMIDIFICADOR
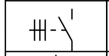	UD	UMIDOSTATO DE DESUMIDIFICADOR
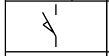	FC	CHAVE FIM DE CURSO
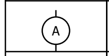	A	AMPERÍMETRO
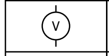	V	VOLTÍMETRO
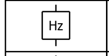	Hz	FREQUECÍMETRO
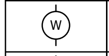	W	WATTÍMETRO
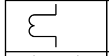	TC	TRANSFORMADOR DE CORRENTE
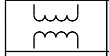	TP	TRANSFORMADOR DE POTENCIAL
	T	TERRA

SIMBOLO	SIGLA	DESCRIÇÃO
	M	MOTOR TRIFÁSICO
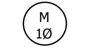	M	MOTOR MONOFÁSICO
	M	MOTOR CORRENTE CONTIÍNUA
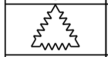	R	RESISTENCIA DE AQUECIMENTO
	SA	SELETOR AMPERÍMETRO
	SV	SELETOR VOLTIMETRO
	RFF	RELÉ FALTA DE FASE
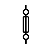	X	BORNE FUSÍVEL
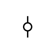	X	BORNE DE FORÇA E COMANDO

TABELA DE CABOS PVB/70ºC - NBR - 6148 ABNT

SÉRIE MÉTRICA (MM²)	AMPÈRES	SÉRIE MÉTRICA (MM²)	AMPÈRES
1,5	15,5	50	134
2,5	21	70	171
4	28	95	207
6	36	120	239
10	50	150	272
16	66	185	310
25	89	240	364
35	111	300	419

Rev.	Desc.	Data	Nome
05	As-Built de Fábrica	20/08/2019	Diego Almeida
04	Para Aprovação	14/06/2019	Diego Almeida
03	Conforme Comentários	07/06/2019	Diego Almeida
00	Emissão Inicial	28/05/2019	Ray Alves

TAG QE: QE-01

Simbologia

Nº VL BZX-QE-001-R05

Notas:

br-SAUTER

USP

Cliente
USP - Universidade de São Paulo

Obra
Absorption Refrigeration Cycle

Folha 5 De 44

SIMBOLO	DESCRIÇÃO
	FUSÍVEL
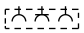	TOMADA
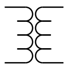	TRANSFORMADOR DE POTENCIAL
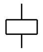	BOBINA / RELÉ
	CONTATO REVERSÍVEL
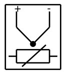	SENSOR DE TEMPERATURA
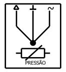	SENSOR DE PRESSÃO
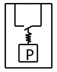	PRESSOSTATO DIFERENCIAL DE AR
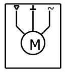	ATUADOR DE VÁLVULA

LEGENDA DE CABOS

ITEM	SIMBOLOGIA	DESCRIÇÃO	APLICAÇÃO	
1	———	CABO SINGELO 750V 70°C # 1,5mm²	FASE (VM) / NEUTRO (AZ) / TERRA (VERDE)	INTERL. INTERNAS
2	———	CABO SINGELO 750V 70°C # 1,0mm²	POSITIVO 24V AC (BR)	
3	———	CABO SINGELO 750V 70°C # 1,0mm²	POSITIVO 24V DC (CZ)	
4	———	CABO SINGELO 750V 70°C # 1,0mm²	NEGATIVO 24V AC/DC (PT)	
5	———	CABO SINGELO 750V 70°C # 0,75mm²	ENTRADAS DIGITAIS CABO SINAL (VM) CABO REF. (PT)	
6	———	CABO SINGELO 750V 70°C # 1,00mm²	SAIDAS DIGITAIS (BR/BR)	
7	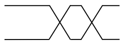	CABO PAR TORCIDO 2x0,75mm²	ENTRADAS ANALÓGICAS (VM/PT) SAIDAS ANALÓGICAS (VM/PT)	
8	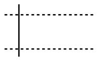	CABO MULTIVIAS OU SINGELO (750V 70°C # 0,75mm²) REF.:POLIRON - 175 CM (XX) CL5 FR Nº Vias x 0,75mm²	ENTRADAS DIGITAIS SAIDAS DIGITAIS	INTERLIGAÇÕES EXTERNAS
9	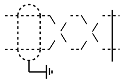	CABO PAR TORCIDO 0,75mm² COM MALHA REF.: POLIRON - 275 MA FR 2 x 0,75mm² (PT/BR)	ENTRADAS ANALÓGICAS SAIDAS ANALÓGICAS	
10	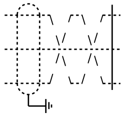	CABO TRIO TORCIDO 0,75mm² COM MALHA REF.: POLIRON - 375 MA FR 3 x 0,75mm² (VM/PT/BR)	ENTRADAS ANALÓGICAS SAIDAS ANALÓGICAS	

Rev.	Desc.	Data	Nome
05	As-Built de Fábrica	20/08/2019	Diego Almeida
04	Para Aprovação	14/06/2019	Diego Almeida
03	Conforme Comentários	07/06/2019	Diego Almeida
00	Emissão Inicial	28/05/2019	Ray Alves

TAG QE:
QE-01

Simbologia

Nº VL
BZX-QE-001-R05

Notas:

br-SAUTER

USP

Cliente
USP - Universidade de São Paulo

Obra
Absorption Refrigeration Cycle

Folha 6
De 44

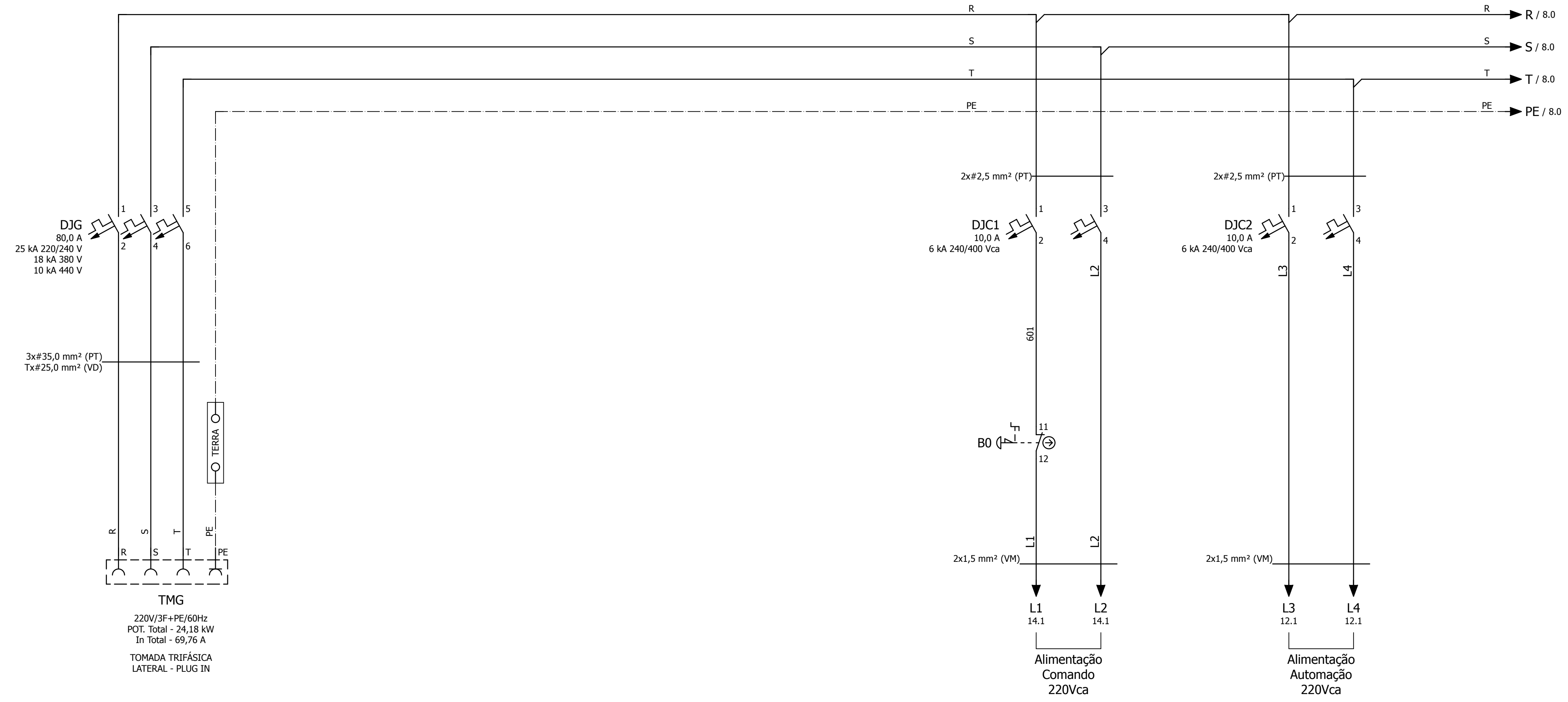

BALANCEAMENTO:

CORRENTE	CORRENTE
R: 75,76 A	R: 24,61 kW
S: 48,21 A	S: 14,11 kW
T: 67,56 A	T: 24,00 kW

Rev.	Desc.	Data	Nome
05	As-Built de Fábrica	20/08/2019	Diego Almeida
04	Para Aprovação	14/06/2019	Diego Almeida
03	Conforme Comentários	07/06/2019	Diego Almeida
00	Emissão Inicial	28/05/2019	Ray Alves

TAG QE: QE-01

Potência

Nº VL: BZX-QE-001-R05

Notas:

br-SAUTER

Cliente: USP - Universidade de São Paulo

Obra: Absorption Refrigeration Cycle

Folha 7 De 44

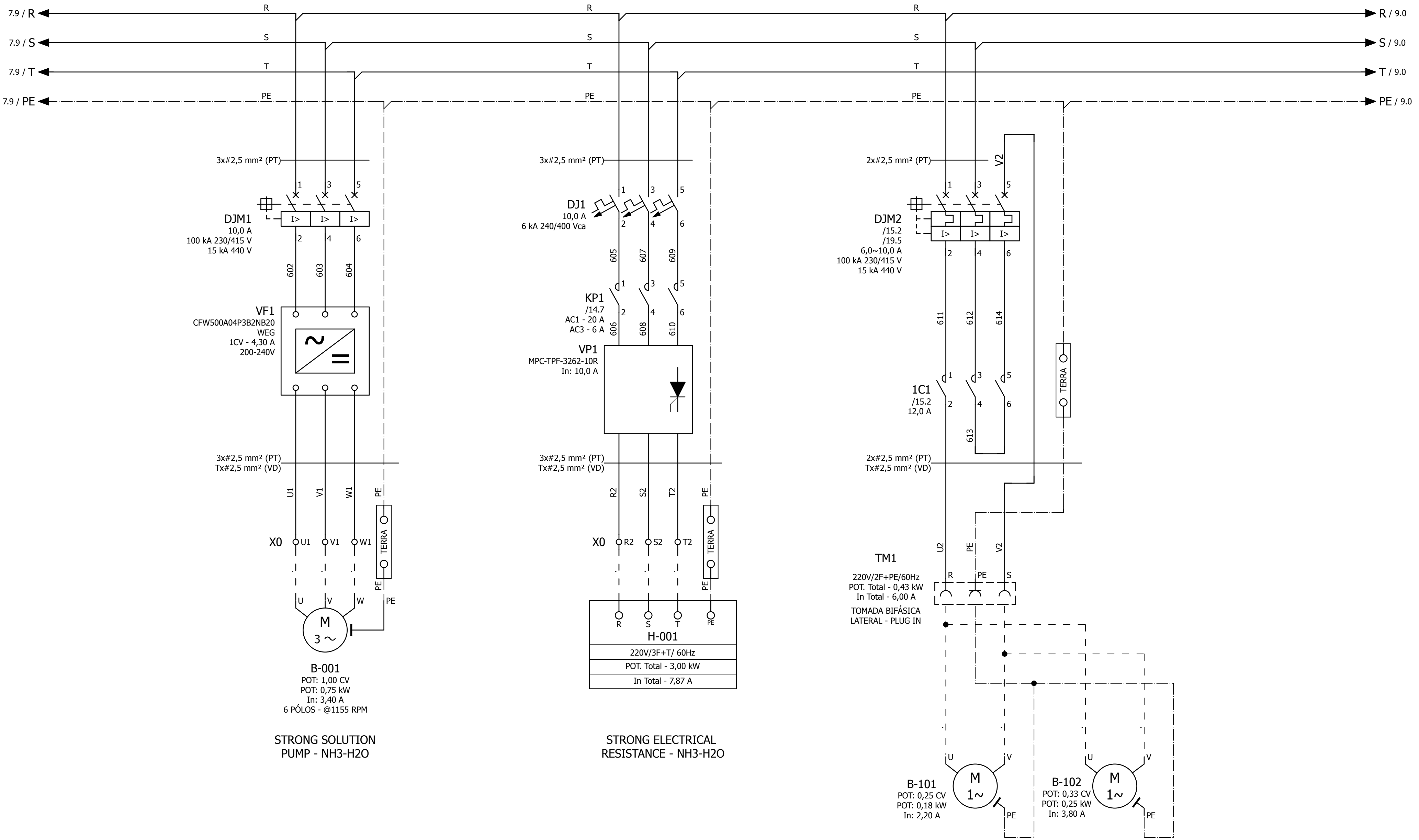

AMMONIA SYSTEM

Rev.	Desc.	Data	Nome
05	As-Built de Fábrica	20/08/2019	Diego Almeida
04	Para Aprovação	14/06/2019	Diego Almeida
03	Conforme Comentários	07/06/2019	Diego Almeida
00	Emissão Inicial	28/05/2019	Ray Alves

TAG QE: QE-01

Potência

Nº VL: BZX-QE-001-R05

Notas:

br-SAUTER

Cliente: USP - Universidade de São Paulo

Obra: Absorption Refrigeration Cycle

Folha: 8

De: 44

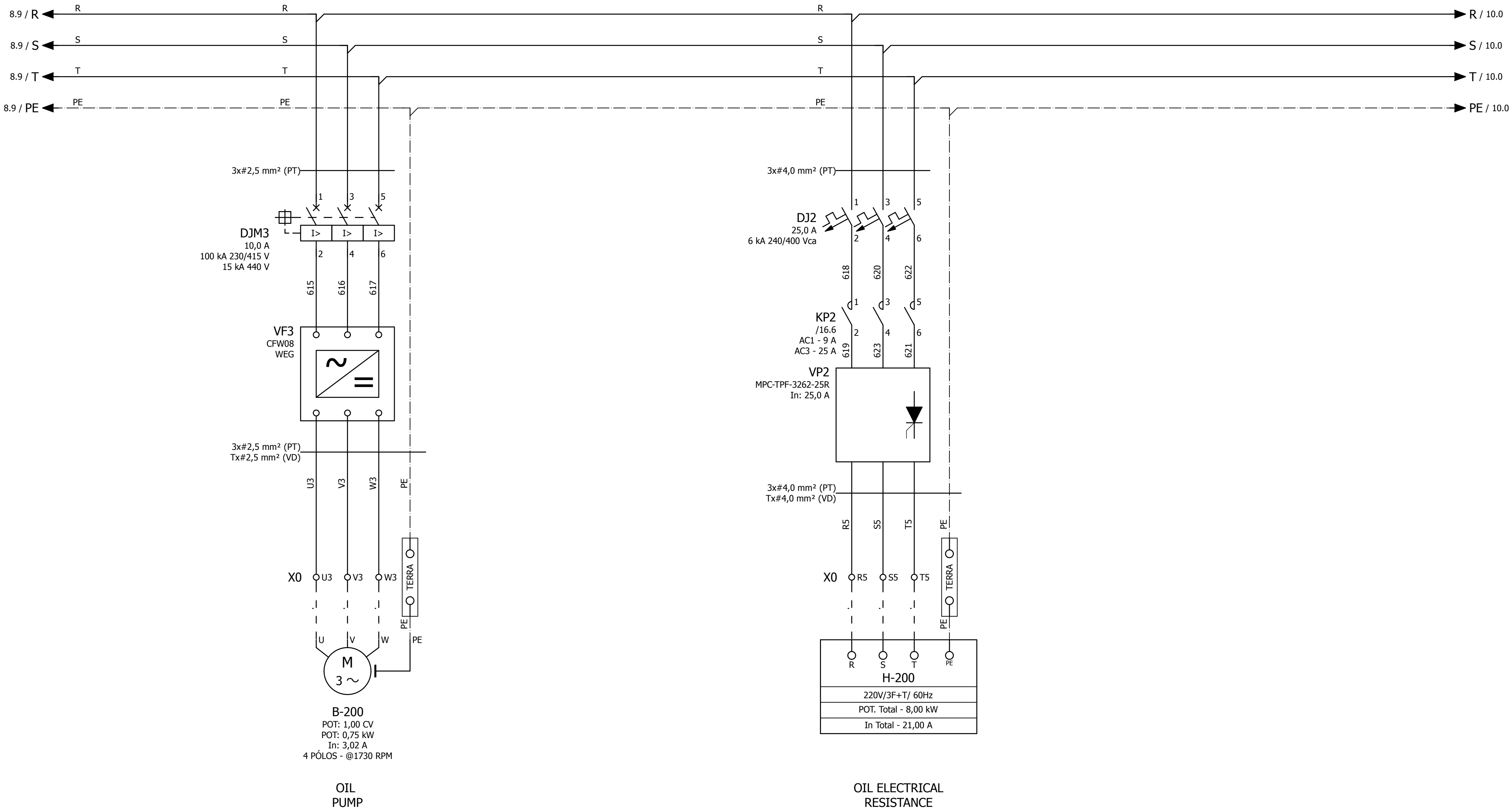

OIL SYSTEM

Rev.	Desc.	Data	Nome
05	As-Built de Fábrica	20/08/2019	Diego Almeida
04	Para Aprovação	14/06/2019	Diego Almeida
03	Conforme Comentários	07/06/2019	Diego Almeida
00	Emissão Inicial	28/05/2019	Ray Alves

TAG QE: QE-01

Potência

Nº VL BZX-QE-001-R05

Notas:

br-SAUTER

USP

Cliente
USP - Universidade de São Paulo

Obra
Absorption Refrigeration Cycle

Folha 9

De 44

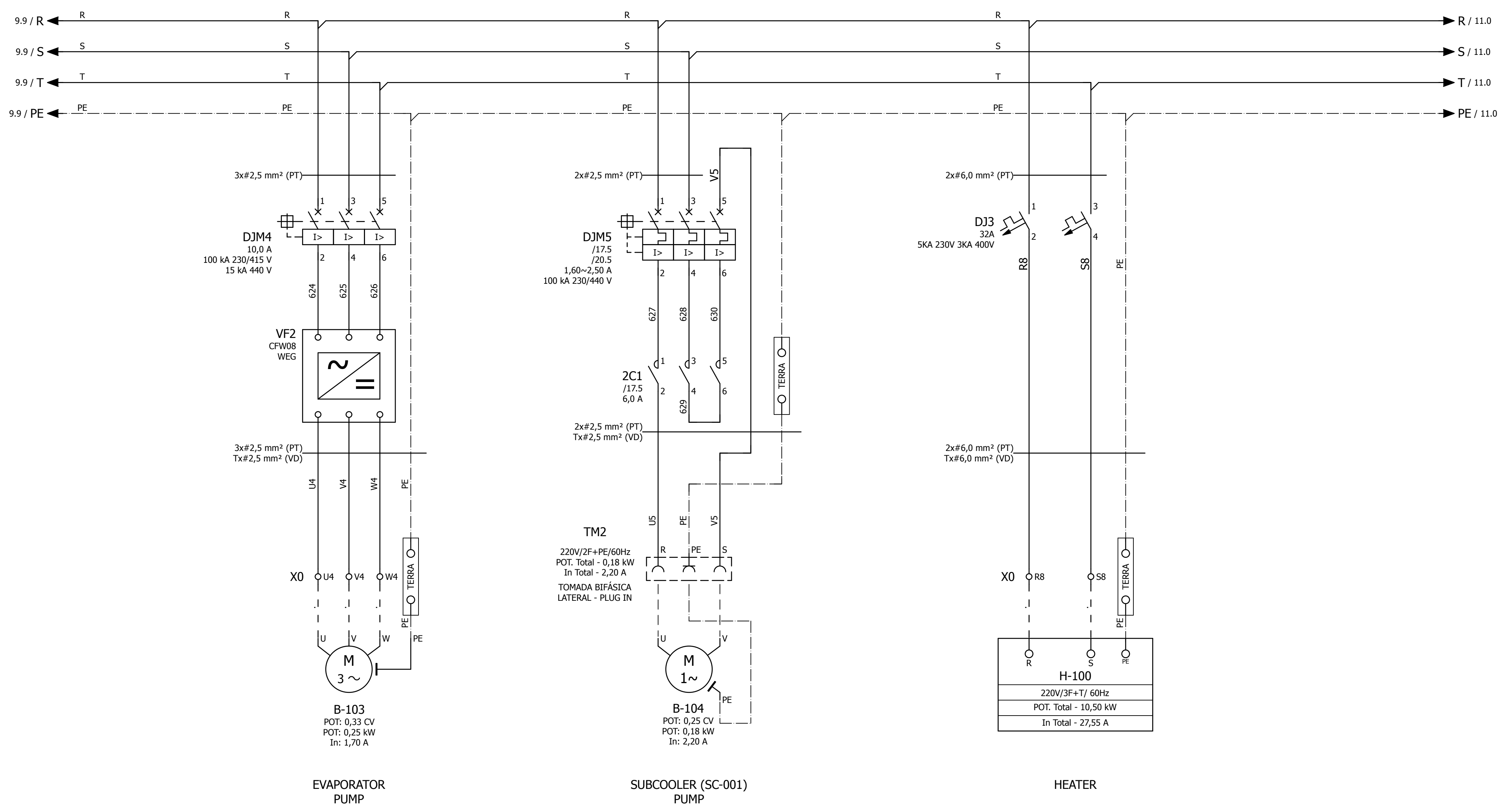

HEATING - COOLING CIRCUIT

Rev.	Desc.	Data	Nome
05	As-Built de Fábrica	20/08/2019	Diego Almeida
04	Para Aprovação	14/06/2019	Diego Almeida
03	Conforme Comentários	07/06/2019	Diego Almeida
00	Emissão Inicial	28/05/2019	Ray Alves

TAG QE: QE-01

Potência

Nº VL: BZX-QE-001-R05

Notas:

br-SAUTER

Cliente: USP - Universidade de São Paulo

Obra: Absorption Refrigeration Cycle

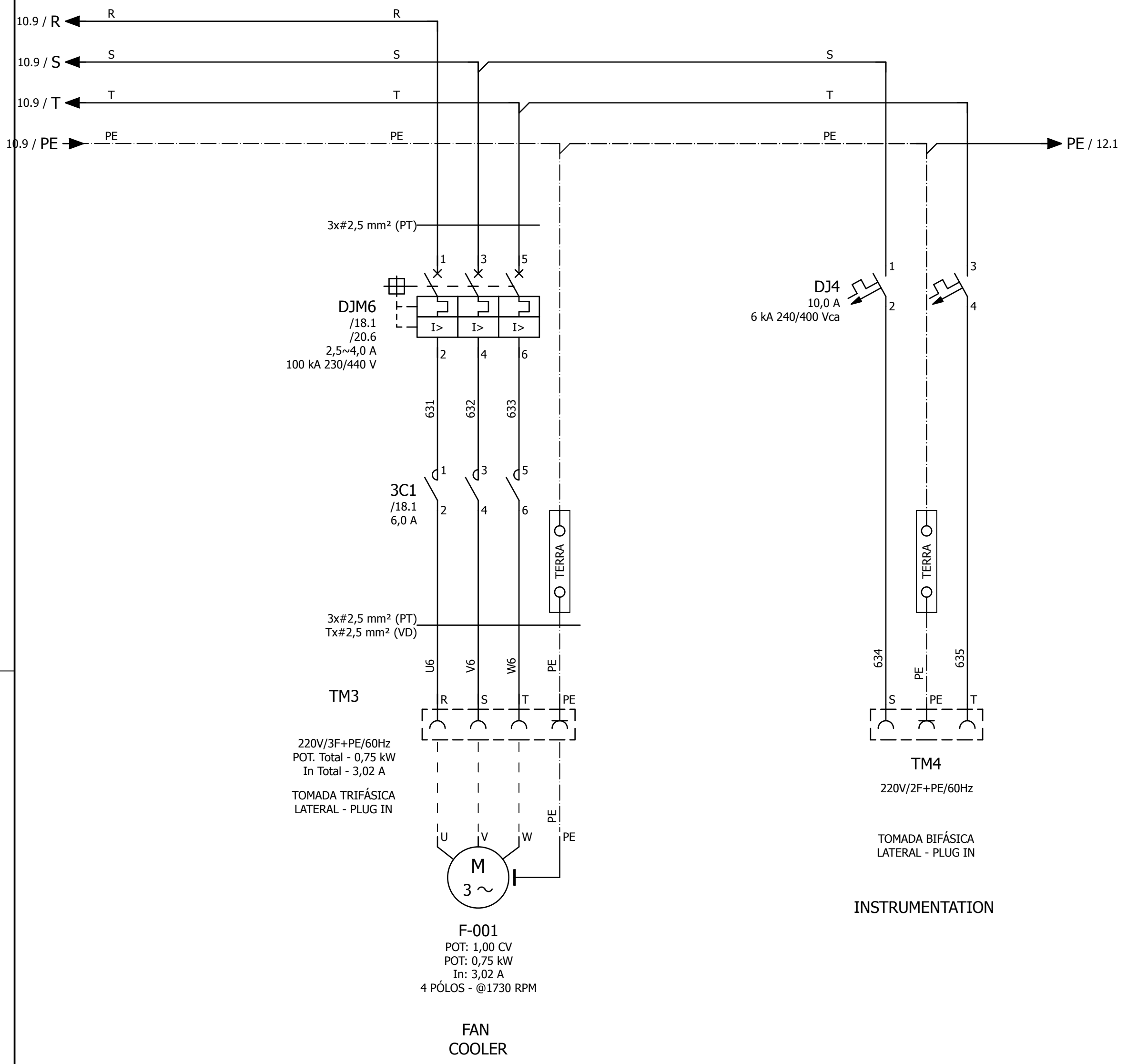

FAN - COOLER SYSTEM

Rev.	Desc.	Data	Nome
05	As-Built de Fábrica	20/08/2019	Diego Almeida
04	Para Aprovação	14/06/2019	Diego Almeida
03	Conforme Comentários	07/06/2019	Diego Almeida
00	Emissão Inicial	28/05/2019	Ray Alves

TAG QE: QE-01

Potência

Nº VL: BZX-QE-001-R05

Notas:

br-SAUTER

Cliente: USP - Universidade de São Paulo

Obra: Absorption Refrigeration Cycle

Folha: 11

De: 44

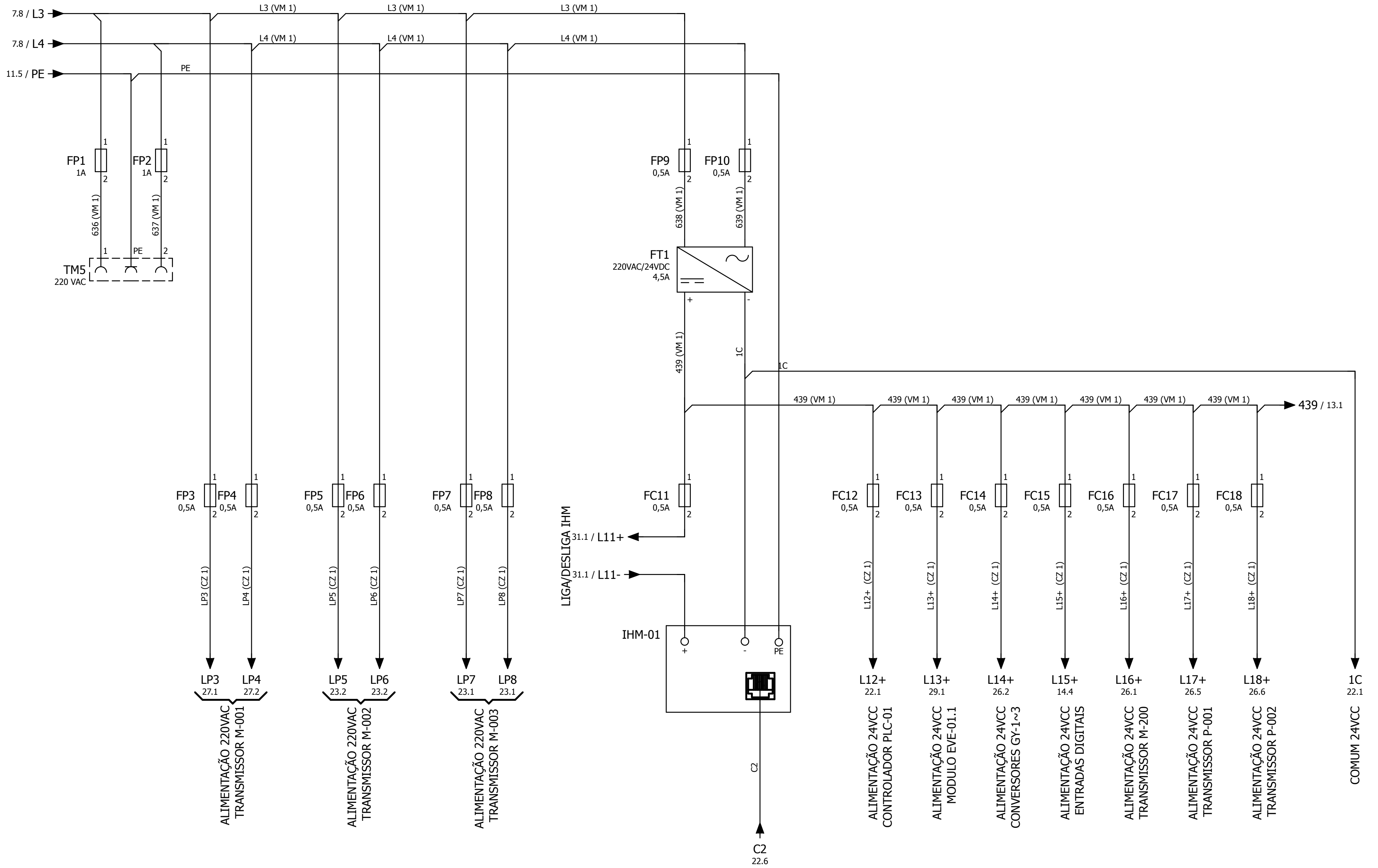

Rev.	Desc.	Data	Nome
05	As-Built de Fábrica	20/08/2019	Diego Almeida
04	Para Aprovação	14/06/2019	Diego Almeida
03	Conforme Comentários	07/06/2019	Diego Almeida
00	Emissão Inicial	28/05/2019	Ray Alves

TAG QE: QE-01

Potência

Nº VL BZX-QE-001-R05

Notas:

br-SAUTER

USP

Cliente
USP - Universidade de São Paulo

Obra
Absorption Refrigeration Cycle

Folha 12
De 44

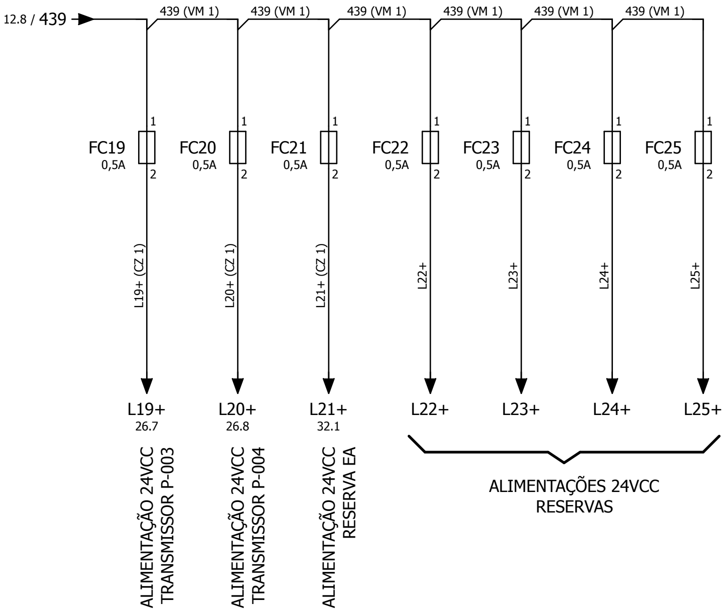

05	As-Built de Fábrica	20/08/2019	Diego Almeida
04	Para Aprovação	14/06/2019	Diego Almeida
03	Conforme Comentários	07/06/2019	Diego Almeida
00	Emissão Inicial	28/05/2019	Ray Alves
Rev.	Desc.	Data	Nome

TAG QE:
QE-01

Potência

Nº VL
BZX-QE-001-R05

Notas:

br-SAUTER

USP

Cliente
USP - Universidade de São Paulo

Obra
Absorption Refrigeration Cycle

Folha
13

De
44

AMMONIA PUMP

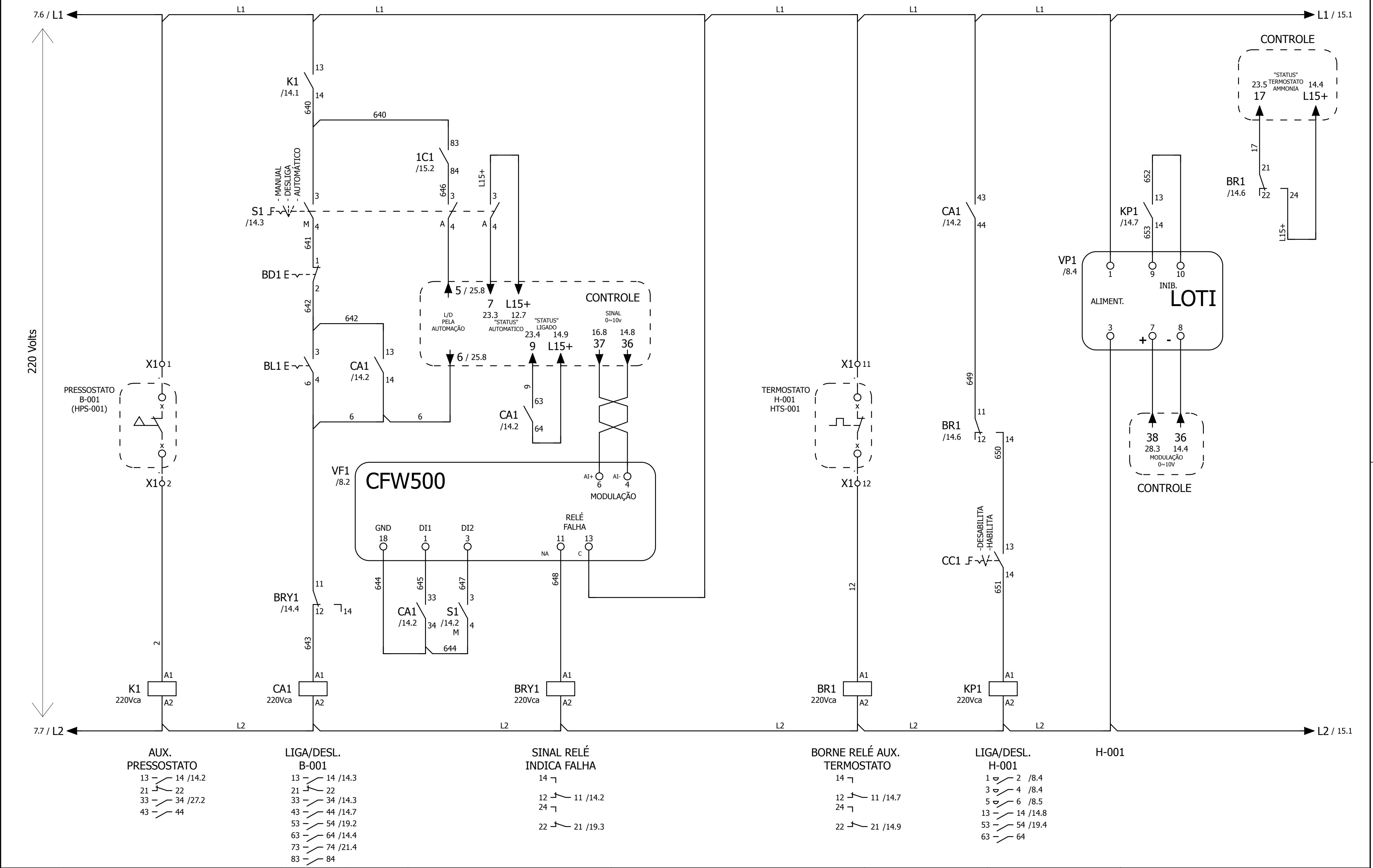

Rev.	Desc.	Data	Nome
05	As-Built de Fábrica	20/08/2019	Diego Almeida
04	Para Aprovação	14/06/2019	Diego Almeida
03	Conforme Comentários	07/06/2019	Diego Almeida
00	Emissão Inicial	28/05/2019	Ray Alves

TAG QE:
QE-01

Nº VL
BZX-QE-001-R05

Comando
Ammonia System

Notas:

br-SAUTER

Cliente
USP - Universidade de São Paulo

Obra
Absorption Refrigeration Cycle

Folha 14 De 44

COOLANT CIRCUIT

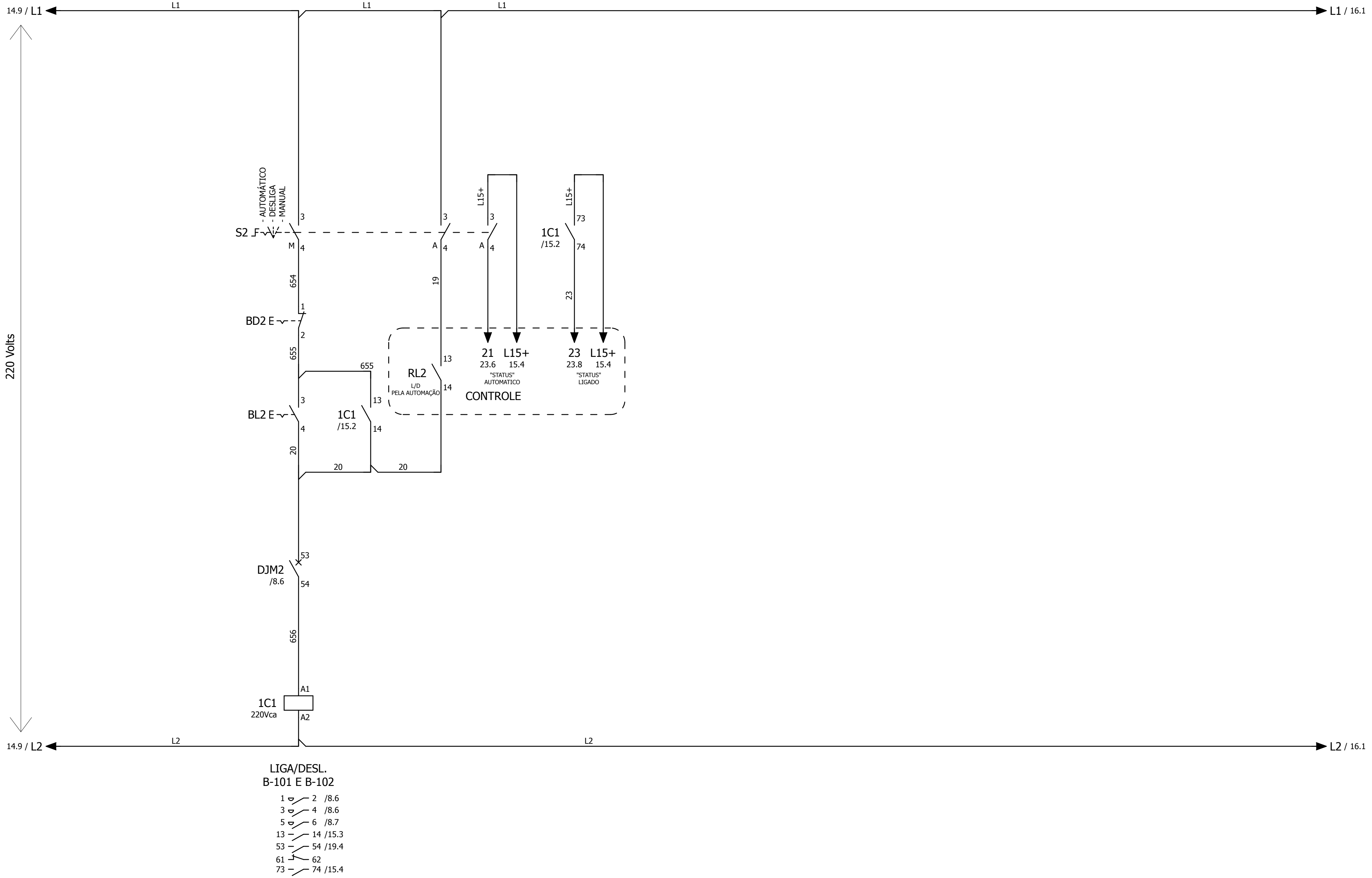

Rev.	Desc.	Data	Nome
05	As-Built de Fábrica	20/08/2019	Diego Almeida
04	Para Aprovação	14/06/2019	Diego Almeida
03	Conforme Comentários	07/06/2019	Diego Almeida
00	Emissão Inicial	28/05/2019	Ray Alves

TAG QE:
QE-01

N° VL
BZX-QE-001-R05

Comando
Ammonia System

Notas:

br-SAUTER

USP

Cliente
USP - Universidade de São Paulo

Obra
Absorption Refrigeration Cycle

Folha 15
De 44

OIL PUMP

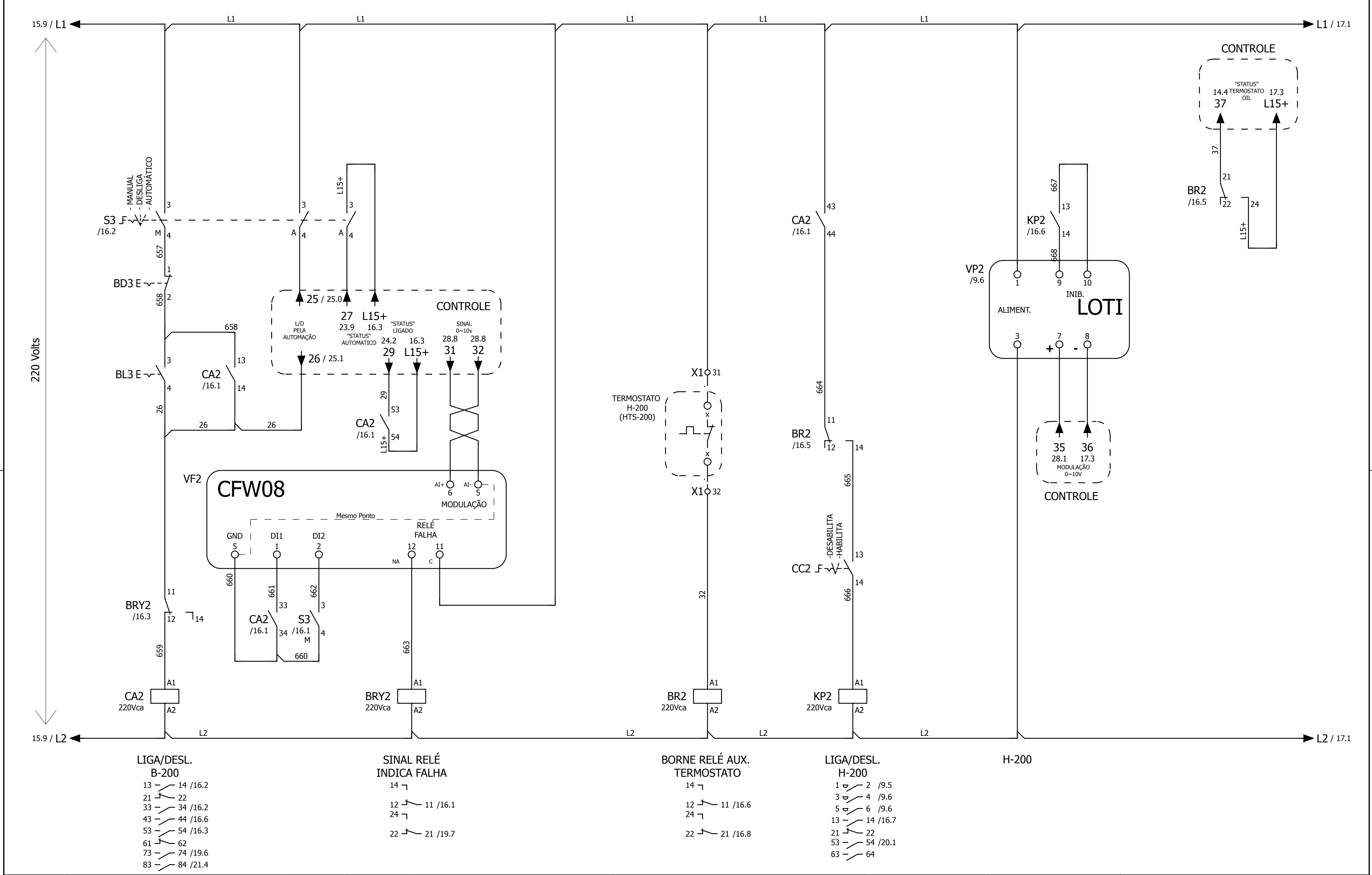

Rev.	Desc.	Data	Nome
05	As-Built de Fábrica	20/08/2019	Diego Almeida
04	Para Aprovação	14/06/2019	Diego Almeida
03	Conforme Comentários	07/06/2019	Diego Almeida
00	Emissão Inicial	28/05/2019	Ray Alves

TAG QE:
QE-01

Nº VL
BZX-QE-001-R05

Comando
Oil System

Notas:

br-SAUTER

USP

Cliente
USP - Universidade de São Paulo

Obra
Absorption Refrigeration Cycle

Folha 16 De 44

COOLAN CIRCUIT

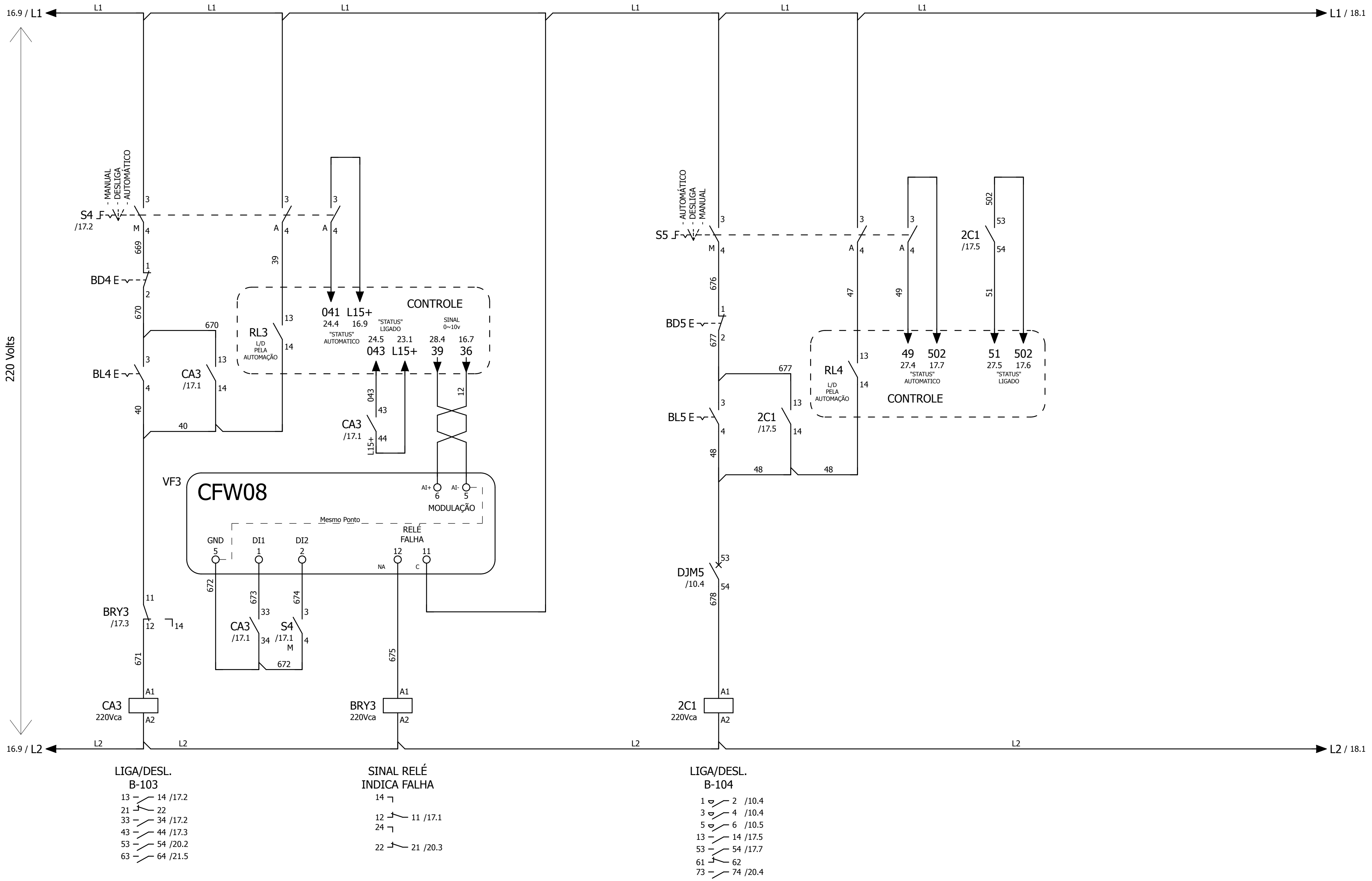

Rev.	Desc.	Data	Nome
05	As-Built de Fábrica	20/08/2019	Diego Almeida
04	Para Aprovação	14/06/2019	Diego Almeida
03	Conforme Comentários	07/06/2019	Diego Almeida
00	Emissão Inicial	28/05/2019	Ray Alves

TAG QE: QE-01

Nº VL: BZX-QE-001-R05

Comando
Coolan Circuit

Notas:

br-SAUTER

Cliente
USP - Universidade de São Paulo

Obra
Absorption Refrigeration Cycle

Folha 17 De 44

FAN - COOLER

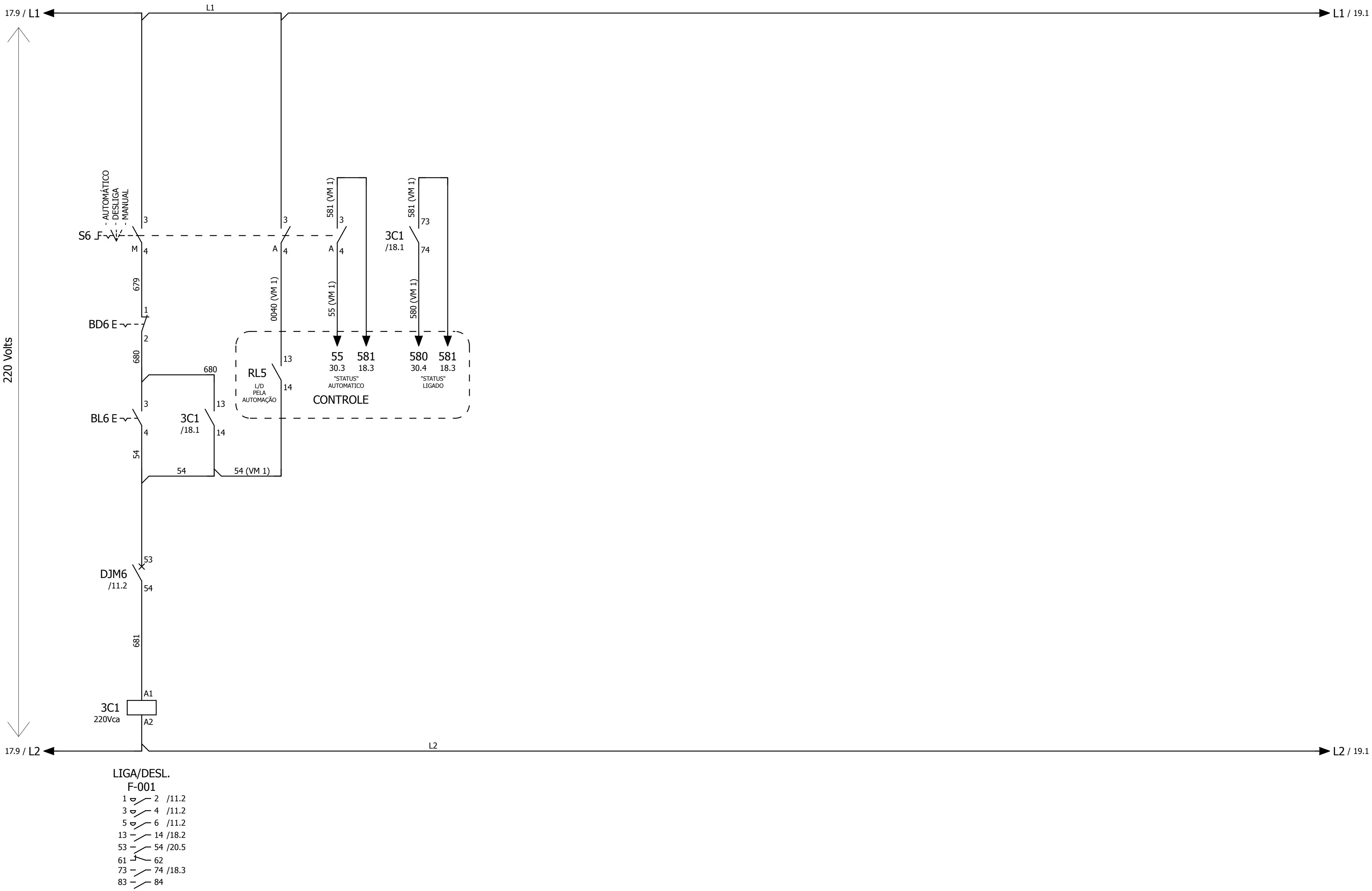

Rev.	Desc.	Data	Nome
05	As-Built de Fábrica	20/08/2019	Diego Almeida
04	Para Aprovação	14/06/2019	Diego Almeida
03	Conforme Comentários	07/06/2019	Diego Almeida
00	Emissão Inicial	28/05/2019	Ray Alves

TAG QE: QE-01

Comando
Fan Cooler

N° VL
BZX-QE-001-R05

Notas:

br-SAUTER

Cliente
USP - Universidade de São Paulo

Obra
Absorption Refrigeration Cycle

Folha 18

De 44

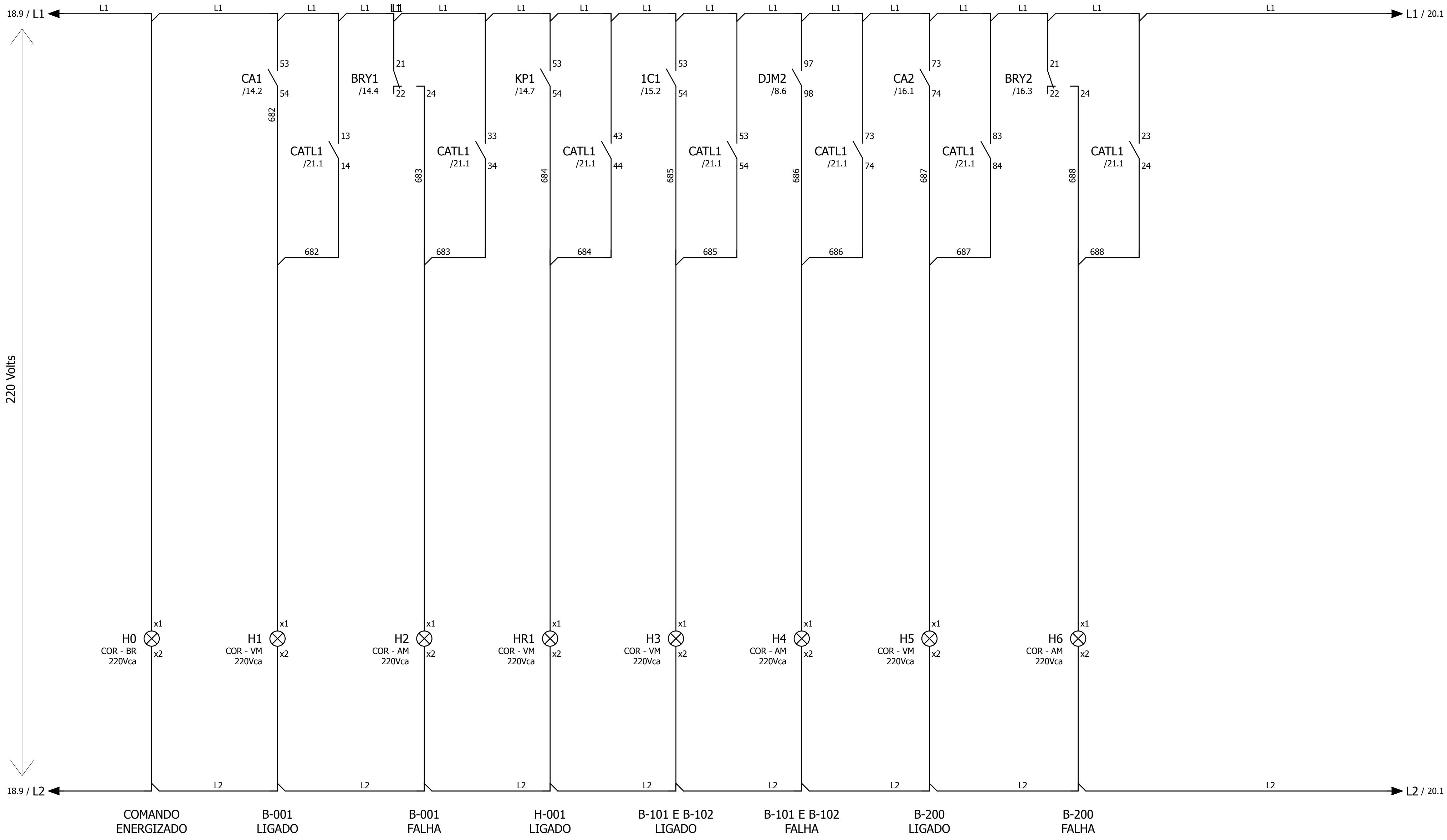

Rev.	Desc.	Data	Nome
05	As-Built de Fábrica	20/08/2019	Diego Almeida
04	Para Aprovação	14/06/2019	Diego Almeida
03	Conforme Comentários	07/06/2019	Diego Almeida
00	Emissão Inicial	28/05/2019	Ray Alves

TAG QE: QE-01

Sinalização

Nº VL BZX-QE-001-R05

Notas:

br-SAUTER

Cliente
USP - Universidade de São Paulo

Obra
Absorption Refrigeration Cycle

Folha 19 De 44

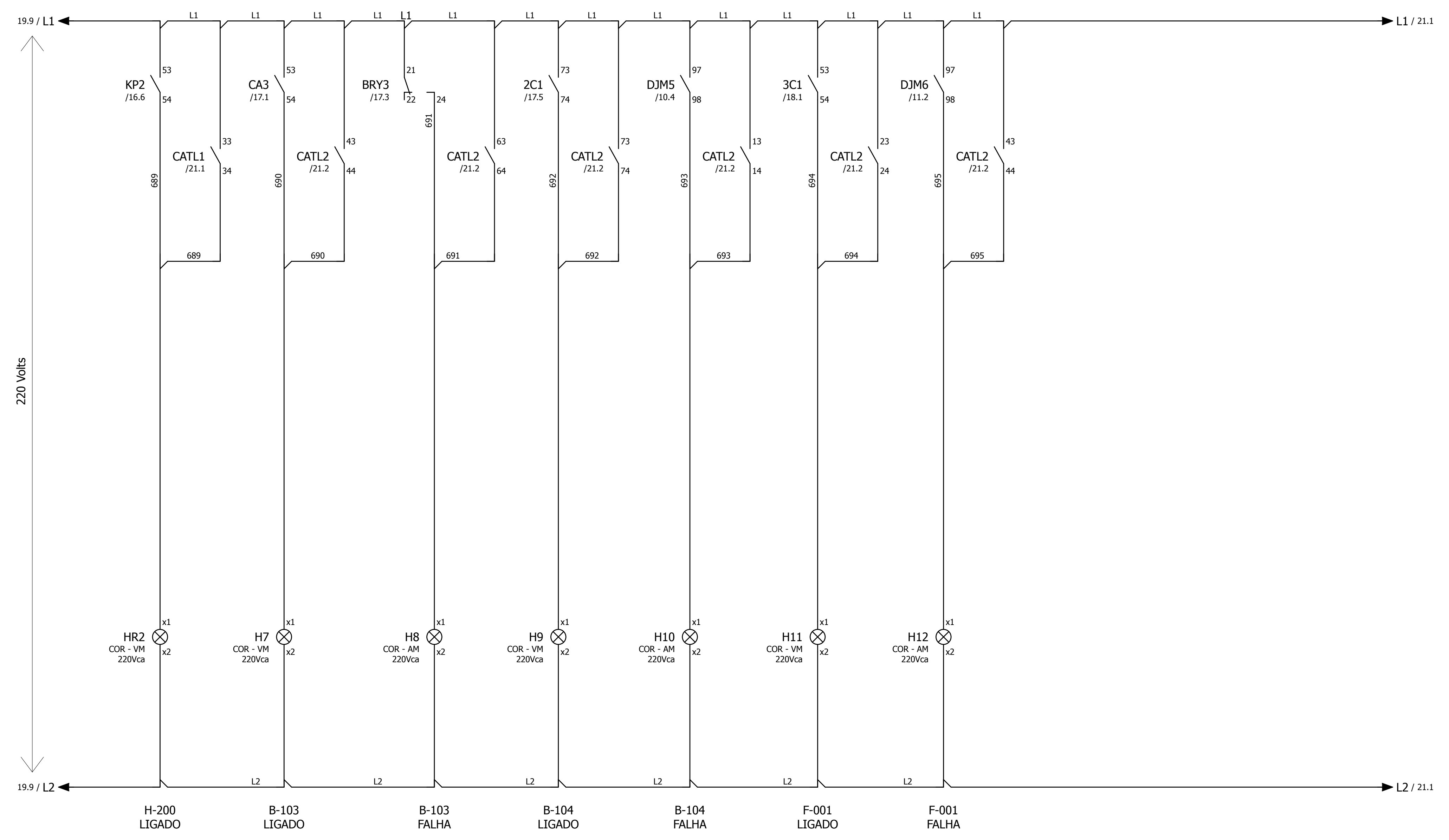

Rev.	Desc.	Data	Nome
05	As-Built de Fábrica	20/08/2019	Diego Almeida
04	Para Aprovação	14/06/2019	Diego Almeida
03	Conforme Comentários	07/06/2019	Diego Almeida
00	Emissão Inicial	28/05/2019	Ray Alves

TAG QE:
QE-01

Nº VL
BZX-QE-001-R05

Sinalização

Notas:

br-SAUTER

Cliente
USP - Universidade de São Paulo

Obra
Absorption Refrigeration Cycle

Folha 20
De 44

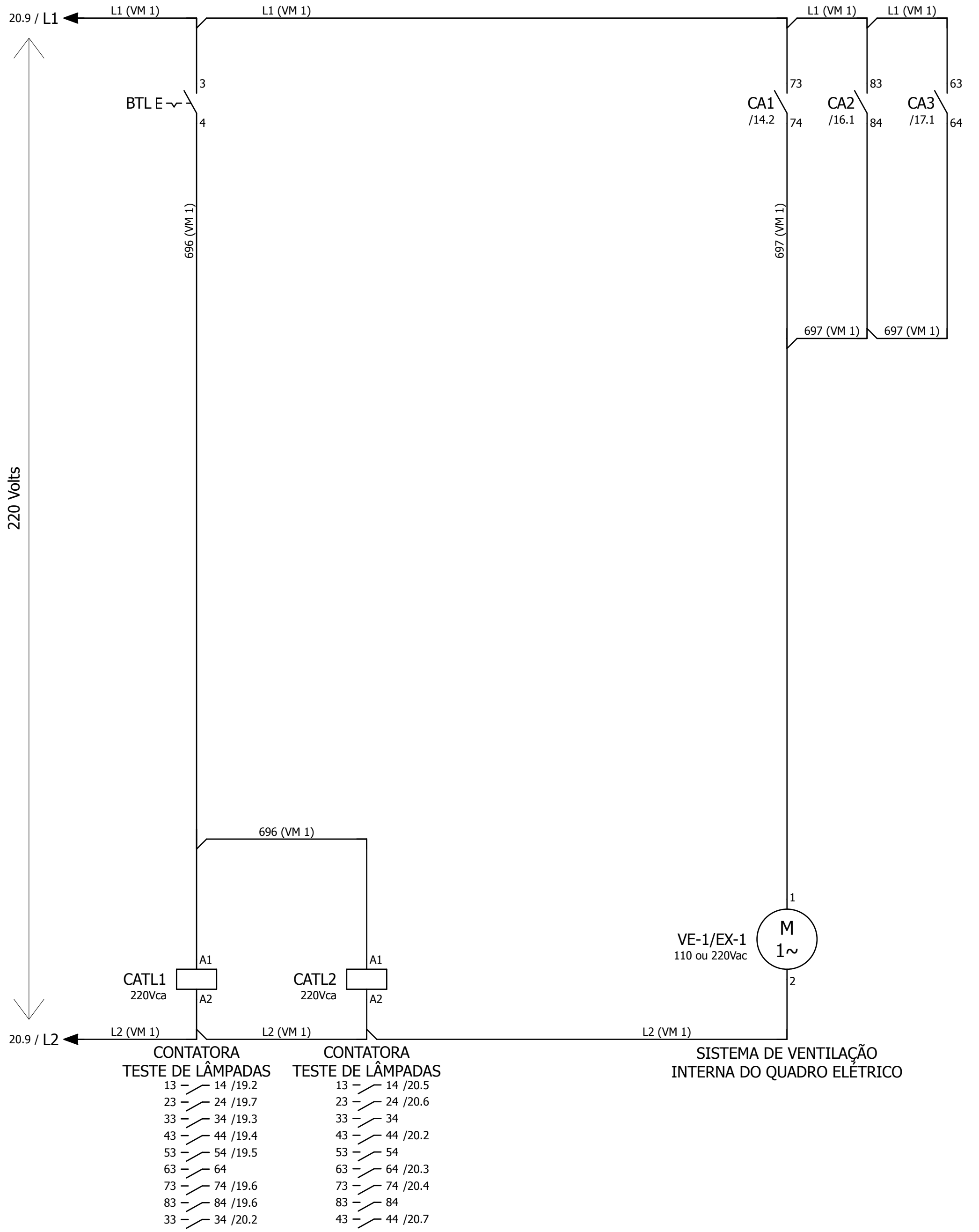

Rev.	Desc.	Data	Nome
05	As-Built de Fábrica	20/08/2019	Diego Almeida
04	Para Aprovação	14/06/2019	Diego Almeida
03	Conforme Comentários	07/06/2019	Diego Almeida
00	Emissão Inicial	28/05/2019	Ray Alves

TAG QE:
QE-01

Sinalização

Nº VL
BZX-QE-001-R05

Notas:

br-SAUTER

USP

Cliente
USP - Universidade de São Paulo

Obra
Absorption Refrigeration Cycle

Folha	De
21	44

MODELO: AVC12600/C/L/U
Réguas bornes: CN10; CN19; CN1; CN18
IP: 192.168.10.1

PLC-01 / ALIMENTAÇÃO - REDE

PLC-01
/23.0
/24.0
/25.0
/26.0
/27.0
/28.0

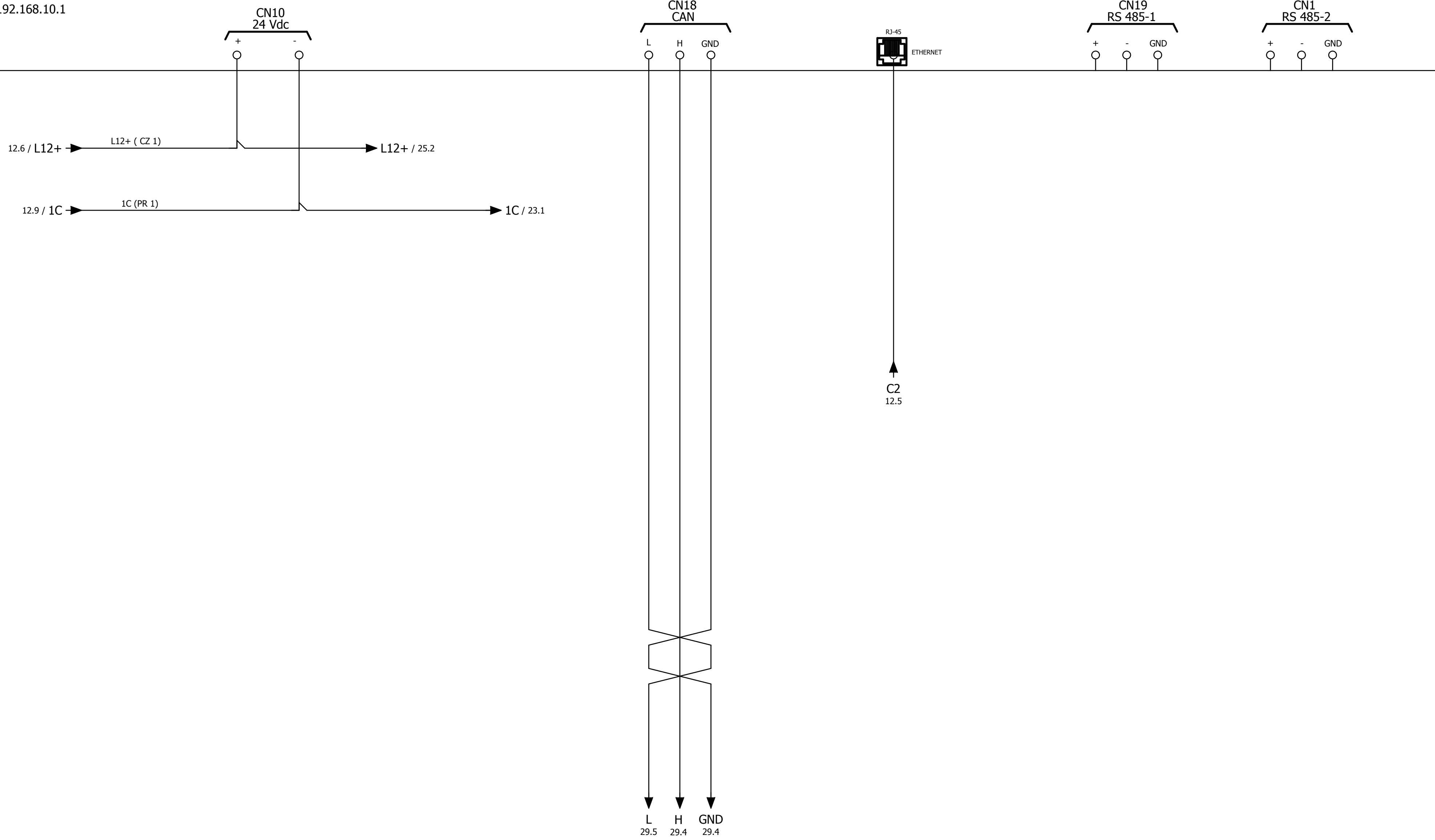

Rev.	Desc.	Data	Nome
05	As-Built de Fábrica	20/08/2019	Diego Almeida
04	Para Aprovação	14/06/2019	Diego Almeida
03	Conforme Comentários	07/06/2019	Diego Almeida
00	Emissão Inicial	28/05/2019	Ray Alves

TAG QE: QE-01

Controlador PLC-01

Nº VL BZX-QE-001-R05

Notas:

br-SAUTER

Cliente
USP - Universidade de São Paulo

Obra
Absorption Refrigeration Cycle

Folha 22 De 44

MODELO: AVC12600/C/L/U
Réguas borne: CN3; CN4
IP: 192.168.10.1

PLC-01 / ENTRADAS DIGITAIS

PLC-01
/22.0

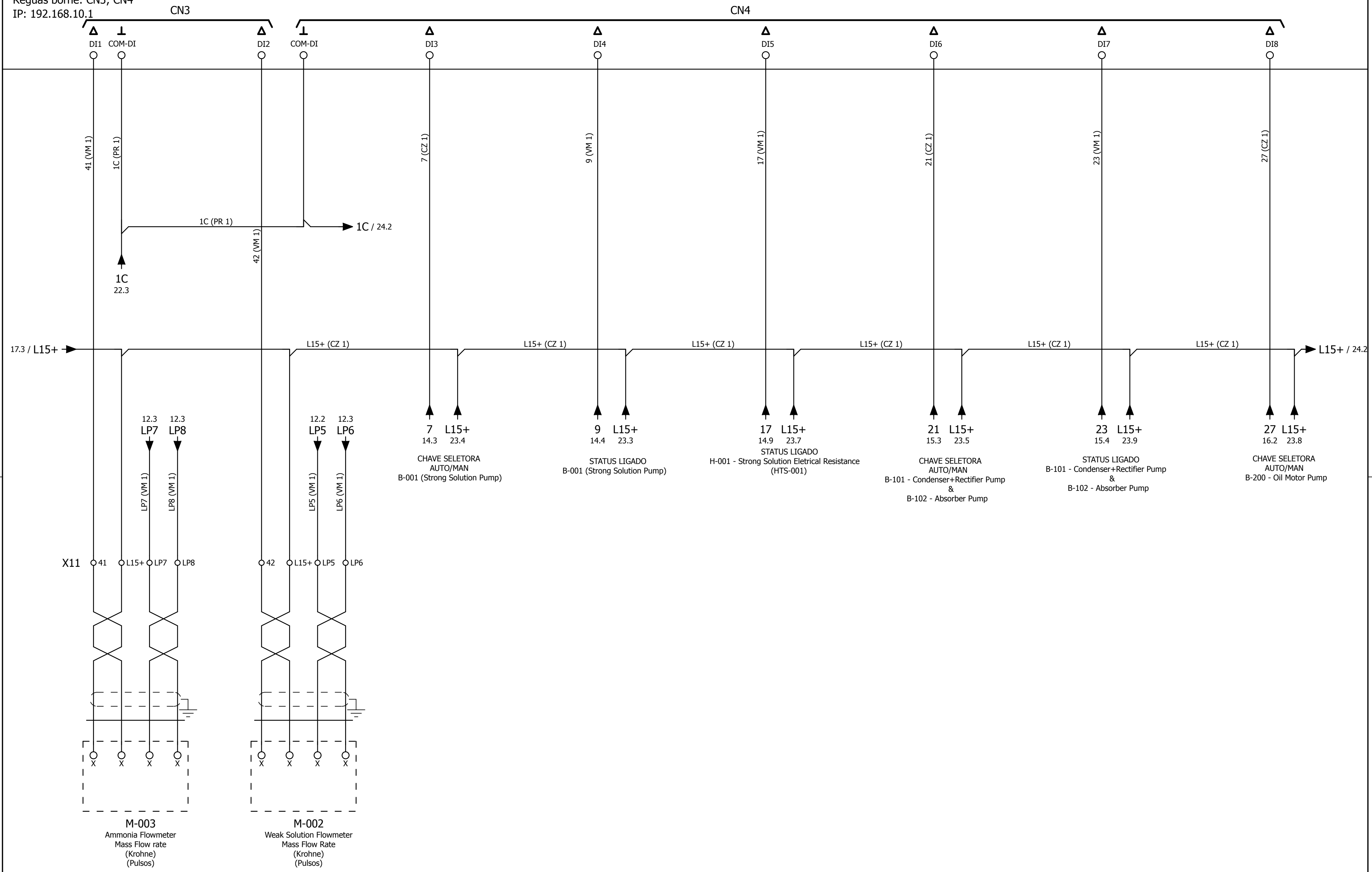

Rev.	Desc.	Data	Nome
05	As-Built de Fábrica	20/08/2019	Diego Almeida
04	Para Aprovação	14/06/2019	Diego Almeida
03	Conforme Comentários	07/06/2019	Diego Almeida
00	Emissão Inicial	28/05/2019	Ray Alves

TAG QE: QE-01

Controlador PLC-01 - ED

Nº VL: BZX-QE-001-R05

Notas:

br-SAUTER

USP

Cliente: USP - Universidade de São Paulo

Obra: Absorption Refrigeration Cycle

Folha: 23 De: 44

MODELO: AVC12600/C/L/U
Réguas borne:CN12
IP: 192.168.10.1

PLC-01 / ENTRADAS DIGITAIS

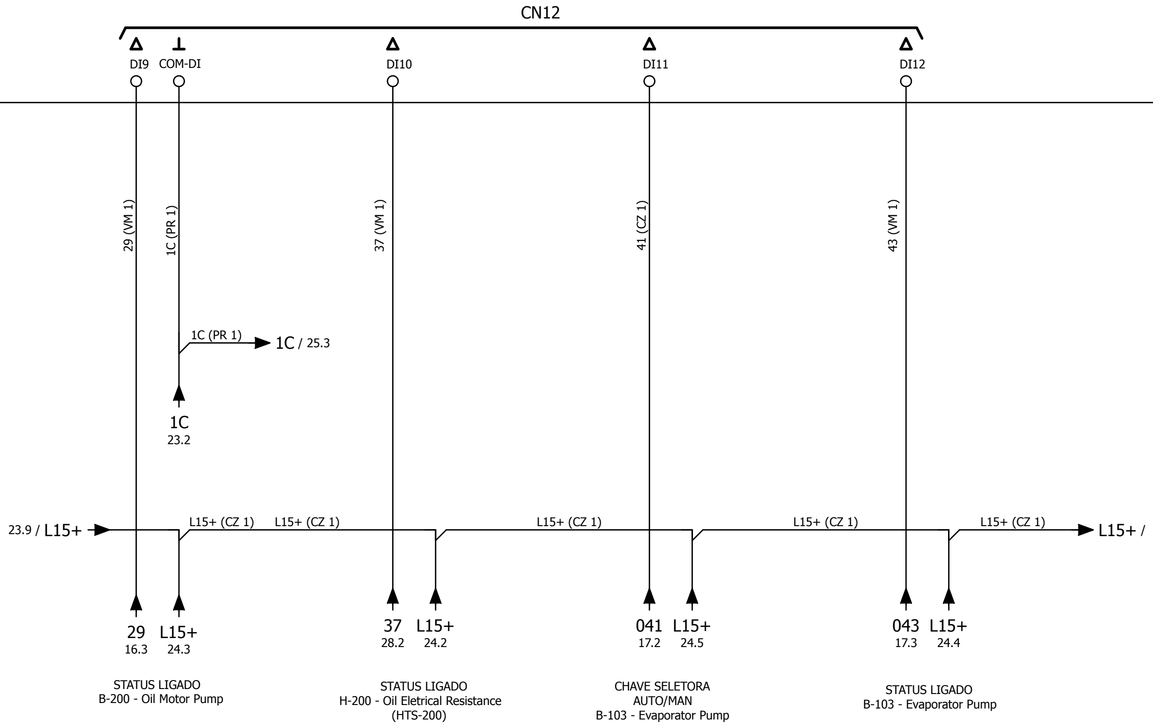

Rev.	Desc.	Data	Nome
05	As-Built de Fábrica	20/08/2019	Diego Almeida
04	Para Aprovação	14/06/2019	Diego Almeida
03	Conforme Comentários	07/06/2019	Diego Almeida
00	Emissão Inicial	28/05/2019	Ray Alves

TAG QE: QE-01

Controlador PLC-01 - ED

N° VL
BZX-QE-001-R05

Notas:

br-SAUTER

Cliente
USP - Universidade de São Paulo

Obra
Absorption Refrigeration Cycle

Folha 24
De 44

MODELO: AVC12600/C/L/U
Réguas borne:CN9
IP: 192.168.10.1

PLC-01 / SAÍDAS DIGITAIS (RELE)

PLC-01
/22.0

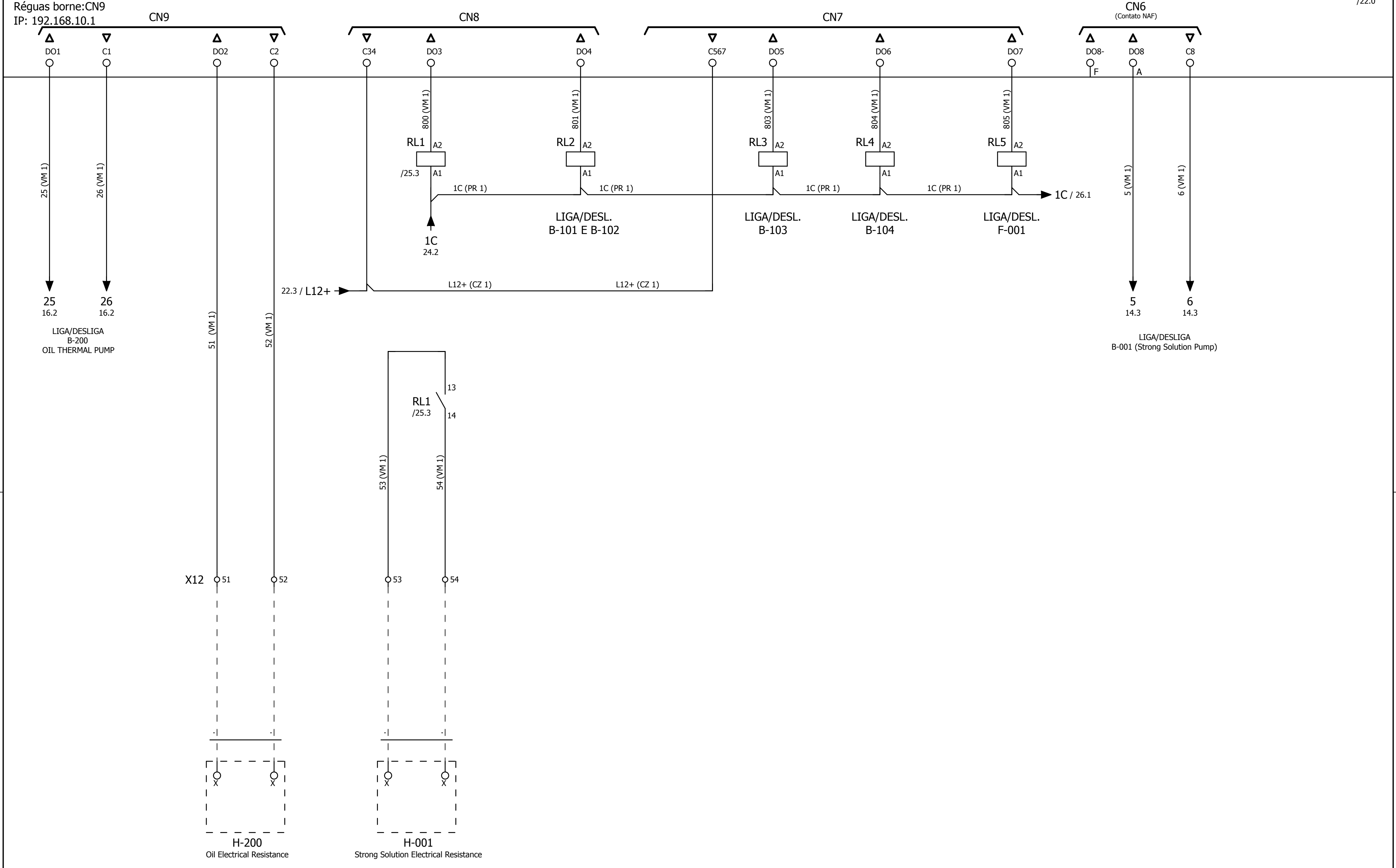

Rev.	Desc.	Data	Nome
05	As-Built de Fábrica	20/08/2019	Diego Almeida
04	Para Aprovação	14/06/2019	Diego Almeida
03	Conforme Comentários	07/06/2019	Diego Almeida
00	Emissão Inicial	28/05/2019	Ray Alves

TAG QE: QE-01

Controlador PLC-01 - SD

Nº VL: BZX-QE-001-R05

Notas:

br-SAUTER

Cliente
USP - Universidade de São Paulo

Obra
Absorption Refrigeration Cycle

Folha 25
De 44

MODELO: AVC12600/C/L/U
Réguas borne:CN5
IP: 192.168.10.1

PLC-01 / ENTRADAS ANALÓGICAS (4~20mA)/(0~10v)

PLC-01
/22.0

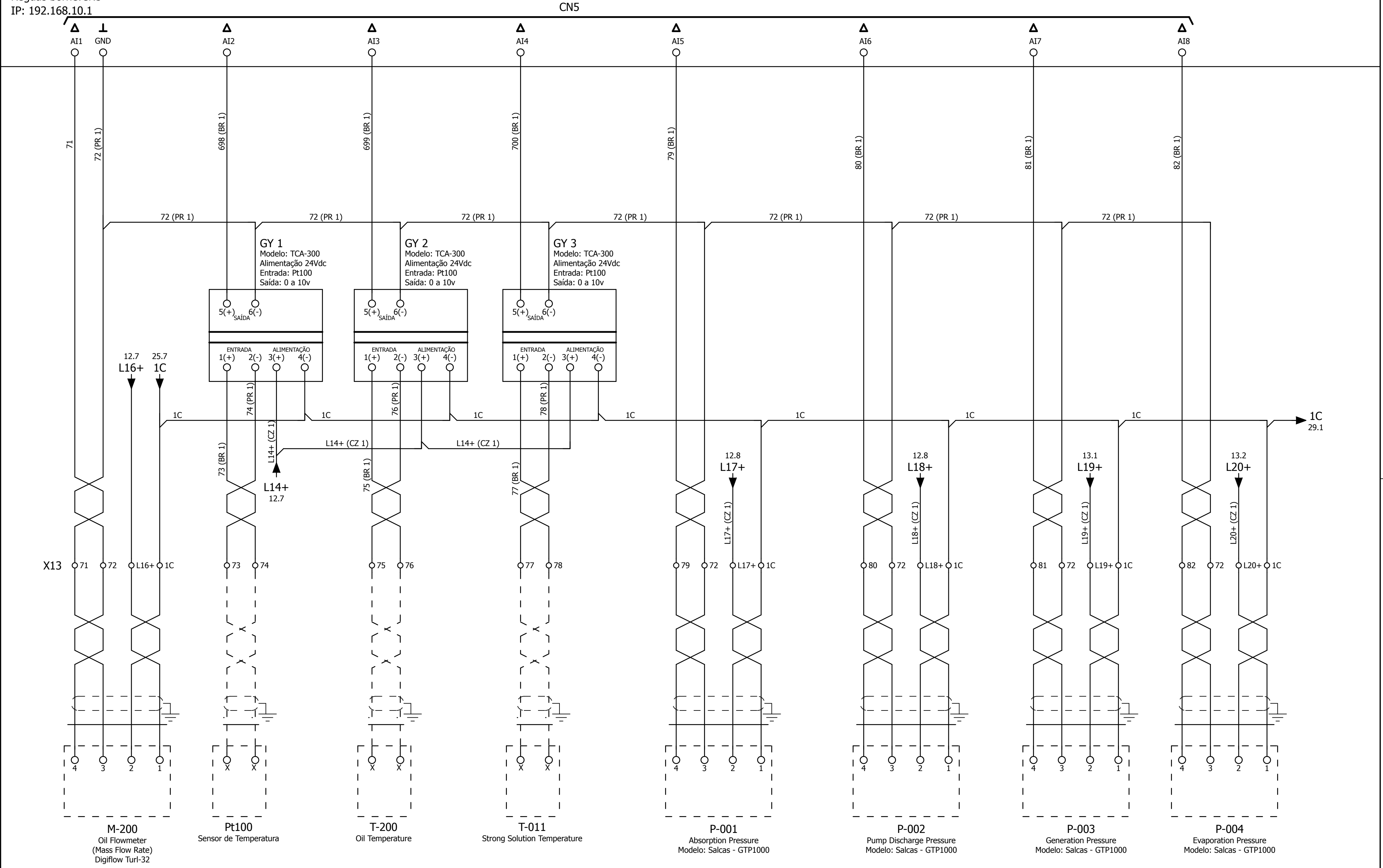

Rev.	Desc.	Data	Nome
05	As-Built de Fábrica	20/08/2019	Diego Almeida
04	Para Aprovação	14/06/2019	Diego Almeida
03	Conforme Comentários	07/06/2019	Diego Almeida
00	Emissão Inicial	28/05/2019	Ray Alves

TAG QE: QE-01

Controlador PLC-01 - EA

Nº VL: BZX-QE-001-R05

Notas:

br-SAUTER

USP

Cliente: USP - Universidade de São Paulo

Obra: Absorption Refrigeration Cycle

Folha: 26 De: 44

MODELO: AVC12600/C/L/U
Réguas borne:CN13
IP: 192.168.10.1

PLC-01 / ENTRADAS ANALÓGICAS (4~20mA) / ENTRADAS DIGITAIS

PLC-01
/22.0

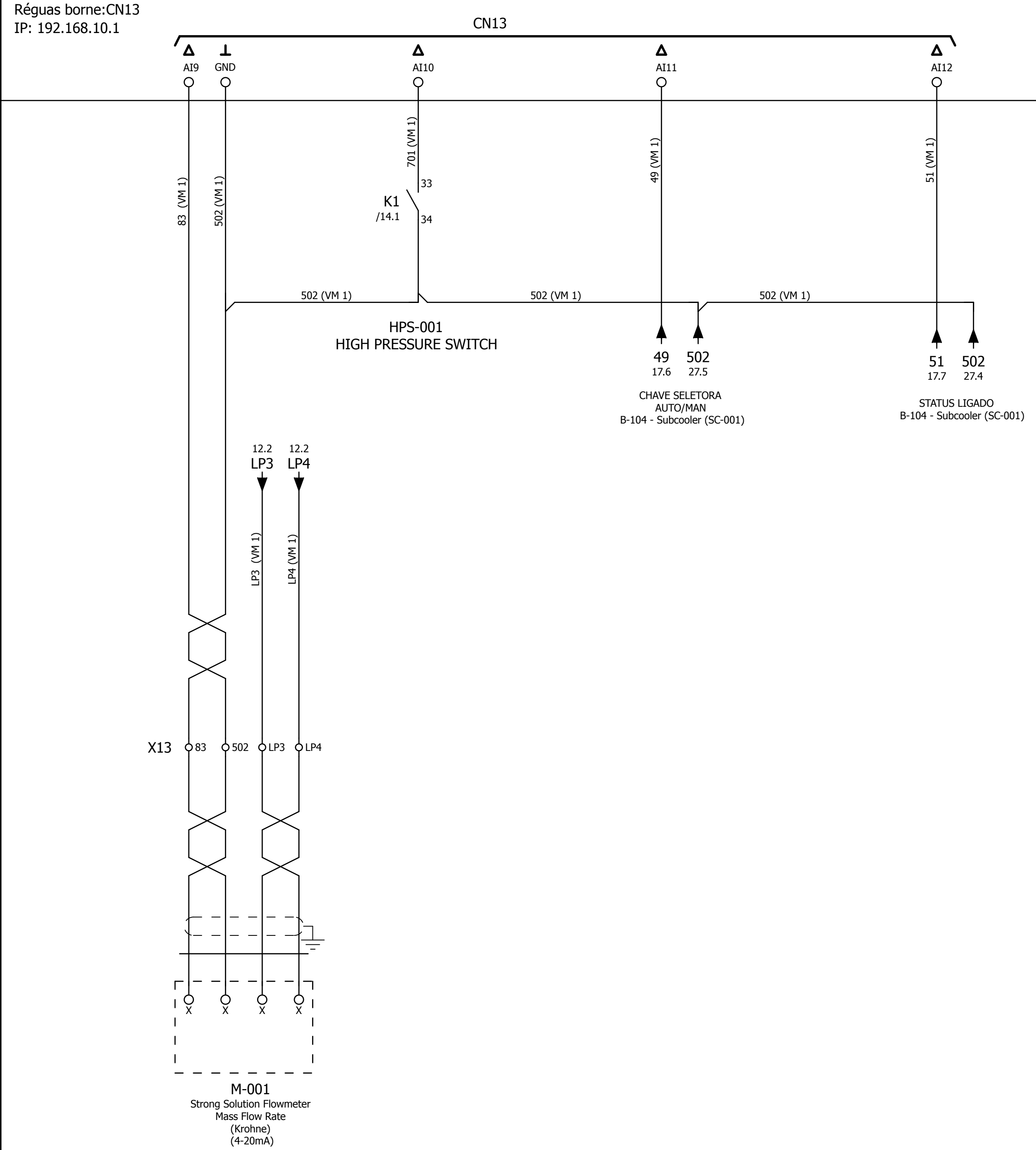

Rev.	Desc.	Data	Nome
05	As-Built de Fábrica	20/08/2019	Diego Almeida
04	Para Aprovação	14/06/2019	Diego Almeida
03	Conforme Comentários	07/06/2019	Diego Almeida
00	Emissão Inicial	28/05/2019	Ray Alves

TAG QE:
QE-01

Nº VL
BZX-QE-001-R05

Controlador PLC-01 - EA

Notas:

br-SAUTER

Cliente
USP - Universidade de São Paulo

Obra
Absorption Refrigeration Cycle

Folha 27
De 44

MODELO: AVC12600/C/L/U
Réguas borne:CN2; CN11
IP: 192.168.10.1

PLC-01 / SAÍDAS ANALÓGICAS (0~10V)

PLC-01
/22.0

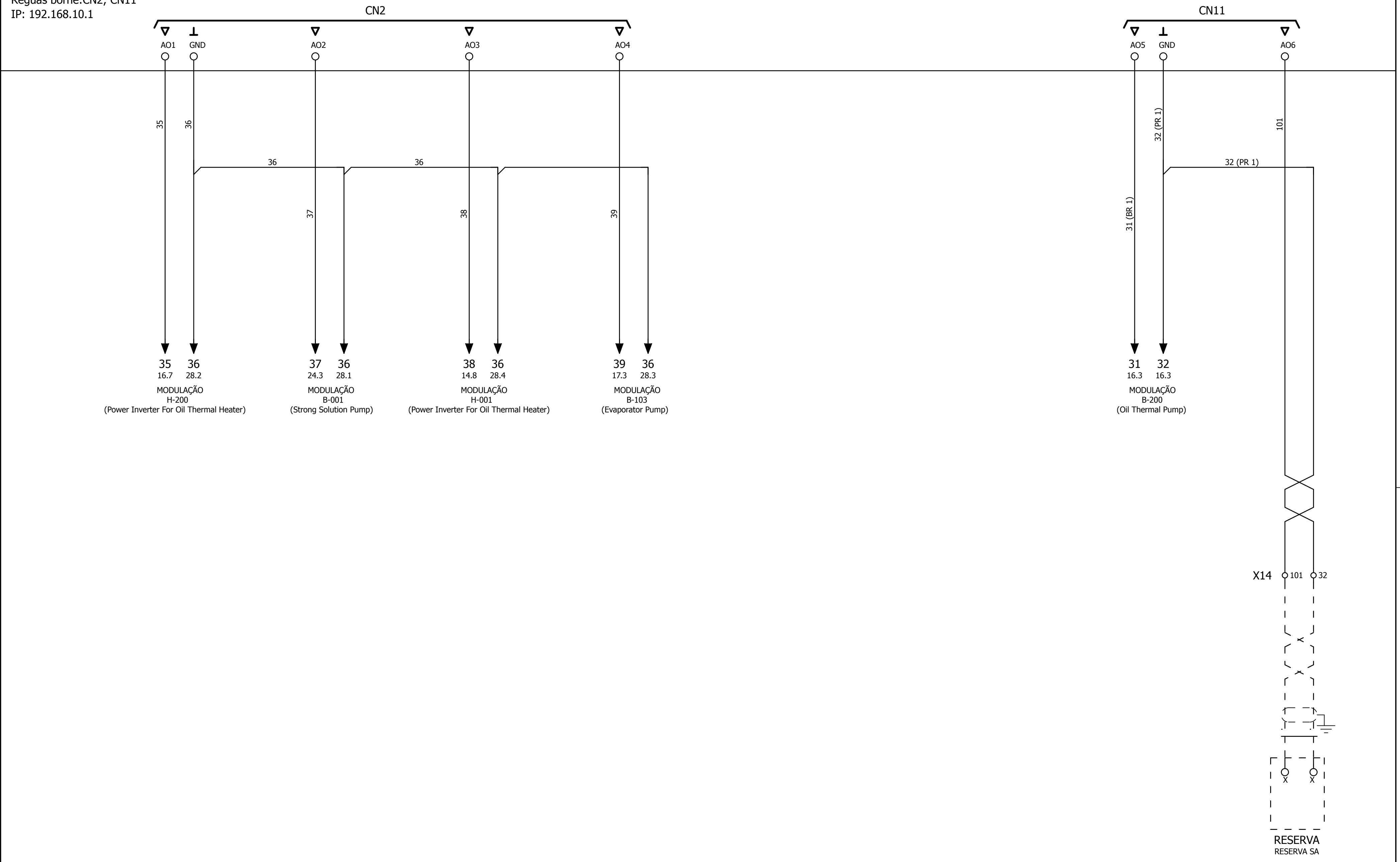

Rev.	Desc.	Data	Nome
05	As-Built de Fábrica	20/08/2019	Diego Almeida
04	Para Aprovação	14/06/2019	Diego Almeida
03	Conforme Comentários	07/06/2019	Diego Almeida
00	Emissão Inicial	28/05/2019	Ray Alves

TAG QE:
QE-01

Nº VL
BZX-QE-001-R05

Controlador PLC-01 - SA

Notas:

br-SAUTER

Cliente
USP - Universidade de São Paulo

Obra
Absorption Refrigeration Cycle

Folha 28
De 44

MODELO: EVE4200
Réguas bornes:

EVE-01.1 / ALIMENTAÇÃO - REDE

EVE-01.1
/30.0
/31.0
/32.0
/33.0

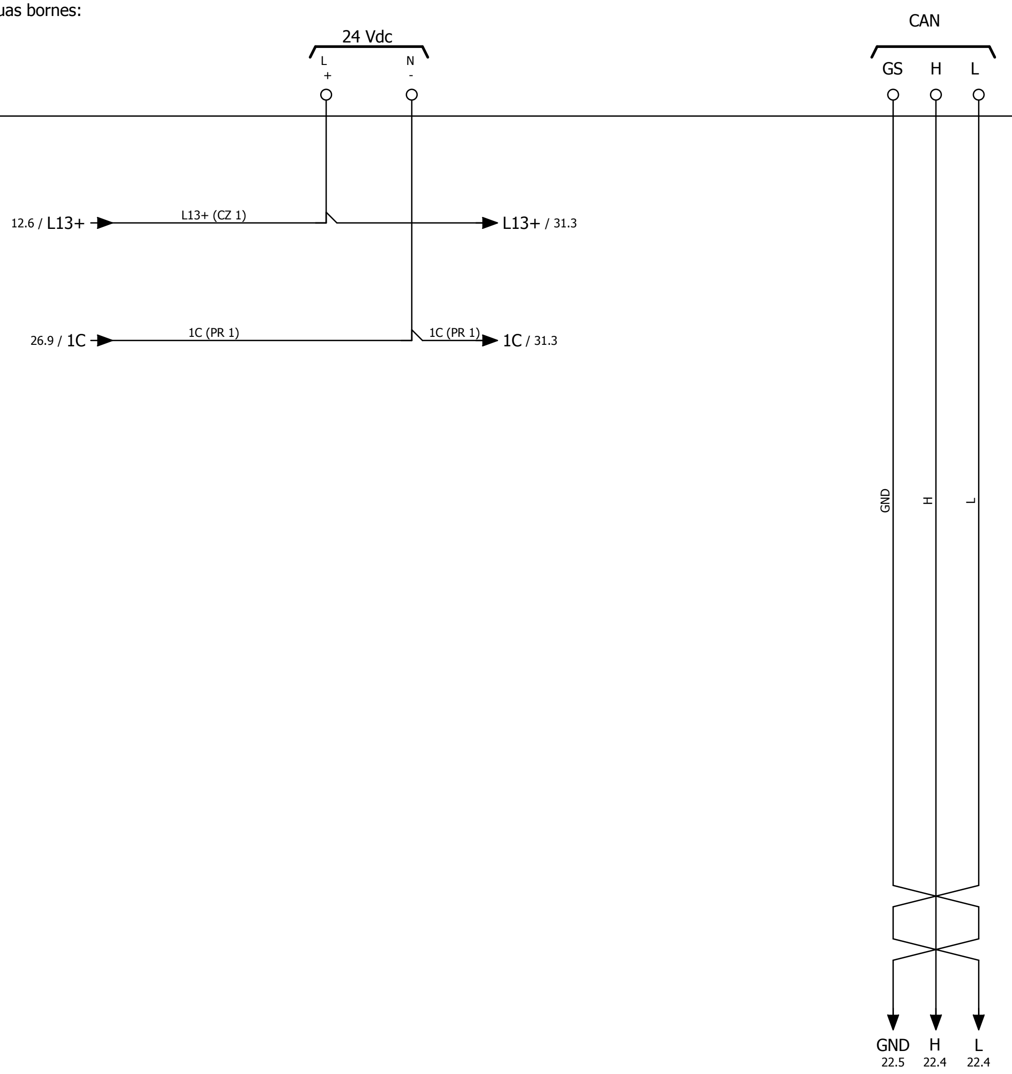

05	As-Built de Fábrica	20/08/2019	Diego Almeida
04	Para Aprovação	14/06/2019	Diego Almeida
03	Conforme Comentários	07/06/2019	Diego Almeida
00	Emissão Inicial	28/05/2019	Ray Alves
Rev.	Desc.	Data	Nome

TAG QE:
QE-01

Controlador EVE-01.1

Nº VL
BZX-QE-001-R05

Notas:

Cliente
USP - Universidade de São Paulo

Obra
Absorption Refrigeration Cycle

Folha 29
De 44

MODELO: EVE4200
Régua borne: CN2

EVE-01.1 / ENTRADAS DIGITAIS

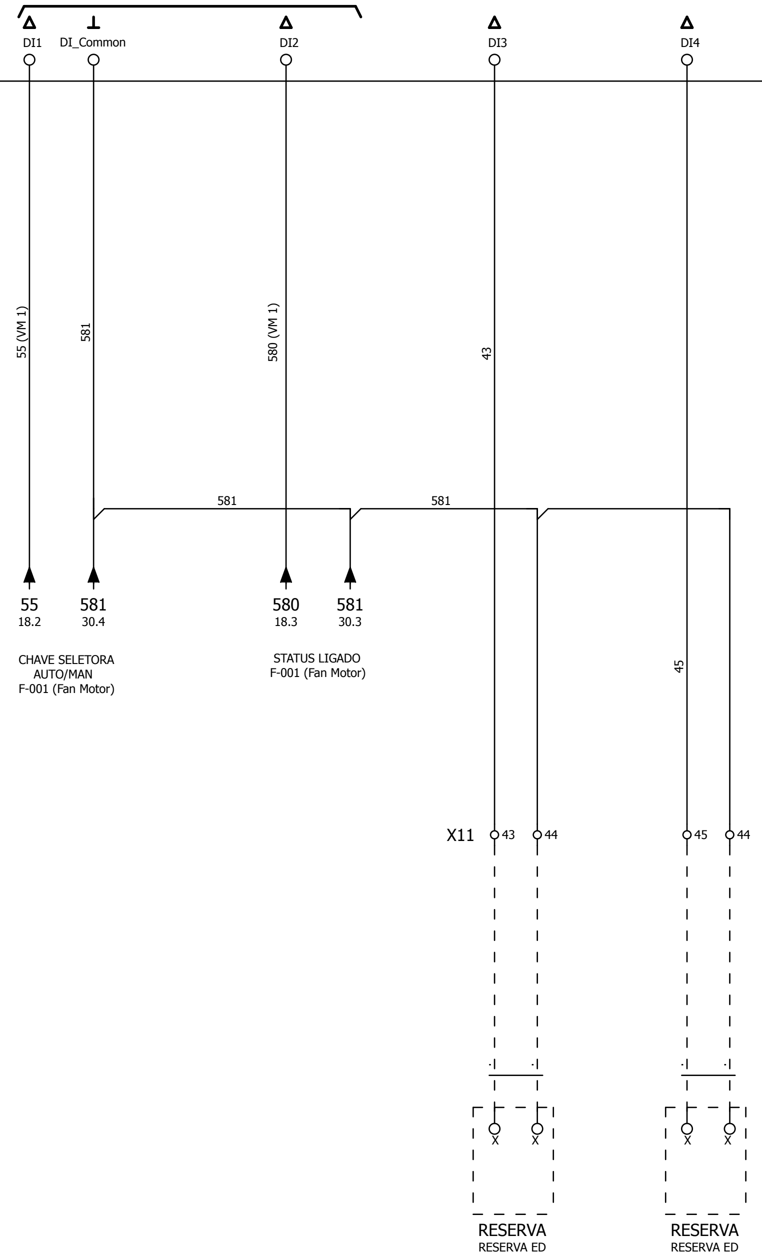

Rev.	Desc.	Data	Nome
05	As-Built de Fábrica	20/08/2019	Diego Almeida
04	Para Aprovação	14/06/2019	Diego Almeida
03	Conforme Comentários	07/06/2019	Diego Almeida
00	Emissão Inicial	28/05/2019	Ray Alves

TAG QE: QE-01

Controlador EVE-01.1 - ED

Nº VL
BZX-QE-001-R05

Notas:

br-SAUTER

Cliente
USP - Universidade de São Paulo

Obra
Absorption Refrigeration Cycle

Folha 30 De 44

MODELO: EVE4200
Réguas borne:

EVE-01.1 / SAÍDAS DIGITAIS (RELE)

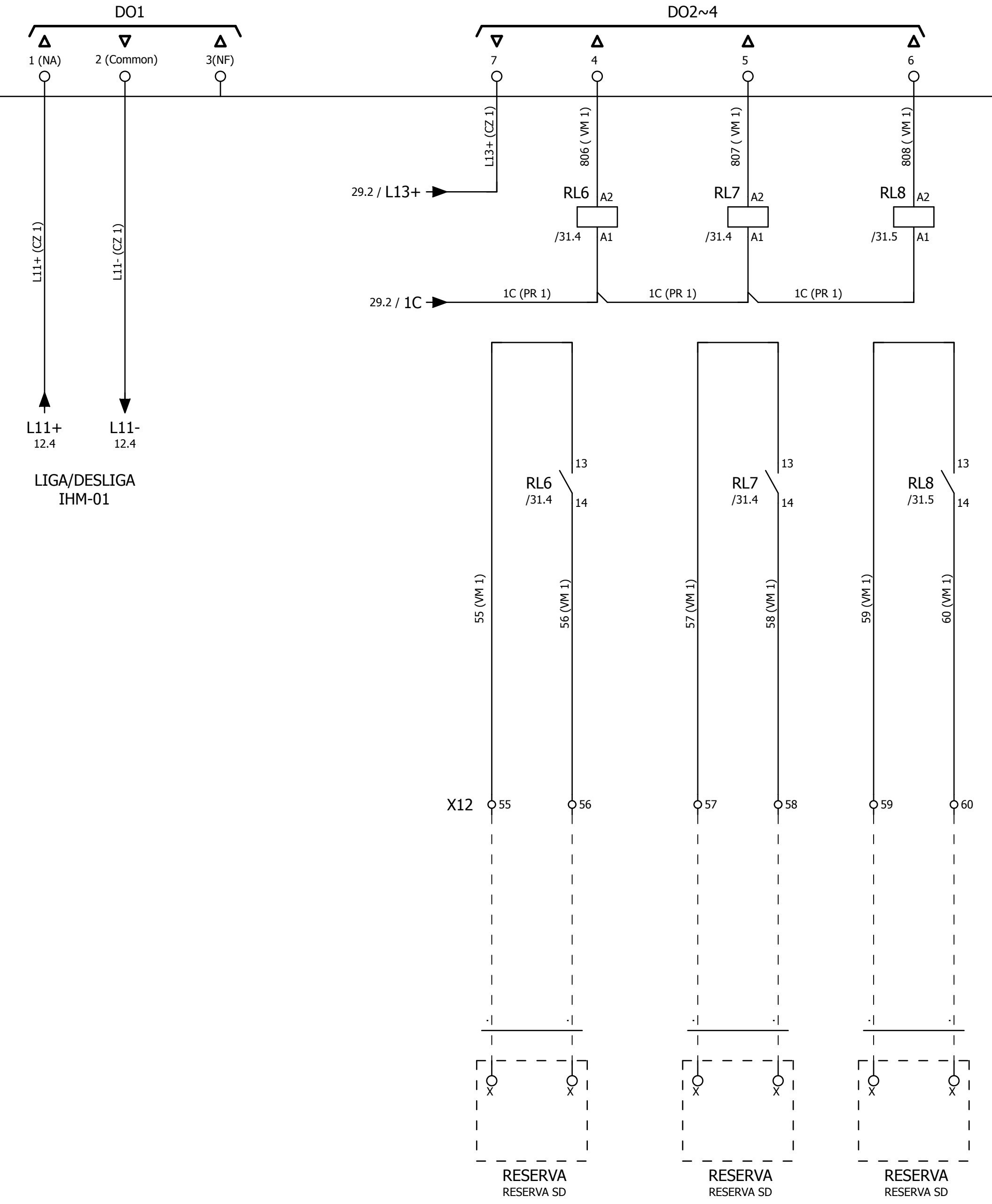

Rev.	Desc.	Data	Nome
05	As-Built de Fábrica	20/08/2019	Diego Almeida
04	Para Aprovação	14/06/2019	Diego Almeida
03	Conforme Comentários	07/06/2019	Diego Almeida
00	Emissão Inicial	28/05/2019	Ray Alves

TAG QE: QE-01

Controlador EVE-01.1 - SD

Nº VL
BZX-QE-001-R05

Notas:

br-SAUTER

Cliente
USP - Universidade de São Paulo

Obra
Absorption Refrigeration Cycle

Folha 31
De 44

MODELO: EVE4200
Réguas borne:

EVE-01.1 / ENTRADAS ANALÓGICAS (4~20mA)

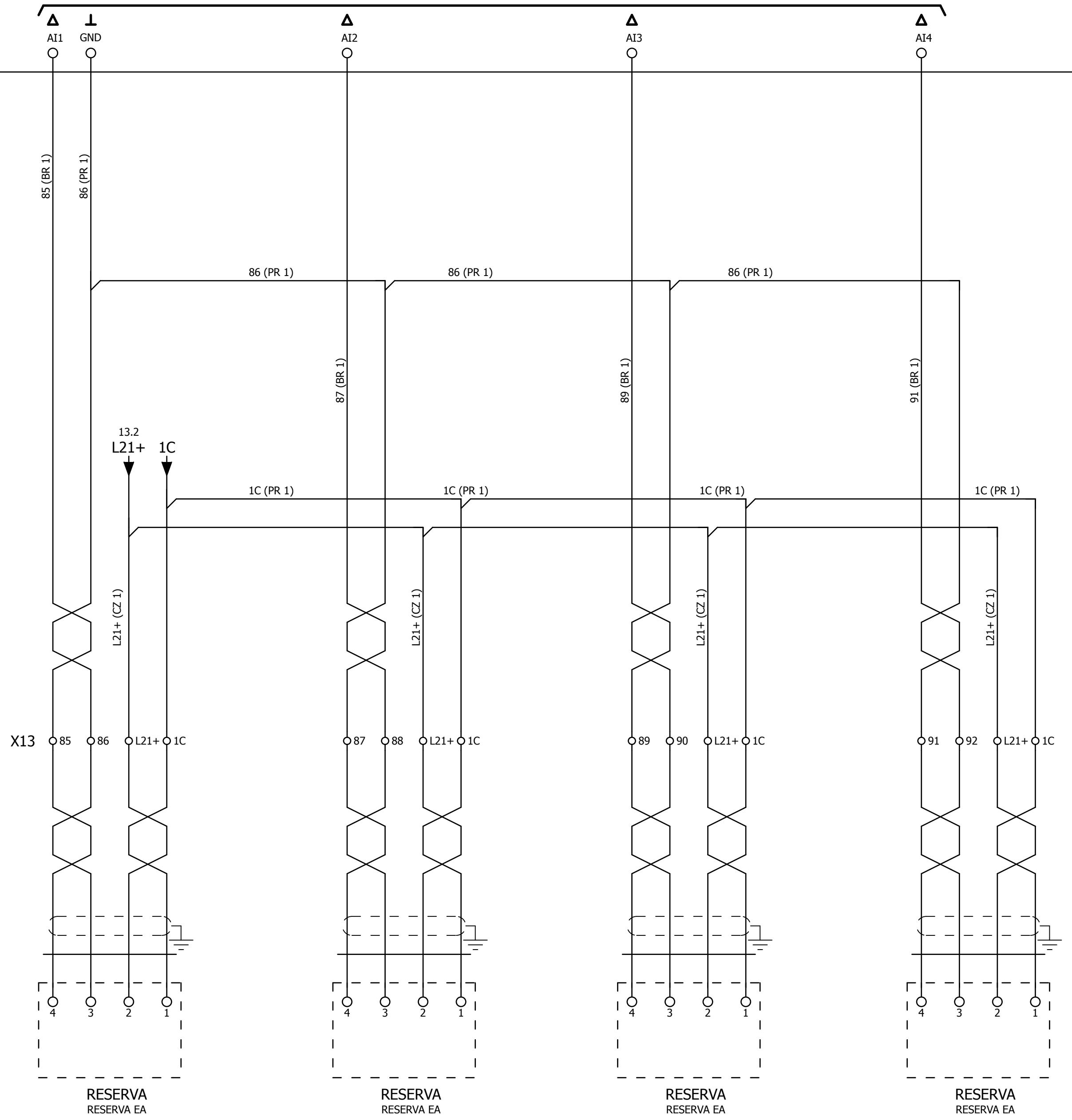

Rev.	Desc.	Data	Nome
05	As-Built de Fábrica	20/08/2019	Diego Almeida
04	Para Aprovação	14/06/2019	Diego Almeida
03	Conforme Comentários	07/06/2019	Diego Almeida
00	Emissão Inicial	28/05/2019	Ray Alves

TAG QE:
QE-01

Nº VL
BZX-QE-001-R05

Controlador EVE-01.1 - EA

Notas:

br-SAUTER

Cliente
USP - Universidade de São Paulo

Obra
Absorption Refrigeration Cycle

Folha 32
De 44

MODELO: EVE4200
Réguas borne:

EVE-01.1 / SAÍDAS ANALÓGICAS (0~10V)

EVE-01.1
/29.0

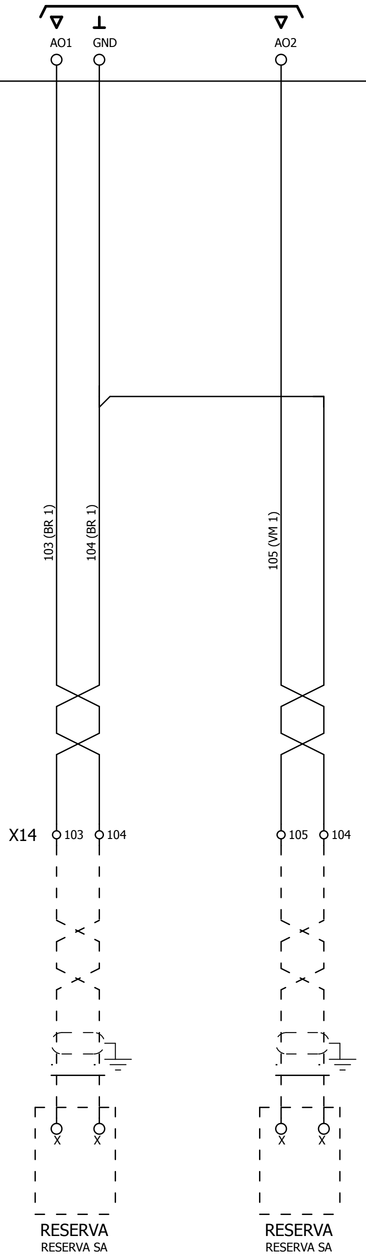

05	As-Built de Fábrica	20/08/2019	Diego Almeida
04	Para Aprovação	14/06/2019	Diego Almeida
03	Conforme Comentários	07/06/2019	Diego Almeida
00	Emissão Inicial	28/05/2019	Ray Alves
Rev.	Desc.	Data	Nome

TAG QE:
QE-01

Controlador EVE-01.1 - SA

Nº VL
BZX-QE-001-R05

Notas:

Cliente
USP - Universidade de São Paulo

Obra
Absorption Refrigeration Cycle

Folha 33 De 44

Diagrama de bornes

Régua

X0

Modelo	Régua X0	Ponto de Conexão	Alvos externos	Ligações de Campo
CTS4UN	U1	U	B-001	Pot: 1,00 CV - 220V / 3F+T
CTS4UN	V1	V	B-001	=
CTS4UN	W1	W	B-001	=
CTS6U	R2	R	H-001	220V/3F+T/60Hz.
CTS6U	S2	S	H-001	=
CTS6U	T2	T	H-001	=
CTS4UN	U3	U	B-200	(OIL PUMP) Pot: 0,33 CV - 220V / 3F+T
CTS4UN	V3	V	B-200	=
CTS4UN	W3	W	B-200	=
CTS6U	R5	R	H-200	(OIL ELETRICAL RESISTANCE) Pot: 8,00 kW - 220V / 3F+T
CTS6U	S5	S	H-200	=
CTS6U	T5	T	H-200	=
CTS4UN	U4	U	B-103	Pot: 0,33 CV - 220V / 3F+T
CTS4UN	V4	V	B-103	=
CTS4UN	W4	W	B-103	=
CTS6U	R8	R	H-100	(OIL ELETRICAL RESISTANCE) Pot: 8,00 kW - 220V / 3F+T
CTS6U	S8	S	H-100	=

Rev.	Desc.	Data	Nome
05	As-Built de Fábrica	20/08/2019	Diego Almeida
04	Para Aprovação	14/06/2019	Diego Almeida
03	Conforme Comentários	07/06/2019	Diego Almeida
00	Emissão Inicial	28/05/2019	Ray Alves

TAG QE: QE-01

Diagrama de bornes X0

Nº VL BZX-QE-001-R05

Notas:

br-SAUTER

USP

Cliente: USP - Universidade de São Paulo

Obra: Absorption Refrigeration Cycle

Folha 34 De 44

Diagrama de bornes

Régua

X1

Modelo	X1	Ponto de Conexão	Alvos externos	Ligações de Campo
CTS2.5UN	1	x	SENSOR	PRESSOSTATO B-001 - (HPS-001)
CTS2.5UN	2	x	SENSOR	=
CTS2.5UN	11	x	SENSOR	TERMOSTATO - H-001 - (HTS-001)
CTS2.5UN	12	x	SENSOR	=
CTS2.5UN	31	x	SENSOR	TERMOSTATO - B-200 - (HTS-200)
CTS2.5UN	32	x	SENSOR	=

Rev.	Desc.	Data	Nome
05	As-Built de Fábrica	20/08/2019	Diego Almeida
04	Para Aprovação	14/06/2019	Diego Almeida
03	Conforme Comentários	07/06/2019	Diego Almeida
00	Emissão Inicial	28/05/2019	Ray Alves

TAG QE: QE-01

Diagrama de bornes X1

Nº VL BZX-QE-001-R05

Notas:

br-SAUTER

USP

Cliente
USP - Universidade de São Paulo

Obra
Absorption Refrigeration Cycle

Folha 35 De 44

Diagrama de bornes

Régua

X11

Modelo	Régua X11	Ponto de Conexão	Alvos externos	Ligações de Campo
CTS2.5UN	41	X	M-003	Ammonia Flowmeter Mass Flow rate
CTS2.5UN	L15+	X	M-003	=
CTS2.5UN	LP7	X	M-003	=
CTS2.5UN	LP8	X	M-003	=
CTS2.5UN	42	X	M-002	Weak Solution Flowmeter Mass Flow Rate
CTS2.5UN	L15+	X	M-002	=
CTS2.5UN	LP5	X	M-002	=
CTS2.5UN	LP6	X	M-002	=
UT 2,5	43	X	RESERVA	RESERVA ED
UT 2,5	44	X	RESERVA	=
UT 2,5	45	X	RESERVA	=
UT 2,5	44	X	RESERVA	=

Rev.	Desc.	Data	Nome
05	As-Built de Fábrica	20/08/2019	Diego Almeida
04	Para Aprovação	14/06/2019	Diego Almeida
03	Conforme Comentários	07/06/2019	Diego Almeida
00	Emissão Inicial	28/05/2019	Ray Alves

TAG QE: QE-01

Nº VL BZX-QE-001-R05

Diagrama de bornes X11

Notas:

br-SAUTER

USP

Cliente
USP - Universidade de São Paulo

Obra
Absorption Refrigeration Cycle

Diagrama de bornes

Régua

X12

Modelo	X12	Ponto de Conexão	Alvos externos	Ligações de Campo
CTS2.5UN	51	X	H-200	Oil Electrical Resistance
CTS2.5UN	52	X	H-200	=
CTS2.5UN	53	X	H-001	Strong Solution Electrical Resistance
CTS2.5UN	54	X	H-001	=
CTS2.5UN	55	X	RESERVA	RESERVA SD
CTS2.5UN	56	X	RESERVA	=
CTS2.5UN	57	X	RESERVA	=
CTS2.5UN	58	X	RESERVA	=
CTS2.5UN	59	X	RESERVA	=
CTS2.5UN	60	X	RESERVA	=

Rev.	Desc.	Data	Nome
05	As-Built de Fábrica	20/08/2019	Diego Almeida
04	Para Aprovação	14/06/2019	Diego Almeida
03	Conforme Comentários	07/06/2019	Diego Almeida
00	Emissão Inicial	28/05/2019	Ray Alves

TAG QE:
QE-01

Diagrama de bornes X12

Nº VL
BZX-QE-001-R05

Notas:

br-SAUTER

USP

Cliente
USP - Universidade de São Paulo

Obra
Absorption Refrigeration Cycle

Folha 37
De 44

Diagrama de bornes

Régua

X13

Modelo	X13	Ponto de Conexão	Alvos externos	Ligações de Campo
CTS2.5UN	71	4	M-200	Display e Sensor de Temperatura Integrado
CTS2.5UN	72	3	M-200	=
CTS2.5UN	L16+	2	M-200	=
CTS2.5UN	1C	1	M-200	=
CTS2.5UN	73	X	Pt100	Sensor de Temperatura
CTS2.5UN	74	X	Pt100	=
CTS2.5UN	75	X	T-200	Oil Temperature
CTS2.5UN	76	X	T-200	=
CTS2.5UN	77	X	T-011	Strong Solution Temperature
CTS2.5UN	78	X	T-011	=
CTS2.5UN	79	4	P-001	Display e Sensor de Temperatura Integrado
CTS2.5UN	72	3	P-001	=
CTS2.5UN	L17+	2	P-001	=
CTS2.5UN	1C	1	P-001	=
CTS2.5UN	80	4	P-002	=
CTS2.5UN	72	3	P-002	=
CTS2.5UN	L18+	2	P-002	=
CTS2.5UN	1C	1	P-002	=
CTS2.5UN	81	4	P-003	=
CTS2.5UN	72	3	P-003	=
CTS2.5UN	L19+	2	P-003	=
CTS2.5UN	1C	1	P-003	=
CTS2.5UN	82	4	P-004	=
CTS2.5UN	72	3	P-004	=
CTS2.5UN	L20+	2	P-004	=

Rev.	Desc.	Data	Nome
05	As-Built de Fábrica	20/08/2019	Diego Almeida
04	Para Aprovação	14/06/2019	Diego Almeida
03	Conforme Comentários	07/06/2019	Diego Almeida
00	Emissão Inicial	28/05/2019	Ray Alves

TAG QE: QE-01

Diagrama de bornes X13

Nº VL

BZX-QE-001-R05

Notas:

br-SAUTER

USP

Cliente

USP - Universidade de São Paulo

Obra

Absorption Refrigeration Cycle

Folha 38

De 44

Diagrama de bornes

Régua

X13

Modelo	Régua X13	Ponto de Conexão	Alvos externos	Ligações de Campo
CTS2.5UN	1C	1	P-004	Display e Sensor de Temperatura Integrado
CTS2.5UN	83	X	M-001	Strong Solution Flowmeter Mass Flow Rate
CTS2.5UN	502	X	M-001	=
CTS2.5UN	LP3	X	M-001	=
CTS2.5UN	LP4	X	M-001	=
CTS2.5UN	85	4	RESERVA	Display e Sensor de Temperatura Integrado
CTS2.5UN	86	3	RESERVA	=
CTS2.5UN	L21+	2	RESERVA	=
CTS2.5UN	1C	1	RESERVA	=
CTS2.5UN	87	4	RESERVA	=
CTS2.5UN	88	3	RESERVA	=
CTS2.5UN	L21+	2	RESERVA	=
CTS2.5UN	1C	1	RESERVA	=
CTS2.5UN	89	4	RESERVA	=
CTS2.5UN	90	3	RESERVA	=
CTS2.5UN	L21+	2	RESERVA	=
CTS2.5UN	1C	1	RESERVA	=
CTS2.5UN	91	4	RESERVA	=
CTS2.5UN	92	3	RESERVA	=
CTS2.5UN	L21+	2	RESERVA	=
CTS2.5UN	1C	1	RESERVA	=

Rev.	Desc.	Data	Nome
05	As-Built de Fábrica	20/08/2019	Diego Almeida
04	Para Aprovação	14/06/2019	Diego Almeida
03	Conforme Comentários	07/06/2019	Diego Almeida
00	Emissão Inicial	28/05/2019	Ray Alves

TAG QE: QE-01

Diagrama de bornes X13

Nº VL: BZX-QE-001-R05

Notas:

br-SAUTER

USP

Cliente: USP - Universidade de São Paulo

Obra: Absorption Refrigeration Cycle

Folha 39 De 44

Diagrama de bornes

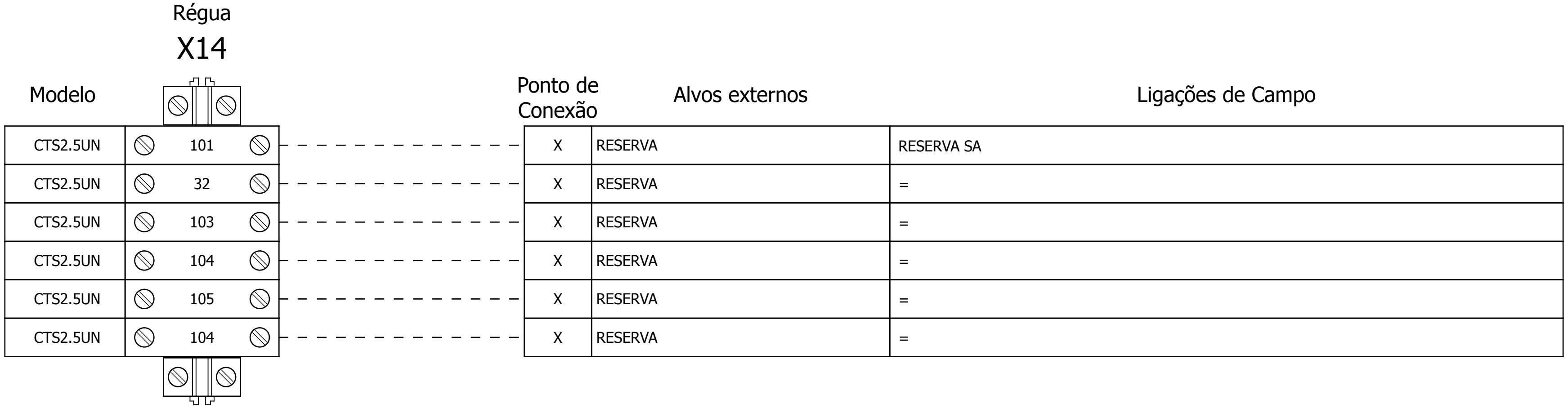

Régua

X14

Modelo	Régua X14	Ponto de Conexão	Alvos externos	Ligações de Campo
CTS2.5UN	101	X	RESERVA	RESERVA SA
CTS2.5UN	32	X	RESERVA	=
CTS2.5UN	103	X	RESERVA	=
CTS2.5UN	104	X	RESERVA	=
CTS2.5UN	105	X	RESERVA	=
CTS2.5UN	104	X	RESERVA	=

Rev.	Desc.	Data	Nome
05	As-Built de Fábrica	20/08/2019	Diego Almeida
04	Para Aprovação	14/06/2019	Diego Almeida
03	Conforme Comentários	07/06/2019	Diego Almeida
00	Emissão Inicial	28/05/2019	Ray Alves

TAG QE: QE-01

Diagrama de bornes X14

Nº VL BZX-QE-001-R05

Notas:

br-SAUTER

USP

Cliente

USP - Universidade de São Paulo

Obra

Absorption Refrigeration Cycle

RELAÇÃO DE PLAQUETAS

ITEM	QDE.	MOD.	TAG	1° LINHA	2° LINHA	3° LINHA
01	01	A	QE	QUADRO ELÉTRICO	QE-01	220V/3F+PE/60Hz
02	01	B	H0	COMANDO	ENERGIZADO	
03	01	B	BL1-BD1-H1	NH_3-H_2O PUMP	LIGA - DESLIGA	
04	01	B	BTL	BOTÃO TESTE	DE LÂMPADA	
05	01	B	H2	B-001	FALHA	
06	01	B	BL2-BD2-H3	CONDENSER/RECTIFIER	LIGA - DESLIGA	
07	01	B	H4	B-101 E B-102	FALHA	
08	01	B	BL3-BD3-H5	OIL PUMP	LIGA - DESLIGA	
09	01	B	H6	B-200	FALHA	
10	01	B	BL4-BD4-H7	EVAPORATOR	LIGA - DESLIGA	
11	01	B	H8	B-103	FALHA	
12	01	B	BL11-BD5-H9	SUBCOOLER	LIGA - DESLIGA	
13	01	B	H10	B-104	FALHA	
14	01	B	BL6-BD6-H11	WATER COOLER	LIGA - DESLIGA	
15	01	B	H12	F-001	FALHA	
16	01	B	HR1	H-001	LIGADO	
17	01	B	HR2	H-200	LIGADO	
18	06	B	CC1	HEATER- NH_3-H_2O	DESLIGA - LIGA	
19	06	B	CC2	HEATER - Oil	DESLIGA - LIGA	
20	06	B	TMG	TOMADA	ALIMENTAÇÃO	GERAL
21	01	B	TM1	TOMADA	B-101 E B-102	
22	01	B	TM2	TOMADA	B-104	
23	01	B	TM3	TOMADA	F-001	
24	01	B	TM4	TOMADA	INSTRUMENTAÇÃO	
25	01	B	DJG	DISJUNTOR	GERAL	
26	01	B	B0	EMERGÊNCIA		
27	06	B	S1 A S6	SELETORA	MAN. - DESL. AUT.	
28	06	B	IHM		IHM-01	

MODELO A

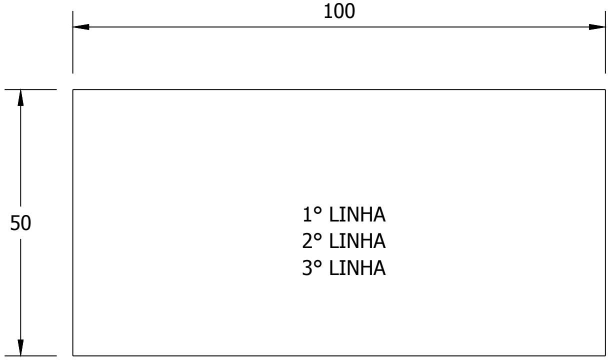

1 - TAG
2 - FUNDO PRETO
3 - LOGOTIPO E NOME NA COR BRANCO
4 - FIXAÇÃO ADESIVADA
5 - DIMENSÕES 50x100x2mm
6 - MATERIAL ACRÍLICO

MODELO B

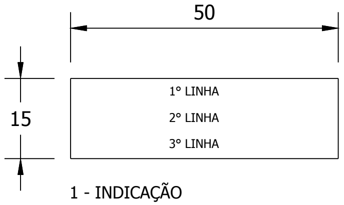

1 - INDICAÇÃO
2 - FUNDO PRETO
3 - CARACTERES NA COR BRANCO
4 - FIXAÇÃO ADESIVADA
5 - DIMENSÕES 15x50x2mm
6 - MATERIAL ACRÍLICO

Rev.	Desc.	Data	Nome
05	As-Built de Fábrica	20/08/2019	Diego Almeida
04	Para Aprovação	14/06/2019	Diego Almeida
03	Conforme Comentários	07/06/2019	Diego Almeida
00	Emissão Inicial	28/05/2019	Ray Alves

TAG QE:
QE-01

Relação de Plaquetas

Nº VL
BZX-QE-001-R05

Notas:

br-SAUTER

USP

Cliente
USP - Universidade de São Paulo

Obra
Absorption Refrigeration Cycle

Folha
41

De
44

DIMENSIONAL DO QUADRO ELÉTRICO

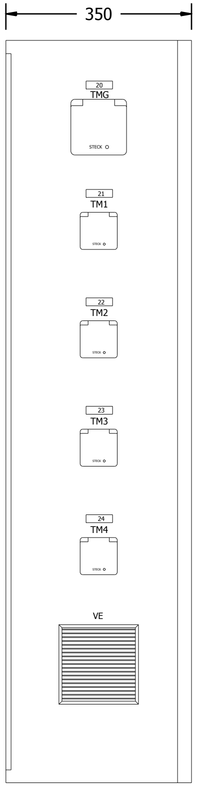

VISTA LATERAL ESQUERDA

EXTERNA

ESCALA 1:10

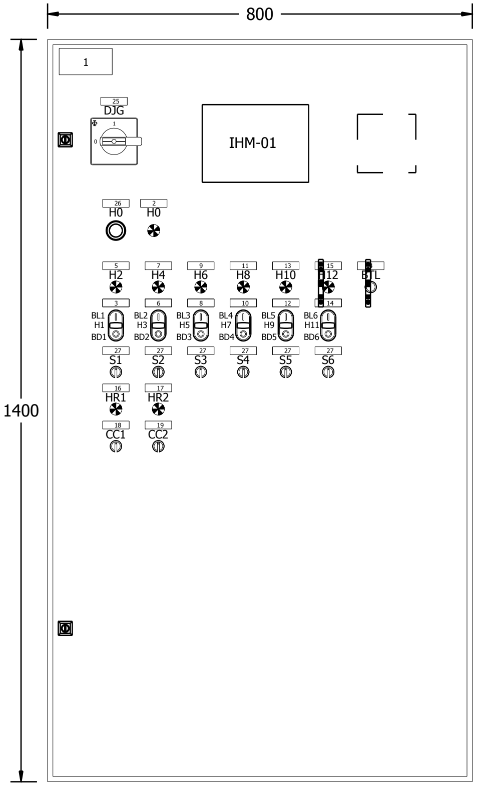

VISTA FRONTAL

EXTERNA

ESCALA 1:10

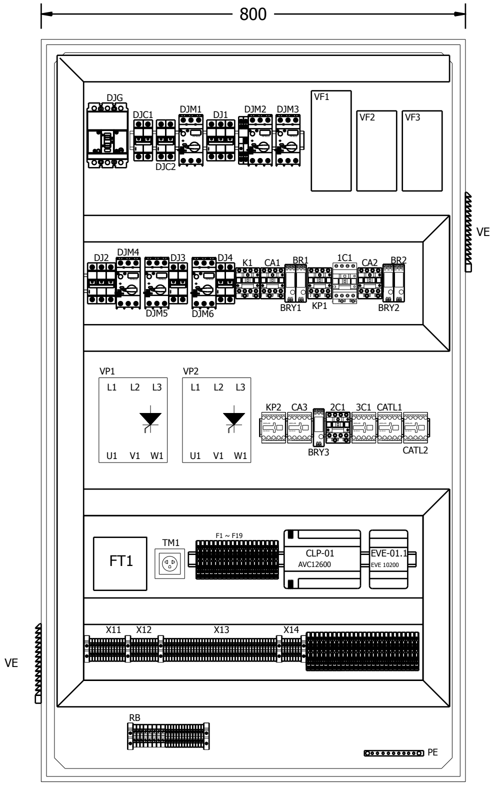

VISTA FRONTAL

INTERNA

ESCALA 1:10

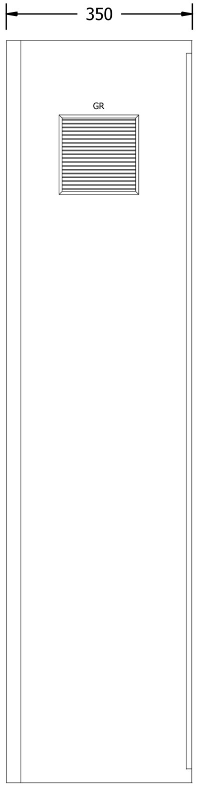

VISTA LATERAL DIREITA

EXTERNA

ESCALA 1:10

Rev.	Desc.	Data	Nome
05	As-Built de Fábrica	20/08/2019	Diego Almeida
04	Para Aprovação	14/06/2019	Diego Almeida
03	Conforme Comentários	07/06/2019	Diego Almeida
00	Emissão Inicial	28/05/2019	Ray Alves

TAG QE:
QE-01

Layout

Nº VL
BZX-QE-001-R05

Notas:

br-SAUTER

Cliente
USP - Universidade de São Paulo

Obra
Absorption Refrigeration Cycle

Folha
42

De
44

Lista de Materiais

TAG	QUANTIDADE	DESCRIÇÃO DA PEÇA	MODELO	FORNECEDOR	CÓDIGO DO SISTEMA VL
B0	1	Botão Tipo Cogumelo Gira Destrava 40mm VM	HB2-ES542	BHS COMERCIAL	42098
B0	1	Bloco de Contato Acionador VM c/ Parafuso 1NF	HB2-BE102	BHS COMERCIAL	42052
BD1...BD6	6	Botões de Comando Duplo Iluminado 1NA+1NF VD/VM	HB2-EW8365	BHS COMERCIAL	42327
BR1;BR2;BRY1...BRY3	5	Borne relé 5A 2NAF 220Vcc/Vca 20mm	Q2R-220	METALTEX	28292
BTL	1	Botão Plástico PT 1NA	HB2-EA21	BHS COMERCIAL	39064
BTL;S1...S6	8	Bloco de Contato Acionador VD c/ Parafuso 1NA	HB2-BE101	BHS COMERCIAL	39059
1C1	1	MINICONTATOR 3P 12A AC3 220V50/60HZ 1NA	LC1K1210M7	SCHNEIDER	330
1C1;2C1;3C1;CA2	4	BLOCO DE CONTATO AUX 3NA+1NF MODELO K	LA1KN31	SCHNEIDER	337
2C1;3C1;KP1	3	MINICONTATOR 3P 6A AC3 220V50/60HZ 1NA	LC1K0610M7	SCHNEIDER	328
CA1...CA3;K1	4	Minicontator Auxiliar 10A 3NA+1NF 220Vca 50/60HZ	CA2KN31M7	SCHNEIDER	333
CA1;CATL1;CATL2	3	BLOCO DE CONTATO AUX 4NA MODELO K	LA1KN40	SCHNEIDER	338
CA3;KP1	2	Bloco de Contato Auxiliar 2NA p/ Modelo K	LA1KN20	SCHNEIDER	336
CATL1;CATL2	2	Minicontator Auxiliar 10A 4NA 220V50/60HZ	CA2KN40M7	SCHNEIDER	334
CC1;CC2	2	Comutador 2Pos. Fixa Manopla Curta 1NA Plást. 22mm	HB2-ED25	BHS COMERCIAL	39105
DJ1	1	MINIDISJ 3P 10A CURVA C 3KA 230/400V	EZ9F33310	SCHNEIDER	254
DJ2	1	Minidisj EASY9 3P 25A Curva C 5KA 23V 3KA 400V	EZ9F33325	SCHNEIDER	257
DJ3	1	Minidisj EASY9 3P 32A Curva C 5KA 230V 3KA 400V	EZ9F33332	SCHNEIDER	258
DJ4;DJC1;DJC2	3	MINIDISJ 2P 10A CURVA C 3KA 230/400V	EZ9F33210	SCHNEIDER	245
DJG	1	Disj Cx Mold 3P 80A 25KA/220V 18KA/380V	EZC100N3080	SCHNEIDER	277
DJG	1	Manopla Rotativa Prolongada p/ Disj EZC100	EZAROTE	SCHNEIDER	3677
DJM1;DJM3;DJM4	3	Disj Motor Magnét 10A 100KA 415V por Alavanca	GV2LE14	SCHNEIDER	8927
DJM2	1	DISJUNTOR MOTOR TERMOMAGNÉTICO 6-10A 415V	GV2ME14	SCHNEIDER	312
DJM2;DJM5;DJM6	3	BLOCO DE CONTATO SINAL 1NA DEF 1NA INST P/ GV2/3	GVAD1010	SCHNEIDER	324
DJM5	1	Disj Motor Termomagnét 1,6-2,5A 100KA/415V	GV2ME07	SCHNEIDER	309
DJM6	1	Disj Motor Termomagnét 2,5-4A 100KA/415V	GV2ME08	SCHNEIDER	310
EVE-01.1	1	Módulo E/S remoto CANbus	EVE4200000500	Schneider Eletric	44521
FC11...FC25;FP1...FP10	25	Borne Porta-Fusível 4mm2 sem led 5x20/5x25 Cinza	CF4U	CONNECTWELL	41996
FC11...FC25;FP3...FP10	23	Fusível de vidro 0,5A	ZH212-0,5A	METALTEX	26227
FP1;FP2	2	Fusível de vidro 1A	ZH212-1A	METALTEX	26228
FT1	1	Fonte Chaveada 100W 110/220V 24VCC 4,5A	LRS-100-24	METALTEX	41094
GY 1...GY 3	3	Condicionador de Sinal Analógico, entrada Pt100, saída 0 à 10v. Alim. 24Vcc	TCA 300-0/100-0/10v	TECNATRON	43710
H0	1	Sinaleiro Plást Led 22mm BR 220/240VCA Monob.	HD16-22 D/W-220	BHS COMERCIAL	39057
H2;H4;H6;H8;H10;H12	6	Sinaleiro Plást Led 22mm AM 220/240VCA Monob.	HD16-22 D/Y-220	BHS COMERCIAL	39058
HR1;HR2	2	Sinaleiro Plást Led 22mm VM 220/240VCA Monob.	HD16-22 D/R-220	BHS COMERCIAL	39056
IHM-01	1	IHM Touch Screen 7" TFT 65K cores + Ethernet	MT8071IP	WEINTEK	41347
KP2	1	CONTATOR 3P 9A (NA + NF AUX) 220V 50/60HZ	LC1D09M7	SCHNEIDER	4021
KP2	1	BLOCO CONTATO AUX FRONTAL 2NA P/ MODELO D/F	LADN20	SCHNEIDER	370
PLC-01	1	Controlador Modbus TCP Master/Slave, Bacnet/IP	AVC1260060500	Schneider Electric	44523
QE-FC-01	1	Caixa Sob 1400x800x350mm RAL7032 IP54 c/Yale	CS1408035	SR SENADOR	40512
RL1...RL8	8	BORNE RELÉ 24VAC/DC 1 CONTATO REVERSÍVEL	PLC-RSC-24UC/21	PHOENIX CONTACT	11510
S1...S6	6	Comutador 3Pos. Fixa Manopla Curta 2NA Plást. 22mm	HB2-ED 33	BHS COMERCIAL	39069
TM1;TM2;TM4	3	Plug 2P+T 16A 200/440V 6H Az	N-3076	STECK	35024
TM1;TM2;TM4	3	Tomada Embut 2P+T 16A 200/250V 6H Az	N-3046	STECK	35011
TM3	1	Plug 3P+T 32A 380/440V 6H VM	N-4276	STECK	18415
TM3	1	Tomada de Embutir 3P+T 32A 220V Azul IP44	N-4249	STECK	34848
TM5	1	TOMADA 2P+T Branca 20A / 250V	TOMADA 2P+T / 20 A	LUMIBRAS	36387
TMG	1	Plug 3P+T 125A 200/250V AZ	S4679W	STECK	
TMG	1	Tomada de Embutir - 3P+T 125 A	S4649W	STECK	
VE-1/EX-1	2	Conjunto Vent 204x204mm 110/230V RAL7032 Bivolt	CVE23-BV	PRABOX	40651
VF1	1	Inversor de Freq 3F 4,3A 1CV 220V	CFW500A04P3BNB20	WEG	40648
VP1	1	Conversor de Potência c/ Fusível 10A 220VCA	MPC-TPF-3262-10R	LOTI	36322
VP2	1	Conversor de Potência c/ Fusível 25A 220VCA	MPC-TPF-3262-25R	LOTI	36323
X0	3	Borne Conexão Parafuso 10mm² CZ	CTS10U	CONNECTWELL	41984
X0	3	Borne Conexão Parafuso 6mm² CZ	CTS6U	CONNECTWELL	41982
X0	11	Borne Conexão Parafuso 4mm² CZ	CTS4UN	CONNECTWELL	41980
X0;X1;X11...X14	7	Poste Plást. DIN 32/DIN35x7,5/DIN35x15 CZ	CA702	CONNECTWELL	42004

Rev.	Desc.	Data	Nome
05	As-Built de Fábrica	20/08/2019	Diego Almeida
04	Para Aprovação	14/06/2019	Diego Almeida
03	Conforme Comentários	07/06/2019	Diego Almeida
00	Emissão Inicial	28/05/2019	Ray Alves

TAG QE:
QE-01

Lista de Materiais

N° VL
BZX-QE-001-R05

Notas:

br-SAUTER

USP

Cliente
USP - Universidade de São Paulo

Obra
Absorption Refrigeration Cycle

Folha 43 De 44

Lista de Materiais

TAG	QUANTIDADE	DESCRIÇÃO DA PEÇA	MODELO	FORNECEDOR	CÓDIGO DO SISTEMA VL
X0;X1;X11...X14	6	Tampa Final CTS2.5UN/2.5UE/4UN CZ	EP2.5/4UN	CONNECTWELL	42013
X1;X11...X14	80	Borne Conexão Parafuso 2,5mm² Cinza	CTS2.5UN	CONNECTWELL	41978

Rev.	Desc.	Data	Nome
05	As-Built de Fábrica	20/08/2019	Diego Almeida
04	Para Aprovação	14/06/2019	Diego Almeida
03	Conforme Comentários	07/06/2019	Diego Almeida
00	Emissão Inicial	28/05/2019	Ray Alves

TAG QE:
QE-01

Lista de Materiais

N° VL
BZX-QE-001-R05

Notas:

br-SAUTER

USP

Cliente
USP - Universidade de São Paulo

Obra
Absorption Refrigeration Cycle

Folha 44
De 44

ANNEX C

Programming code - PLC

Local I / O Mapping

Name	Variable	Type	Description
AIL1		INT	AIL1 analogue input
AIL2	IO_T_130	INT	AIL2 analogue input
AIL3	IO_T_200_OIL_TEMP	INT	AIL3 analogue input
AIL4	IO_T_011	INT	AIL4 analogue input
AIL5	IO_P_001_ABSORPTION_PRESSURE	INT	AIL5 analogue input
AIL6	IO_P_002_PUMP_DISCHARGE	INT	AIL6 analogue input
AIL7	IO_P_003_GENERATION_PRESSURE	INT	AIL7 analogue input
AIL8	IO_P_004_EVAPORATION_PRESSURE	INT	AIL8 analogue input
AIL9		INT	AI9 analogue input
AIL10	IO_HPS_001_HIGH_PRESSURE	INT	AIL10 analogue input
AIL11	IO_B_104_AUTO	INT	AIL11 analogue input
AIL12	IO_B_104_RUN	INT	AIL12 analogue input
DIL1	IO_M_003_AMMONIA_FLOWMETER	BOOL	DIL1 digital input
DIL2	IO_M_002_WEAK_SOLUTION_FLOWMETER	BOOL	DIL2 digital input
DIL3	IO_B_001_AUTO	BOOL	DIL3 digital input
DIL4	IO_B_001_RUN	BOOL	DIL4 digital input
DIL5	IO_H_001_THERM	BOOL	DIL5 digital input
DIL6	IO_B_101_102_AUTO	BOOL	DIL6 digital input
DIL7	IO_B_101_102_RUN	BOOL	DIL7 digital input
DIL8	IO_B_200_AUTO	BOOL	DIL8 digital input
DIL9	IO_B_200_RUN	BOOL	DIL9 digital input
DIL10	IO_H_200_THERM	BOOL	DIL10 digital input
DIL11	IO_B_103_AUTO	BOOL	DIL11 digital input
DIL12	IO_B_103_RUN	BOOL	DIL12 digital input
DOL1	IO_B_200_TURN_ON	BOOL	DOL1 digital output
DOL2	IO_H_200_TURN_ON	BOOL	DOL2 digital output
DOL3	IO_H_001_TURN_ON	BOOL	DOL3 digital output
DOL4	IO_B_101_102_TURN_ON	BOOL	DOL4 digital output
DOL5	IO_B_103_TURN_ON	BOOL	DOL5 digital output
DOL6	IO_B_104_TURN_ON	BOOL	DOL6 digital output
DOL7	IO_F_001_TURN_0N	BOOL	DOL7 digital output
DOL8	IO_B_001_TURN_ON	BOOL	DOL8 digital output
DOL9		BOOL	DOL9 digital output
DOL10		BOOL	DOL10 digital output
DOL11		BOOL	DOL11 digital output
DOL12		BOOL	DOL12 digital output
AOL1	IO_H_200_MOD	INT	AOL1 analogue output
AOL2	IO_B_001_MOD	INT	AOL2 analogue output
AOL3	IO_H_001_MOD	INT	AOL3 analogue output
AOL4	IO_B_103_MOD	INT	AOL4 analogue output
AOL5	IO_B_200_MOD	INT	AOL5 analogue output
AOL6		INT	AOL6 analogue output
FDI1_counter	teste_counter	UDINT	FDI1 Input counter
FDI1_frequency	teste_freq	UDINT	FDI1 Input frequency
FDI2_counter		UDINT	FDI2 Input counter
FDI2_frequency		UDINT	FDI2 Input frequency
FDI1_value	teste_value	BOOL	FDI1 Input value
FDI2_value		BOOL	FDI2 Input value
FDI1_reset_counter		BOOL	FDI1 reset input counter value
FDI2_reset_counter		BOOL	FDI2 reset input counter value

Field I / O Mapping

Name	Type	In/Out	Description
IO_F_001_AUTO	BOOL	Input	
IO_F_001_RUN	BOOL	Input	
IO_HMI_TURN_ON	BOOL	Output	
IO_M_001_STRONG_SOLUTION_FLOWMETER	INT	Input	
IO_M_200_OIL_FLOWMETER	INT	Input	
IO_F_001_TEMP	INT	Input	
IO_B_104_TEMP	INT	Input	

EEPROM Parameters

Address	Name	Device type	Application type	Size	Default value	Min	Max
16384	E2_B_101_102_103_CMD	Signed 16-bit	BOOL		1		
16385	E2_B_101_102_RESET_ALARM	Signed 16-bit	BOOL		0		
16386	E2_B_103_RESET_ALARM	Signed 16-bit	BOOL		0		
16387	B_103_SETPOINT_FREQ	Signed 16-bit	INT		200	200	600
16388	E2_B_104_CMD	Signed 16-bit	BOOL		1		
16389	E2_B_104_RESET_ALARM	Signed 16-bit	BOOL		0		
16390	E2_F_001_RESET_ALARM	Signed 16-bit	BOOL		0		
16391	E2_F001_LIM_TEMP_LIGA	Signed 16-bit	INT		0		
16392	E2_F001_LIM_TEMP_DESLIGA	Signed 16-bit	INT		0		
16393	E2_F001_LIM_TEMP	Signed 16-bit	INT		0		
16394	E2_F001_LIM_TEMP_TIMER	Unsigned 32-bit	UDINT		10		
16396	E2_B_200_CMD	Signed 16-bit	BOOL		1		
16397	E2_B_200_RESET_ALARM	Signed 16-bit	BOOL		0		
16398	E2_T_130_LIM_MIN	Signed 16-bit	INT		0		
16399	E2_T_130_LIM_MAX	Signed 16-bit	INT		1000		
16400	E2_T_200_LIM_MIN	Signed 16-bit	INT		0		
16401	E2_T_200_LIM_MAX	Signed 16-bit	INT		2000		
16402	E2_T_011_LIM_MIN	Signed 16-bit	INT		0		
16403	E2_T_011_LIM_MAX	Signed 16-bit	INT		2000		
16404	E2_P_001_LIM_MIN	Signed 16-bit	INT		0		
16405	E2_P_001_LIM_MAX	Signed 16-bit	INT		250		
16406	E2_P_002_LIM_MIN	Signed 16-bit	INT		0		
16407	E2_P_002_LIM_MAX	Signed 16-bit	INT		250		
16408	E2_P_003_LIM_MIN	Signed 16-bit	INT		0		
16409	E2_P_003_LIM_MAX	Signed 16-bit	INT		0		
16410	E2_P_004_LIM_MIN	Signed 16-bit	INT		0		
16411	E2_P_004_LIM_MAX	Signed 16-bit	INT		0		
16412	E2_M_001_LIM_MIN	Signed 16-bit	INT		0		
16413	E2_M_001_LIM_MAX	Signed 16-bit	INT		1000		
16414	E2_M_200_LIM_MIN	Signed 16-bit	INT		120		
16415	E2_M_200_LIM_MAX	Signed 16-bit	INT		1200		
16416	E2_B_104_LIM_MIN	Signed 16-bit	INT		0		
16417	E2_B_104_LIM_MAX	Signed 16-bit	INT		0		
16418	E2_IO_M_003_AMMONIA_FLOWMETER_PULSE_RATE_MIN	Signed 16-bit	INT		0		
16419	E2_IO_M_003_AMMONIA_FLOWMETER_PULSE_RATE_MAX	Signed 16-bit	INT		10000		
16420	E2_IO_M_003_AMMONIA_FLOWMETER_LIM_MIN	Signed 16-bit	INT		0		
16421	E2_IO_M_003_AMMONIA_FLOWMETER_LIM_MAX	Signed 16-bit	INT		0		
16422	E2_IO_M_002_WEAK_SOLUTION_FLOWMETER_PULSE_RATE_MIN	Signed	INT		0		

Address	Name	Device type	Application type	Size	Default value	Min	Max
		16-bit					
16423	E2_IO_M_002_WEAK_SOLUTION_FLOWMETER_PULSE_RATE_MAX	Signed 16-bit	INT		10000		
16424	E2_IO_M_002_WEAK_SOLUTION_FLOWMETER_LIM_MIN	Signed 16-bit	INT		0		
16425	E2_IO_M_002_WEAK_SOLUTION_FLOWMETER_LIM_MAX	Signed 16-bit	INT		0		
16426	E2_B_200_PID_P	Unsigned 16-bit	UINT		1500		
16427	E2_B_200_PID_I	Unsigned 16-bit	UINT		500		
16428	E2_B_200_PID_D	Unsigned 16-bit	UINT		900		
16429	E2_B_200_PID_ACTION	Signed 16-bit	BOOL		1		
16430	E2_B_200_PID_HAB	Signed 16-bit	BOOL		1		
16431	E2_B_200_SETPOINT_M_200	Signed 16-bit	INT		0		
16432	E2_B_200_SETPOINT_FREQ	Signed 16-bit	INT		100	100	200
16433	E2_B_200_TIMER_TURN_OFF_ALARM_H200	Signed 16-bit	UDINT		100		
16434	E2_P_002_SETPOINT_PRESSURE	Signed 16-bit	INT		70		
16435	E2_P_003_SETPOINT_PRESSURE	Signed 16-bit	INT		70		
16436	E2_H_200_SETPOINT_T_200	Signed 16-bit	INT		1300	0	1300
16437	E2_H_200_PID_P	Unsigned 16-bit	UINT		100		
16438	E2_H_200_PID_I	Unsigned 16-bit	UINT		1500		
16439	E2_H_200_PID_D	Unsigned 16-bit	UINT		100		
16440	E2_H_200_PID_ACTION	Signed 16-bit	BOOL		1		
16441	E2_H_200_PID_HAB	Signed 16-bit	BOOL		1	E2_B_101_102_103_CMD	
16442	E2_H_001_PID_P	Unsigned 16-bit	UINT		100		
16443	E2_H_001_PID_I	Unsigned 16-bit	UINT		1000		
16444	E2_H_001_PID_D	Unsigned 16-bit	UINT		100		
16445	E2_H_001_PID_ACTION	Signed 16-bit	BOOL		1		
16446	E2_H_001_PID_HAB	Signed 16-bit	BOOL		1		
16447	E2_H_001_SETPOINT_T_011	Signed 16-bit	INT		0		
16448	E2_B_001_PID_P	Unsigned 16-bit	UINT		1500		
16449	E2_B_001_PID_I	Unsigned 16-bit	UINT		500		
16450	E2_B_001_PID_D	Unsigned 16-bit	UINT		900		
16451	E2_B_001_PID_ACTION	Signed 16-bit	BOOL		1		
16452	E2_B_001_PID_HAB	Signed 16-bit	BOOL		1		
16453	E2_B_001_SETPOINT_M_001	Signed 16-bit	INT		0		
16454	E2_B_001_SETPOINT_FREQ	Signed 16-bit	INT		200	200	600
16455	E2_B_001_CMD	Signed 16-bit	BOOL		1		
16456	E2_B_001_RESET_ALARM	Signed 16-bit	BOOL		0		
16457	E2_B_001_TIMER_TURN_OFF_ALARM_H001	Signed 16-bit	UDINT		200		
16458	E2_AMMONIA_TURN_ON	Signed 16-bit	BOOL		0		
16459	E2_AMMONIA_TURN_OFF	Signed 16-bit	BOOL		0		
16460	E2_AMMONIA_LOOP_RESET_POP_UP	Signed 16-bit	BOOL		0		

Address	Name	Device type	Application type	Size	Default value	Min	Max
16461	E2_COOLANT_LOOP_RESET_POP_UP	Signed 16-bit	BOOL		0		
16462	E2_HEATING_LOOP_RESET_POP_UP	Signed 16-bit	BOOL		0		

Status Variables

Address	Name	Device type	Application type	Size	Default value	Min	Max	Scale	Offset	Unit	Format	AccessL
8960	SV_B_101_102_ALARM	Signed 16-bit	BOOL					1	0			Always visible
8961	SV_B_103_ALARM	Signed 16-bit	BOOL					1	0			Always visible
8962	SV_B_104_ALARM	Signed 16-bit	BOOL					1	0			Always visible
8963	SV_F_001_ALARM	Signed 16-bit	BOOL					1	0			Always visible
8964	SV_F001_TEMP_ALARM	Signed 16-bit	BOOL					1	0			Always visible
8965	SV_B_200_VF_FREQ	Signed 16-bit	INT					1	0			Always visible
8966	SV_B_200_ALARM	Signed 16-bit	BOOL					1	0			Always visible
8967	SV_B_001_VF_FREQ	Signed 16-bit	INT					1	0			Always visible
8968	SV_B_001_ALARM	Signed 16-bit	BOOL					1	0			Always visible
8969	SV_T_130_TEMP_CONV	Signed 16-bit	INT					1	0			Always visible
8970	SV_T_200_OIL_TEMP_CONV	Signed 16-bit	INT					1	0			Always visible
8971	SV_T_011_CONV	Signed 16-bit	INT					1	0			Always visible
8972	SV_P_001_ABSORPTION_PRESSURE_CONV	Signed 16-bit	INT					1	0			Always visible
8973	SV_P_002_PUMP_DISCHARGE_CONV	Signed 16-bit	INT					1	0			Always visible
8974	SV_P_003_GENERATION_PRESSURE_CONV	Signed 16-bit	INT					1	0			Always visible
8975	SV_P_004_EVAPORATION_PRESSURE_CONV	Signed 16-bit	INT					1	0			Always visible
8976	SV_M_001_STRONG_SOLUTION_FLOWMETER_CONV	Signed 16-bit	INT					1	0			Always visible
8977	SV_M_200_OIL_FLOWMETER_CONV	Signed 16-bit	INT					1	0			Always visible
8978	SV_AMMONIA_POP_UP	Signed 16-bit	BOOL					1	0			Always visible
8979	SV_P_002_PUMP_DISCHARGE_HIGH_PRESSURE	Signed 16-bit	BOOL					1	0			Always visible
8980	SV_P_003_GENERATION_PRESSURE_HIGH_PRESSURE	Signed 16-bit	BOOL					1	0			Always visible
8981	SV_M_002_WEAK_SOLUTION_FLOWMETER	Signed 16-bit	INT					1	0			Always visible
8982	SV_M_003_AMMONIA_FLOWMETER	Signed 16-bit	INT					1	0			Always visible
8983	SV_F_001_AUTO	Signed 16-bit	BOOL					1	0			Always visible
8984	SV_F_001_RUN	Signed 16-bit	BOOL					1	0			Always visible
8985	SV_F_001_TEMP	Signed 16-bit	INT					1	0			Always visible
8986	SV_B_104_TEMP	Signed 16-bit	INT					1	0			Always visible
8987	SV_AMMONIA_LOOP_POP_UP	Signed 16-bit	BOOL					1	0			Always visible
8988	SV_COOLANT_LOOP_POP_UP	Signed 16-bit	BOOL					1	0			Always visible
8989	SV_HEATING_LOOP_POP_UP	Signed 16-bit	BOOL					1	0			Always visible
8990	SV_COOLANT_LOOP_ALARM	Signed 16-bit	BOOL					1	0			Always visible

PROGRAM B_101_102

```
        VAR
B_101_102 : partida;
    END_VAR
```

1

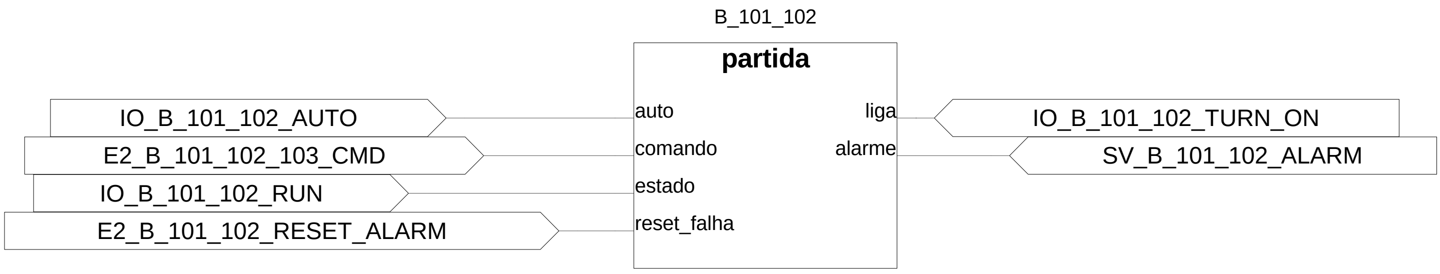

Project : PLC_01_PLC PROGRAM : B_101_102	
Release : PLC_01_PLC	Ver :1.00
Author :	Date:15/06/2020
Note :	Page:1 of 1

PROGRAM B_103

```
       VAR
B_103 : partida;
VF_FREQ : Convert;
FREQ : INT;
zzxczx : CTD;
NONAME : INT;
   END_VAR
```

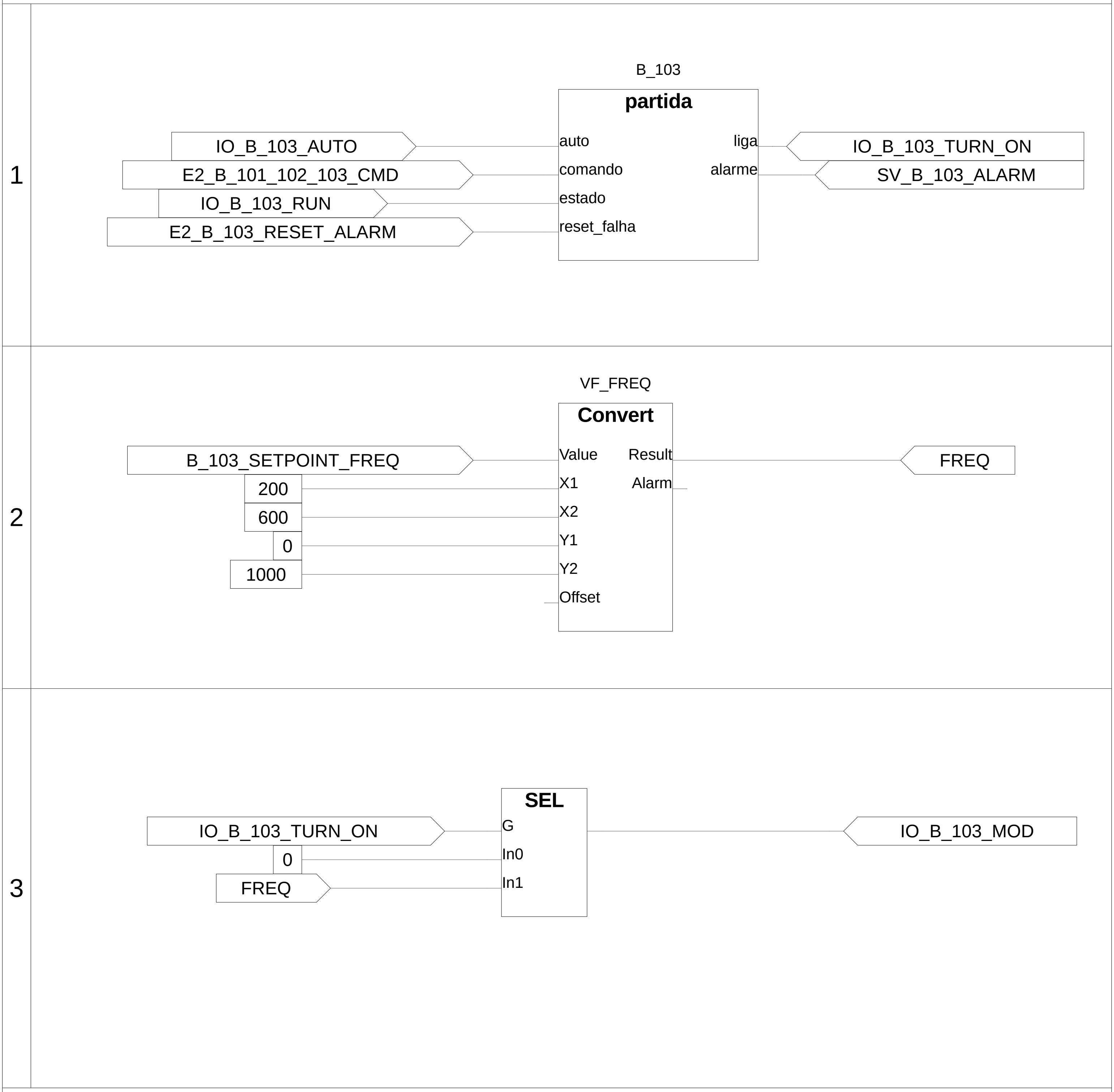

Project : PLC_01_PLC PROGRAM : B_103	
Release : PLC_01_PLC	Ver :1.00
Author :	Date:15/06/2020
Note :	Page:1 of 1

PROGRAM B_104

```
      VAR
B_104 : partida;
B_104_AUTO : BOOL;
pid : PID_Timed;
B_104_RUN : BOOL;
NONAME : INT;
   END_VAR
```

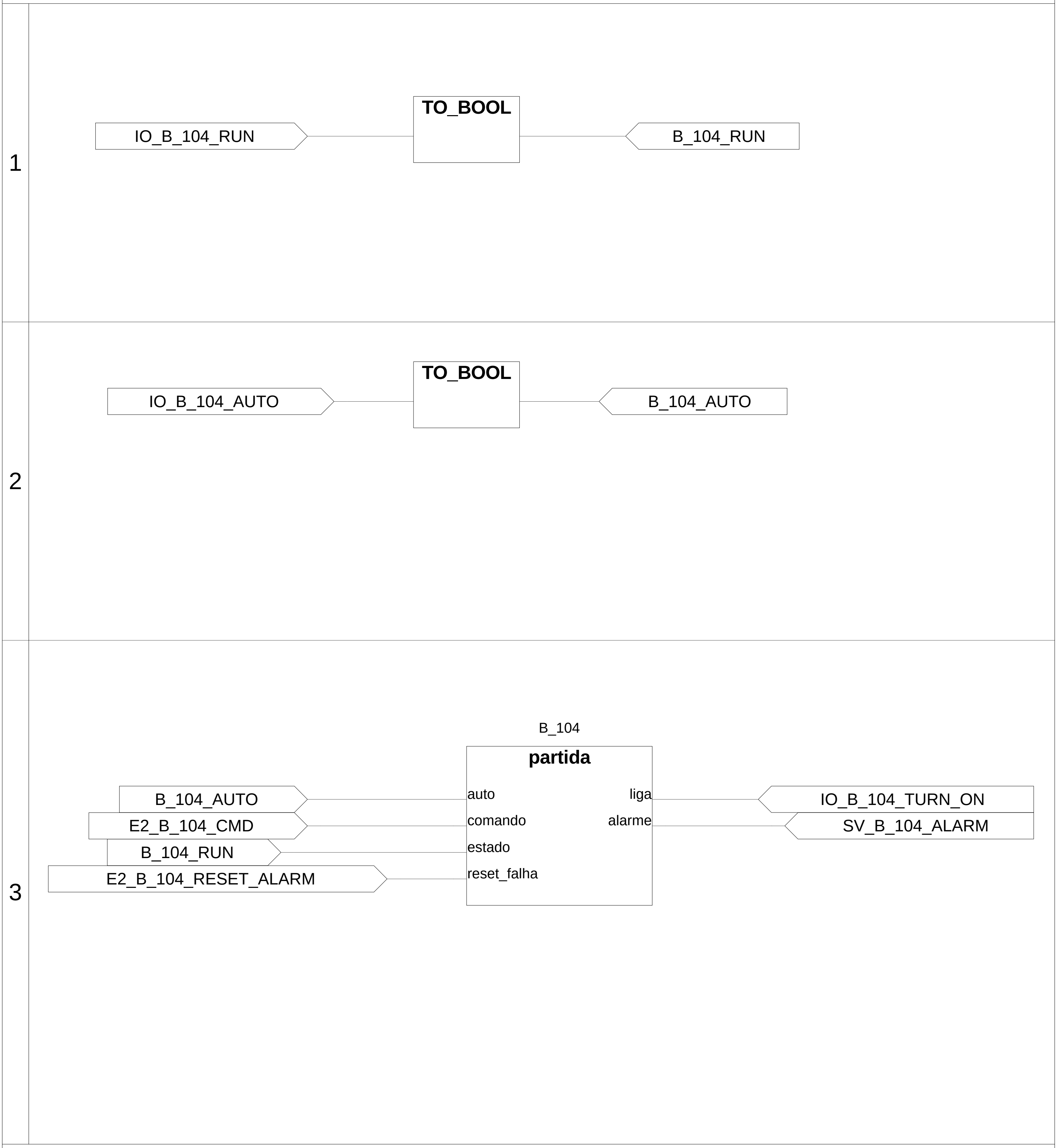

Project : PLC_01_PLC PROGRAM : B_104	
Release : PLC_01_PLC	Ver :1.00
Author :	Date:15/06/2020
Note :	Page:1 of 1

PROGRAM F_001

```
      VAR
F_001 : partida;
RS1 : RS;
perm : BOOL;
ton1 : TON;
   END_VAR
```

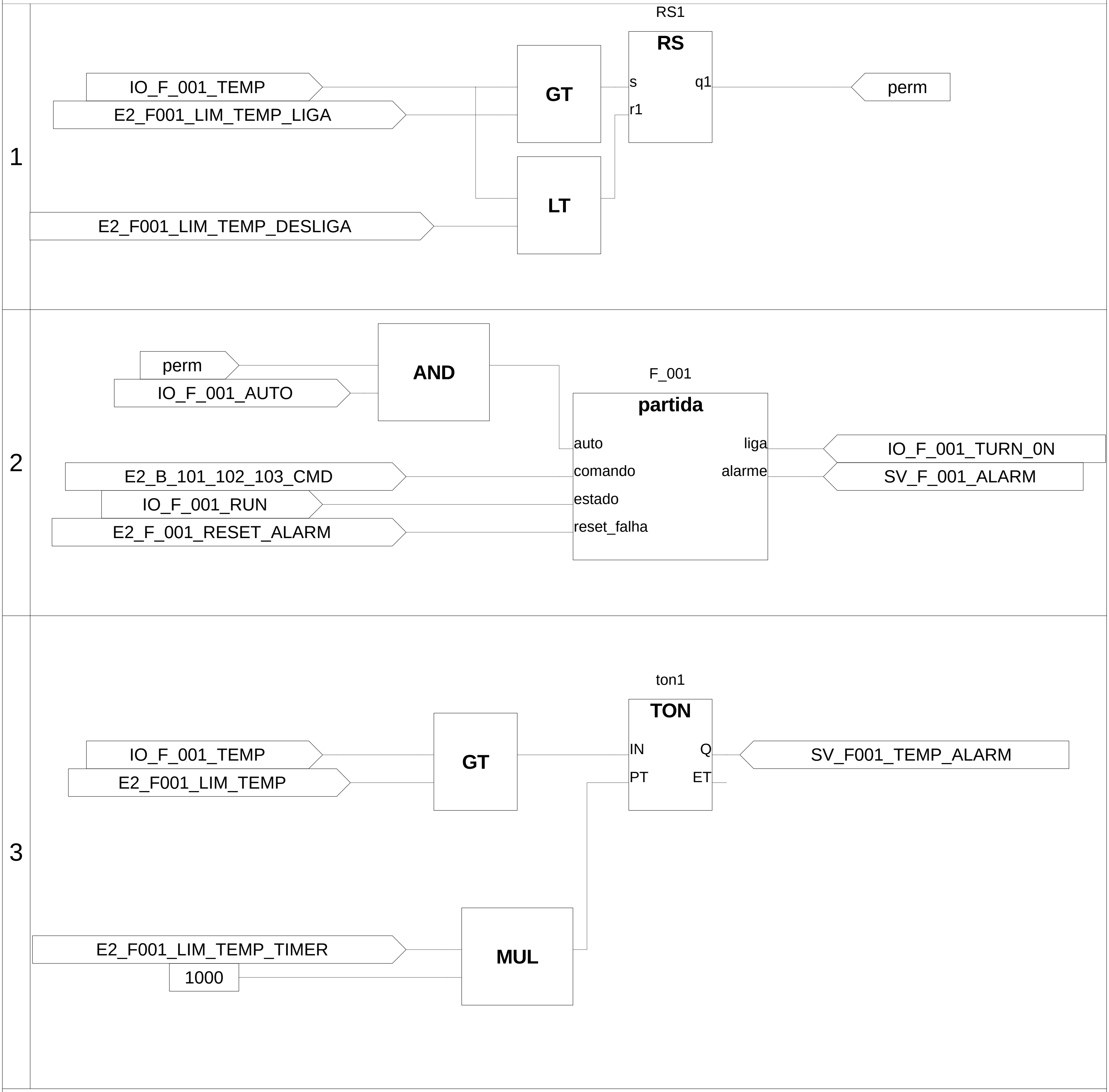

Project : PLC_01_PLC PROGRAM : F_001	
Release : PLC_01_PLC	Ver :1.00
Author :	Date:15/06/2020
Note :	Page:1 of 1

PROGRAM B_200

```
        VAR
B_200 : partida;
B_200_PID : PID_Timed;
mod_pid : INT;
VF_FREQ_1 : Convert;
b_turn_off : BOOL;
ton1 : TON;
ton1_0 : TON;
conv2_0 : Convert;
   END_VAR
```

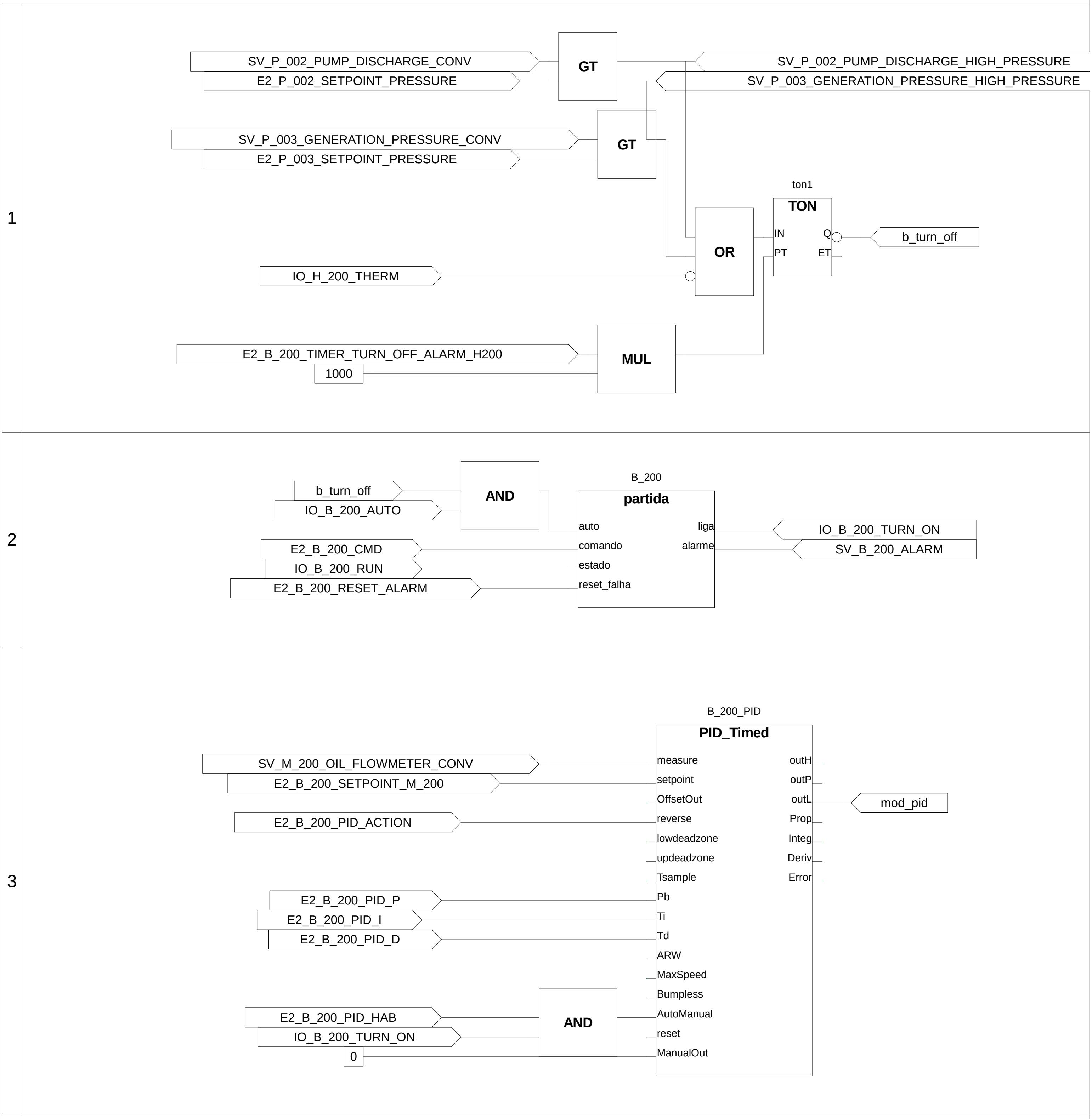

Project : PLC_01_PLC PROGRAM : B_200	
Release : PLC_01_PLC	Ver :1.00
Author :	Date:15/06/2020
Note :	Page:1 of 2

4

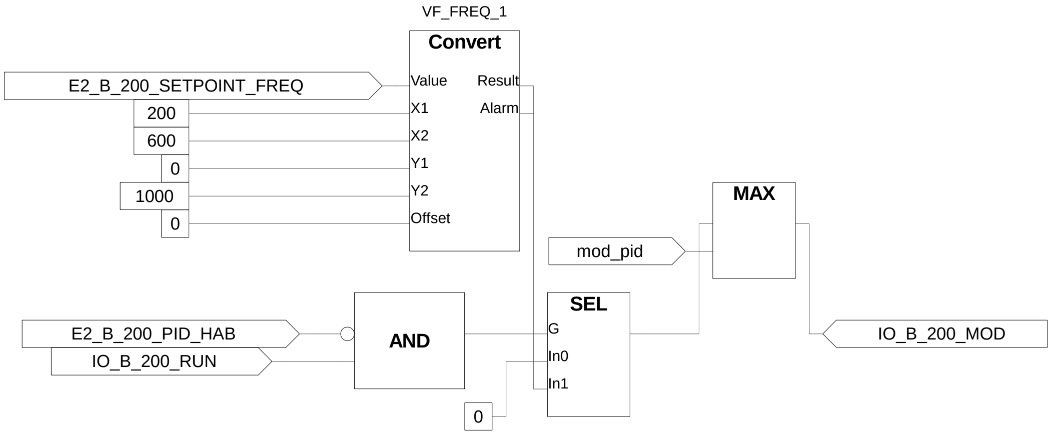

5

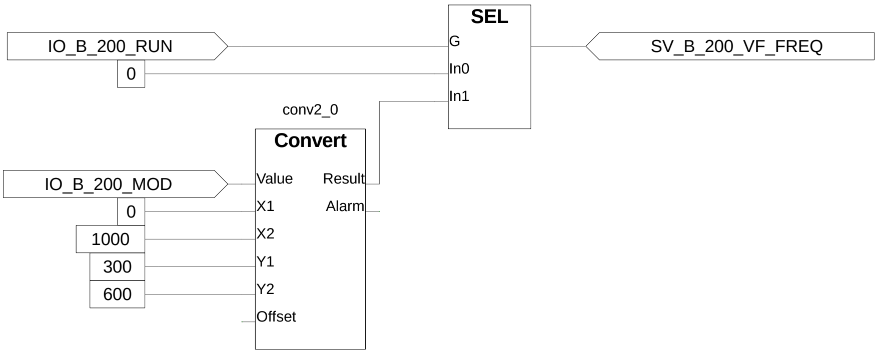

Project : PLC_01_PLC PROGRAM : B_200	
Release : PLC_01_PLC	Ver :1.00
Author :	Date:15/06/2020
Note :	Page:2 of 2

PROGRAM H_200

```
        VAR
perm : BOOL;
H_200_PID : PID_Timed;
    END_VAR
```

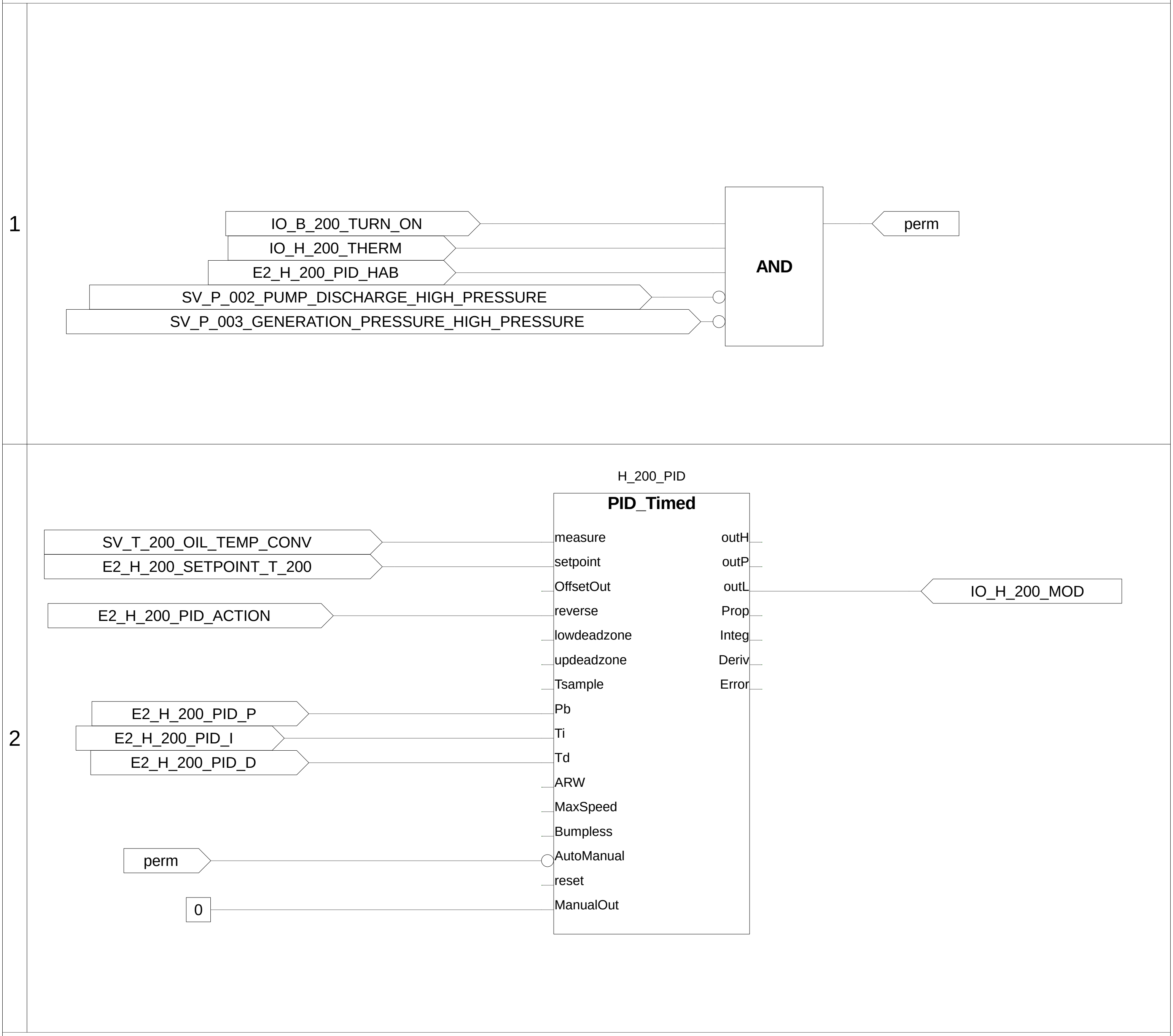

Project : PLC_01_PLC PROGRAM : H_200	
Release : PLC_01_PLC	Ver :1.00
Author :	Date:15/06/2020
Note :	Page:1 of 1

PROGRAM B_001

```
      VAR
B_001_PID : PID_Timed;
mod_pid : INT;
VF_FREQ_1 : Convert;
rs1 : RS;
r_trig1 : R_TRIG;
rs2 : RS;
ammonia_perm : BOOL;
B_001_permissao : permissao;
ton1 : TON;
perm : BOOL;
HPS_001_high_pressure : BOOL;
b_001_perm : BOOL;
r_trig2 : R_TRIG;
conv2 : Convert;
conv2_0 : Convert;
teste1 : ARRAY[ 0..129 ] OF BOOL;
   END_VAR
```

1

Analog input is used as digital inlet. High Pressure Switch HPS-001 is installed at the ammonia-water circuit and it's 17.5 bar fixed.

Channel Cfg_AI-10 - DI. Current automation block converts true/false to 0/1 bool

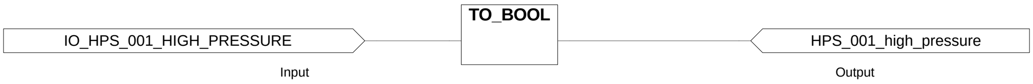

2

Status variables SV from High pressure for pump discharge P-002 (Channel AI-6) and generation pressure P-003 (Channel AI-7) transductors.

Status variables SV for Fan cooler status F-001 (Channel - DI-2 EVE) and Status Strong Solution Electrical Resistance (Channel DI-5).

On-delay timer

IN= Timper input

PT= Preset time value

Q=Timer output

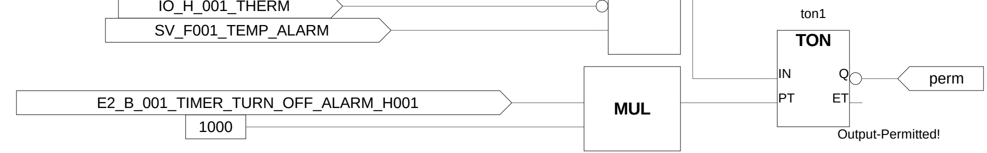

Output-Permitted!

EEPROM E - E2 B-001 Timer - 300ms x 1000= 30s to turn off

Requirements to turn on the strong solution pump B-001

3

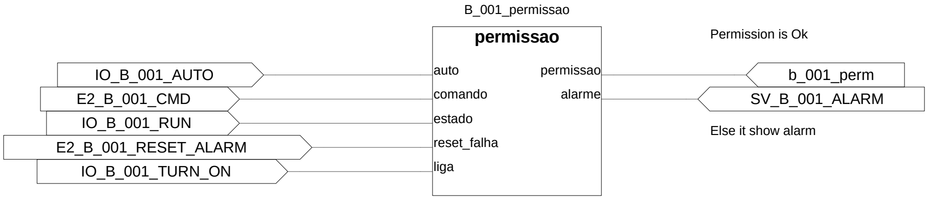

Permission is Ok

Else it show alarm

Requirements to turn on the strong solution pump B-001

(Auto mode) IO_B_001_AUTO, (No fail status) E2_B_001_CMD,

(On Bottom) IO_B_001_RUN, (Reset alarm if it applies) E2_B_001_RESET_ALARM,

(Feedback pump is on) IO_B_001_TURN_ON

4

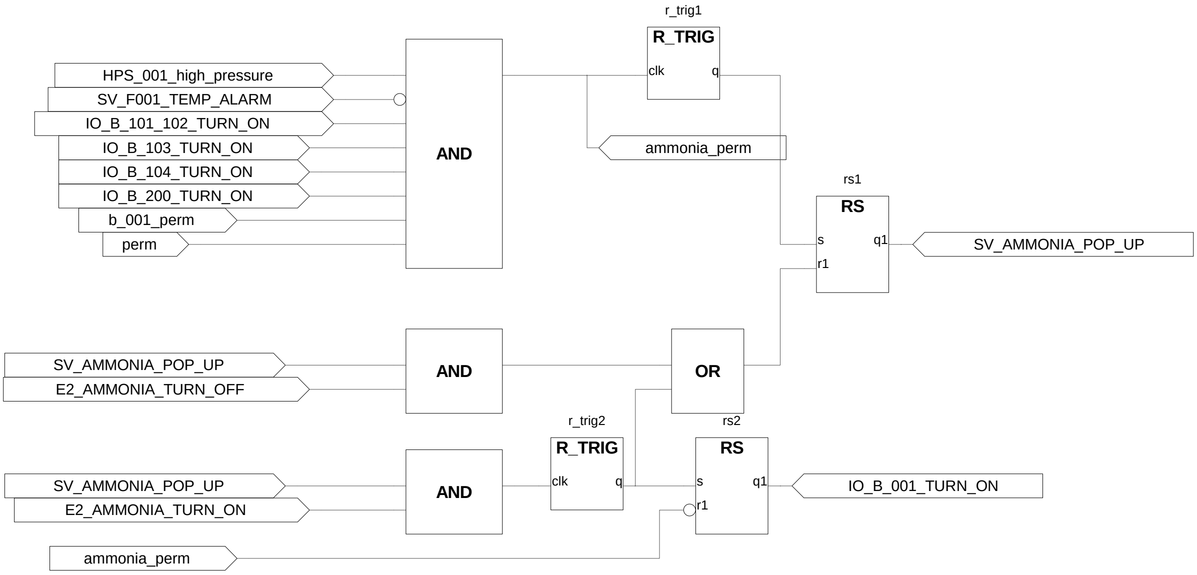

Project : PLC_01_PLC PROGRAM : B_001	
Release : PLC_01_PLC	Ver :1.00
Author :	Date:15/06/2020
Note :	Page:1 of 2

5

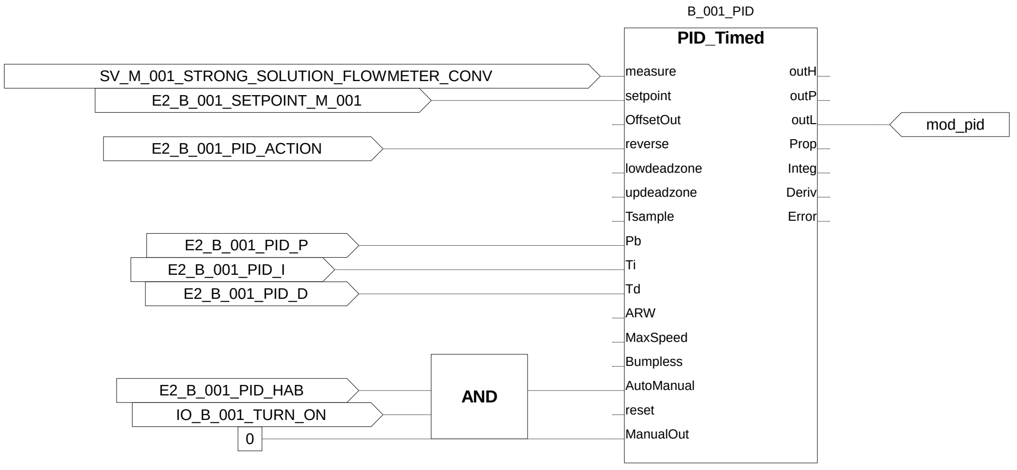
B_001_PID
PID_Timed
SV_M_001_STRONG_SOLUTION_FLOWMETER_CONV
E2_B_001_SETPOINT_M_001
E2_B_001_PID_ACTION
E2_B_001_PID_P
E2_B_001_PID_I
E2_B_001_PID_D
E2_B_001_PID_HAB
IO_B_001_TURN_ON
0
AND
measure
setpoint
OffsetOut
reverse
lowdeadzone
updeadzone
Tsample
Pb
Ti
Td
ARW
MaxSpeed
Bumpless
AutoManual
reset
ManualOut
outH
outP
outL
Prop
Integ
Deriv
Error
mod_pid

6

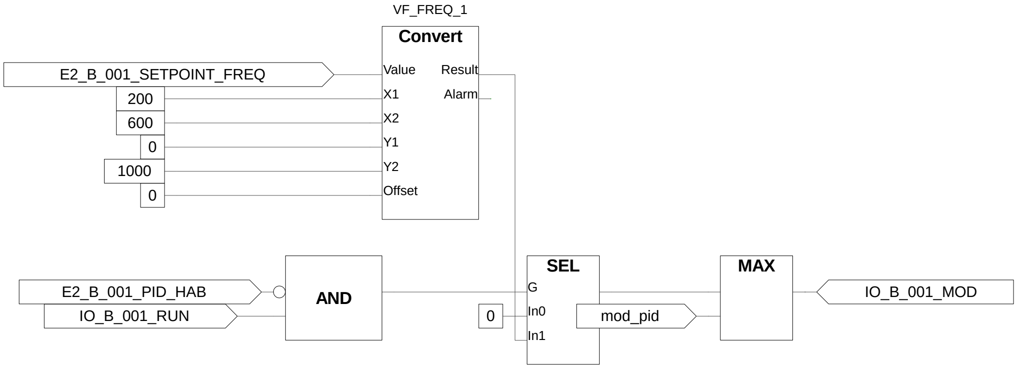
VF_FREQ_1
Convert
E2_B_001_SETPOINT_FREQ
200
600
0
1000
0
Value
X1
X2
Y1
Y2
Offset
Result
Alarm
E2_B_001_PID_HAB
IO_B_001_RUN
AND
SEL
G
In0
In1
0
mod_pid
MAX
IO_B_001_MOD

7

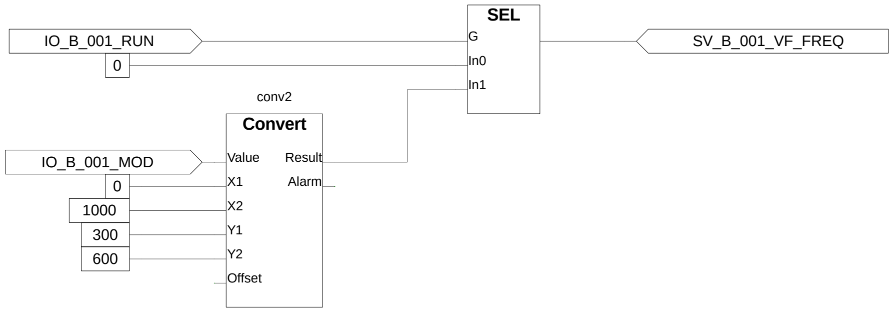
SEL
G
In0
In1
IO_B_001_RUN
0
SV_B_001_VF_FREQ
conv2
Convert
IO_B_001_MOD
0
1000
300
600
Value
X1
X2
Y1
Y2
Offset
Result
Alarm

ANNEX D

Strong solution pump

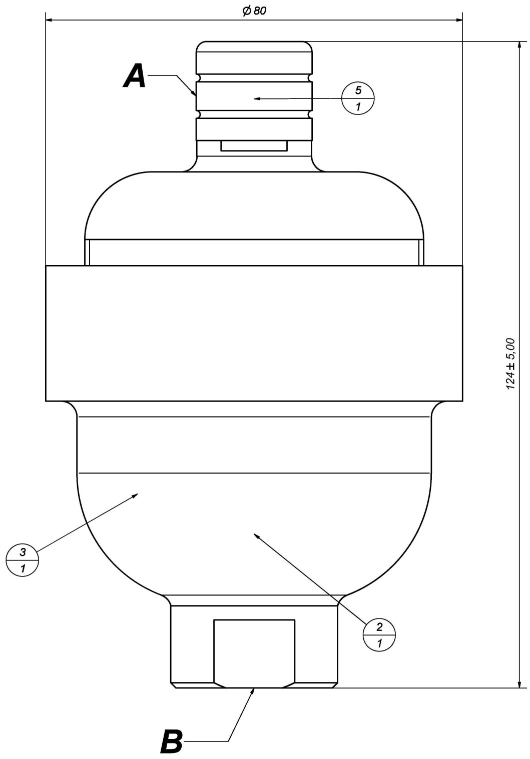

DADOS TECNICOS			
NORMA CONS.: ASME SEC VIII DIV.I			
TIPO DE CONSTRUÇÃO: ROSCADO			
NORMA DE SOLDA: S/ SOLDA			
DADOS DO PROJETO			
PRESSÃO DE PROJETO	BAR	220	220
TEMPERATURA DE PROJETO	°C	100	100
PRESSÃO MAX. TRAB. ADM.	BAR	220	220
TEMPERATURA DE SERVIÇO	°C	70	70
PRESSÃO DE TESTE	BAR	286	286
RADIOGRAFIA CILINDRO	---	NÃO	---
EFICIENCIA DAS JUNTAS	---	S/SOLDA	---
ALIVIO DE TENSÃO	---	S/SOLDA	---
TOLERANCIA A CORROSÃO	---	0	---
FLUIDO	---	ÁGUA	NITROGÊNIO
		ACUMULADOR	MEMBRANA

CONEXÕES						
POS.	QTD.	DIÂMETRO	CLASSE	PESC. ESP.	DENOMINAÇÃO	OBSERVAÇÃO
A	01	5/8" UNF	220	---	CARRE. N2	---
B	01	1/2" NPT	220	---	ENTRAD./SAIDA OLEO	---

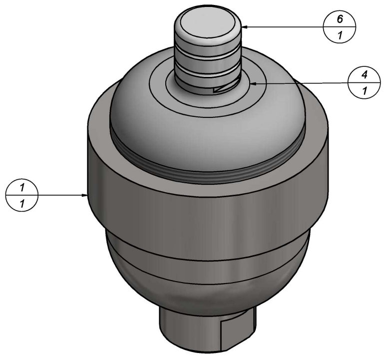

01	01		CONF.TABELA	CONF.TABELA
REV.	QTD.	DESCRIÇÃO	MATERIAL	CÓD. MATERIAL

TOLERÂNCIAS LINEARES						
0 A 6	6 A 30	30 A 120	120 A 315	315 A 1000	1000 A 2000	2000 A 4000
± 0,1	± 0,2	± 0,3	± 0,5	± 0,8	± 1,2	± 2

DIN 7168 (MÉDIO)

TOLERÂNCIAS ÂNGULARES			
ATÉ 10mm	ACIMA 10mm ATÉ 50mm	ACIMA 50mm ATÉ 120mm	ACIMA 120mm
1°	30°	20°	10°

DIREITOS DE REPRODUÇÃO TOTAL OU PARCIAL RESERVADOS.

SUPERFÍCIE DIN 3141 - Gr. 3.					
SIMBOLO:	∼	▽	▽▽	▽▽▽	▽▽▽▽
Rt (µm) 1µm = 0,001mm	BRUTO	16	6,3	4	1

CONJUNTO:
ACUMULADOR MEMBRANA ROSCADO 0,2 LITRO
VITON AISI 316L - 1/2 NPT

INSTRUVIAL
Equipamentos Industriais

Nº DO DESENHO:
02.00.0014

CÓDIGO DE SISTEMA
015-00007

LISTA DE MATERIAIS				
ITEM	QTY	DESENHO	DESCRIÇÃO	MATERIAL
1	1	02.03.0029	CORPO INFERIOR	AISI 316L
2	1	02.03.0021	POSTIÇO PARA MEMBRANA 0,2 L	AISI 316L
3	1	02.03.0019	MEMBRANA VITON 0,2 LITROS	VITON
4	1	02.01.0002	CORPO SUPERIOR	AISI 316L
5	1	01.01.0005	NUCLEO DA VALVULA	AISI 316L
6	1	01.01.0017	PROTETOR DA VALVULA	ALUMÍNIO

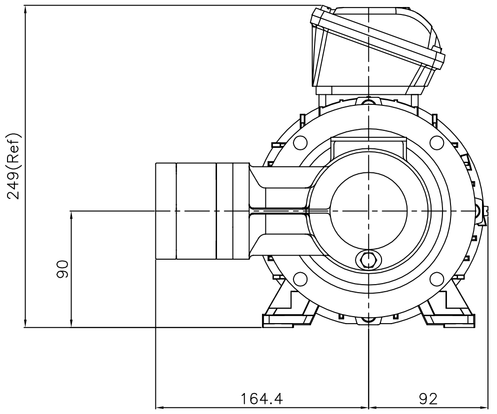

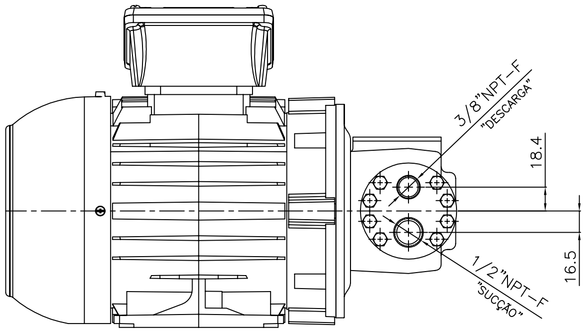

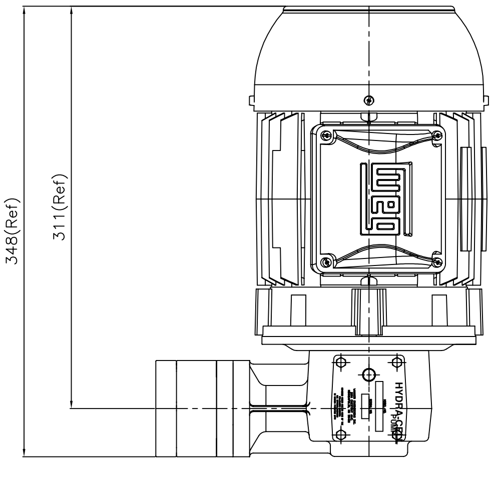

Título: CONJ. MOTO BOMBA - F20XASEHFEHJ		Nome	Data	Revisão:
Desenho nº: MB-P-H-MM-A72-000-000	Projetado por:	FFB	18/02/19	Massa:
	Revisado por:	MDF	18/02/19	Escala:
Material: N/A	Aprovado por:	CMA	19/02/19	Folha: 1 /1 Tam: A3

F			
E			
D			
C			
B			
A	Primeira Liberação	FFB	18/02/19
	Anotação de revisão	Autor	Data

Observações:
-Todas as dimensões em milímetros, exceto onde especificado

INSTRUVIAL
Equipamentos Industriais